

**DEVELOPMENT AND MICROSTRUCTURAL IMPROVEMENT
OF SPIN CAST HIGH-SPEED STEEL ROLLS**

by

Konstantin V. Redkin

M.S., Materials Science and Engineering, University of Pittsburgh, USA, 2009

M.S., Civil and Industrial Engineering, South Ural State University, Russia, 2004

Submitted to the Graduate Faculty of
Swanson School of Engineering in partial fulfillment
of the requirements for the degree of
Doctor of Philosophy

University of Pittsburgh

2013

UNIVERSITY OF PITTSBURGH
SWANSON SCHOOL OF ENGINEERING

This dissertation was presented

by

Konstantin V. Redkin

It was defended on

July 24, 2013

and approved by

Jeffrey S. Vipperman, Ph.D., Associate Professor,

Department of Mechanical Engineering and Materials Science

Calixto Isaac Garcia, Ph.D., Research Professor,

Department of Mechanical Engineering and Materials Science

Patrick Smolinski, Ph.D., Associate Professor,

Department of Mechanical Engineering and Materials Science

Piervincenzo Rizzo, Ph.D., Associate Professor,

Department of Civil and Environmental Engineering

Dissertation Director: Jeffrey S. Vipperman, Ph.D., Associate Professor,

Department of Mechanical Engineering and Materials Science

Copyright © by Konstantin V. Redkin

2013

DEVELOPMENT AND MICROSTRUCTURAL IMPROVEMENT OF SPIN CAST HIGH-SPEED STEEL ROLLS

Konstantin V. Redkin, PhD

University of Pittsburgh, 2013

A detailed microstructural analysis was conducted on a series of radial shell samples extracted from commercially produced centrifugally spin casted high-speed steel (HSS) work rolls for finishing hot strip mills (HSM). The systematic microstructural analysis was coupled with a numerical and experimental investigation to improve the life of HSS rolls. An integrated computational-experimental approach was developed to optimize the response of the HSS roll material that permitted the enhancement of the microstructure and properties of the HSS roll shell layer. Local continuous microstructural transformations through the thickness of the shell: carbide formation, precipitation, dissolution sequence and phase changes, were studied in great details. The analyses were conducted with the aid of advanced metallographic and experimental methods, finite-element (FE) analysis, and using commercial software systems to conduct thermodynamic-kinetics predictions.

In order to analyze a response of the HSS roll to the hardening heat treatment (HT) and to control stress-strain evolution, a 3-D FE model was developed of the composite structure of the roll. The multilayered model considers nonlinear material properties of each individual layer as a function of temperature, based on measured chemical composition gradients through the HSS shell. Transient coupled thermal-stress analysis was performed, using actual measured surface temperatures as boundary conditions (BC) for the FE model. The allowable thermal stress-strain levels were established and compared with a) thermodynamically predicted high temperature

mechanical properties and b) room temperature test results of the shear strengths for the shell, bonding and core. In addition, sub-structuring and image-based processing techniques were implemented to aid in the development of a meso-scale FE model to simulate the local response of a given microstructural constituents and matrix under particular thermal conditions. The fundamental interpretation of multilayered structure and multi-scale approach help to understand the kinetics phenomena associated with continuous local microstructural transformations due to nonlinear heat transfer. The results from the microstructural observations were in good agreement with the numerical predictions.

The major impact of this work clearly indicated that a refined as-cast structure prior to the heat treatment promoted an increased precipitation of carbides during final hardening, which greatly improved strength and performance. A non-conventional HT was defined and implemented in order to provide an additional degree of microstructural pre-conditioning, which homogenized the matrix throughout the HSS shell. The new HT defined the austenitization temperatures and times to modify the morphology of brittle interdendritic eutectic carbide networks and, hence, facilitating the kinetics of dissolution of these carbides. This behavior caused an increase in the solute content of the matrix. As a result, the matrix hardness and strength were increased during subsequent hardening HT in comparison to the conventional HT routes used for as-cast HSS rolls. Reports about rolls with the new material that have been placed in service indicate that the rolls last 50-70% longer.

TABLE OF CONTENTS

PREFACE.....	XVII
1.0 BACKGROUND OF HSS ROLLS.....	1
1.1 HORIZONTAL CENTRIFUGAL CASTING	18
1.2 HIGH TEMPERATURE HARDENING HEAT TREATMENTS	23
1.3 NUMERICAL MODELING AND SIMULATIONS OF THE ROLLS.....	31
1.3.1 Finite element modeling approach	31
1.3.2 Computational thermodynamics and kinetics	34
1.3.3 Computational fluid dynamics approach	34
2.0 AIMS AND OBJECTIVES	36
3.0 EXPERIMENTAL PROCEDURES	41
3.1 MATERIALS DESCRIPTION	41
3.2 METALLOGRAPHY AND SAMPLE PREPARATION.....	43
3.2.1 Sample preparation and chemical etching	43
3.2.2 Optical-digital microscopy.....	44
3.2.3 Hardness measurements and Optical Emission Spectroscopy (OES)	44
3.2.4 Scanning electron microscopy	46
3.2.5 Electron backscatter diffraction.....	47
3.2.6 Image analysis and processing.....	47
3.2.7 X-ray diffraction analysis	48
3.3 RE-HEATING–RE-MELTING PROCEDURES.....	51
3.4 THERMODYNAMIC-KINETIC ANALYSIS	52

3.5	NUMERICAL ANALYSIS	53
3.5.1	CFD formulation.....	54
3.5.2	FEA formulation.....	60
3.5.2.1	Sub-structured 1-D radial models	61
3.5.2.2	Axisymmetric longitudinal model.....	69
3.5.2.3	Full-scale roll model.....	70
3.5.2.4	Image-based microstructural FEA	76
3.5.2.5	Statistics, work flow and models summary	81
4.0	RESULTS AND DISCUSSION	87
4.1	THERMODYNAMIC AND KINETICS PHASE TRANSFORMATIONS.	89
4.2	MICROSTRUCTURAL ANALYSIS	106
4.2.1	Analysis of as-cast microstructure	114
4.2.2	The role of preliminary heat treatment.....	123
4.2.3	Hardening response using conventional and non-conventional heat treatments	129
4.2.4	Proposed model of microstructural evolution in HSS material	135
4.3	CFD APPROACH TO EXPLAIN CAST SEGREGATIONS	145
4.4	FINITE-ELEMENT MODELING.....	147
4.4.1	Sub-structured 1-D radial thermal models	148
4.4.2	Axisymmetric thermal model	154
4.4.3	Coupled thermal-structural analysis of the full-scale HSS roll.....	155
4.4.4	Micro-scale heat transport.....	159
4.5	EXPERIMENTAL CHARACTERIZATION.....	164
4.5.1	Ambient and in-situ high temperature X-Ray diffraction analysis	164
4.5.2	Bulk and microhardness analysis.....	172

	4.5.3 Image processing and phase balance analysis.....	179
5.0	CONCLUSIONS	186
6.0	SUMMARY	190
7.0	FUTURE RESEARCH	192
	BIBLIOGRAPHY	195

LIST OF TABLES

Table 1. Typical chemical HSS composition (wt%).....	5
Table 2. Analyzed HSS shell samples	42
Table 3. FE models and associated mesh statistics.....	81
Table 4. Predicted transformations as a function of temperature and %C variations.....	98
Table 5. Summary of microstructural observations.....	138
Table 6. General schematics of microstructure evolution in HSS shell during HT.....	140
Table 7. Detected oxides vs. temperature	171

LIST OF FIGURES

Figure 1. Schematic of a finishing stand in HSM.....	3
Figure 2. Structure of HSS roll: (a) schematics of radial cross-section of a roll body, (b) actual as-cast roll, (c) CAD model of bi-metallic HSS roll, (d) transitional microstructure of conventional as-cast HSS shell	4
Figure 3. Example of typical ductile iron core microstructure	5
Figure 4. Schematic layout of different types of rolls in a hot strip mill (HSM).....	7
Figure 5. Actual HSM train in operation [15].....	7
Figure 6. Extreme hot rolling conditions at HSS stands [15]	8
Figure 7. Examples of catastrophic failures of the rolls: a) de-bonding between the shell and core, b) transverse brittle fracture of the barrel due to thermal shock, c) overload at the brittle neck	9
Figure 8. Roll bite behavior in the strip	12
Figure 9. Contacts stress: a) photoelastic image of the contact [29], b) rolling simulation [30] ..	13
Figure 10. Transformed 2-D SEM images (ImageJ): (a) tempered martensitic matrix with secondary $M_{23}C_6$, Cr-rich carbides and eutectic MC, V-rich; (b) interdendritic region with retained austenite and partially decomposed eutectic M_2C (Mo-rich) into M_6C and MC carbides	14
Figure 11. Thermal fatigue cracks	16
Figure 12. Main stages of horizontal centrifugal casting with stationary vertical core pouring ..	20
Figure 13. Free body diagram of a particle in centrifugal field	21
Figure 14. Effect of austenitization temperature and time on hardness (HRC) [67]	27
Figure 15. General schematics of high temperature hardening	28
Figure 16. HSS tested coupons and high temperature XRD procedure.....	49

Figure 17. Temperature steps with regard to predicted equilibrium diagrams	50
Figure 18. Temperature-time profiles of the re-heating-re-melting procedures	51
Figure 19. HSS coupons with attached thermocouples in Dilatometry furnace	52
Figure 20. Predicted liquid viscosity as a function temperature and composition	55
Figure 21. Predicted density as a function temperature and composition	56
Figure 22. CFD model: domain geometry and meshing	57
Figure 23. Radial semi-1-D sub-structured model of the HSS shell and core	61
Figure 24. Radial sub-structured models of the roll	62
Figure 25. Radial cut-off HSS sample with sparks on surface from GD-OES measurements	63
Figure 26. Measured compositional gradient along the HSS shell, intermix and core	64
Figure 27. Predicted density of the layers vs. temperature	65
Figure 28. Predicted thermal conductivity of the layers vs. temperature	65
Figure 29. Predicted specific heat of the layers vs. temperature	66
Figure 30. Considered surface boundary condition scenarios	67
Figure 31. Example of mesh quality control in 11-layer radial model: (a) original mesh, (b) highlighted error estimates at contacts due to different mesh sizes	68
Figure 32. CAD roll model: (a) full-scale roll model, (b) 10°-axisymmetric model	69
Figure 33. BCs of axisymmetric model: combined external temperature and convection	70
Figure 34. Full-scale modeling: (a) original CAD drawing of the roll geometry, (b) imported and meshed CAD model in ANSYS WB	71
Figure 35. Predicted instantaneous linear expansion coefficients of the layers vs. temperature ..	72
Figure 36. Predicted Young's modulus of the layers vs. temperature	72
Figure 37. Generated material database in ANSYS WB	73
Figure 38. ANSYS WB: coupled thermal-stress analysis schematic	74
Figure 39. ANSYS WB: project tree of coupled thermal-stress analysis	75

Figure 40. FE shape quality control in full-scale 3-D model by interactive individual bar selection	76
Figure 41. Selected region for micro-scale heat transport analysis	79
Figure 42. Meso-scale model: processed SEM micrograph imported as CAD model to ANSYS WB	79
Figure 43. Predicted thermal properties of the carbides and matrix for the meso-scale FE model	80
Figure 44. General work flow of multi-scale FE thermal approach	82
Figure 45. Scheme I. Multi-scale multi-physical FEM formulation: actual geometry→ CAD model→ Meshing→ Prediction of material properties as a function of temperature, using measured compositions→ Assignment of NL properties to each individual domain→ Apply pyrometer (or infra-red) readings as BCs→ perform transient heat analysis coupled with transient structural→ compare observed microstructure and calculated heating-cooling rates	84
Figure 46. Scheme II. Image processing and FE discretization of a local point in the HSS shell: boundaries detection, vectorization of SEM micrograph→ transferring created CAD model to CAE→ meshing and BCs assignment	86
Figure 47. Predicted solidification patterns of fixed composition in: a) Pandat , b) JmatPro	90
Figure 48. Solidification: (a) predicted bulk composition as function of temperature during solidification, (b) predicted solid and liquid phase balance.....	92
Figure 49. Predicted carbon concentration in individual phase during solidification	92
Figure 50. Predicted density of each phase during solidification	94
Figure 51. Radial measurements of volume fraction of eutectic carbides in as-cast shell (S-shell)	95
Figure 52. Comparison of low and high carbon groups and its effect on the predicted liquid-solid region	96
Figure 53. Predicted equilibrium carbon diagram at the high temperature region	97
Figure 54. Predicted equilibrium phase fractions as a function of temperature (fixed composition)	99
Figure 55. Predicted carbon concentration in each phase as a function of temperature (equilibrium)	100
Figure 56. Equilibrium diagrams of intermix and core materials	101

Figure 57. Predicted CCT-TTT diagrams (100 μm grain size).....	102
Figure 58. Predicted CCT-TTT diagrams (250 μm grain size).....	103
Figure 59. Effect of different HT on surface of HSS shell (top left: P0-cast; top right: P0-P; bottom left: P0-A; bottom right: P0-P+A, Table 2)	107
Figure 60. Clean γ -eutectic cells with decorating M ₂ C and MC.....	108
Figure 61. Formed petal-like MC inside γ -eutectic cells.....	108
Figure 62. Coral-like MC developed inside γ -eutectic cells.....	108
Figure 63. Radial HSS shell with conventional microstructure (P0-cast) and associated HRC hardness profile.....	109
Figure 64. Hardness profile vs. bulk chemical variations (conventional case)	110
Figure 65. Continuous pearlite development in conventional HSS material within intermix region (surface to core; analogy with pearlite colonies development for rail steel by Arzamasov, [44]).....	112
Figure 66. (a) Re-melted HSS as-cast material in the lab conditions (no centrifugal field): example of dendrite growth and formation of solute-rich boundaries with coral-like eutectic MC carbides, V-rich (dark grey) and M ₂ C, Mo-rich (white) at accelerated air cooling; (b) example of dendrite clusters formation in centrifugal field (Murakami etching; clusters highlighted with curved dash-lines).....	115
Figure 67. EDS line scanning of the solute-rich eutectic boundaries in the refined cast (S-shell)	116
Figure 68. Point-wise EBSD of V _x C _y and surrounding matrix: (a) highlighted scanned points on the surface of V _x C _y eutectic carbide, (b) example of Kikuchi pattern for individual point	117
Figure 69. 2-D EDS mapping of eutectic boundary region in the conventional cast, including fibrous-like troostite pearlite (Cr-rich fibers and Mo-rich tips) and eutectic M ₂ C (Mo _x Cr _y C), MC (V _x C _y) carbides.....	118
Figure 70. Conventional cast showing fibers of troostite with Mo-rich tips	120
Figure 71. Conventional cast showing M ₂₃ C ₆ (Cr-rich) in conventional matrix	120

Figure 72. Refined as-cast solute-rich boundary' rims with fine $(\text{Mo-V-Cr})_x\text{C}_y$ (white); $(\text{Cr-Mo})_x\text{C}_y$ (dark).....	120
Figure 73. Refined as-cast mixed matrix with fine secondary precipitation along α' plates.....	120
Figure 74. General schematic of as-cast microstructure.....	121
Figure 75. Effect of initial as-cast condition and different bulk composition on response to preliminary HT: (a) P0-P (conventional), (b) SPH-P (refined cast)	124
Figure 76. EDS line scanning, showing local segregation and nonhomogeneous matrix of conventionally cast HSS material (P0-P) after preliminary HT nearby solute-rich eutectic boundaries	125
Figure 77. EDS spot scans on V-rich complex blocky carbide unaffected by preliminary HT .	126
Figure 78. Preliminary HT (SPH-P). Mixed spheroidized and lamellar matrix structure with eutectic MC, precipitated $(\text{V-Mo-Cr})_x\text{C}_y$ alloy carbides and new spheroidized ppts	127
Figure 79. Preliminary HT (SPH-P). Interdendritic boundary with friable M_2C (white) and MC (dark).....	127
Figure 80. Schematic of preliminary heat treated microstructure for the refined cast material .	128
Figure 81. Partially transformed M_2C with fine Mo-V epitaxial carbides (conventional HT, CA41)	130
Figure 82. Zoomed transient Mo-V epitaxial peanut-like carbides (conventional HT, CA41)..	130
Figure 83. Broken interdendritic carbide networks (non-conventional approach, P9DT)	131
Figure 84. Improved matrix with $(\text{V-Cr-Mo})_x\text{C}_y$ precipitates, <200 nm (non-conventional, P9DT)	131
Figure 85. Comparison of microstructures after high temperature double (P9DT-left) and triple (P9TT- right) tempering HT	133
Figure 86. Generalization of the high temperature HT influence on the preliminary refined as-cast material	134
Figure 87. Microstructure evolution after different processing routes	138
Figure 88. Non-conventionally heat treated spun-cast HSS roll (a, b, e) versus CPC roll (c, d, f)	144
Figure 89. Velocity vector field distribution from 3-D CFD simulation of horizontal spin casting of the melt subjected to the centrifugal forces, [110]	146

Figure 90. Example of transient FE analysis of heating and quenching cycles (each section in the shell 6mm)	149
Figure 91. Predicted thermal profiles of 1-D models (3 vs. 11 layers): Case I ($T_{\gamma 1}$ - T_{i1}), Case II ($T_{\gamma 2}$ - T_{i2}) and Case 3 (pyrometer, $T_{\gamma 2}$ - T_{i2})	150
Figure 92. Comparison of 3 and 11-layers models ($T_{\gamma 1}$) with actual pyrometer readings ($T_{\gamma 2}$) vs. critical melting temperatures of individual layers	151
Figure 93. Pyrometer thermal loading ($T_{\gamma 2}$) at the surface and related response at the intermix and bonding	152
Figure 94. Temperature difference within layers.....	153
Figure 95. Predicted thermal gradients in the HSS layers	153
Figure 96. Isotherms at arbitrary times, showing heat front propagation	154
Figure 97. Comparison of axisymmetric and 3-, 11-layer 1-D radial models	155
Figure 98. Thermal profiles in (a) axisymmetric model compared with 1-D cases, (b) full-scale roll model.....	156
Figure 99. Predicted thermal-stresses due to thermal gradients	157
Figure 100. Resulting thermal strains in the HSS shell and intermediate layer	157
Figure 101. Resulting thermal stresses in the HSS shell and intermediate layer.....	158
Figure 102. Predicted mechanical properties of HSS shell during quenching as a function of the grain size	158
Figure 103. Example of nonlinear FE micro-scale heat transport simulation and its comparison with resulting microstructure: (a) SEM image of the as-cast microstructure; (b) meshed FE model of actual SEM image given in (a) ; (c) predicted total heat flux developed during heating cycle (heat flow- from left to right, vertical dash lines are the propagating heat front, the curved dash lines are the advancing flux at the Mo-rich boundaries); (d) directional heat flux (horizontal axes, negative direction, from right to left) due to quenching the left edge (vertical dash lines are the propagating heat flux (negative direction); curved lines are the residual retarded flux in the Mo-rich zones, leaving the cool front behind; (e) zoomed as-cast Mo-rich eutectic interdendritic carbides with troostite pearlite (dark area) as in (a); (f) resulting decomposed M_2C into M_6C and MC after high temperature hardening (after (c), (d) HT).	161
Figure 104. Scheme III: comparison of simulated heat fluxes and conventional hardened microstructure	162

Figure 105. Scheme IV: detailed microscopic observations, validating the micro-scale FE simulation.....	163
Figure 106. Example of conventional XRD profiles for different locations in HSS shell (BTK): surface (Loc1), middle (Loc2) and bonding (Loc3)	165
Figure 107. HT effect on crystal structure of high carbon P0 HSS shell: as-cast, combined preliminary and austenitization, individual preliminary and austenitization conditions	166
Figure 108. In-situ HT-XRD diffractograms for as-cast P0 and S-shell materials (high vs. low %C)	169
Figure 109. Example of lattice expansion behavior.....	170
Figure 110. Example of VHN hardness measurements along the conventional radial sample (P0-cast)	172
Figure 111. Averaged VHN profiles of conventional material (P0 samples, Table 2) vs. HT ...	173
Figure 112. Overall bulk HRC profiles of HSS radial samples	174
Figure 113. Selected bulk HRC profiles of conventional and improved materials	175
Figure 114. Micro-VHN of the matrix and carbides (Olympus and Keyence OM)	176
Figure 115. Micro-VHN of the matrix.....	176
Figure 116. HRC indenter and local deformation of the matrix (P9DT).....	178
Figure 117. Example of OM processing for individual carbides identification in P0-cast (Pax It)	180
Figure 118. Example of SEM micrograph processing (ImageJ): VC and Mo ₂ C selection (dark vs. white)	181
Figure 119. Total carbide volume fraction along the HSS shells	182
Figure 120. Volume fraction (%) of VC and Mo ₂ C along the P9DT HSS shell	183
Figure 121. Example of geometrical changes of VC along the P9DT shell	184

PREFACE

...A way to knowledge through the labyrinth

Thank God for being with me!

I would like to highly appreciate W. Fulbright International Scholarship, Bureau of Educational and Cultural Affairs, U.S. Department of States and University of Pittsburgh, Swanson School of Engineering, Mechanical Engineering and Materials Science Department for providing me a chance to achieve scientific-academic goals and enrich life with international experience. Special thanks go to Office of International Services (OIS), University of Pittsburgh.

My academic advisers, Dr. Jeffrey Vipperman, Dr. Patrick Smolinski, and Dr. Piervincenzo Rizzo, are gratefully acknowledged from the bottom of my heart for their help, guidance, challenging questions and thesis revision. Special appreciation pertains to Prof. Calixto Isaac Garcia for believing in me, encouragement, support and advice during all these years.

This work could not be accomplished without collaboration, technical assistance, regular meetings and support from Christopher Hrizo, Kevin Marsden, Joseph College, Charles Novelli (WHEMCO Inc.) and Raymond Schleiden, Ronald Martin (United Rolls Inc.).

I proudly thank my previous institutions and schools, including South Ural States University, Lyceum No.11 and School No.34, Chelyabinsk, Russia.

Finally, I thank my wife, son and parents for their love, support and motivation.

Konstantin V. Redkin, November 2013

1.0 BACKGROUND OF HSS ROLLS

What do we know about tool steels? According to the chronological table [\[1\]](#) of historical technological development of tool steel applications, the very first documented hardened steel tool dates back to 1200 B.C. The modern tool steel history can be counted from 18-19th centuries with the more recent understanding of alloy design philosophies and development of heat treatment and quenching techniques. The main development objective was to make steel harder and harder so that it is able to cut other metals without losing its strength, particularly at higher cutting rates. In the early 20th century tool steels became much more complex and heavily alloyed, reflecting the needs of current industrial demands [\[2\]](#).

Special alloys of tool steels were developed and implemented into the hot rolling mills due to its superior mechanical properties at elevated temperatures. The current work discusses high-speed steel (*HSS*) material, which is a multi-component ferrous-based alloy, Fe-C-X, where the X is alloying element (*V, Mo, Cr, W, Co etc.*). *HSS* is mainly used in hot rolling applications of ferrous alloys. The genesis of *HSS* roll development goes back to 1980-90's [\[3\]](#). Despite over three decades of development and applications, there still remain a series of fundamental questions regarding the roll material properties under extreme loading conditions.

The objective of this work is to obtain an understanding of how spin cast rolls attain their microstructure and hence their mechanical properties. In order to achieve this objective, the fundamental knowledge of the processing-microstructure-property relationship of horizontal spin

cast HSS work rolls must be achieved. The advantages of the spin-cast manufacturing are as following:

- 1) well-established method;
- 2) production of a high density casting;
- 3) high efficiency;
- 4) high productivity and cost savings.

The need to produce spin-cast HSS rolls with extended life is not only technologically attractive, but an economic necessity. These demands are driven by users and roll producers having more cost efficient and advanced technologies [4, 5, 6, 7, 8, 9, 10, 11]. An example of advanced technologies include: electro-slag re-melting, continuous pouring for cladding, vacuum-degassing techniques, and powder metallurgy, advanced coatings, and forging. These methods promote better damage tolerance, surface quality and extend the service life of the rolls (*or rolling campaign*). Further, they represent an important challenge to the conventional well-established spin casting technology. Hence, it is highly desirable to improve the quality and performance of conventionally horizontal spin cast HSS rolls, without the need of any major capital investments.

The quality of the hot rolled steel strip and the productivity (*tonnage/month or the length of the rolling campaign*) of the hot strip mill (*HSM*) are two of the most critical concerns in a steelmaking plant. The term “campaign” of a roll is the effective life of the roll. The longer a roll is used, the higher the tonnage of steel processed using the same roll. Figure 1 depicts strip manufacturing using four rolls: two work HSS rolls, contacting the rolled strip, and two Back-up (*BU*) rolls (*not considered in present work*), supporting the former ones. Since the HSS roll is directly in contact with the strip, it must have high heat tolerance. The main characteristics of the hot rolled strip (*shape, surface condition and dimensional tolerances*) are directly related to the

shape profile and surface quality of the work rolls (*the rolls contacting a strip, Figure 1*). These features equate to requiring high surface tolerance, increased thermo-mechanical fatigue endurance, wear and abrasive resistance in the roll barrel at elevated temperatures.

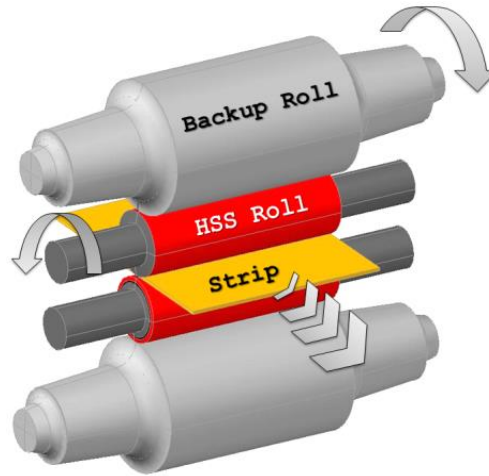


Figure 1. Schematic of a finishing stand in HSM

The manufacturing of the HSS rolls is a multi-casting process. The HSS rolls are usually bi-metallic, consisting of the shell and core. The HSS shell tube is being centrifugally spin casted, while a ductile iron core is poured statically after the shell is solidified to create the shaft, which is shown in the dark grey of Figure 1. Some more details on the casting procedures can be found in Section 1.1.

An example of actual HSS roll and its composite structure are shown in Figures 2b, 2c, respectively. The radial cross section of the roll in Figure 2a consists of several layers: HSS (*working layer, grey*), intermediate layer (*green*), fusion line (*red*) and the core (*gradient color*). The layer in between the working HSS shell material and core is usually named the “bonding zone”, which includes the “intermediate layer” (*or intermix*) and a fusion line, simply called “fusion” or “bondline” [102]. The thickness of this HSS shell is two-four inches, depending on the

roll design and requirements. The corresponding continuous microstructure from the surface of HSS shell in as-cast condition (*i.e. after the solidification*) to the transition region of the ductile iron core of a conventional spin-cast roll is shown in Figure 2d. The visible carbides (*dark color*) in Figure 2d are the developed eutectic (*i.e. appeared from the liquid*) and precipitated (*from solid solution*) phases. They are coarsening continuously from surface to the core (*left-to-right*). These interconnected carbide networks are very brittle and as a fact facilitate intergranular fracture in conventional HSS grades [12, 13, 14].

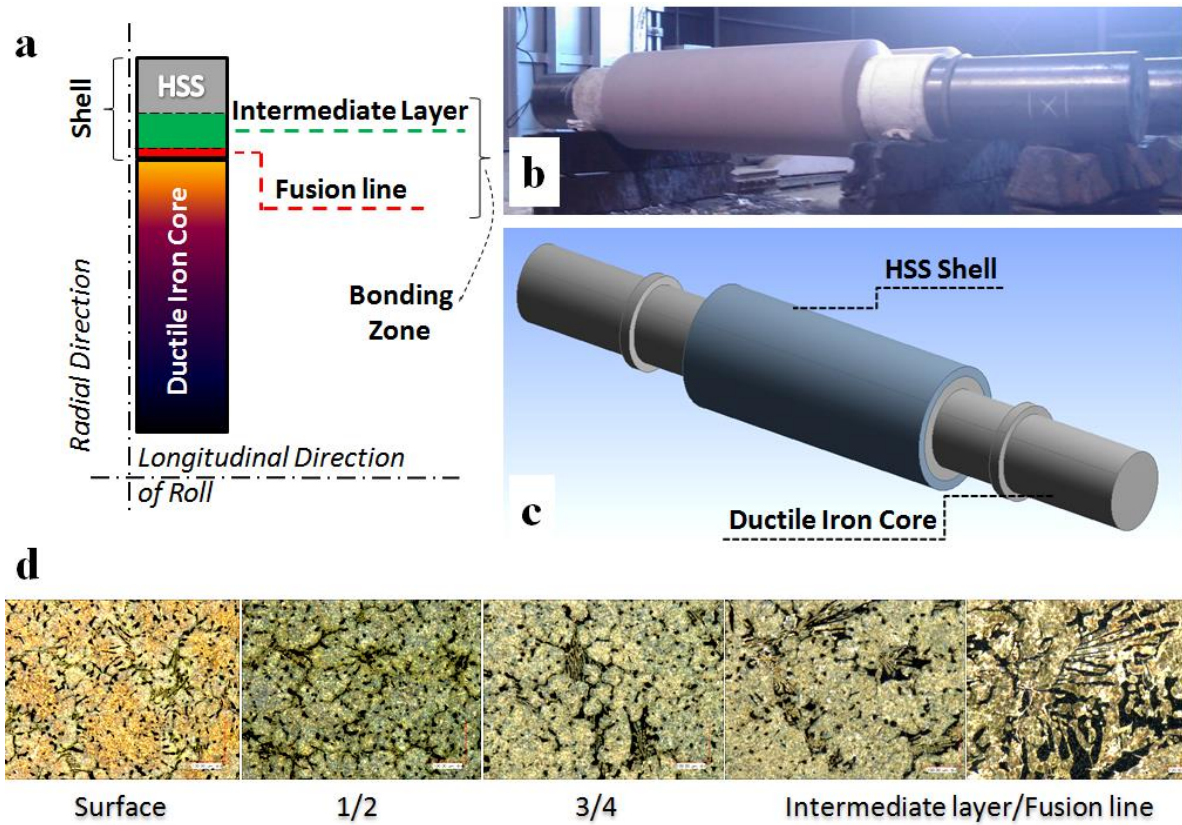


Figure 2. Structure of HSS roll: (a) schematics of radial cross-section of a roll body, (b) actual as-cast roll, (c) CAD model of bi-metallic HSS roll, (d) transitional microstructure of conventional as-cast HSS shell

The outer HSS shell is heavily alloyed to ensure that in this section the alloyed carbides and hardness of the matrix are developed during solidification and subsequent thermal treatments. A typical range of chemical composition of the HSS material is given in Table 1.

Table 1. Typical chemical HSS composition (wt%)

C	Si	S	Mn	P	Ni	Cr	Mo	V	W
1.7-2.2	0.50-0.90	0.020 max	0.50-0.75	0.030 max	0.10-1.0	3.5-5.5	5.0-7.0	3.0-6.0	0-6.0

A common microstructure of the ductile iron core is presented in Figure 3, and is comprised of spheroidal graphite nodulars distributed in pearlitic matrix with some eutectic carbides. The core saves cost and is able to withstand bending loads since it is relatively flexible.

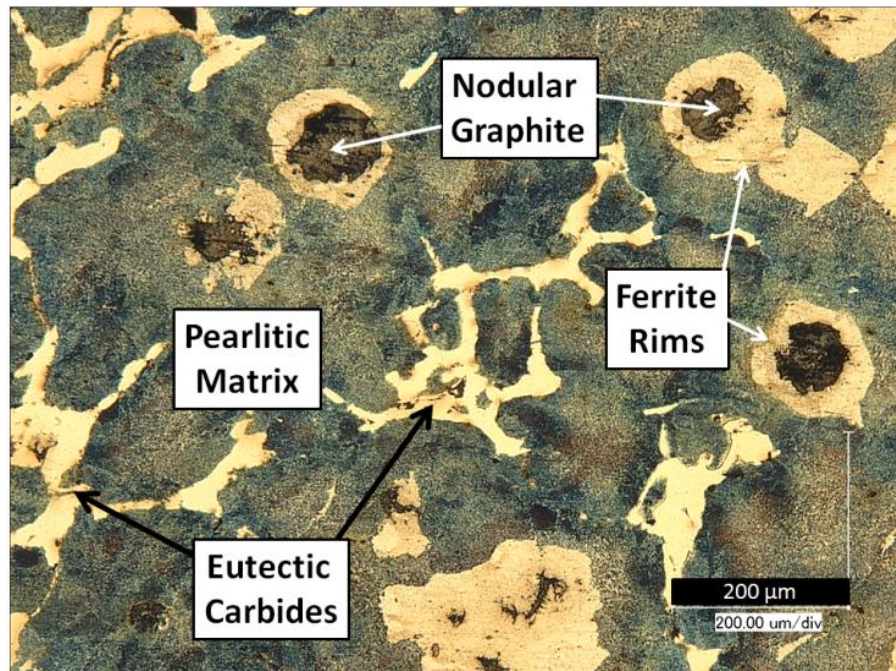


Figure 3. Example of typical ductile iron core microstructure

In contrast, the highly alloyed shell is able to resist extreme surface conditions. If no early failure occurs with the roll then the service life of HSS work rolls is mainly dictated by the shell thickness: as soon as the outer layer is worn then the roll is basically of no more use. Traditionally the rolls' efficiency and capacity are assessed by: 1) frequency of grinding-machining routine maintenance, 2) tonnage per worn millimeter (*ton/mm*) of the shell (*or tonnage per roll, ton/roll*), and 3) kilometers rolled per mm of roll consumption (*km/mm*). The need for maintenance operations (*roll replacement, repairs, inspection, surface grinding etc.*) can be minimized in case of improved thermo-mechanical characteristics of HSS roll. Therefore, some cost savings can be achieved.

A hot strip rolling mill (*HSM*) consists of several stands of rolls as shown schematically in Figure 4 and actual HSM finishing train in Figure 5 [15]. The positions of HSS work rolls in Figure 4 are marked as F1, F2, and F3, which are located between roughing (*R1 and R2*) and the later finishing rolls (*F4-F6*) named “ICDP” (*indefinite chill double poured*). The rolls that are of interest to this study are the rolls used in stands F1, F2 and F3. The HSS work rolls of “F4” position are “swinging”, which can belong to either group: HSS or ICDP. The typical range of chemical compositions (*below corresponding schematics*), possible dominating degradation mechanism of the rolls along the HSM, and solutions to these problems (*bottom part*) are also given in Figure 4.

Speaking of routine maintenance mentioned above, it can be seen in Figure 5 that the spare HSS roll piles are prepared for each individual stand along the HSM to be replaced.

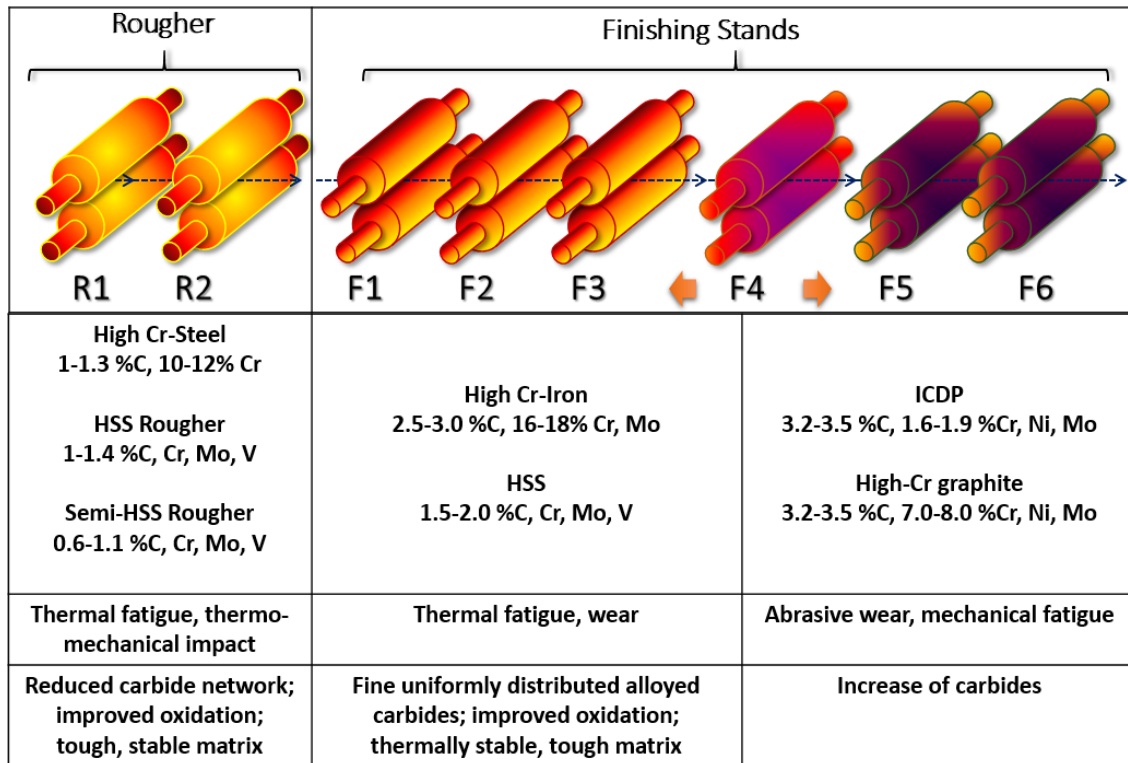


Figure 4. Schematic layout of different types of rolls in a hot strip mill (HSM)

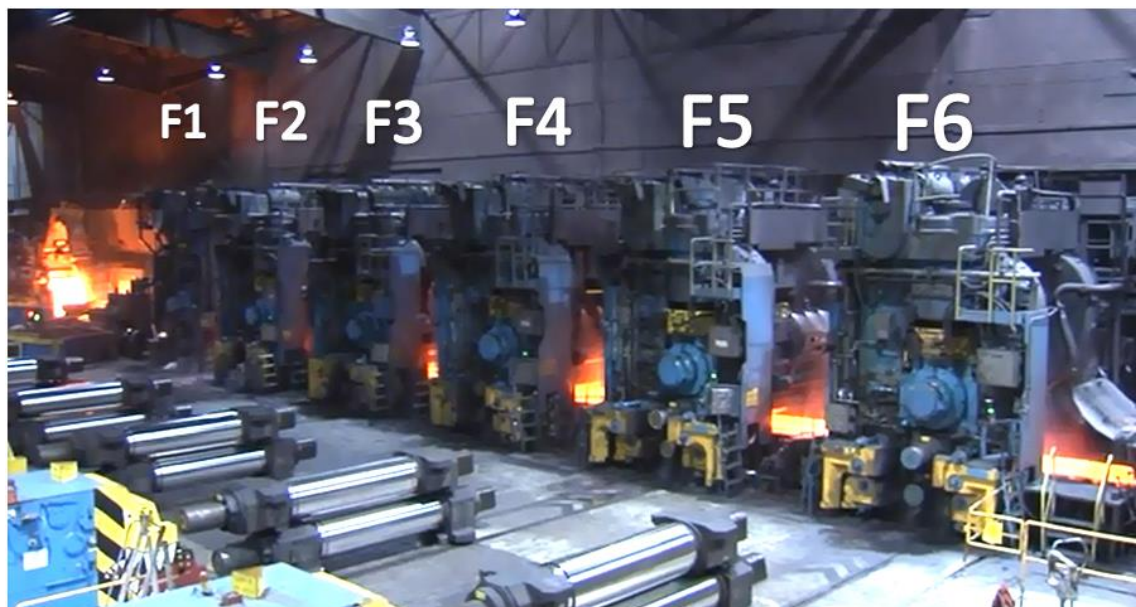


Figure 5. Actual HSM train in operation [15]

A close look at the actual assembly of the finishing stand is also shown in Figure 6, where you can see a water spray quenching of both: highly heated rolling strip and contacting HSS rolls [15].

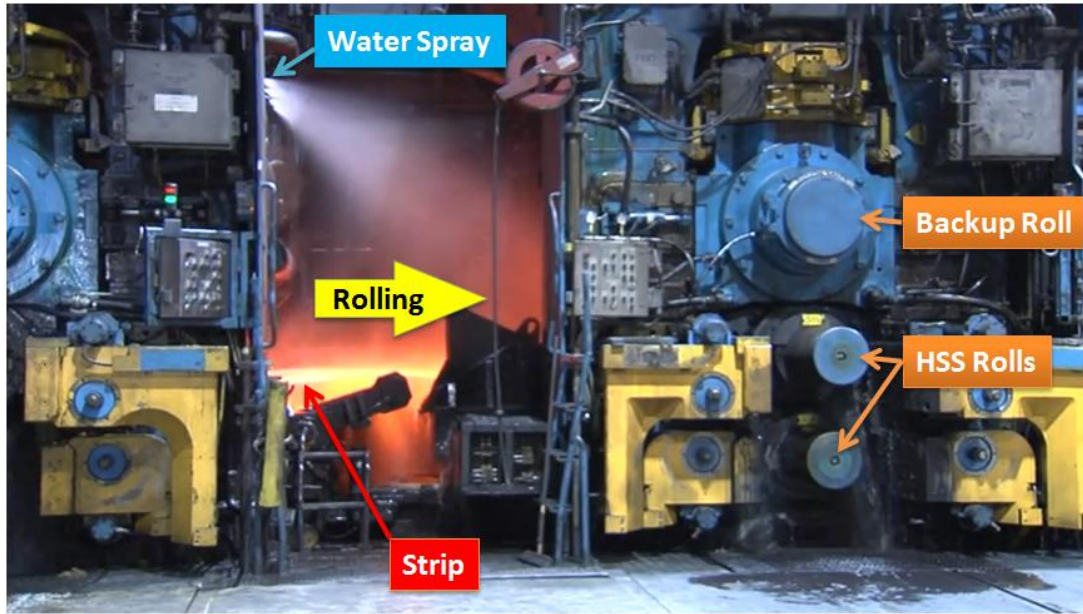


Figure 6. Extreme hot rolling conditions at HSS stands [15]

As it is discussed in [15, 16, 17], essentially, HSS rolls ($F1$, $F2$, and $F3$) are simultaneously exposed to two extreme loadings: thermal fatigue and abrasive wear. In other words, the HSS surface is subjected to competing degradation mechanisms, such as: oxide peeling, scale encrustation; possible cold and hot cracking (*combined residual, thermal and mechanical stresses*); low-cycle thermal fatigue (*periodic expansions and contractions due to temperature fluctuations*); high contact loadings (*periodic stresses due to roll bite*); abrasive wear and non-stationary periodic loading (*vibration, dynamic, and impact*). The significance of each damage factor on the HSS roll depends on the type of rolled materials (*for example, Fe-based versus Al-based, or versus Ti-based alloys*), reduction levels, friction, loading type, oil lubrication, rolling

parameters, and the pre-existing history of the roll (*residual stresses, internal defects and damages due to manufacturing, shipping, transportation, and maintenance*). In general, these parameters, defining the tribology (*i.e. friction, lubrication, heat transfer and wear*) of the rolls, must be considered in the development of HSS materials. The HSS rolls have to be designed specifically for each individual rolling mill taking into account its equipment capacity and required length of the rolling campaign. Ultimately, the roll life span and performance are related to a number of factors, including the type of a casting technology, heat treatments (*HT*) routes, machining, transportation, in-service conditions and even seasonal effects. Therefore, the structural integrity, service life and reliability of the HSS rolls are dependable on multiple interrelated technological factors, materials and mechanical aspects, which can very often yield to catastrophic failures, shown in Figure 7, and consequently downtime cost.

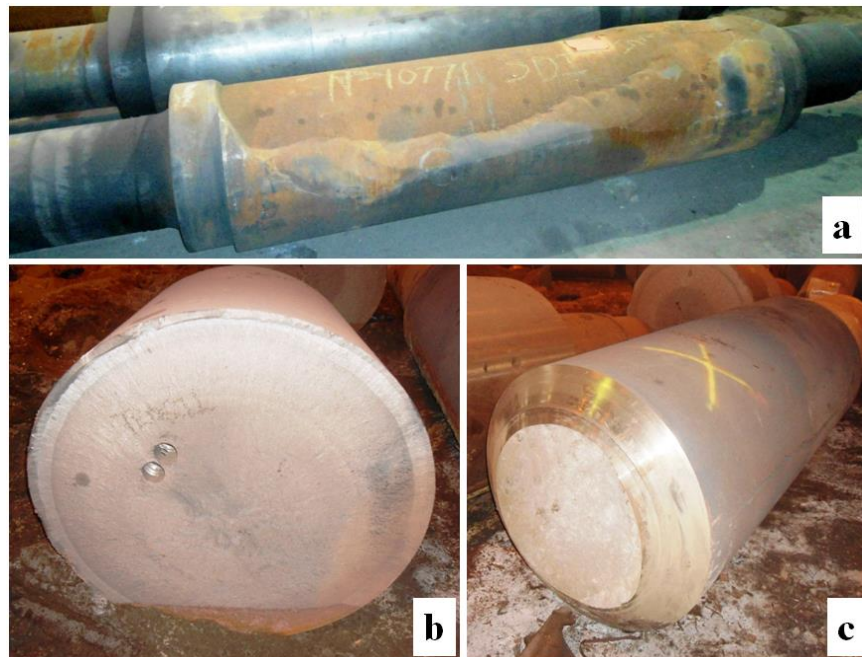


Figure 7. Examples of catastrophic failures of the rolls: a) de-bonding between the shell and core, b) transverse brittle fracture of the barrel due to thermal shock, c) overload at the brittle neck

A possible explanation of the accidents in Figure 7 can be given as following: Figure 7a shows a de-bonding between the shell and the core, which happened due to insufficient strength and toughness of the bonding (*presence of brittle coarse carbides*). It is a fundamental casting issue of the composite rolls, where two or even three dissimilar materials have to be jointed. The detailed analysis and design of the bonding is discussed in [18]. Figure 7b shows the transverse cross-sectional brittle fracture in the center of the roll barrel. This accident took place because of the thermal shock (*i.e. high temperature gradient between the surface and the core*) and insufficient fracture toughness of the core material. The origin of the brittle crack was found at the center of the core, which occurred from the combination of high tensile stresses along the roll and simultaneous excessive compressive stresses on the surface due to rapid quenching (*water spray*). Effects of the thermal shocks on the rolls are discussed in [19, 20]. Finally, in Figure 7c another transverse cross-sectional brittle fracture is shown at the transition from the barrel to the journal. This failure can be also explained by a combination of the factors: 1) change of geometry (*transition from the barrel to the journal*); 2) a brittle neck due to casting segregation (*dilution of alloying elements from the shell to the higher carbon core forming brittle carbides*); 3) and overload during operational procedures (*a human factor*). Similar cases are discussed in [21]. Therefore, the structural integrity of the rolls is defined and controlled by multiple interrelated parameters.

Nonetheless, the present work focuses only on the improvement of the HSS shell in order to prolong the rolling campaign. Many of the desired properties of the HSS shell material have competing requirements at the microstructural level. Desirable characteristics include “red hardness” (*explained below*), wear resistance, fracture toughness, low-cycle thermal fatigue limit, high temperature corrosion resistance, and low surface friction (*by means of controlled oxidation*

behavior). These properties can be achieved by having the proper composition, type and volume fraction of specific alloyed carbides spread uniformly throughout a relatively soft matrix. The primary aim of this work is to determine the influence of the unique morphology, distribution and crystallography of the carbides and the type of the matrix on the microstructural properties, hence, thermo-mechanical characteristics of the HSS shell material.

The following sections provide a review of the most important factors, effecting roll's performance and endurance, such as: frictional contact mechanics, oxidation, thermal fatigue and abrasive wear.

Frictional contact mechanics governs the phenomena of the tribology (*i.e. friction, lubrication and wear*) of the thermal contact fatigue in the work roll. Oxidation is a major contributor to deterioration and deformation of the roll surface. The formation of complex oxides (*i.e. composite metal-oxide layers with different thermal and mechanical characteristics*) affects the surface roughness and, therefore, influences the wear mechanism [26]. For the finishing stands the friction has to be reduced in contrast with the rougher rolls. The oxide layer formed have to be uniform on the surface, because it serves as a lubricant, slows down decarburization and heat exchange at the contact zone with the rolled material [35, 36]. In case if the oxide layer is scaling and breaking (*oxide scale*), then the friction at the roll-strip interface increases. Increased friction requires higher rolling loading and can also lead to excessive “roll-bite” (*gripping at roll-strip interface*), shown in Figure 8. Bite angle (*or “contact arc”*) consists of the three angles: ϕ_1 , ϕ_2 , ϕ_3 , corresponding to elastic zone, plastic deformation and elastic recovery in the strip, respectively [22, 23, 24]. The deformed area in the working roll is shown with red segment, where a slip and adhesion take place. The roll bite behavior in the strip is investigated by Remn-Min Guo, showing that the pressure distribution along the arc of contact (*or shape of “friction hill” in the pressure*

distribution diagrams) can be significantly changed, depending on the rolling parameters and material properties [25]. Bite angle and rolling speed relationships as a function of friction and surface conditions for roughing and early finishing stands in HSM are discussed in [16, 22, 23, 24, 25, 27]; these parameters are outside the scope of this work.

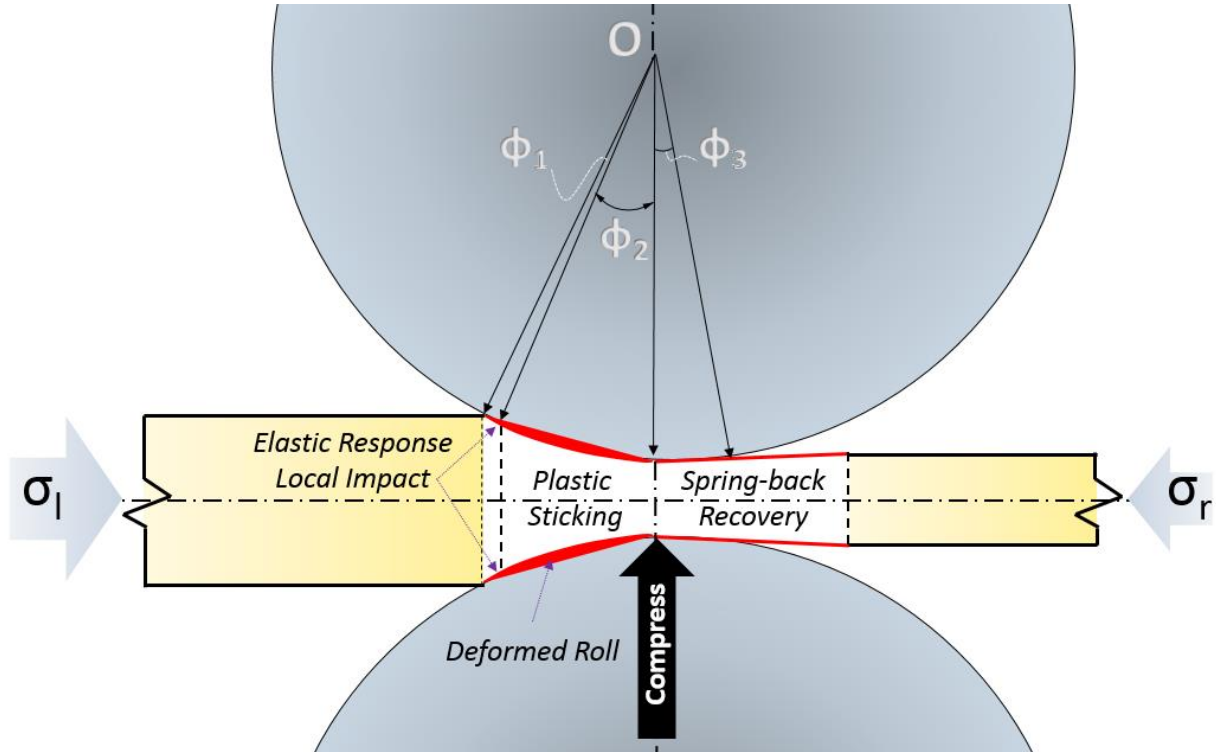


Figure 8. Roll bite behavior in the strip

Experimental and simulation examples of the contact at a roll-strip interface are shown in Figure 9. As a classical example, Figure 9a shows photoelastic image [29], revealing stresses in a local contact area developed by simultaneous normal and tangential forces. In Figure 9b the FE implicit simulation of the rolling process is shown [30], where a real-time and developed residual stress-strains can be predicted in the roll and strip simultaneously.

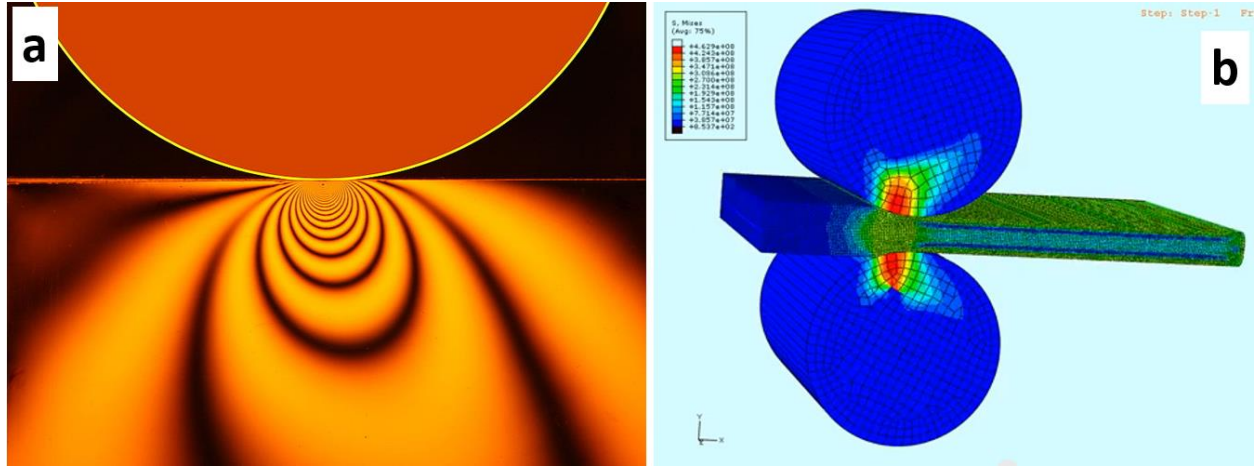


Figure 9. Contacts stress: a) photoelastic image of the contact [29], b) rolling simulation [30]

For a complete description of the contact loadings it is important to remind, that on the other side of the working roll the contact pressure is created by a back-up (*BU*) roll. The roll force longitudinal distribution and inter-roll contact force between *BU* and *HSS* rolls is investigated by K.Marsden et al. [28], taking into consideration continuous variable crown (*CVC*) roll shifting and work roll bending shape control. The contact stress spalling issues between the rolls are discussed in [126] in terms of the local stress-strain distributions and loading modes (*instantaneous overload and high-cycle fatigue*). It was shown that critical shear stresses can be exceeded well below the roll surface, initiating cracking, hence, leading to catastrophic failures.

Again speaking of oxidation, it is a diffusion-controlled process. Its nature depends on service temperatures, environment (*humidity, oil lubrication*) and the material (or “*substrate*”), specifically the *HSS* matrix and its carbides [31, 32, 33, 34]. Frictional behavior depends on complex oxide formation and matrix microhardness, which affect the surface quality of the roll [26]. Moreover, in practice, a sticking issue due to adhesion might rise as a consequence of poor temperature control, lubricant “break-down”, non-uniform local oxidation and microhardness variability.

Figure 10 shows an example of conventional HSS substrate, where various types of carbides are annotated. Figure 10a is relevant to the matrix, while Figure 10b depicts interdendritic boundary with eutectic carbides. Evidently, the local segregations react differently to the oxide formation, because of compositional variations (*local diffusion*) and surface roughness (*surface energy*).

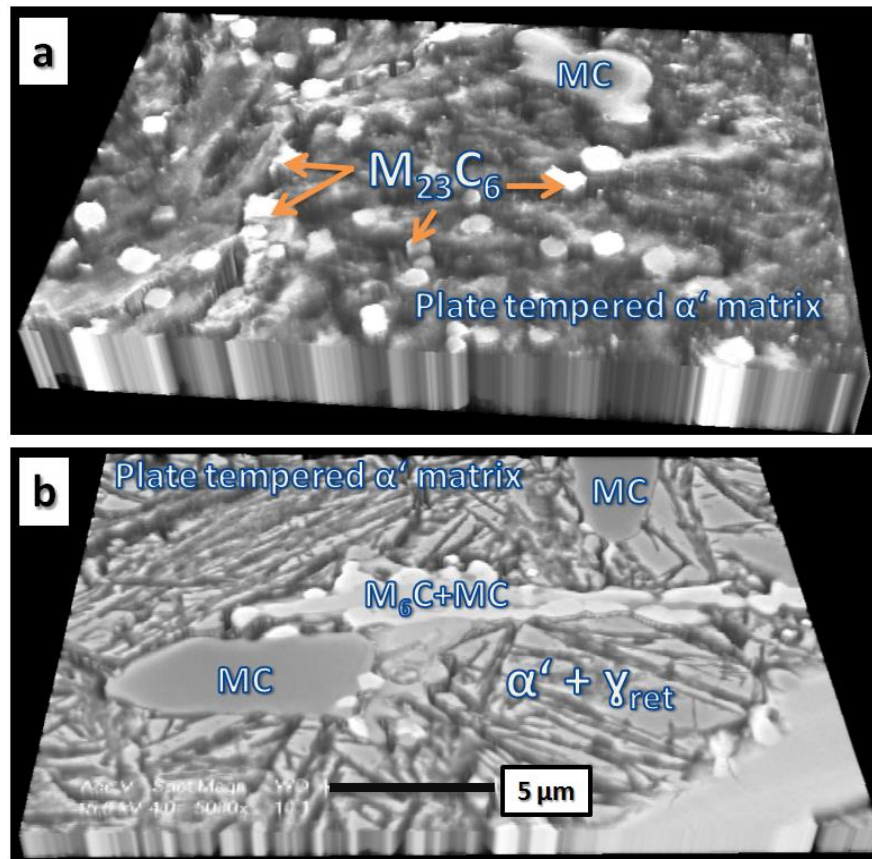


Figure 10. Transformed 2-D SEM images (ImageJ): (a) tempered martensitic matrix with secondary $M_{23}C_6$, Cr-rich carbides and eutectic MC, V-rich; (b) interdendritic region with retained austenite and partially decomposed eutectic M_2C (Mo-rich) into M_6C and MC carbides

The reported starting oxidation temperatures are in the range of 500-700 $^{\circ}C$ [31, 32, 33, 127]. All studies reported that the oxidation takes place first at the carbide-matrix interface. It has

a direct dependence on the temperature, time and local segregations. The type of the carbides, their composition and distribution affect the oxidation kinetics. The oxide nucleation rate is higher if the amount of carbides is higher, because the surface energy is increased with increased carbide-matrix interface. Nonhomogeneous carbide distribution leads to uneven oxide layer. A sequence and a direction of preferential oxidation growth is a function of time, local chemical gradients and local diffusion process controlled by environment (*e.g.*, *oxygen*) and metal ions fluxes. Nonetheless, there are some contradicting conclusions regarding the sequence of preferential oxide development. In one case, it was concluded that “the oxidation involves the matrix only” [31, 127]. It has been justified by the high oxidation resistance of the carbides due to locally increased alloying content, in particular with chromium. But another later in-situ investigation [32, 33] observed the rapid spreading of the oxide scale over the surface of carbides first and only then propagating into the matrix. Also this in-situ analysis of oxidation behavior revealed different morphologies and configurations of the oxides developed depending on a location (*matrix or carbides*), temperature and environment. Oxidation certainly effects the surface roughness. With the excess of some carbides, for example, MC, V-rich, and uneven oxide scale the friction might be increased, as a consequence, requiring more power supply to the roll stands.

In spite of this controversy, all reviewed studies fulfil each other; and it can be postulated that the more uniformly the carbides are distributed and the finer they are, the more flat and homogeneous will be the oxide layer; therefore, the surface roughness can be reduced. Hence, the more controlled friction and homogeneous wear are expected to be. Moreover, the uniform distribution will prevent fall-outs of carbides, spalling and chipping of the HSS shell surface. It is believed in this work that the oxide behavior can be improved with uniform microstructure: fine, disconnected carbides and homogeneous matrix enriched with alloying content.

The second main issue during hot rolling deformation is the thermal fatigue and related “hot” cracking (or “fire cracking”) discussed in multiple works [37, 38, 39, 40]. Crack networks mainly appear on the surface of the roll and originate at the carbide-matrix interface with subsequent propagation along the brittle eutectic interdendritic boundaries, Figure 11.

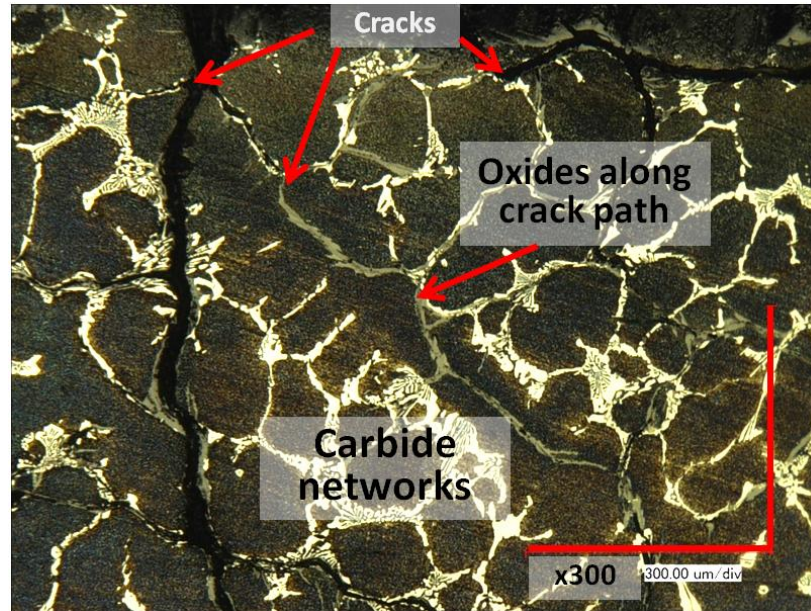


Figure 11. Thermal fatigue cracks

The thermal fatigue occurs due to repeated changes of temperature (*heating-quenching*), leading to volumetric changes within the shell, according to the thermal properties of the microconstituents in the shell. Additionally, the defects are accumulated because of the elastic-plastic thermal strains at the surface of the shell and, consequently, networks of cracks produced at high temperature (*often called “hot cracks”*) appear. Periodic plastic thermal strains combined with mechanical loading change the material properties, reducing its toughness and causing deep cracks to propagate. The oxides which are formed on the surface can also penetrate inside these deep surface cracks, facilitating their growth and decarburizing the matrix of the HSS shell

material. Brittle interdendritic eutectic carbide networks along the grain boundaries are very harmful promoting such crack initiation and propagation.

The third challenge that plays a major role in surface deterioration is the prevailing abrasive wear that occurs in the water-oil environment at elevated temperatures. The wear process involves oxidation, fracture, friction (e.g., *rolling, sliding, impact etc.*) and other mechanisms. The tribology of the roll surface, which is very complex, helps to govern the amount of wear. Describing a degradation process in general, the wear can be of three main types: 1) mechanical, 2) chemical, and 3) thermal. But these terms are insufficient to describe all damaging factors. More detailed classification of wear parameters in terms of friction type, contact shape and pressure, temperature, environment, wear mode and type etc. is given by Stachowiak [35]. Kaplanov et al. [27] also discussed a multifunctional mathematical model, where the friction coefficient is a function of material composition, surface roughness, and thickness of lubricant layer, type of lubricant, contact angle, rolling speed and temperature.

If the matrix or other microstructure of HSS shell is not stable enough, then local diffusion (e.g., *interstitial carbon diffusion*) might take place, leading to softening and, hence, to insufficient resistance to wear. It happens, due to the lack of alloying elements in the matrix, leading to the coagulation (*i.e. spheroidizing growth*) of carbides [41]. If the carbides become coarser, there is a decrease in quantity leading to longer distances between them and resulting loss of hardness. It is desirable for the HSS rolls to have high “hot hardness”, or “red hardness” (*hardness at elevated temperatures*). This property requires proper oxidation behavior, which is achieved by means of matrix stability (*one that is homogenized, solute-rich, and tempered*) and uniform alloyed carbide distribution (*the type, morphology, composition*).

It can be concluded that proper mixing and uniform distribution of the carbides through the thickness of the shell will be strongly related to the following factors: a) refined solidification cell sizes, b) a controlled solidification process, c) enhanced hardenability of the austenitic matrix, and d) optimized thermo-mechanical processing and transformation behavior. Reducing the amount of interdendritic continuous carbide network and distributing the refined carbides throughout the matrix can facilitate that the required performance and designed service life of the HSS rolls are met.

1.1 HORIZONTAL CENTRIFUGAL CASTING

It is well-accepted that the life of the roll begins with the chemical composition, casting and solidification processes. In general, solidification is a heterogeneous transformation, where the growth of the crystallizing phase is controlled by heat transport. In case of horizontal centrifugal casting, this phenomenon becomes more complex, because of additional forced mixing of the molten metal while it is being crystallized. The convection heat transfer becomes predominant, where the local mass turbulence is driven by thermal gradients and centrifugal forces. As a consequence, the solid phase migrates, segregates and precipitates from the liquid to the outer or inner diameter of the shell depending upon its density. Possible chemical inhomogeneity through the shell layer in this case is due to so called “gravitational liquation” controlled by density difference between solid and liquid phases, also including insoluble liquid phases during crystallization [[42](#), [43](#)].

One of the fundamental issues of relatively large cast products is the formation of eutectic brittle phases and carbide networks. These are formed by the rejection of high alloy content into

the liquid between the growing and colliding dendrites. Such interdendritic segregations are very brittle, because of the carbides formed inside them, having crack-like defects and lattice misfit by default. As the matter of the fact, it considerably lowers the fracture toughness of the material and reduces alloying content in the matrix. The grown columnar dendritic structure is very dense, but because of the weak boundaries, the equiaxed eutectic austenite cells are more preferable [44].

As an example of developing eutectic carbides during solidification, A. Bedolla-Jucuinde et al. [45] conducted a detailed three-dimensional investigation of M_7C_3 (*Cr-rich*) carbide and discussed its nucleation and growth from the surface of primary dendrites.

This sort of a classical dendrite formation decorated with interdendritic eutectic carbides has even been observed even for rapid cooling with the rates about 10^6 Ks^{-1} [2, 46].

A simple description of centrifugal horizontal spin casting process to produce HSS rolls is illustrated in Figure 12. In the top row of figures, the material is melted and poured into cast, laid horizontal and spun. The HSS shell tube is produced by spinning the HSS melt inside the molds until solidification is completed. The middle row of pictures shows the monitoring of the process along with transferring the completed shell. In the bottom figures, the shell is placed in a mold and the ductile iron core is cast.

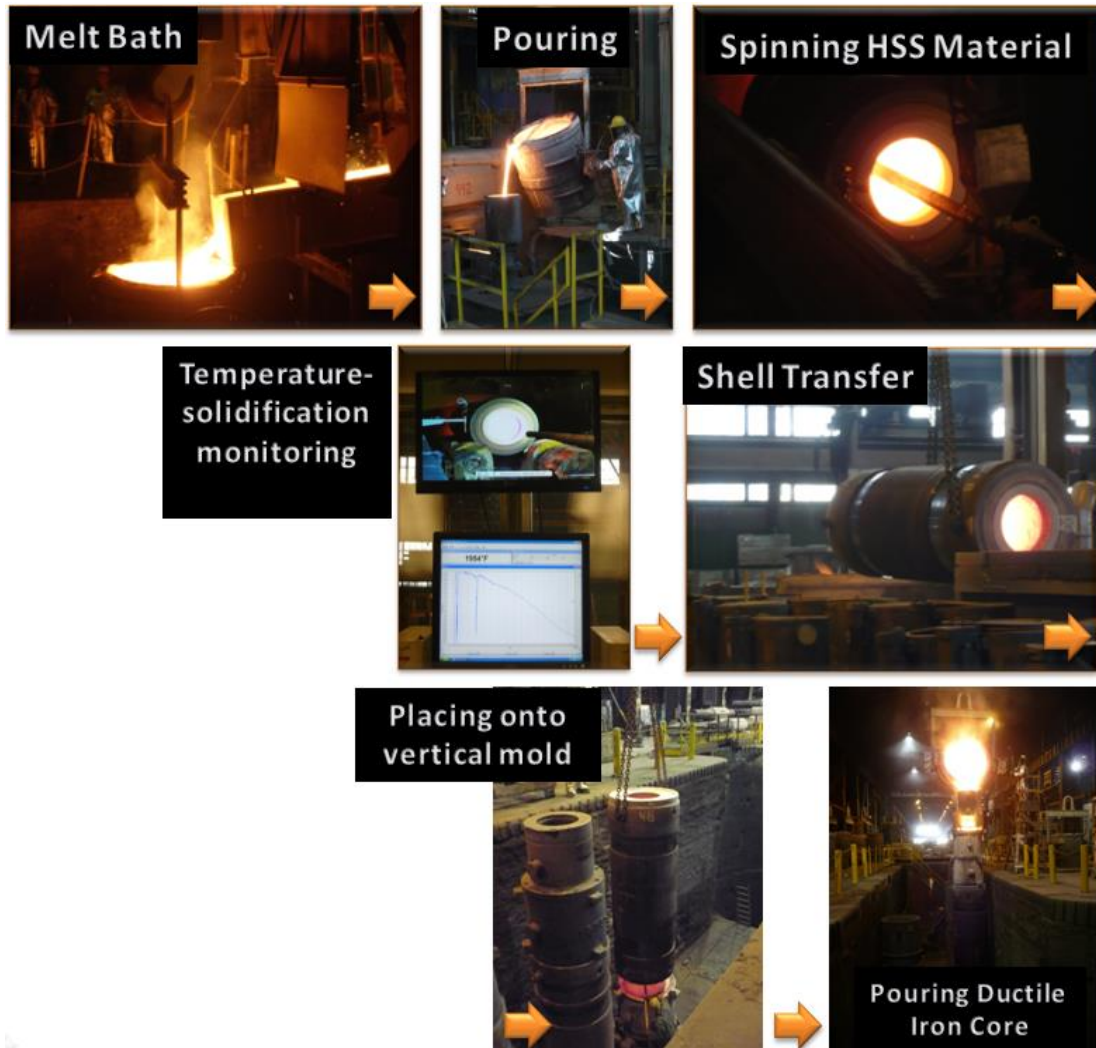


Figure 12. Main stages of horizontal centrifugal casting with stationary vertical core pouring

Figure 13 shows a schematic of a particle (*i.e., precipitate in a melt*), which is subjected to forces resulting from gravity and the centripetal acceleration caused by the shell rotation during centrifugal horizontal spin casting. The applied centripetal acceleration varies between 40-100 G, depending on the specifics of the process and related manufacturing parameters.

During horizontal centrifugal casting segregation takes place either on the inner and/or the outside surface of the shell tube. The segregation behavior is a function of precipitate density and applied angular velocity. The Gibbs free energy of formation dictates the precipitation sequence over time, i.e. first the appearance of solids in the liquid, with subsequent crystallization (*growth of dendrites*). At the same time, the solidification mechanism is driven by the thermal gradient and solute segregation (*i.e., a type of microsegregation due to the diffusion of excess solute content into the residual liquid during propagation of the solidification front*). The centrifugal forces break the solidification front, and new nucleuses appear in the liquid, providing more nucleation sites. Therefore, there are several factors, affecting the segregation: a) different densities of atom clusters, b) high rotation speed and precipitation sequence, c) insufficient solidification rate, d) possibility of two solidification fronts.

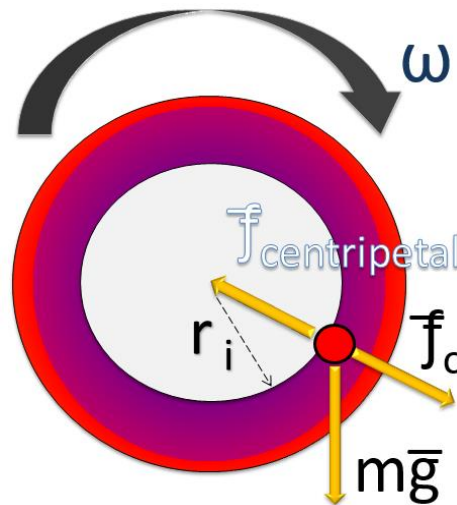


Figure 13. Free body diagram of a particle in centrifugal field

The major factors, promoting segregation, are strongly related to two solidification fronts moving to collide from different directions to the same end point. In order to avoid this behavior

unidirectional solidification has to be the preferred solidification mechanism which needs to be controlled [132].

Several numerical and computational models of the phenomenological dendrite growth behavior are discussed in the literature [47, 48, 49, 50]. This information shows that the mechanism of dendrite development depends considerably on thermal gradients (*under static conditions*). Modelling and simulation of the solidification structure during centrifugal casting are also discussed where prediction of grain structure and columnar-to-equiaxed transition are shown to be controlled by the superheat of the liquid (*stationary case*). Macro-segregation is a function of particle clustering and agglomeration formation under the centrifugal field [51].

In addition to macrosegregation, another deleterious factor that produces casting cracks is liquation, which is produced by the complex tearing forces present at the mixed solid-liquid interface. It is shown that the formation of casting cracks can be controlled and suppressed by proper simultaneous selection of the mold material, protective coloration and oxide preventing fluxes, pouring temperatures, cooling rates and rotational speed [17, 42, 43, 51].

Microstructural refinement of the as-cast structure has been studied in several works [52, 53, 54, 55, 56, 57, 58, 59, 60, 61]. In summary, high levels of refinement can be achieved by: 1) addition of rare earth (*RE*) elements; 2) controlling cooling rates and rotational speeds while regarding critical temperatures; 3) combination of the former two; 4) application of external electro-magnetic fields.

In summary, the review of the literature seems to clearly indicate that the casting method, has important implications in the final as-solidified microstructure and hence the mechanical properties of HSS rolls. In addition, it appears that there is a dearth of information regarding kinetics data for carbide formation, precipitation sequence and volume fraction of carbides.

Similarly information regarding phase transformations during solidification under a centrifugal force field is also limited in the literature. One of the objectives of this thesis is to fill the gaps of understanding regarding microstructure, carbide formation and precipitation during the solidification that takes place in the horizontal spin casting of HSS rolls.

1.2 HIGH TEMPERATURE HARDENING HEAT TREATMENTS

Solid-state transformations in simple or single phase systems are usually driven by diffusion, nucleation and growth. One example of a simple solid-state transformation system could be the cold rolling and annealing behavior of pure Fe of very dilute (*ultra-low carbon*) steels. In multi-component systems (*higher carbon and other alloying elements*), e.g. high speed steels, the microstructure consists of two or more microstructural components. In this case the liquid to solid or solid-solid phase transformation is more complicated. Among some of the additional metallurgical reactions that must be considered are: a) diffusionless transformation; b) spinodal decomposition; c) change in crystal structure; d) strains due to volumetric changes; e) incomplete transformations (*retained austenite*); and f) precipitation of various species. During the decomposition behavior of highly alloyed austenite (*austenite with high carbon content and other alloying elements*) to lower transformation temperature microconstituents under equilibrium (*slow cooling*) or non-equilibrium (*fast cooling*) conditions there could be two types of the diffusion: long-range and short-range [62, 63]. The rate of diffusion is a function of time and temperature. The long-range diffusion is mainly driven by both: the bulk concentration differences and thermal gradient, for instance, between the layers (*shell, intermix and core*). It can also take place inside these individual layers, depending on the chemical inhomogeneity levels. However, the short-

range diffusion is expected to occur within an atomic spacing, for example, within complex blocky carbides. This observation implies that it is very important to maintain a uniform temperature for sufficient time throughout the entire shell in order to homogenize the matrix. As a result, the as-cast compositional gradient is reduced, and at the same time, the structural integrity of the roll is controlled, preventing re-melting and de-bonding of the core.

High speed tool steels can have hypoeutectoid or hypereutectoid carbon contents. Their microstructure is very complex, having multiple microconstituents, carbides and phases. For example, in some hypereutectoid (*high carbon content*) high speed tool steels the matrix contains mixtures of tempered and un-tempered martensite, and bainite as the major constituents. In addition, the matrix might contain second phase particles, eutectic interdendritic carbides, alloyed carbides and retained austenite. The coarse interdendritic carbides and the retained austenite must be dissolved or transformed using additional heat treatments to prevent their deleterious effects to the mechanical properties of the steel.

The detailed nucleation studies of the main eutectic carbides, such as: M_2C (Mo_2C) and MC (VC) types were given in [53, 54, 56, 57, 58, 59, 60, 64], where the 3-D deep etching techniques were used in order to reveal the morphology of the carbides and their growth behavior. It can be summarized that MC-type carbides might have three main morphologies, which are commonly named: (1) idiomorphic, (2) petal-like (*rod-like*, “*chicken-feet-like*”) and (3) coral-like (or “*chrysanthemum-like*”). The morphology depends primarily on vanadium content and rough solidification rate ((1)-*slow*, (2)-*moderate* or (3) *rapid*). But [54] also shows controversial cases and mixed unexplainable behavior of MC, referring to chemical composition influence. According to the same source, the faster cooling rate does not affect the volume fraction of MC, except for the alloys with higher vanadium content. But finer size and more uniform distribution at faster

solidification rates is reported in [53], with the increase of total volume fraction of eutectic carbides. Sources [53] and [54] report controversial conclusions on the solidification rate influence on MC (VC) morphology. The precipitation of eutectic vanadium carbides can be observed along the boundaries and inside austenite cells, which is explained graphically based on the liquidus-surface V-C diagram [66], where reduced amount of liquid phase can be formed by both: peritectic and eutectic reactions, with the decreased carbides' amount along the boundaries.

The branch-like Mo₂C carbide development, which begins as a rod-like nuclear form, is discussed in [53, 64] and it has a spontaneous character, due to its high concentration in residual liquid. But most importantly the carbide's branches are growing with the austenite, and the transformation is completed at the end of the eutectic reaction. With increased solidification rate, Mo₂C carbides become finer, but still present at the boundaries in sharp branch-like morphology. Phase transformation refinement of these carbides during austenitization is investigated in [56, 57] on M2 commercial HSS as a function of T_γ and time. 3-D deep etching techniques revealed possible intermediate transformation states of the carbides comparing: 1) long time annealing at 780 °C (*no obvious effect*); 2) then 1050 °C (*only partial decomposition*); and 3) 1100 °C (*4hrs*) or 1150 °C (*2 hrs.*) treatments promoted complete decomposition. Partial decomposition of Mo₂C was discussed in the paper, which was confirmed by the observed peanut-like Mo-V fine epitaxial carbides that were partially dissolved in conventionally treated HSS rolls.

Therefore, due to the observed controversy concerning the effect of solidification rates on MC-morphology, preliminary re-heating/re-melting experiments on refined as-cast HSS material will be done in the laboratory conditions (*inert atmosphere*), confirming some of the above mentioned statements. See Section 3.3 of experimental setup and discussion of the results in

Section [4.2.1](#), where the melting temperature is established and verified with thermodynamic predictions; and carbides morphologies were compared and analyzed.

Classic tool steel hardening methods employ high temperature heat treatments to dissolve as much of the carbides present and the elements from these carbides will enrich the matrix to provide additional solid solution. In some highly alloyed types of HSS materials the approximated amount of carbides dissolved is approximately 10 to 12% from heating [\[67\]](#). However, it is important to mention that these levels of dissolution are a function of the temperature and holding time used during the heat treatments. In HSS materials the decrease in the volume fraction or amount of carbides is almost entirely due to the dissolution of chromium-rich $M_{23}C_6$ carbides shown previously in Figure [10a](#), their dissolution temperature is about 2000°F (1093°C). Continued heating above 1900°F (1038°C) starts to dissolve tungsten-molybdenum-rich carbide M_6C . Another precipitation species often found in HSS are the vanadium-rich eutectic MC carbide. These carbides are very stable with much higher dissolution temperature. Hence during typical heat treatments their dissolution is minimal. Figure [14](#) demonstrates the effect of carbide dissolution on hardness of T1-type HSS as function of austenitization temperature and time [\[67\]](#). The vertical axis gives the Rockwell C Hardness, which is seen to rapidly develop and then plateau with treatment time. The maximum hardness of the system is reached when complete carbide dissolution is achieved. Partial dissolution of carbides at lower heat treatment temperatures resulted in lower values of hardness.

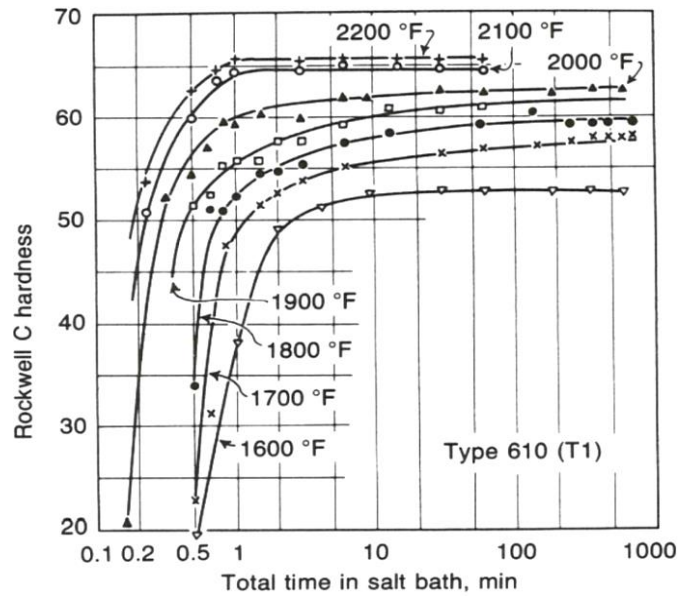


Figure 14. Effect of austenitization temperature and time on hardness (HRC) [67]

To achieve high “red hardness” levels in HSS tooling, high austenitization temperatures are required. The understanding of the effect of time-temperature on the dissolution of carbides in tool steels is applicable to the heat treatment of HSS rolls. However, in general, for most of the roll manufacturers, the application of the classical HT practice to HSS rolls is not directly applicable to spin cast rolls due to their multi-layer compositional structure.

Before performing a hardening HT the preliminary HT is done. The role of preliminary HT (*or soft annealing as it is commercially known*) is to produce a soft structure for the following high temperature hardening HT, minimizing the energy of the system. It can be achieved by different temperature-time regimes (*steady annealing below A_{c1} ; start above A_{c1} with linear decrease; fluctuating regime with the A_{c1} mean*), depending on initial microstructure [68, 69], where A_{c1} is the temperature, at which austenite starts to form. The influence of the preliminary HT on as-cast microstructure was studied in [68, 69], where the annealing temperature is suggested to be

increased in order to achieve proper matrix coagulation. The results of the preliminary HT on conventional and refined grades is discussed in Section [4.2.2](#).

Then after the preliminary HT the high temperature hardening heat treatments of HSS shell are performed, consisting of multiple steps. This is the main focus of this work. Hardening continuous steps (*see top of Figure 15*) include: 1) pre-heating (*to avoid thermal shock*), 2) heating to high austenitization temperature (T_y) and holding at this temperature (*to achieve fully austenitic structure and carbides dissolution*), 3) cooling (*e.g., combined quenching and air cooling to room temperature (ACRT)*) to the desired transformation tempering temperature, and 4) immediate subsequent single or multiple tempering treatments (*see bottom of Figure 15*).

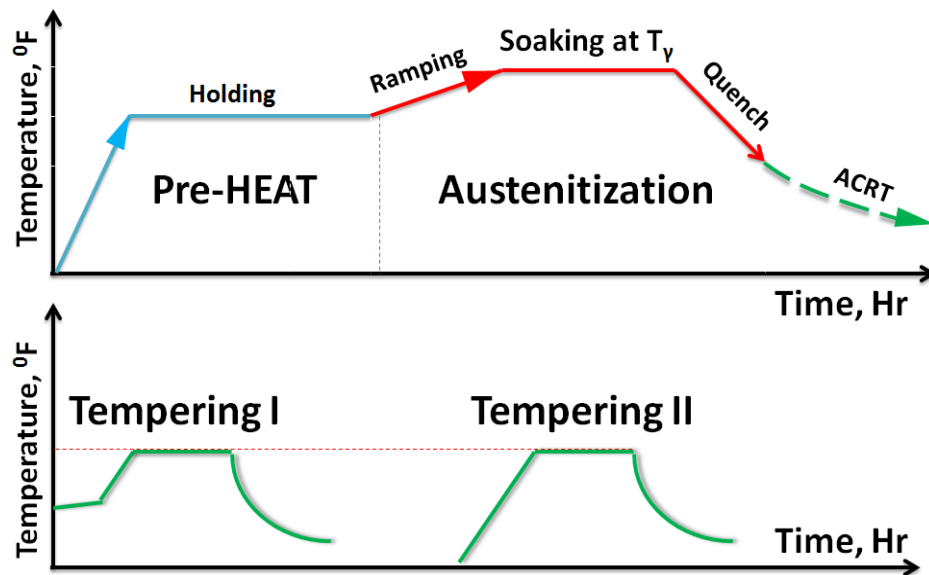


Figure 15. General schematics of high temperature hardening

The purposes of the high temperature tempering are as following: 1) to reduce internal microstructural stresses of brittle phases formed, 2) to transform the retained austenite to bainite or martensite, and 3) to develop additional secondary hardening (*or hardness increase as a*

function of time and tempering temperature) because of newly formed martensite from retained austenite and secondary carbides precipitated from initial martensite. There are many influencing factors on secondary hardening, hence, the microstructure evolution has to be controlled in order to predict a contribution from each original and newly formed phase. The tempering can be repeated to achieve desired microstructure and mechanical properties (*e.g., hardness*). Most importantly, multiple tempering HTs enable one to develop thermally stable matrix and increase alloyed carbides amount. The effect of the cooling or quenching temperature on the microstructure and mechanical properties of HSS material can be summarized as follows: 1) hardenability of HSS materials is related to the austenitization temperature (T_γ) due to high alloy content; 2) with T_γ increase, carbon and other alloying elements supersaturate eutectic γ -cells; 3) more retained austenite is expected upon cooling due to its stabilization and martensite start temperature (M_s) decrease after higher T_γ ; 4) increased T_γ up to some value, depending on composition, increases the bulk hardness, but with the further increase a drop in hardness can be observed. This can be explained in terms of the lowering of the M_s temperature with higher carbon and other alloys in solid solution. Hence at normal quenching temperatures not all of the austenite can transform to martensite, hence austenite becomes retained; 5) the tensile strength is increased but the impact toughness is decreased with higher T_γ . The last point is related to austenite grain coarsening, meaning that the tensile strength is controlled by microstructural and compositional effects, while the impact toughness seems to be mainly controlled by both the type of martensite and the coarser austenite grain sizes.

The effect of tempering temperature on precipitation hardening is well-understood and multiple studies have been published on this topic [70, 71, 72]. In general, it is well-known that during tempering the formation of fine alloyed carbides leads to secondary hardening. This

reaction is a function of temperature and the alloy content in the matrix. Tempering can be done in single or multiple steps, depending on the volume fraction of retained austenite in the matrix. An optimal tempering temperature has to be established in order to obtain the desired hardness and thermal stability of the HSS material. Very often dependent of the composition of the matrix, the first wave of fine precipitates formed remain very stable and further tempering treatments will produce additional fine precipitation hence the overall effect of the tempering does not cause a decrease in the hardness of the matrix. At this point the matrix of the HSS becomes thermally stable.

Room-temperature (*RT*) hardness measurements are a common test used to rate the quality of HSS materials, since they show the attainable hardness along the shell. But it can differ significantly from the more important “hot hardness” or “red hardness” measurements. The red hardness is relevant to elevated temperatures, replicating service conditions, where high hardness has to be retained. In other words, the red hardness characterizes a resistance to the tempering. It has to be emphasized that the hardness at RT does not determine the high temperature performance of the roll. Moreover, the time factor is of the utmost importance, because the hardness of heated HSS material has to be maintained during a long operational time [41]. As surfaces are in contact during the use of tool steels or rolls, thermal contact and friction initiate a softening response of the material. Reduced wear resistance is mainly due to the local diffusion of alloying elements, which basically implies that some structural irreversible transformations might take place, changing the material properties upon cooling [114, 115, 116, 117, 118, 119]. In order to avoid such instabilities a high red hardness has to be developed, which can be achieved by multi-step high tempering (*see Section 4.2.3*).

Cast bi-metallic rolls, specifically HSS work rolls, pose challenges when attempting to achieve the high austenitization temperatures commonly used for HSS materials. The core of the cast HSS roll is comprised of iron material possessing a relatively low melting point [120, 121]. High temperature austenitization treatments used on commercial HSS material must not allow the liquation of core material and possible de-bonding between the shell and core. Hence, the nature of the bi-metallic product potentially limits both the material response (*microstructure development*) during HT and, as a consequence, resulting performance. The HT process adds considerable value to roll performance. Unfortunately, the final microstructure of a non-properly heat treated roll limits the final mechanical properties hence the performance of as- cast HSS rolls.

To address the challenge described in the previous section the current research was conducted with the goal of studying and defining the thermal parameters that will permit the optimum heat treatment to pre-condition the as-reheated microstructure to develop the best combination of microstructure-properties after cooling and additional tempering treatments, Figure 15.

1.3 NUMERICAL MODELING AND SIMULATIONS OF THE ROLLS

1.3.1 Finite element modeling approach

In general, the roll design can be divided into three main categories: I) manufacturing stage, II) actual service, and III) repair. The main focus in this work was the manufacturing (*i.e., casting and HT*).

The first modeling effort focused on the manufacturing stage, in particular, the spin casting process and complex heat treatment routes. The spin casting can be horizontal, vertical or at an angle [42]. The heat treatment is usually a long term process.

The second and third categories of modeling can include, but not limited to: 1) mechanical contact simulation, 2) fatigue endurance assessment, 3) fracture mechanics, 4) mill stand assembly, 5) degradation of the material, and 6) mathematical models for the hot rolling strip process.

Each category can be considered as a multiphysical problem, where complex phenomena could be coupled, for example: thermal-stress, multi-phase flow, fluid-structure interaction, and heat and mass transport. At the same time, the multi-scale issue needs to be addressed too, because microstructural behavior defines the thermo-mechanical response and even the service life of the full-scale roll. It is especially very important to consider in the case of transitional microstructures, varying through the working shell of the roll. The question is how the local point, representing microstructure, responds to the heat treatment, and eventually, to its service environment? For this, it is important to consider some of the existing numerical and computational approaches applicable to resolve the question. In fact, the multi-scale simulations can be done, using different techniques and numerical methods, for example, density functional theory (*DFT*), molecular dynamics (*MD*), Monte-Carlo (*MC*) simulations, and continuum level methods. The selection of the appropriate method depends on the scale considered (*domain size and time*) and physics involved. According to [73], the scales are divided into several levels: 1) electronic (*ab initio*) or quantum representation of the matter, discussing interaction of the sub-atomic particles, 2) atomistic level described by statistical mechanics, 3) meso-scale methods, 4) and continuum (*microscopic, macroscopic*). In other words, the simulations can be performed using discrete or continuum methods, for example,

particle-based or finite element analysis, respectively. The current work considers only continuum methods, used to analyze the bulk material with microstructural emphasis (*meso-scale modeling*).

In recent years the intense development of digital image-based computational approaches has been facilitated by modern advanced microscopic experimental equipment and computer-aided technologies. The collected data points are created from scanned images of the material structure, which can in turn be used as inputs to numerical approximation methods. It has been shown that image-based FEM is very effective tool with several advantages [74, 78, 79]. It enables one to analyze a local micro-scale behavior of various materials, where in-situ measurements are either very complex or just impracticable. There are several primary computational-approximation methods developed, such as: extended finite-element method (*X-FEM*, [74, 75, 77]); meshless method [76]; voxel-based FEM, [74]; computed tomography scanning with 3-D image reconstruction for FEA, [78]; and the “OOF” (*finite-element analysis of microstructures*) approach linked with electron back scatter diffraction (*EBSD*) scanning, oriented toward understanding micro-scale phenomena, [79]. The accuracy of boundary models and homogenization issues are discussed in detail in several works [80].

The idea behind it is to provide some more clues about the micro-scale phenomena, in order to understand the general behavior of the bulk material. Usually such simulations are computationally expensive. Moreover, such approaches require a lot of professional understanding and ability to develop the model.

In this present work, the author tries to offer an alternative approach to assess microstructural behavior during HT by using well-known commercial products. The developed applied engineering technique is discussed in more details in Sections 4.4.3 and 4.4.4.

1.3.2 Computational thermodynamics and kinetics

Essentially, the thermodynamic and kinetic predictions have to be interpreted with caution and can be only considered as an approximation, because of the assumptions made and simplified implemented models in the software. For instance, the Scheil model assumes local equilibrium at the solid-liquid interface [82]. It is not relevant to the spin casting, because the solidification front is under centrifugal forces, therefore, affecting the diffusion and precipitation sequence.

Certainly, similar arguments could be made regarding any experimental heat and solidification studies (*DTA, Dilatometry, and others*) unless the experiments closely replicate industrial heating-cooling rates and conditions [82, 83, 84, 85]. This is particularly true given the controversy regarding the data and interpretations reported in the literature, where individual groups have tried to predict the behavior of heterogeneous alloys with different compositions and manufacturing conditions.

Keeping in mind that most of the thermodynamic databases are built on such reported results, it is very important to have up-to-date relevant modules in the software and validate predictions with our own experiments or/and observations. The ideal option would be to use at least two thermodynamic packages to fulfill a possible lack of data points and correlate predicted results to each other.

1.3.3 Computational fluid dynamics approach

It has been shown for many years that the computational fluid dynamics (*CFD*) is a very practical tool in studying fluid flow behavior in complex systems and applications. It became even more popular with advanced technological development of computer and software engineering.

Especially, in recent years, with developing parallel numerical codes and multiprocessor hardware, CFD is being positioned as the key to innovation, providing robust solutions and advanced visualization techniques for the post-processing analysis. As an example, some popular commercial and open-source software, which capable to simulate hot metal casting, are listed here: ANSYS Fluent, ANSYS CFX (USA, [86]); Start-CD (USA, [87]); Pro-Cast (France, [88]); Solid Cast (USA, [89]); COMSOL (Sweden, USA, [90]); OpenFOAM (*castingOpenFOAM*, [91]) etc. The main differences between the programs are: 1) the level of developed numerical models for specific problems (*i.e. physics, which can be considered*), and 2) the way to find a solution by approximation (*i.e. discretization*) method, for example, Finite Element (*FEM*), Finite Difference (*FDM*), and Finite Volume Method (*FVM*). There are many components in numerical methods (*e.g., consistence, stability, convergence, conservation, boundness, physics involved, accuracy, iterative methods to solve a system of linear equations etc.*), which can be compared between specific programs. The two suitable and available programs were used in the current work, ANSYS CFX and Star-CD.

Based on the literature review, there were no examples found related to the CFD of centrifugal spin casting of the mill rolls, in particular.

2.0 AIMS AND OBJECTIVES

Based on the review of modern roll manufacturing, several key problems have been identified:

1. The frequency of roll failure is becoming too high due to the increased loading and aggressive environments leading to considerable economic losses. This trend is especially apparent for conventionally casted and heat treated rolls. Hence, the alloy design and resulting thermo-mechanical properties require careful attention.
2. Poor chemistry control and large variability can lead to non-uniformity of microstructures, and therefore, to variations in mechanical properties throughout the roll.
3. Many fundamental questions remain unsolved, such as: what are the allowable residual stress levels and how are they redistributed during HT? What level of stress is permissible to ensure cohesion between the HSS shell and the core?
4. Optimization of chemistry levels to achieve the desired solidification pattern during casting and the material hardening response due to HT is required in order to achieve required thermo-mechanical properties. This issue remains a big dilemma despite a wealth of accumulated world-wide knowledge and experience. Moreover, some technological restrictions have to be taken into account, including: equipment constraints, safety concerns and production/supply timelines, when trying to achieve the desired changes for the roll material.

A review of the literature on spin-cast rolls clearly indicated that some major changes in the processing must be done in order to achieve the required roll performance. This can be done by improving the mechanical properties (*fracture toughness, wear resistance, red hardness, etc.*). However, in order to achieve the desired mechanical properties of the HSS shell layer two major

changes in the current processing must be done: 1) optimization in the alloy design of the shell material; and 2) microstructural improvement through heat treatments and phase transformation behavior. These changes can be addressed in the following ways:

1. Improved alloy design of the HSS shell material considering current manufacturing practices and limitations.
2. Improvement of spin casting processing parameters, especially better control of pouring temperatures, time intervals, rotational speed and cooling rates, are needed with regard to unidirectional solidification. The importance of this point focuses on controlling the precipitation sequence of alloyed carbides, i.e. MC, M₂C, M₆C, M₇C₃, and M₂₃C₆ (*M-sum of metal atoms, C-carbon*), while subjected to a centrifugal force field and while avoiding liquation. Such microstructural refinement, resulting from controlled solidification, provides better kinetic response to subsequent HTs.
3. The solidification behavior must be coupled with the improved HT routes. The expected benefits are to produce sufficient amounts and uniform distribution of the various carbides throughout the working HSS shell and an increase of alloying elements in the solid solution: to produce a tough, stable matrix during cooling and subsequent tempering treatments.
4. The implementation of modern surface hardening methods, for example, low/high frequency induction (*LFI/HFI*) and laser surface hardening techniques should be investigated. However these methods are beyond the scope of this thesis.

Thus, extended service life and improved performance of the shell material can be achieved by developing and controlling the microstructure via proper alloy design and subsequent heat treatments (*HT*). The main purpose of this work was to achieve improved microstructure of HSS

shell materials by developing non-conventional HTs, efficient accelerated quenching techniques, and appropriate alloy design.

This work resulted in improved as-cast structure of the shell and the development of a non-conventional heat treatment. These were achieved through proper chemistry selection and the development of HT regimes (*optimization of HT processing parameters with respect to existing equipment*). Simultaneously, the bonding integrity of the composite roll structure and constraints of the equipment capacity will be considered. Hence, the following objectives for this project were formulated and executed:

1. Systematic microstructural analysis of existing industrial HSS shell subjected to different HT conditions (*identification and classification of microconstituents, carbides, and matrix*).
2. Develop a microstructural evolution model for HSS casting and hardening HT, considering the sequence of carbides precipitation and phase transformations with the aid of thermodynamic-kinematic modeling.
3. Investigate continuous local microstructural transformations as a function of thermal gradient and radial depth in the HSS shell by combined thermodynamic-kinetics predictions and microstructural characterization of individual components mentioned above with FEM multi-scale approach.
4. Develop an integrated FE coupled thermal and structural approach to simulate hardening HT, which will establish the limits of HT parameters (*temperature and time*), considering the allowable thermal stress-strain conditions.

5. Develop a meso-scale FE model to simulate the local response of the microstructure to HT conditions. The FE model of the microstructure will be developed using sub-structuring and image-based techniques.
6. In-situ high temperature X-ray diffraction of oxidation response to solid-state transformations
7. Verify and validate the theoretical predictions through experimental means on test samples. The test methods included: a) microstructural analysis through optical and digital microscopy, b) scanning electron microscopy (*SEM*) with energy-dispersive spectroscopy (*EDS*), c) electron back scatter diffraction (*EBS**D*), d) bulk and microhardness measurements of the matrix, c) standard and high temperature X-Ray diffraction, d) phase balance analysis by microstructural image processing techniques, and e) re-heating-re-melting experiments on as-cast structure.

In summary, the above mentioned goals and objectives can be realized using theoretical predictions, computational approximation methods and experimental approaches:

1. Goals of experimental microstructural characterization of the HSS shell:
 - Identify the precipitates, microconstituents and second phase particles
 - Completely describe: the thermodynamic behavior of different carbides
 - Study dissolution behavior of the carbides
 - Define the type of matrix
 - Determine the microstructural evolution for different HTs through the HSS shell
2. Simulation and predictions:
 - Thermodynamic-kinetics studies
 - Computational fluid dynamics

- Finite-element analysis
- Sub-structuring and image-based finite element analysis

3. Experimental verification and validation:

- Advanced metallographic techniques and methods, including: specimen preparation, special etching to reveal particular carbides and detailed characterization, using OM, SEM with EDS and EBSD
- Conventional and in-situ high temperature X-ray diffraction
- Re-heating-re-melting experiments (*austenitization*)
- Phase balance analysis
- Hardness measurements: bulk, macro-, micro- (*VHN, HRB, HRC*)

3.0 EXPERIMENTAL PROCEDURES

Most of the materials characterization and all of the computational work was done using the facilities of Materials Micro-Characterization Laboratory (*MMCL*) at the Mechanical Engineering and Materials Science Department, University of Pittsburgh. The exceptions included that the materials were machined and prepared at the WHEMCO and/or United Rolls facilities. Most of the samples were supplied in an “as-etched” condition. In addition, the chemical composition of the investigated materials was determined at Spectrographic Technologies and Verichex Company, using the latest Foundry-Master Pro metal analyzer by Oxford-Instruments. Finally, the in-situ high temperature XRD was conducted using PANalytical’s company facilities.

3.1 MATERIALS DESCRIPTION

A detailed systematic microstructural evaluation was conducted on a set of 15 radial samples in as-cast, annealed, quenched, and tempered conditions, including worn material. The radial samples were sectioned from the rings removed from an edge of different commercial HSS work barrels with the diameters ranging from 40 to 50”, depending on the roll design. The rolls were industrially horizontally spun casted. The radial samples were 2-4” long, with the cross-sections approximately of 1×1”. Each radial sample included HSS shell (*complete or partial*), intermediate layer (*or intermix*) and the beginning of the core material (*fusion line and bonding*). Table [2](#) provides a list of these 15 test cases (*HSS radial samples*). The various entries represent different casting and HT conditions, including samples removed from the worn rolls after being in service.

Table 2. Analyzed HSS shell samples

#	Sample ID	HT	Wt.%C	Type of material
1	P0	Cast	2.0-2.2	Conventional as-cast
2	P0	P	2.0-2.2	Conventional as-cast + P
3	P0	A	2.0-2.2	Conventional A
4	P0	P+A	2.0-2.2	Combined P and A
5	S0	P	1.8-2.0	Refined as-cast + P
6	S0	P+A	1.8-2.0	Refined as-cast + Combined conventional P+A
7	S02	P+A	1.8-2.0	Refined as-cast + Increased T_γ
8	S-shell	Cast, no core	1.8-2.0	Only cast shell, no poured core
9	BTK	Worn shell	1.8-2.0	Worn after actual service
10	HTC	Worn shell	1.8-2.0	Worn after actual service
11	CPC	Worn shell	1.8-2.0	Worn after actual service
12	SPH	P	1.8-2.0	Refined as-cast + P
13	CA41	P+A+DT	1.8-2.0	Refined as-cast + P + DT + accelerated cooling
14	P9DT	P+A+DT	1.8-2.0	Refined as-cast + Non-conventional HT + DT
15	P9TT	P+A+TT	1.8-2.0	Refined as-cast + Non-conventional HT + TT
<i>Note: Cast- centrifugal horizontal casting; P-preliminary HT; A-austenitization; DT-double tempering; TT-triple tempering</i>				

Each sample has an identifier (*column 2*) and is either high carbon or low carbon (*column 4*). The cases vary by the material (“conventional”, “worn” conventional, or “refined” – see *column 5 of Table 2*). The conventional (*or conventionally casted and heat treated*) material existed before this study; and the material with the refined as-cast microstructure was developed through the course of this research. The type of HT is also given in the Table 2 (*see column 3*; “P” for Preliminary, “A” for austenitization, “DT” for double tempering, “TT” for triple tempering). The reader is cautioned not to confuse the “Px” used in the identifier (*column 2*) with the preliminary HT given in column 3. All 15 samples had compositions within the ranges given in Table 1.

The P0-group represents a relatively high carbon group, whereas S0- is a lower carbon group. The S02 roll is subjected to relatively high austenitization temperatures (T_γ), enabling

dissolution of fine eutectic and secondary precipitated carbides dispersed in the as-cast matrix, alternating with interdendritic solute-rich regions. The S-shell experimental sample (*sample 8*) is machined from an actual size tube shell produced by spin casting, but without the poured core, in order to assess a pure state of developed cast microstructure. The BTK, HTC, CPC are radial samples from rolls used in an actual service environment. CPC stands for “continuous pouring for cladding”; abbreviations of BTK and HTC are just the customer references. Hence, the remaining HSS material is near the intermix region. SPH demonstrates the refined as-cast structure after typical preliminary HT. CA41 represents improved cast microstructure processed conventionally, but with accelerated cooling. The P9DT and P9TT samples are from rolls prepared as a result of this research. They have a finer grain size and a uniform high hardness profile due to improved casting procedures and HT routes.

3.2 METALLOGRAPHY AND SAMPLE PREPARATION

3.2.1 Sample preparation and chemical etching

Standard metallographic techniques and methods were used to analyze the samples, including grinding, polishing, and etching in accordance with the ASTM E3-11 standard. For optical and digital metallography, the samples were prepared by grinding with 180, 240, 320, 400 and 600 grit silicon carbide sandpaper, with final polishing achieved through using 1.0 μ m and then 0.05 μ m alumina powder. Two standard surface etching techniques were used in this study: 2-4% Nital and LePera’s etching. For more detailed three-dimensional investigation of microstructures, both Murakami and 10% Nital deep etching techniques were implemented. Both used a soaking time

of approximately 1 minute, which provided satisfactory results for the characterization of the microconstituents.

3.2.2 Optical-digital microscopy

The optical microscopy was done using an Olympus BX-60 and a Keyence VHX-600 Series digital fiber-optic microscope (*54Mega pixel CCD camera and actuator*). Different types of lenses with light field and dark field filters were used in order to achieve suitable micrograph quality that highlighted the microconstituents for the subsequent image processing and phase balance analysis. As-polished and etched samples were analyzed from surface to the bond line at different magnifications, including: 100X, 300X, 500X, 1000X, 2000X, 5000X. Continuous and step-wise imaging were conducted. For example, the continuous micrographs at 100X and 300X are stitched together in order to visualize the transitional behavior of the microstructure. The stitched imaging is compared with the microhardness indentation profile, where each VHN indentation is made at 1mm steps from the surface to the bonding line. The higher resolution images are also taken radially with a 3-5mm step, depending on the desired precision and microstructural variability in each particular sample.

3.2.3 Hardness measurements and Optical Emission Spectroscopy (OES)

The surface hardness measurements are conducted at room temperature, using a digital HRC-hardness Rockwell C (*150 kgf*), HRB-hardness Rockwell B (*100kgf*) and Leco M-400 Vickers (*VHN- Vickers hardness number, 300, 500, 1000 gram-load with 10-12 seconds dwell time*). The bulk hardness (*HRC, HRB*) testing of the metallic matrix was performed according to ASTM E18

along the radial samples in the as-polished condition with a $\frac{1}{4}$ '' step. A point-wise and line hardness indentation of the matrix in the radial direction from the surface to the bond line were performed in accordance with ASTM E384. The microhardness VHN measurements of the matrix and individual carbides were performed using 10, 20, and 50 gram loads with 10-15 seconds of dwell time. These measurements were conducted in three locations: at the surface, middle, and bonding lines. At least 15-30 indentations were made for each location at different spots. Bulk VHN, HRB, HRC hardness measurements were performed at room temperature (*RT*), including VHN measurements of the matrix and some selected carbides. Because of the varying microstructure and relatively rough surface due to the carbides even after polishing, different loads were applied (*300g, 500g and 1000g*) and VHN values were compared. Different loads had to be applied due to fine and coarse microstructure variability through the considered HSS shell.

Decrease and non-uniformity in hardness through the thickness of the conventional HSS shell and considerable drop at the intermix zone led to an assumption of the cast segregations and bonding of two dissimilar materials, respectively. In order to verify it, the chemical composition gradient was analyzed with glow discharge-optical emission spectrometry (*GD-OES*) in general accordance with ISO 14707:2000E First Edition (*2000-18-15*). The carbon and sulfur contents were determined by combustion using combustometric methods (*LECO*) in accordance with ASTM standard E1019-03. Considerable dilution of the alloying content from the surface to the core was observed in conventionally casted rolls. The chemical equilibrium was not even achieved after conventional heat treatment procedures. The step-wise hardness profiles from the surface of the roll were compared to the measured compositional gradients and superimposed with optical micrographs (*see Section [4.2](#)*).

The precise measurements, with 1mm step size from the surface of the roll down to the core and with 10 seconds of dwell time, initially revealed the hard zone, a transient region with gradually decreasing hardness, and a more stabilized area of relatively lower hardness before the fusion line. Each location was compared with the corresponding OM and SEM continuous imaging taken at different magnifications to assess the microstructural influence on the hardness properties. The same HSS roll type was subjected to different HT routes (*austenitization with double or/and triple tempering, preliminary HT and both combined*); then radial samples were machined again from the removed ring of the roll body, and hardness measurement with microstructural observations were taken repeatedly and compared.

3.2.4 Scanning electron microscopy

Scanning electron microscopy (*SEM*) and energy-dispersive X-ray spectroscopy (*EDS, or also EDX, EDAX*) analysis was done using a JEOL 6610V and Philips XL-30 field emission gun (*FEG*) SEM systems, both equipped with orientation imaging microscopy (*OIM*) for electron backscatter diffraction (*EBSD*)-image quality (*IQ*) analysis. SEM and EDX spectroscopy were used for the characterization of the microstructures and for semi-quantitative EDS X-ray microanalysis. The samples were etched with different microstructural etching reagents for tool steels, such as: 2% Nital, 10% Nital (*deep etching*), Murakami [[128](#)], Picral, depending on type of analysis and following image processing. EDS analysis included: detailed individual carbides semi-quantitative analysis; local segregations via line and area scanning; the studies of intermix zone and fusion line between the shell and the core; 2-D mapping of interdendritic segregations. The SEM analysis was conducted with a 20 - 25 kV accelerating voltage. Backscatter electron mode (*BSE*) provides excellent contrast and visualizes local segregations: white areas are associated with Mo-rich

carbides; dark grey- V-rich; intermediate color (*light grey*) is mostly corresponding to compounds having Cr, Mo and V.

3.2.5 Electron backscatter diffraction

For the electron backscatter diffraction (*EBSD*) microanalysis, which is also interfaced with SEM, additional sample preparation was required. The radial samples in the as-cast condition were also sliced at the roll surface with the aid of water jet cutting system (*performed at WHEMCO facilities*). Then the cut round coupons (*10 mm in diameter, 2 mm thick*) are mounted in conductive Cu-based powder and polished for 3-4 hours using Buehler VibroMet Polisher. EBSD-IQ analysis was used for a more comprehensive, quantitative and detailed identification and examination of the microconstituents (*different phases, carbides, fine precipitates*) in terms of crystalline structure.

3.2.6 Image analysis and processing

Capturing, image processing and quantitative measurements were performed, using a computer controlled Bioquant Image Prime [92] and PaxIt [93] image analysis systems attached to an optical microscopes with Leco digital cameras. Open-source ImageJ [94] software was also used for additional post-processing, filtering, and thresholding. All equipment and instrumentation was used in accordance with its relevant procedures described in corresponding manuals and instructions.

The image analysis of OM and SEM micrographs was performed in order to assess the volume fraction of individual carbides and phases, in particular, their morphology as a function of

radial distance from the surface of the HSS roll. Different etching techniques were applied in order to reveal particular features in the microstructures and distinguish the phases. Initial SEM/EDS analysis enables one to relate the identified microconstituents to OM images, which can be used for statistical data collection. In other words, the produced continuous OM images also represent transitional microstructure at lower magnification and contain more data points. All micrographs are taken between the surface and the bond line of each sample. Depending on the magnification, either continuous, or step-wise imaging was produced. The continuous images can be stitched together and superimposed with the microhardness indentation profiles (*see Section [4.2](#) and [4.5.2](#)*). It helps to correlate the microstructure with the hardness results. In addition to the OMs, continuous SEM micrographs taken at lower magnifications ($\times 100$, $\times 300$), providing good statistical data for the phase balance (*frequency of occurrence*) and distribution of each individual phase/carbide along the shell. The higher magnification images are used for more precise analysis of the microconstituent's morphologies.

3.2.7 X-ray diffraction analysis

Conventional X-ray diffraction (*XRD, Cu-radiation*) scans were performed at three spots (*surface, middle, and intermix zone*) on a polished surface (*or slightly etched with 2% Nital*) of the HSS radial samples in order to assess any possible crystallographic changes as a function of radial depth. XRD analysis was done using Philips Analytical X-Ray PW3710 based X'Pert Diffractometer systems. The XRD plots (*X-ray intensity vs. 2-theta diffraction angle*) were analyzed using PANalytical's X'Pert High Score Plus software. The system provided detailed information on phase composition, crystallographic texture, and crystalline quality and compared to EBSD results.

The second XRD unit includes a platinum hot stage capable of temperatures up to 1100°C. In-situ observations of diffusion reactions with increased temperature were performed using high temperature X-ray diffraction (*HT-XRD*). Additionally, in-situ high temperature XRD (*HT-XRD*), or often called “non-ambient XRD”, studies were done on two improved and conventional compositions, having low (*S-shell, as-cast*) and high carbon (*P0-as-cast*), during a heating cycle under laboratory conditions (*air atmosphere*), using a Co-radiation beam source. Coupons (*12mm dia., 2mm thick.*) were produced from the surface of the HSS shells by wire EDM (*electrical discharge machining*) and are shown in Figure 16 (*top left corner*).

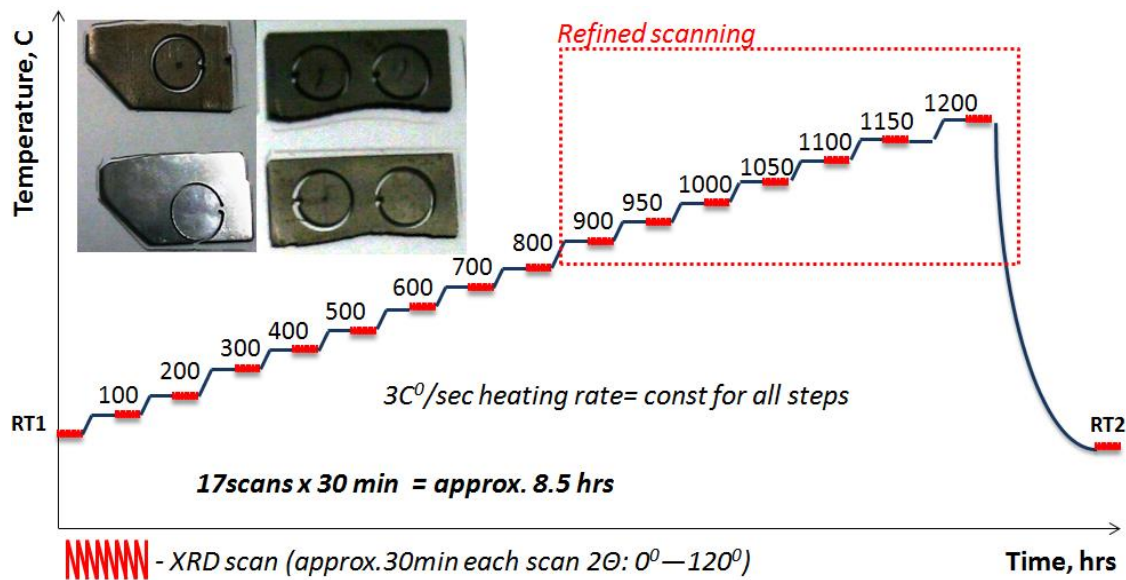


Figure 16. HSS tested coupons and high temperature XRD procedure

The procedure was correlated with the predicted equilibrium carbon diagram for the particular alloy, shown in Figure 17.

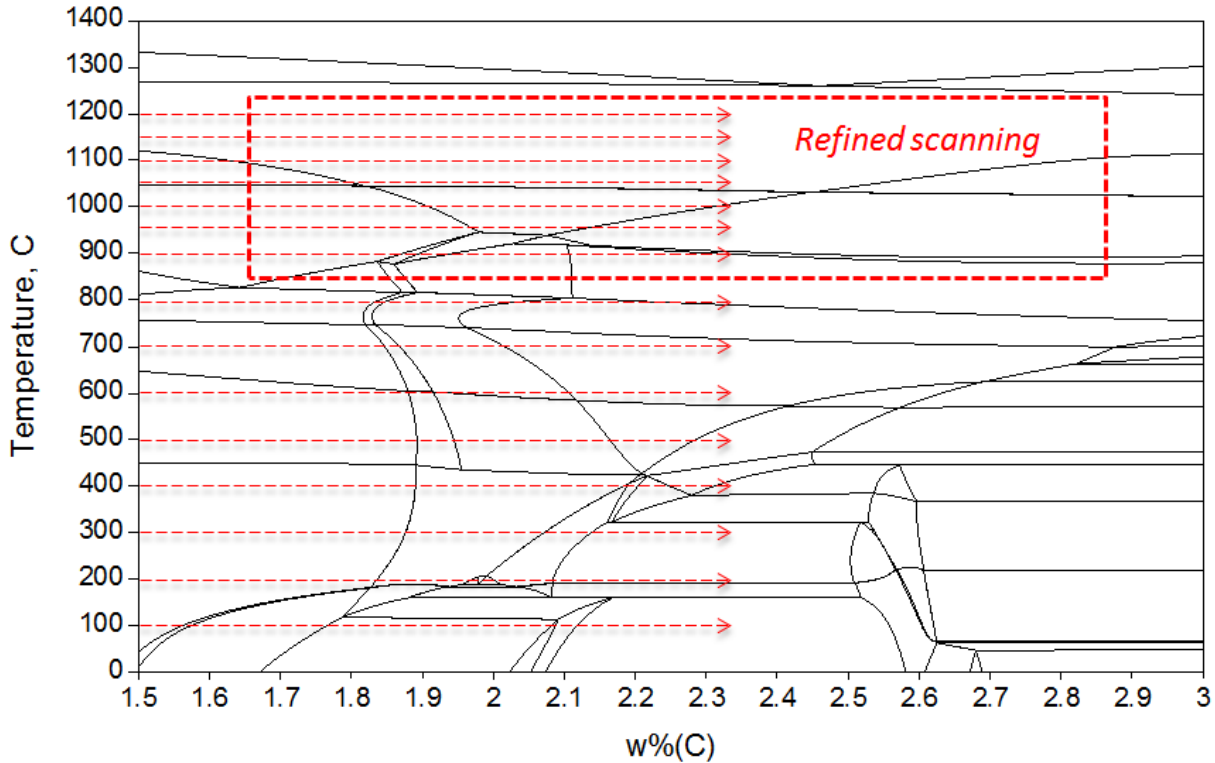


Figure 17. Temperature steps with regard to predicted equilibrium diagrams

The refined scanning (50°C step from 900°C, red rectangular area in Figure 17) at the high temperature region was considered in order to trace the solid-state transformation, associated oxidation and define the critical carbide's dissolution temperature. Each step takes approximately 30 minutes with 0-120° 2 θ angle range scanning; hence, it took at least 4 hours to get up to the high temperature range, starting from 900°C. The complete heating cycle was accomplished within 6 hours; the whole experiment took no more than 9 hours. It was assumed that this amount of time was sufficient for the diffusion to reach equilibrium in the relatively small sample. Notice that the heating rate resembles an industrial setup; therefore, the procedures were close to each other. The Figure 16 shows selected re-heating thermal path.

The oxidation study was not the main part of the current work, but in order to get the general assessment of the possible oxide formations and behavior as a function of temperature,

some observations were made in a dry air environment (*see Section 4.5.1*). The in-situ oxidation behavior from RT to 1200°C was studied with HT-XRD for the first time of considered spin cast HSS grades. This approach helped to relate the solid-state transformations to the oxidation patterns. The similar studies can be found in [111, 112, 113].

3.3 RE-HEATING-RE-MELTING PROCEDURES

In addition, to the industrially processed roll materials, laboratory heat treatments were done on samples in as-cast condition (*high (P0) and low (S-shell) carbon, Table 2*). The preliminary heat treatment was not included into consideration. The purpose of these re-heating experiments was: 1) to establish the critical dissolution temperature (*optimal austenitization*) of the transient carbides and segregations; 2) to define related sufficient soaking time to make the dissolution-decomposition complete. The effects of heating and cooling rates were also considered. Figure 18 shows an example of two applied heat treatments, where austenitization temperatures ($T_{\gamma 1}$, $T_{\gamma 2}$), soaking times (t_1 , t_2) and heating-cooling rates (hr_1 , hr_2 and cr_1 , cr_2 , respectively) were varied.

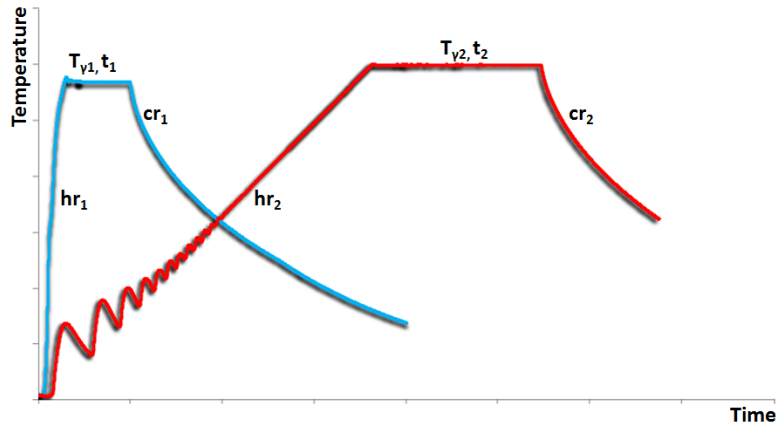


Figure 18. Temperature-time profiles of the re-heating-re-melting procedures

The metal processing is conducted, using Theta dilatometry furnace in an inert atmosphere. The coupons (12mm in diameter, 2 mm thick) were produced from the surface of the as-cast HSS shell. The R-type thermocouple (*i.e. platinum (negative) and platinum-13% rhodium (positive) wires*) was attached to the surface by tack-welding machine, Figure 19.

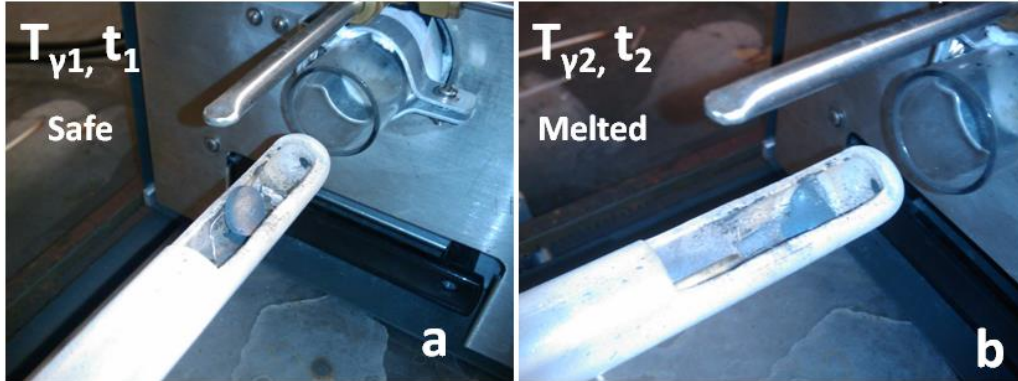


Figure 19. HSS coupons with attached thermocouples in Dilatometry furnace

The results of these re-heating experiments are discussed in Sections 4.2 and 4.2.1.

3.4 THERMODYNAMIC-KINETIC ANALYSIS

Thermodynamic and kinetics predictions were made for several iron-based alloys and compositions with the aid of commercial software packages Pandat 8.0 [130] and JMatPro 4.0 [131]. In Pandat a thermodynamic database for multi-component iron-based alloys was used, which includes experimental data of HSS alloys. Equilibrium (*lever rule*) and non-equilibrium (*modified Scheil-Gulliver*) approaches were utilized in order to predict the behavior of multi-component systems and determine the phase transformation temperatures, phase balance, volume

fraction, partitioning of components, phase compositions, and thermo-physical, mechanical properties for both the bulk material and its microconstituents. Solidification behavior and solid-state transformations were predicted.

Using the CALPHAD (*“calculation of phase diagrams”*, [[129](#)]) method implemented in JMatPro and Pandat software, the thermodynamic modeling was done on provided and measured chemistries in order to predict the phase balance at the equilibrium state and during kinetic transformations (*e.g. solidification and solid-state transformations*). The effects of alloying elements have been analyzed, regarding the changes on the predicted phase diagrams, and compared to actual microstructural observations. The predicted thermo-mechanical and physical properties as a function of temperature were used as an input for the FE and CFD material models. The results and implications are discussed in Section [4.1](#).

3.5 NUMERICAL ANALYSIS

The implementation of numerical analysis was applied in nature: there was no need to create a new code or offer a new numerical algorithm. But rather the use of the existing techniques and methods to aid in the understanding of the spin casting process; and development of coupled thermal-stress and micro-scale heat transfer models of the HSS roll and its microstructure, respectively. A complex, multi-scale integrated FE approach to simulate the heat transfer through the HSS roll body, considering the composite structure and nonlinear properties of individual domains was developed for the first time (*based on reviewed literature sources*). In the current work, all the factors such as: multi-scale heat transfer, temperature dependent properties, compositional and thermal gradients in the shell, stress-strain development, had to be taken into consideration. The

nonlinear thermal-physical properties of the given and developed materials were not available in the literature. Also the accurate representation of the HSS shell as a composite, using data from chemical analysis was not offered before. Developed novel image-based microstructural FEA, which is based on combined microstructural analysis, SEM/EDS, thermodynamic predictions and image processing, provided an alternative way to analyze micro-scale nonlinear heat transfer (*see Section [3.5.2.4](#)*), using available software products (*ANSYS WB [\[125\]](#), JMatPro, Pandat, AutoCAD [\[100\]](#), ImageJ [\[94\]](#)*). Moreover, an attempt to simulate horizontal spin casting of the HSS molten metal, using CFD approach with the aid of Star-CD [\[87\]](#), was done for the first time, again according to reviewed available literature (*see Section [3.5.1](#)*). Therefore, the developed complex modeling, which is described in the following sections, combines all these factors, approaches and experimental techniques.

3.5.1 CFD formulation

At the beginning of this program, it was a big unknown what happens to the molten metal during pouring and centrifugal spin casting. Such questions were raised, because of the problems observed in conventionally casted material: coarse microstructure with mixed columnar dendrites and cluster segregations (*see Section [4.2.1](#)*). Therefore, some efforts had to be made in order to better understand the general behavior of the spinning melt inside the chamber as a function of several parameters described below and to explain the observed micro-, and macro-segregation issues (*Section [4.2.1](#)*).

CFD analysis was utilized to understand the very first stages of the horizontal spin casting process: distribution of the molten HSS material inside the spinning chamber and air interaction at the moment of injecting and spinning the melt.

The present paper reports some preliminary results on the multiphase modeling of the melt behavior in the horizontal spinning chamber. Three-dimensional (3-D) CFD model of the HSS melt was developed in a novel way based upon the volume-of-fluid technique, using Star-CD []. Notice that for the centrifugal spinning the fluid flow velocity has to be solved in a rotating reference frame. It is important to recognize a difference with respect to standard stationary casting simulations, which are widely available elsewhere.

The liquid properties, used in the modeling, were predicted with thermodynamics software based on actual chemical composition analysis performed on different heats. In Figures [20](#) and [21](#) the liquid viscosity and density of the melt are shown, respectively. The effect of carbon concentration is also taken into account, where the lower carbon concentration alloy shows higher liquid viscosity and density (*Figures [20](#), [21](#)*).

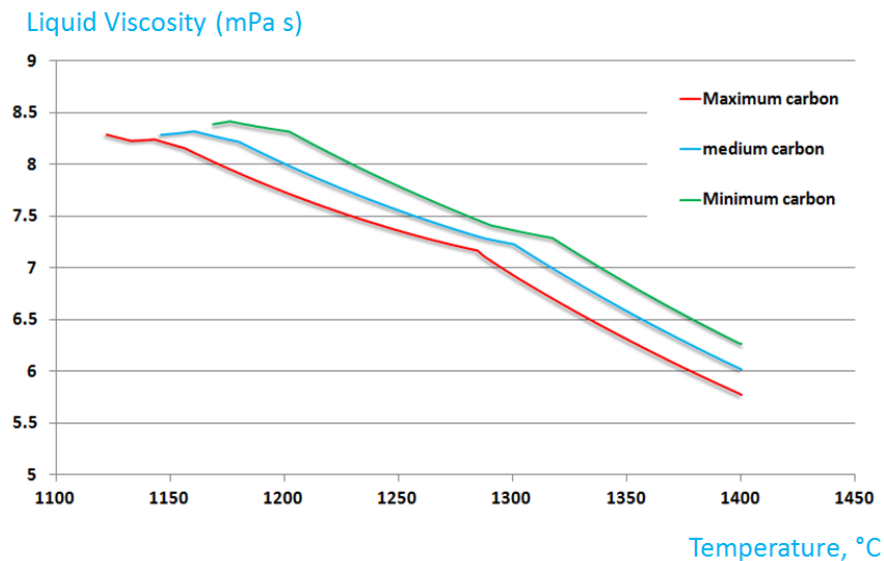


Figure 20. Predicted liquid viscosity as a function temperature and composition

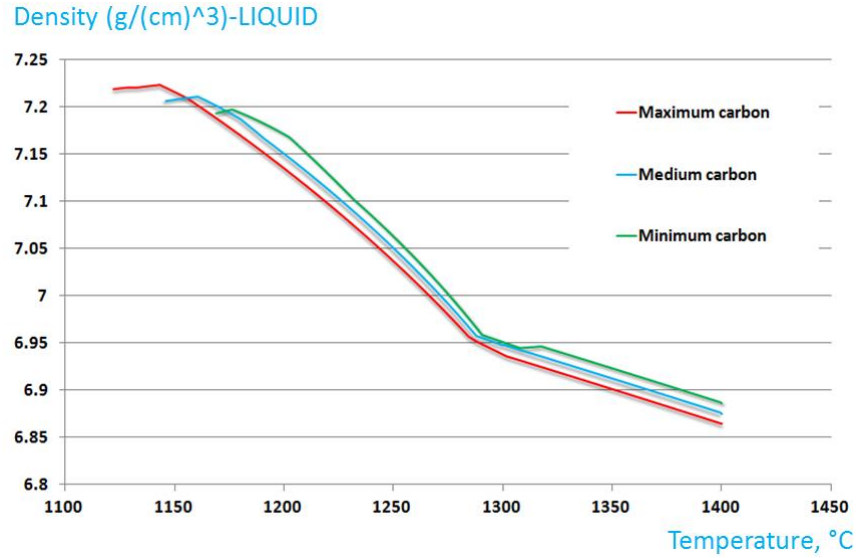


Figure 21. Predicted density as a function temperature and composition

The CFD model consisted of two main domains: 1) the inlet (*parallelepiped*), and 2) the spinning chamber (*cylinder*), shown in Figure 22. The mesh consisted of 200,000 volume elements. The inlet, or “feeding arm”, stays stationary all the time, while the mold chamber is spinning. The melt is being supplied through the feeding arm at particular rate, which continuously flows down to the inner surface of the spinning mold by the influence of gravity. Therefore, the liquid metal distributes along the mold by viscous and centrifugal forces. Three types of boundary conditions were utilized:

- 1) Inlet with prescribed velocity, volume fractions, temperature and turbulence parameters, representing the feeding-arm.
- 2) Split-flow outlet (*i.e. outflow*); the condition “consumes” the flow rate in the near-boundary computational cells.
- 3) Rotating non-slip mold wall (*i.e. fluid velocity coincides with wall velocity*) with standard wall functions for the turbulence model. The angular velocity of rotation was corresponding to actual industrial data and assigned to spinning BCs.

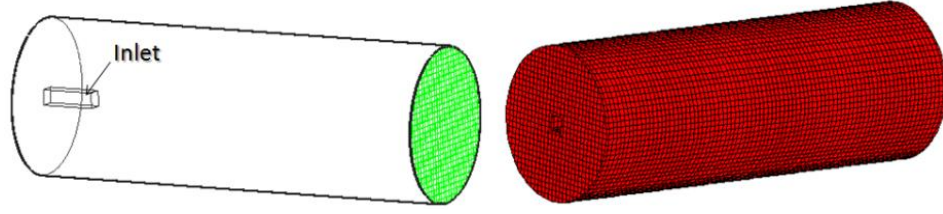


Figure 22. CFD model: domain geometry and meshing

The heat transfer between melt-wall and melt-air were taken into account. A brief mathematical description of the developed CFD model is given below. The model is based on the Volume-of-Fluid (VOF) approach [95, 96, 97] which utilizes separate continuity equations for each phase:

$$\frac{\partial \alpha_s}{\partial t} + \nabla(\alpha_s \vec{U}) = 0, \quad (1)$$

$$\frac{\partial \alpha_a}{\partial t} + \nabla(\alpha_a \vec{U}) = 0, \quad (2)$$

where α is the volume fraction of a phase, and \vec{U} is the flow velocity. Indices s and a are assigned for the steel and air, respectively. Then the following volumetric constraint can be applied:

$$\alpha_a + \alpha_s = 1 \quad (3)$$

The flow is assumed to be homogeneous within a computational volume. Therefore, the main physical properties of the multiphase mixture are calculated based on the homogeneity assumption:

$$\rho = \rho_a \alpha_a + \rho_s \alpha_s, \quad (4)$$

$$\mu = \mu_a \alpha_a + \mu_s \alpha_s ,$$

where ρ is the density and μ is the dynamic viscosity.

The predicted viscosity of the steel follows the empirical theological expression (*see Figure 20*):

$$\mu_s = \mu_s(T) \quad (5)$$

The momentum equation has been modified to predict the equivalent flow parameters for both phases:

$$\rho \frac{\partial \vec{U}}{\partial t} + \rho \vec{U} \nabla \vec{U} = -\nabla p + (\mu + \mu_t) \Delta \vec{U} + \rho \vec{g} + \vec{F}_c \quad (6)$$

where μ_t is the turbulent viscosity; g is the acceleration due to gravity; and \vec{F}_c is the capillary force.

The turbulent viscous behavior can be described, using a k - ε turbulent viscous model [95, 96, 97], solving two more additional scalar equations for turbulent kinetic energy transfer (k) and the rate of its dissipation (ε):

$$\mu_t = 0,09\rho \frac{\kappa^2}{\varepsilon}, \quad (7)$$

$$\frac{\partial(\rho\kappa)}{\partial t} + \nabla(\rho\vec{u}\kappa) = \nabla\left(\frac{\mu + \mu_t}{\sigma_\kappa}\nabla\kappa\right) + \kappa(G - \rho\varepsilon), \quad (8)$$

$$\frac{\partial(\rho\varepsilon)}{\partial t} + \nabla(\rho\vec{u}\varepsilon) = \nabla\left(\frac{\mu + \mu_t}{\sigma_\varepsilon}\nabla\varepsilon\right) + \frac{\varepsilon}{\kappa}(C_1G - C_2\rho\varepsilon), \quad (9)$$

$$G = (\nabla\vec{u} + \nabla\vec{u}^T) : \nabla\vec{u}, \quad (10)$$

$$\sigma_\varepsilon = \frac{\kappa^2}{[0,3(C_1 - C_2)]} \quad (11)$$

where $C_1=1.44$; $C_2=1.92$; $\sigma_\kappa=1.0$, and $\kappa=0.4187$ is von Karman's constant [98].

Finally, the energy equation is:

$$\rho \frac{\partial e}{\partial t} + \rho\vec{U}\nabla e = -\nabla(p\vec{U}) + \nabla(p\tau\vec{U}) + \rho\vec{g}\vec{U} + \vec{F}_c\vec{U}, \quad (12)$$

where e is energy and τ is the viscous stress tensor.

Equations 1, 2, 6, 8, 9, 12 were spatially discretized via MARS (*i.e. monotone advection and reconstruction scheme*, [95]) and then solved by the three-time level implicit technique SIMPLE (*solution algorithm*, [95]).

Note that the simulation of the phenomenological dynamic behavior of molten HSS inside a horizontal spinning chamber was made with the aid of 3-D CFD simulations for the first time, based on the review of open literature sources. The results permitted three-dimensional visualization, which demonstrated, that: 1) the localized turbulence of the molten metal can form non-homogeneities in the HSS shell; 2) possibility of formation of two solidification fronts due to contact with the mold and air entrapment through the opening of the spinning chamber; both of these fronts influence unidirectional solidification, which is controlled by the convective transport

in the melt. It is important to mention that the work done using CFD approach was with the sole idea of providing a better understanding of the complex solidification reactions observed. The results of the simulation are discussed in more details in Section [4.3](#).

3.5.2 FEA formulation

The major effort was for FEA modeling, which simulated the transient heat transfer during austenitizing heat treatments and associated thermal-stresses. The purpose of any HT is to achieve the desired microstructure, which controls the mechanical properties. Therefore, the primary goal of the modeling is to predict the heat transfer through initially nonhomogeneous shell structure. The original assumption was that it could be possible to heat treat through the shell at higher austenitization temperatures, transforming brittle carbide networks and equalizing local chemical non-homogeneities. At the same time, it is necessary to control the microstructural transformations (*e.g., carbides dissolution behavior*) during the HT in order to provide uniform thermo-mechanical properties, radially and longitudinally in the HSS shell. The main emphasis is made on radial heat transfer and related microstructural transformations.

Heat transfer analysis of the composite roll structure during HT is a complex process, where the varying microstructure of the shell and dissimilar core material have to be considered. Accordingly, the thermo-physical properties are varying as a function of position in the roll. Only radial compositional gradients were considered in the present work. It is assumed that the chemistry is constant along the axis of the roll, which is not always the case especially for the core, which is being casted vertically and statically in considered case. The core could have macro-segregations as in conventional cast ingots, but assumed to be homogeneous and isotropic in the developed FE models.

In the current work four different FE models were developed in terms of geometry (*scale, orientation and considered domains*), boundary conditions and material properties: 1) 1-D radial model (see Section [3.5.2.1](#)), 2) axisymmetric longitudinal 10° sector (see Section [3.5.2.2](#)), 3) full-scale roll model (see Section [3.5.2.3](#)), and 4) microstructural image-based FE model (see Section [3.5.2.4](#)). For all developed thermal FE models, the heat conduction formulation is considered to be nonhomogeneous, with constant and time-varying boundary conditions established from pyrometer readings discussed below.

3.5.2.1 Sub-structured 1-D radial models

The purpose of simplified 1-D radial models is to study the heat transfer through the HSS shell during HT, taking into account compositional variations. Therefore, the 1-D radial model was sub-structured, consisting of multi-layers with individual material properties. Two types of 1-D radial model are considered, having 3 and 11 homogenized layers, representing the roll structure with uniform and high compositional gradients, respectively. In Figure [23](#) the 1-D FE model is shown; where the centrally cut radial rod includes the multi-layered HSS shell, intermix zone and core.

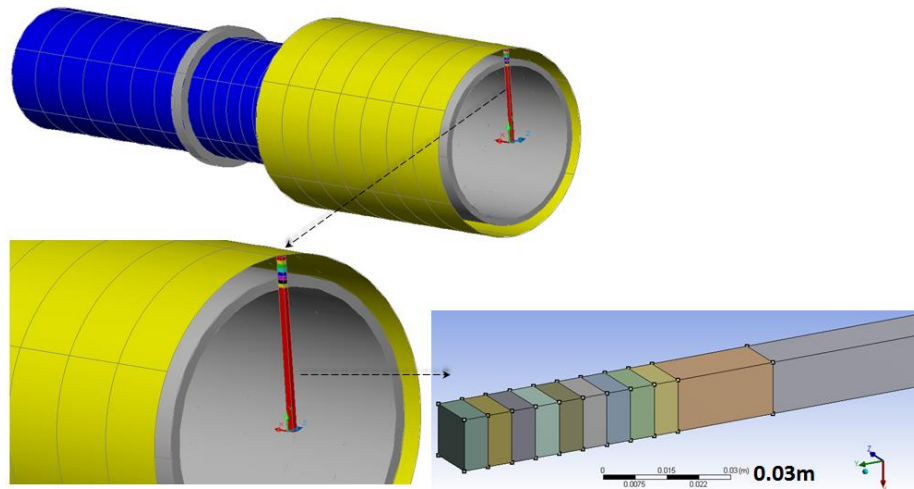


Figure 23. Radial semi-1-D sub-structured model of the HSS shell and core

The number of layers depended upon the desired degree of accuracy and the actual chemical variability through the shell (Figure 24). The shown 11-layer model has 9 sub-domains in HSS shell, intermediate layer (*intermix*) and core domain; whereas in contrast the 3-layer model has the homogenized shell and the same intermix and core. The 3-layer model represents improved roll structure and material. The predicted material properties for this 1-D radial 3-layer model were also used for the 3-layer axisymmetric (see Section 3.5.2.2) and 3-layer full-scale roll models (see Section 3.5.2.3).

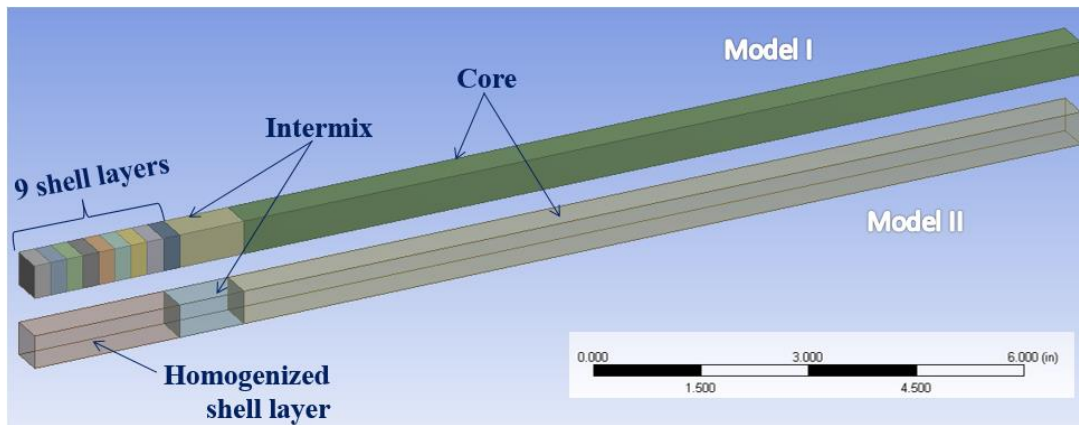


Figure 24. Radial sub-structured models of the roll

Each particular layer (*i.e. domain*) is considered isotropic and homogeneous along the roll. The core material was assumed to be uniform, neglecting common cast segregations. Full nonlinear thermal transient analysis was done on the sub-structured models (*11 and 3 layers*), representing the compositional variation of the roll in the radial direction. The 11-layer model (*i.e. 9 layers of HSS shell, intermix and core*) represented the conventional as-cast material, while the 3-layer model (*improved case*) consisted only of a homogenized HSS shell, intermix and core. A

simplified 1-D approach was compared with axisymmetric models, which took advantage of the axial symmetry to reduce computational time.

The material properties of the layers were predicted based on corresponding actual chemical compositions, which were measured as a function of the radius, using optical emission spectrometer (*OES*). The carbon and sulfur contents were determined by combustion, using Leco combustometric methods in accordance with ASTM standard E1019-03. All other elemental contents were determined by glow discharge-optical emission spectrometry (*GD-OES*) in general accordance with ISO 14707:2000E First Edition (2000-18-15). In Figure 25 actual radial cut-off sample from the HSS shell is shown, where GD-OES spark spots are visible on the surface, representing measured locations.

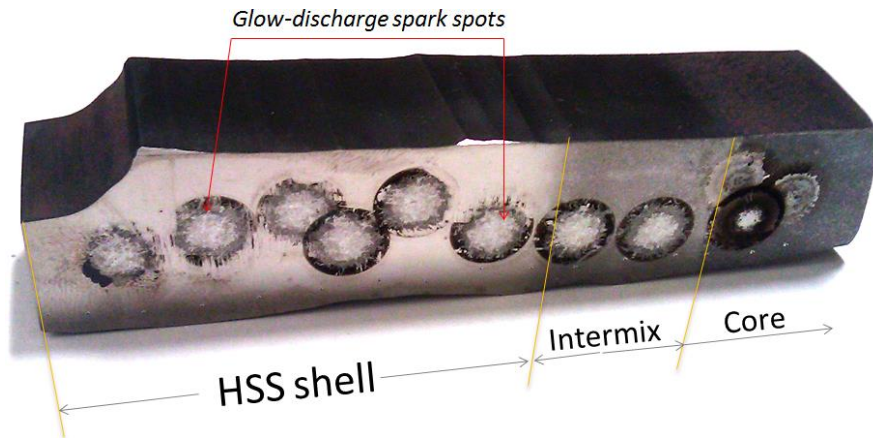


Figure 25. Radial cut-off HSS sample with sparks on surface from GD-OES measurements

Figure 26 shows a curve-fitting of the results, measured by GD-OES, i.e. chemical distribution (*weight %*, *vertical axis*) in conventional as-cast material as a function of radial depth (*distance from the surface of the roll*, *horizontal axis*).

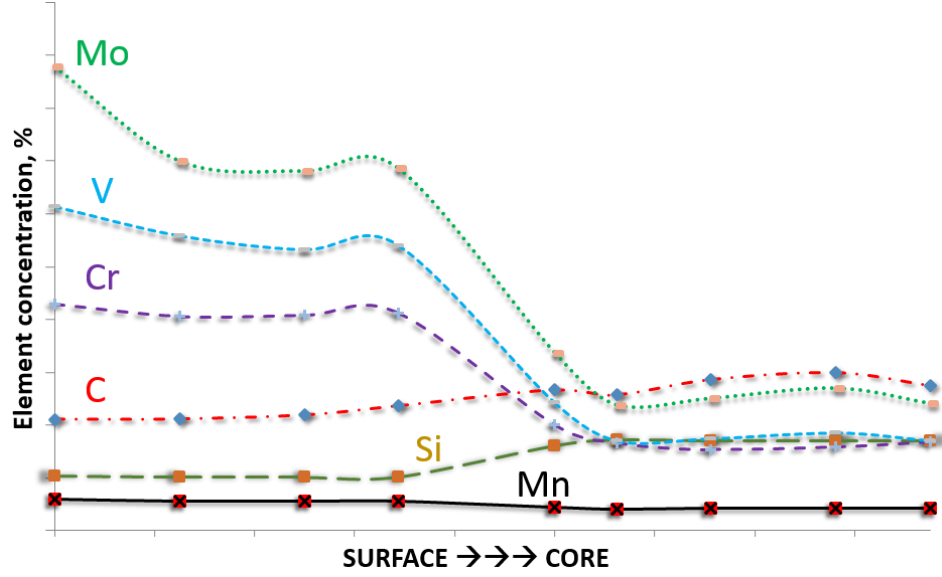


Figure 26. Measured compositional gradient along the HSS shell, intermix and core

The nonlinear material properties are predicted for each individual layer, using measured radial compositional gradient (*Figure 26*) and thermodynamic analysis (*see Sections 3.4 and 3.5.2.1*). The diffusion coefficient is determined by thermal conductivity, heat capacity and density, which are temperature and domain dependent in the composite model. For example, based on OES analysis, these properties were predicted, using JMatPro. *Figures 27, 28, 29* show density, thermal conductivity and heat capacity, respectively, for sub-structured 11-layer radial model (*Figure 24*). The “P11” to “P19” are abbreviations of corresponding OES sparks (“*burn spots*”, *Figure 25*) made from surface to the core, which represent individual domains in HSS shell.

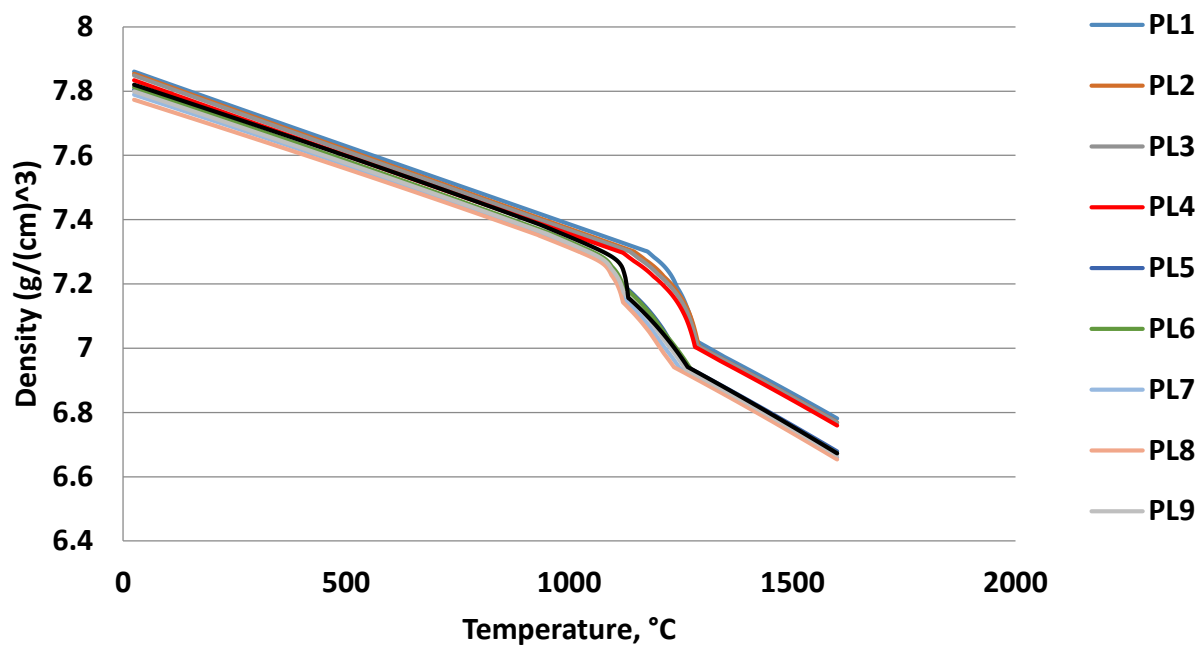


Figure 27. Predicted density of the layers vs. temperature

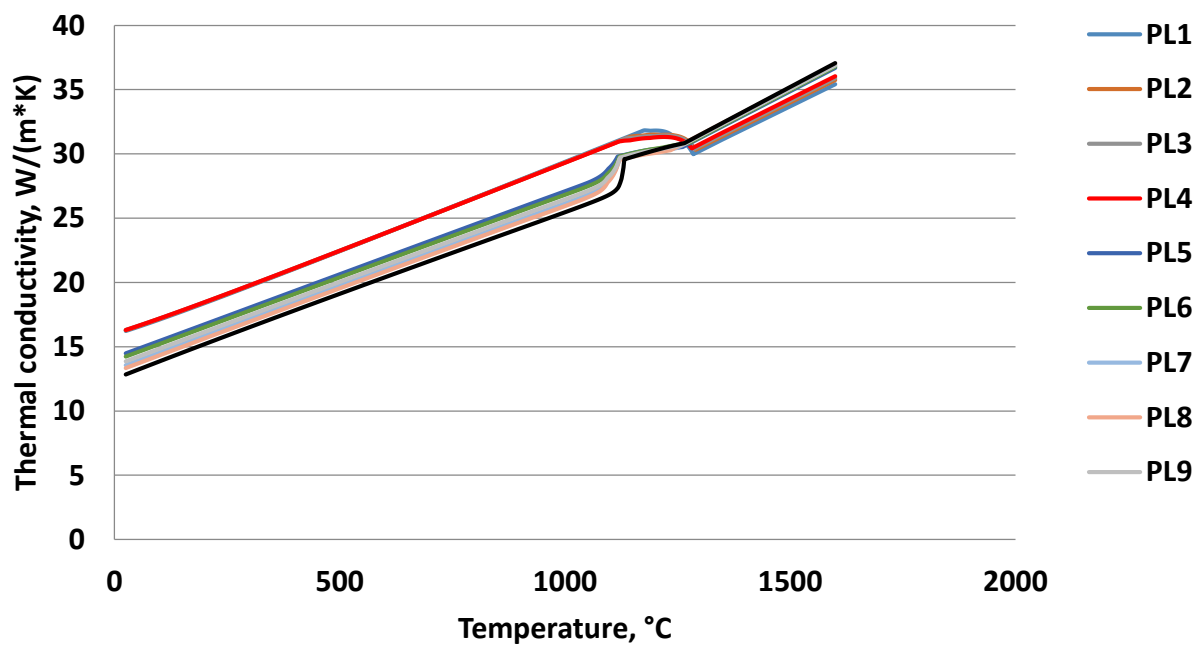


Figure 28. Predicted thermal conductivity of the layers vs. temperature

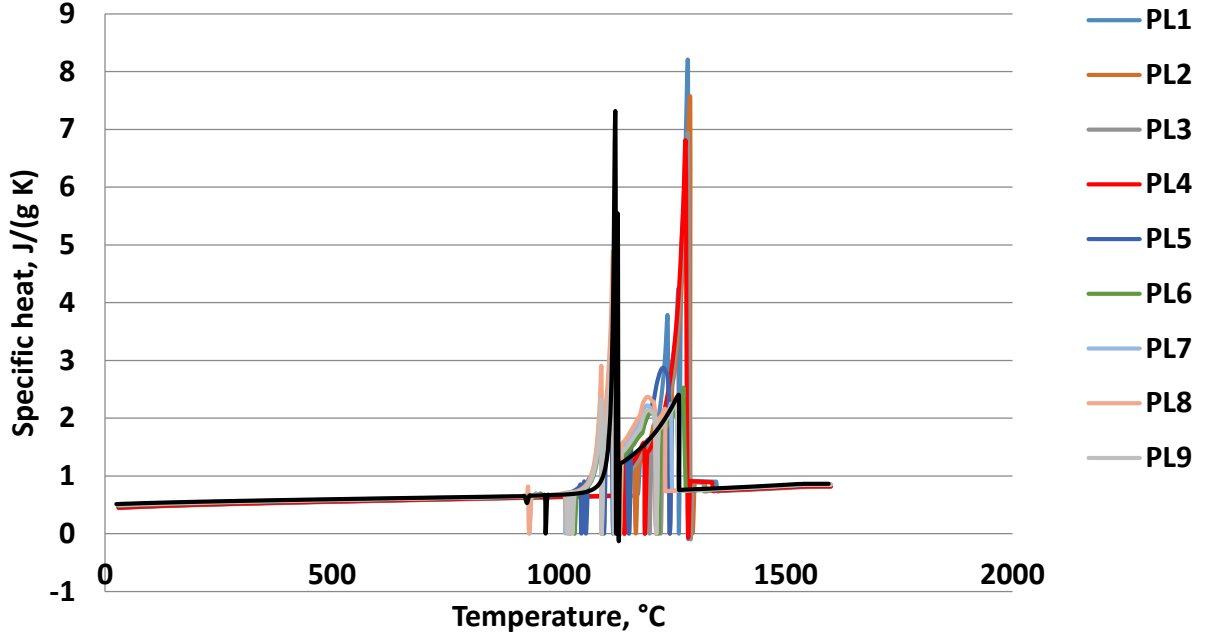


Figure 29. Predicted specific heat of the layers vs. temperature

A scattering of the heat capacity values at high temperature range (*Figure 29*) can be attributed to both the phase transformation reactions (*e.g., dissolution*) and existing database (*or/and numerical approximations*) of the thermodynamic software.

Three scenarios of boundary conditions (*BC*) were investigated. Using the 1-D models built with 3- and 11-layers, the radial heat transfer was studied. Theoretical austenitizing temperatures and corresponding initial conditions of the HT were applied on the surface of the 3- and 11-layer FE models. Two theoretical cases were considered: $T_{\gamma 2} [T_{i2}]$ (*Case 1*) $>$ $T_{\gamma 1} [T_{i1}]$ (*Case 2*), where T_{γ} and T_i are the austenitizing and initial temperatures, respectively (*Figure 30*). In the third scenario (*Case 3, Figure 30*), actual point-wise pyrometer readings acquired from the surface of the spinning roll were used as the tabulated temperature input for the developed semi-1-D models (*possible temperature fluctuations during cooling due to the roll rotation are neglected*). The time required to heat through the shell was determined, assuming adiabatic conditions (*i.e. no heat*

dissipation). The thermal gradients during heating, isothermal hold and quenching were determined.

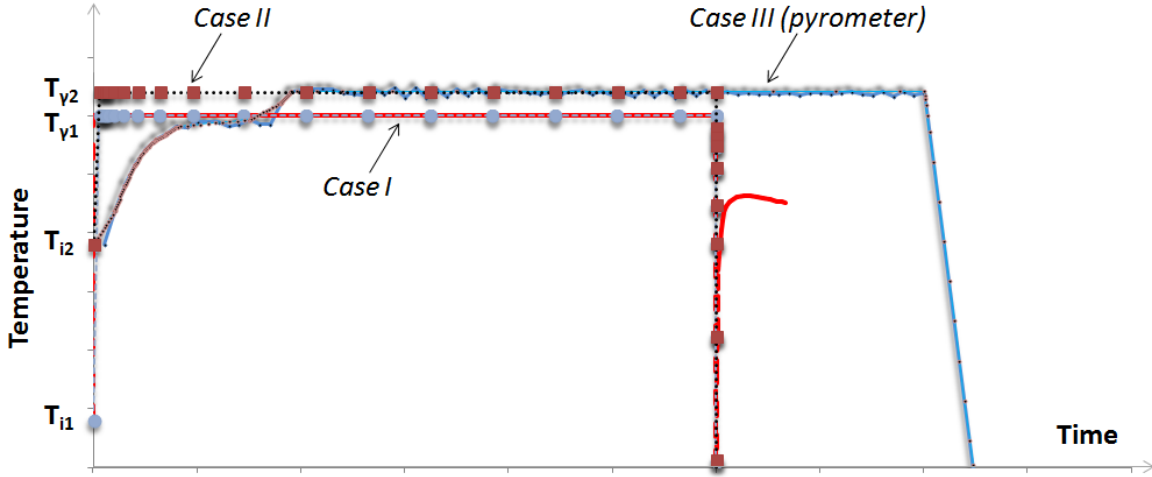


Figure 30. Considered surface boundary condition scenarios

In order to investigate the effects of meshing on the solutions, 2-3 different meshing techniques (*e.g. MultiZone, Hex Dominant or Sweep*) were used individually for different domains to consider mesh quality, solution efficiency (*rapid meshing and solution*) and approximation (*convergence and stability*). The meshes in the high gradient regions had to be refined even more, using the “Sizing Method”, but keeping in mind the factors like: micro-scale, iterative solution, nonlinear material properties. Because the further refinement at the domain’s boundaries raises the cumulative numerical error (*i.e. global truncation error, precision, and round-off*) exponentially. Therefore, a compromise had to be made. The hex-dominant meshing or other types of higher-order elements (*hexahedra-dominant and/or quadrilateral-dominant mesh*) were found to be more robust, reducing computational time. Speaking of the mesh quality controls, different criteria can be chosen in ANSYS WB to characterize the mesh (*e.g., element quality, aspect ratio, Jacobian ratio, skewness, warping factor etc.*). Complete description of the mesh metric can be

found in Meshing User's Guide [99]. Below in Figure 31 an example of mesh quality control is given for 1-D model during transient thermal analysis. The highlighted regions with red-green and light blue represent detected locations, giving raise in accumulated error as a function of time. These shown locations are right at the boundaries between the HSS shell and the intermix and fusion line, which was explained by the different element size used and introduced contact elements between domains after importing the CAD model. In spite of that, a small error value was estimated and was neglected.

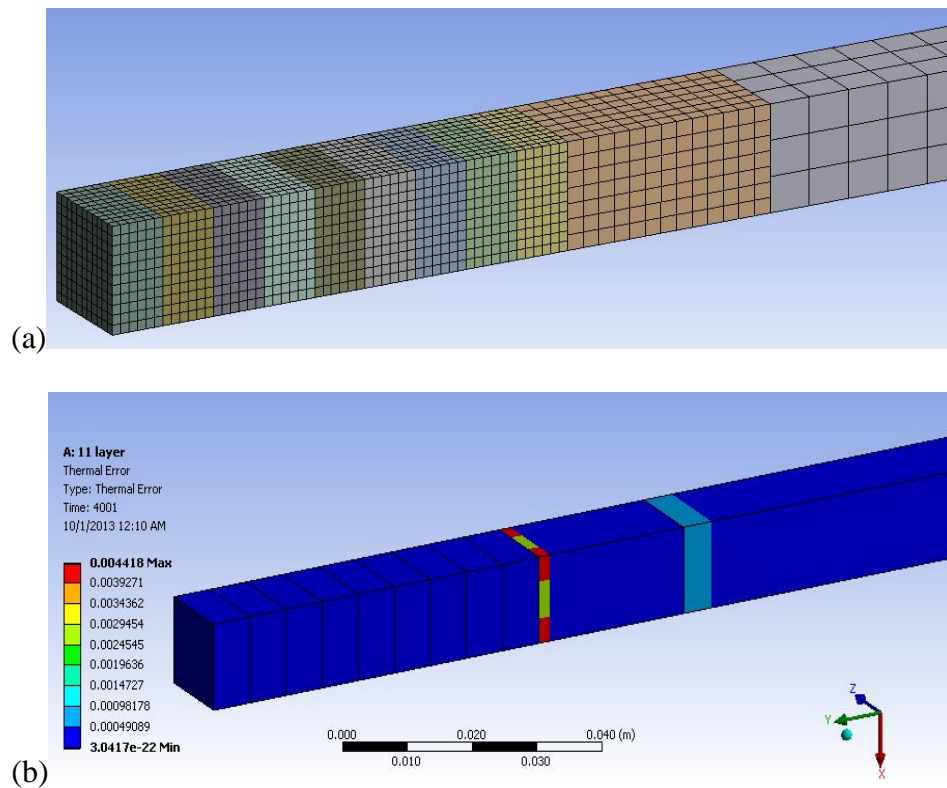


Figure 31. Example of mesh quality control in 11-layer radial model: (a) original mesh, (b) highlighted error estimates at contacts due to different mesh sizes

3.5.2.2 Axisymmetric longitudinal model

The second axisymmetric FE model was made with only 3 homogenized layers (*shell, intermediate layer and core*), the same ones considered in 1-D 3-layer radial model, in order to account for convection at the journals.

The full scale and axi-symmetric (10° sector, 3-layers) models permitted investigation of different boundary conditions along the roll body, Figures [32a](#) and [32b](#), respectively.

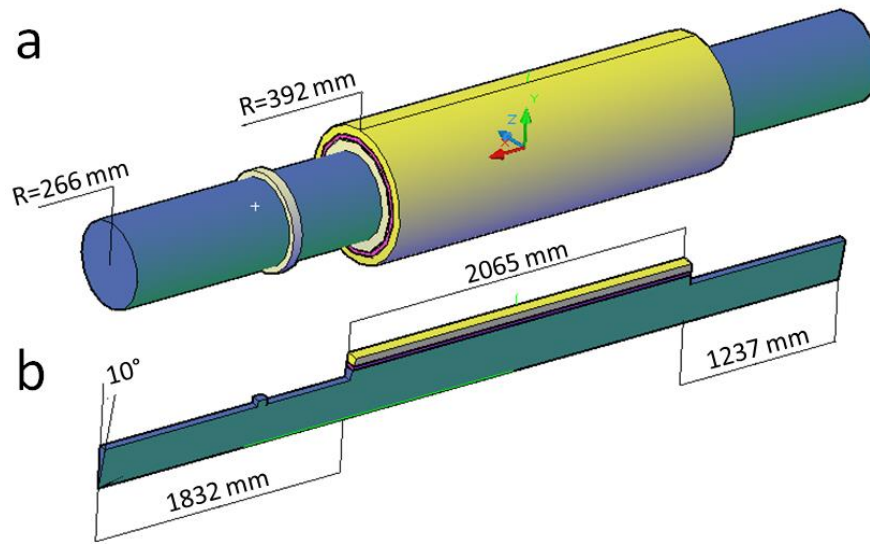


Figure 32. CAD roll model: (a) full-scale roll model, (b) 10° -axisymmetric model

In order to investigate temperature distribution along the roll the axisymmetrical model (Figure [32](#)), which consisted of 3 homogenized layers (*HSS shell, intermix and core*), was subjected to the following BC: 1) previously described boundary conditions applied to the roll body (*surface theoretical and acquired temperatures*), and 2) combined external temperature with convective heat transfer (*radiation is neglected*), applied only to the journals (Figure [33](#)), because of the furnace setup. The convective heat transfer coefficient, corresponding to the “stagnant air-horizontal cylinder”, expressed as a function of temperature, was selected from ANSYS WB

materials database. Basically, the BC in case 2 of the axisymmetrical model helped to evaluate an effect of non-uniform cooling along the roll.

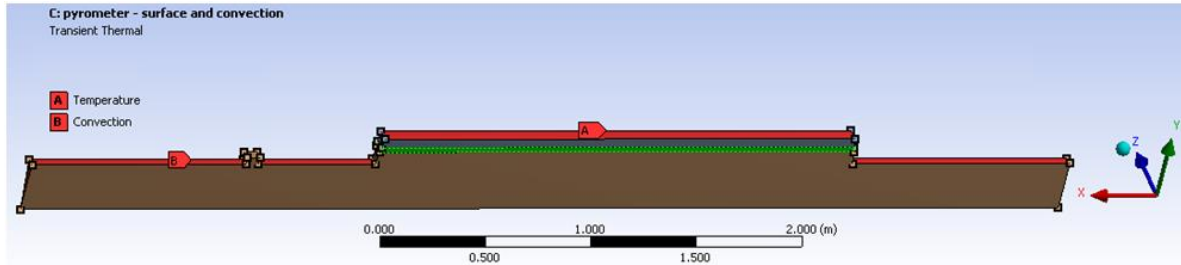


Figure 33. BCs of axisymmetric model: combined external temperature and convection

3.5.2.3 Full-scale roll model

The third full-scale 3-D FE model was made with the same 3 homogenized layers, but was used for coupled analysis during HT.

FEA was performed, using ANSYS Workbench (ANSYS WB, [125]) on the actual cast roll geometry (Figure 34a) and taking into account its composite structure (*i.e.* HSS shell, intermix zone and core). All domains are considered to be homogeneous and isotropic. The core including the journals (*or necks for the bearings*) are made with ductile iron core, which assumed to be homogeneous and isotropic. The CAD model of the roll was imported into the ANSYS WB Design Modeler, using “sat” (*i.e. transferred only solids*) file format. After importing the model, ANSYS WB automatically detects and assigns contact elements (*e.g., surface-to-surface*) between individual parts. All introduced contacts were described as “bonded”, meaning no separation is allowed. More detailed information about this technique can be found in ANSYS WB manual [99]. The full-scale model development is shown in multiple steps in Figure 34, where actual schematics show the geometry (Figure 34a), corresponding to the as-cast condition, *i.e.* before the hardening

HT. This geometry was used to recreate a 3-D CAD solid model (*Figure 34b*) of the roll body, which has subsequently meshed (*Figure 34c*). Based on the mesh convergence analysis, i.e. difference of the results is not exceeding 5%, the mesh was made sufficiently fine in the shell layers to adequately capture the higher thermal gradients during heating and, especially, upon cooling (*Figure 34c*).

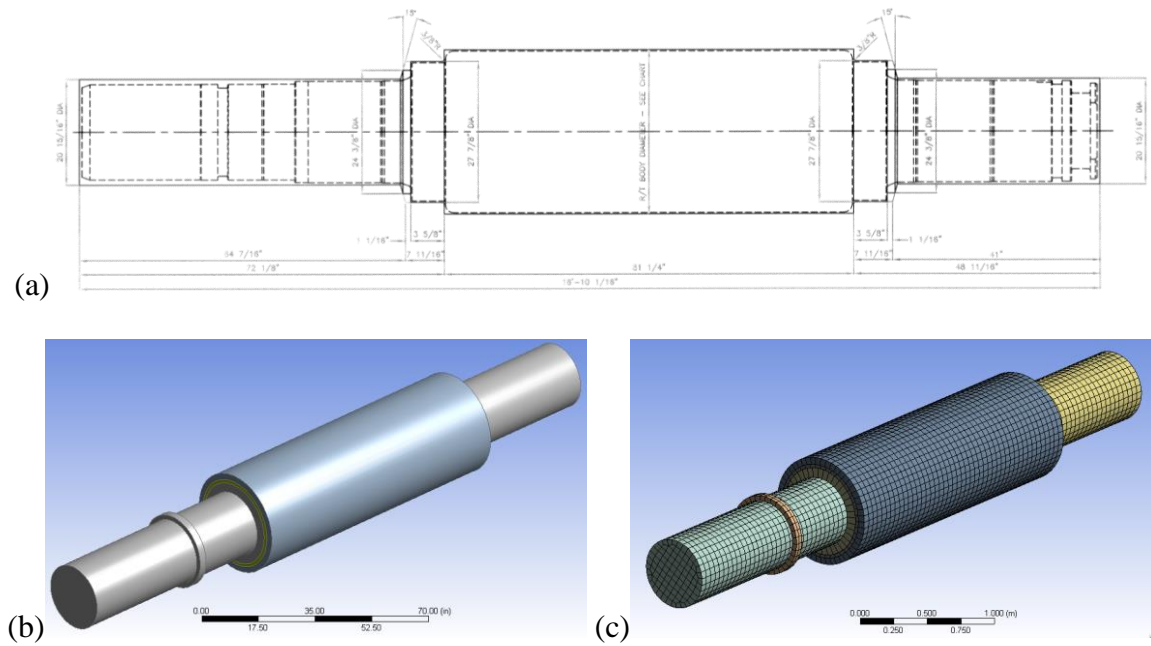


Figure 34. Full-scale modeling: (a) original CAD drawing of the roll geometry, (b) imported and meshed CAD model in ANSYS WB

Thermo-physical and mechanical properties for each considered homogenized, isotropic layer of the full-scale FE roll model (*3-layers*) were predicted with the thermodynamic software, using measured chemical compositions of the improved cast (*Table 2*) as an input. As an example, predicted instantaneous linear expansion coefficient and Young's modulus for the shell, intermediate layer and the ductile iron core are shown in *Figures 35* and *36*, respectively.

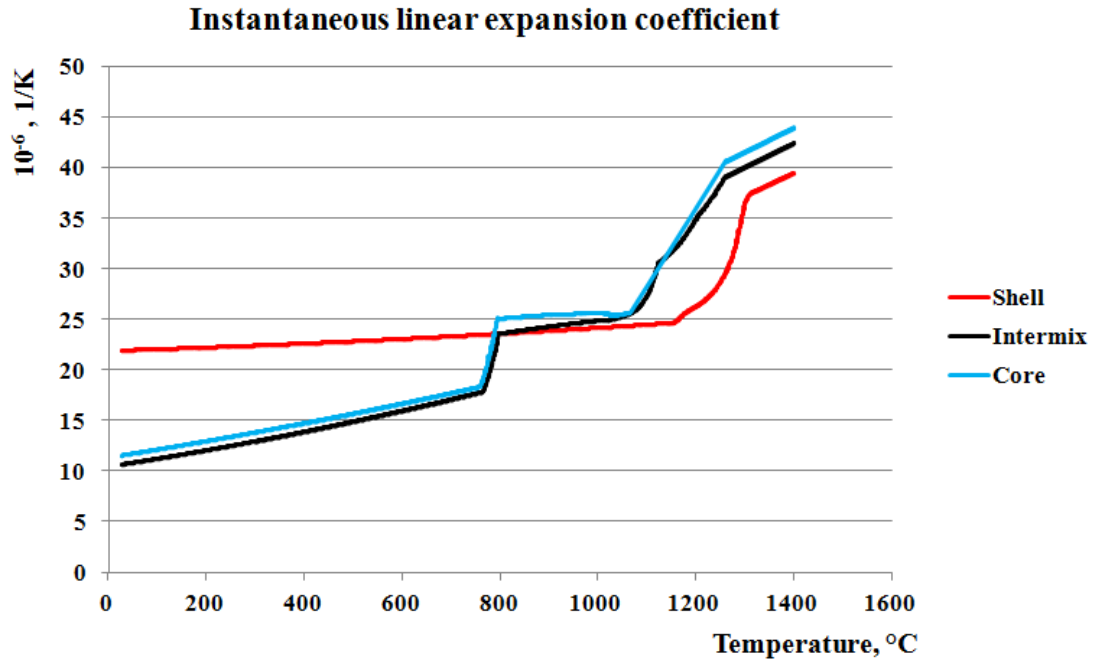


Figure 35. Predicted instantaneous linear expansion coefficients of the layers vs. temperature

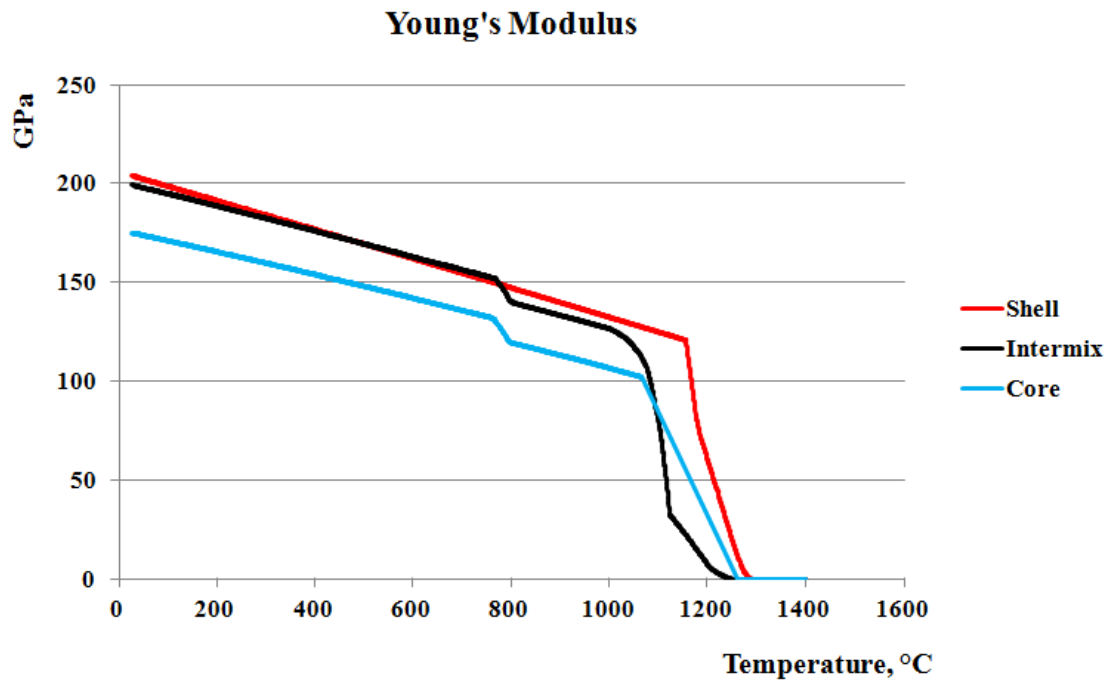


Figure 36. Predicted Young's modulus of the layers vs. temperature

In Figure 37 an example of the user-defined material database in ANSYS WB environment is shown. Five main characteristic as a function of temperature are used in the FEA for all developed models including: density, isotropic thermal conductivity, specific heat, isotropic instantaneous coefficient of thermal expansion and isotropic elasticity.

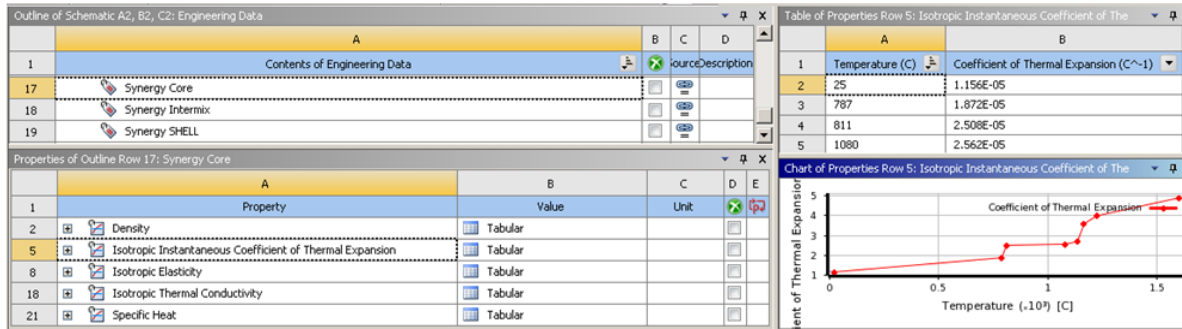


Figure 37. Generated material database in ANSYS WB

Moreover, the present work examines thermo-mechanical stress evolution during high temperature hardening HT operations (*i.e. heating and quenching*). The thermal stresses occur from the thermal gradients, for example, from the alternating of heating-cooling within either similar or dissimilar materials, as a result of the differences in thermal expansion behavior. There are several reasons for the thermal gradient to occur: a) relatively low (*or high*) initial temperature and high heating (*or cooling*) rates on surface; b) non-uniform thermal properties due to compositional changes; c) possible phase transformations affecting thermal characteristics during HT, which is also taken into account. Therefore, it is important to control volumetric distortions in the composite roll body that result from the thermal gradients and phase transformations during HT, preventing hot cracking and de-bonding between the layers, or even inside the “homogeneous” domains, taking into account temperature dependent mechanical properties.

Two types of thermal boundary conditions were applied on the 3-D full-scale model simultaneously: 1) tabulated surface temperature from the pyrometer readings, 2) convection at the journals, corresponding to dry air at RT, during quenching stage of the roll body. For the structural analysis only bearing supports were assigned to the journals, considering HT stage. The coupled thermal-stress analysis was also performed in ANSYS WB, where the selected unfavourable temperature loads were transferred to the steady-state thermal module and coupled with mechanical model to predict thermal stresses. In other words, the results from thermal transient analysis at particular time steps were applied as BCs in the structural steady-state thermal-stress model.

The integrated ANSYS WB environment provides the possibility of linking the steady-state thermal and static structural analyses (*to predict mechanical stresses that can de-bond the HSS layer*), as shown in Figure 38 (*the possibility of linking simultaneously both thermal and structural transient analyses is computationally expensive and not discussed here*). As it can be seen, the material library, roll geometry and meshed FE model are transferred, including the temperature results. Fixed BCs at the journals were assigned to the full-scale model in structural analysis.

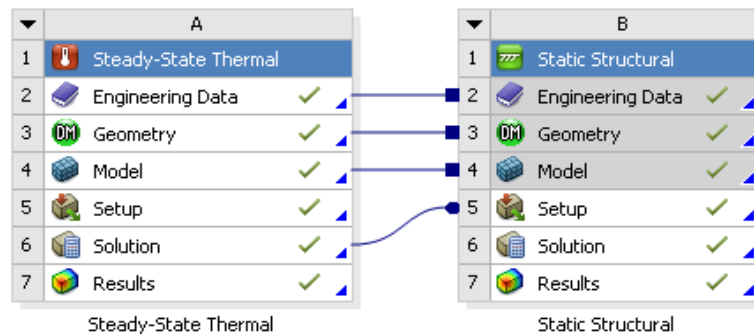


Figure 38. ANSYS WB: coupled thermal-stress analysis schematic

The temperature data from a steady-state thermal solution is used as the initial temperature distribution for the static structural analysis. An example of the project tree for the coupled analysis, where the thermal loads are transferred, is shown in Figure 39.

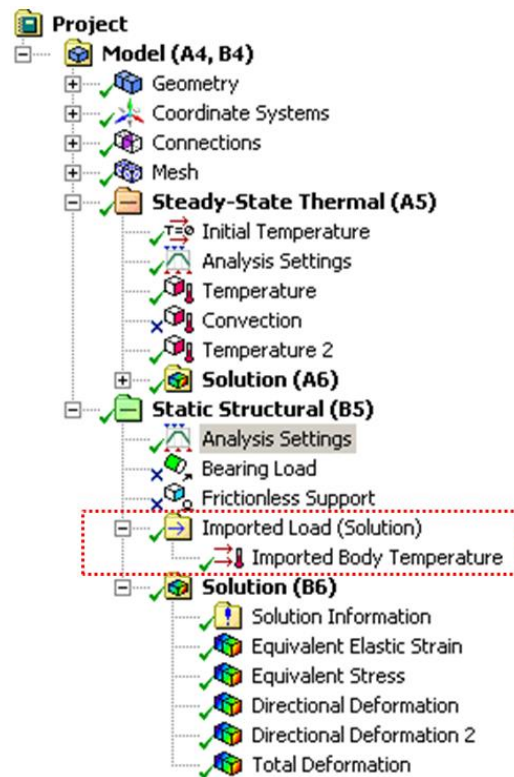


Figure 39. ANSYS WB: project tree of coupled thermal-stress analysis

The mesh and the nodes numbering must be identical for both: thermal and structural FE models, because the resulting temperature values are assigned for each particular node. Based on that, the displacements are calculated in the static structural analysis. Therefore, the mesh size should be initially fine in order to get convergence in the structural analysis.

The allowable thermal stress-strain levels were established as a function of thermal gradients in the HSS shell and intermediate layer and compared with thermodynamically predicted high-temperature mechanical properties and measured shear strengths of the bonding.

An example of mesh quality control for the full-scale roll model is shown in Figure 40. It demonstrates shape quality control via interactive distribution diagram, containing statistics of elements and their configurations. Simple selection (“click”) on the diagram highlighted corresponding finite elements in the model (*top left window, Figure 40*), which helped to identify related volumes in the model. This technique was used to improve FE composite HSS roll model based on elements shape quality in particular domains.

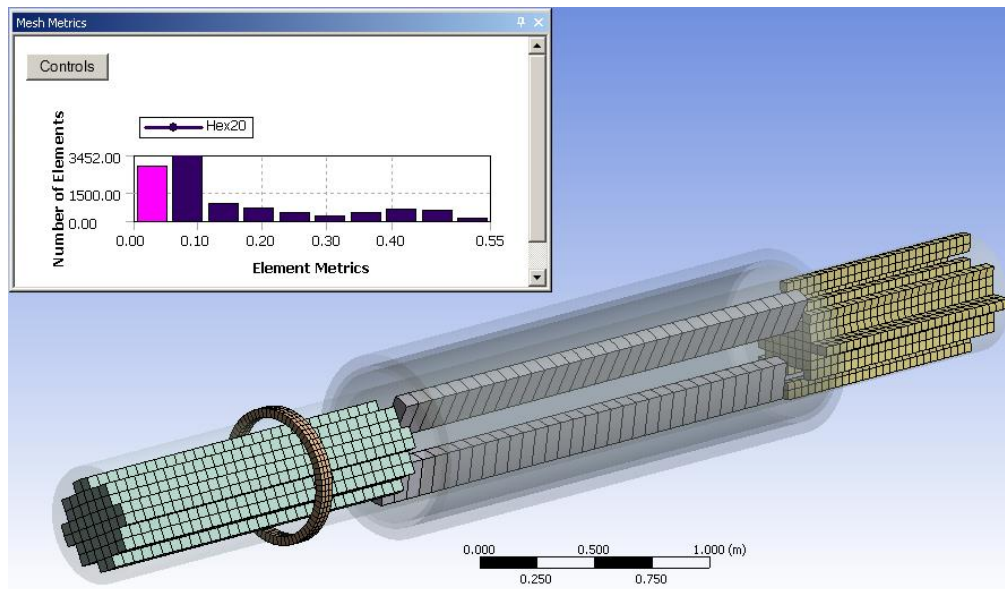


Figure 40. FE shape quality control in full-scale 3-D model by interactive individual bar selection

3.5.2.4 Image-based microstructural FEA

Finally, the fourth microstructural FE approach was developed to simulate meso-scale heat transfer through the local point in the HSS shell, based on actual processed SEM.

In order to better understand the continuous local microstructural transformations in the HSS shell, taking place because of the compositional gradient and different local heating-cooling

rates, an attempt was made to simulate a point-wise microstructural response to the HT. The detailed microstructural thermal model simulated the local response of individual microstructural constituents, i.e. the carbides and/or matrix, under various HT conditions.

A microstructural image (*e.g.*, *SEM micrograph*) with desired scale is reconstructed in a CAD program by transferring it from raster to vectored format. Grain boundaries are automatically detected, so that individual domains (*i.e. microconstituents*) can be recognized. Then created CAD model is being imported into any available CAE software (*e.g.*, *ANSYS WB*). Each particular micro-domain and surrounding matrix have to be described in terms of their thermo-physical properties, which is a hardest part in this type of the modeling. Basically, individual databases have to be created for each considered phase. Where to take such properties, especially, as a function of temperature? In order to do that, the local compositions have to be measured first, which can be done with the aid of EDS or/and Hyper-Probe analysis. As an assumption, each micro-domain is considered to be isotropic and homogeneous in the micro-model, therefore, the local compositions were averaged. For infinitesimal point it is a valid assumption, but its spatial position within a roll shell has to be kept in mind due to possible bulk chemical gradient. The location of considered point was selected nearby the intermix zone (*discussed below*). Next, measured local compositions can be used as an input in thermodynamic software, which enables one to predict the desired properties. The bulk composition can be also used as an input in this case, because some commercial thermodynamic software already generate the properties for individual phases. Hence, it is recommended to use both local and bulk compositions if available for more accurate predictions. Generated material properties have to be strictly analyzed and compared between each other, using related in-situ observations and measurements of similar phase systems in the literature. Having database created, the properties (*e.g. thermal conductivity, heat capacity and*

density used for thermal analysis) are assigned for relevant micro-domains. The next steps of FE modeling are conventional [[122](#), [123](#), [124](#)] : a) description of boundary conditions, b) meshing, c) solution, and d) post-processing and analysis (*e.g., comparison with actual microstructural observations before and after HT*). This approach enables one to explain dissolution-decomposition behavior of the considered phases by using micro-scale heat transfer results [[81](#)].

More specifically, the proposed image analysis and processing of actual SEM micrographs from as-cast material (*PO cast*, [Table 2](#)) for the FE modeling uses a previously developed thresholding algorithm, which can identify individual boundaries and materials within the matrix with the aid of Image J [[94](#)] and AutoCAD [[100](#)]. Experimental EDS analysis enables one to collect the compositional data for each considered micro-constituent. Averaged EDS results were used to generate nonlinear thermal properties and then assign them to each considered phase. The predicted individual material properties were compared to sources in the literature and thermodynamic databases of similar systems [[66](#), [101](#), [102](#), [103](#), [104](#), [105](#)].

The predicted cooling-heating rates along the HSS shell from 1-D radial model (*3 layers*) were used as BCs to the fourth developed meso-scale thermal FE model. The location was selected next to the intermix boundary, which is a limiting (*furthest necessary*) location, [Figure 41](#). Presumably, a maximum heat should reach this position, dissolving the carbides, hence, homogenizing the shell. Therefore, previously defined heating-cooling rates, corresponding to the intermix boundary, were used as the BCs for that local point.

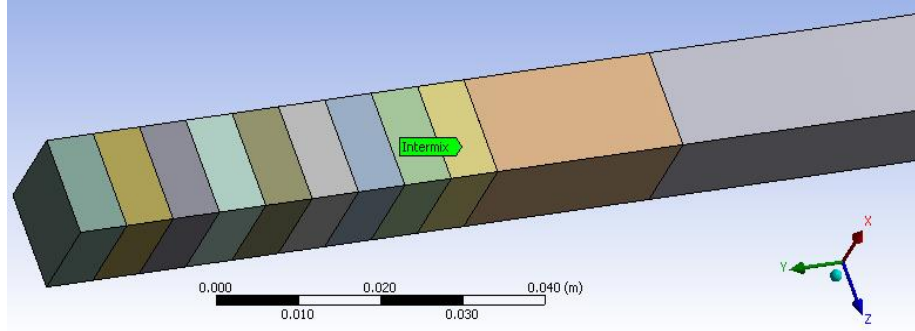


Figure 41. Selected region for micro-scale heat transport analysis

The meso-scale FE model ($150 \times 250 \mu\text{m}$) was developed based on processed scanning electron micrograph (SEM) shown in Figure 42, representing local microstructure of as-cast material next to the intermix zone. Time-varying boundary conditions (*derived heating and cooling rates, °C/s, at the intermediate layer*), simulating heating and cooling cycles, were applied to the left edge of the model.

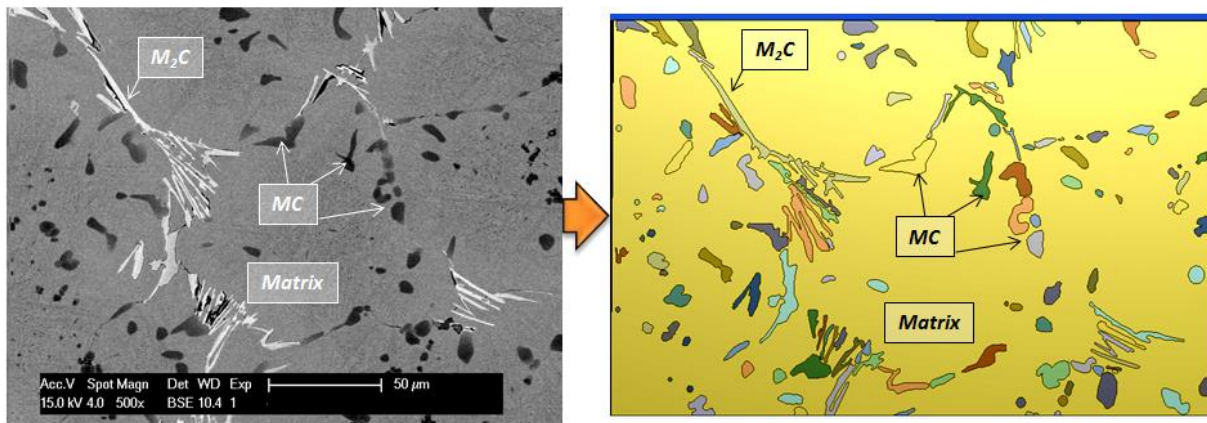


Figure 42. Meso-scale model: processed SEM micrograph imported as CAD model to ANSYS WB

The energy-dispersive X-ray spectroscopy (*EDS or/and Hyperprobe*) analysis were used to differentiate the microconstituents and measure their compositions. The EDS data was gained and averaged for each microconstituent, i.e. matrix, eutectic V-rich (*MC*) and Mo-rich carbides

(M_2C). Hence, the nonlinear thermal characteristics were predicted in thermodynamic software, using both the bulk chemistries and averaged EDS results. The approximate nonlinear properties behavior of considered microconstituents is presented in Figure 43. These uniquely predicted characteristics as functions of temperature were compared to available literature sources, showing similar thermal behavior.

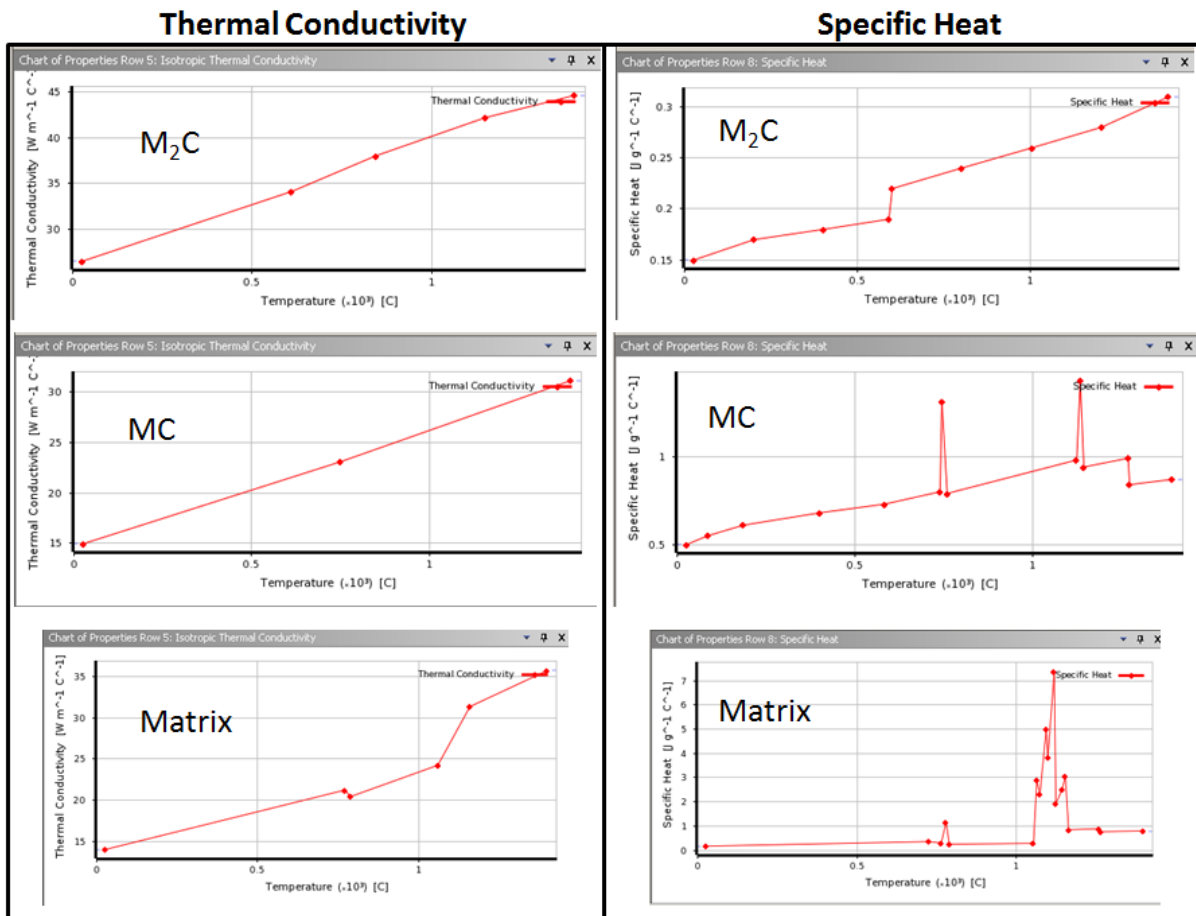


Figure 43. Predicted thermal properties of the carbides and matrix for the meso-scale FE model

3.5.2.5 Statistics, work flow and models summary

In summary, all developed FE models and related mesh type are shown in Table 3.

Table 3. FE models and associated mesh statistics

Model Type	Mesh Method/ mapped mesh type	Elements type	Total #nodes	Total # elements
1D 3layers	Body Sizing/Hexa	Solid90, Conta174, 175, Targe170	4880	837
1D 13 layers	Body Sizing/Hexa	Solid90, Conta174, 175 Targe170	40568	12102
10° axisymmetric	Multi-zone/Hexa	Solid90, Conta174, 175, Targe170	9157	2212
360 ° full-scale	Multi-zone/Hexa	Thermal:Solid90, Conta174, 175, Targe170; Structural: Solid186, Conta174,Target170, Combi14	294689	107639
Micro-model	Multi-zone/Hexa-Prism	Solid90, Conta174, 175 Targe170	426205	107268

As can be seen from Table 3, the full and micro-scale models contained considerable number of the nodes. In the thermal analysis, the number of equations is approximately equal to the number of the nodes (*i.e. only one unknown- temperature*); whereas for the structural analysis this number is at least tripled, because of the 3 unknown degrees-of-freedom (*displacements*) in each node of element type, for example, “Solid186”. But in general for thermoelastic simulation, there could be 16 unknowns: 6 stress components, 6 deformation components, 3 displacements and 1 temperature. The main complexity comes from the transient formulation, where the number of time steps (*loads*) is equivalent to the actual heat treatment time. To solve each time step, several or even hundreds of iterations might be needed in order to get a converged solution. For example, to do the coupled analysis of the full-scale roll model without considering the symmetry (*case of non-symmetric boundary conditions, not considered*) at least 24 billion equations have to be solved, which is very computationally expensive: first 10-20 seconds of actual HT simulation would require 2-3 days on Intel Core i7 processor machine. Therefore, in order to reduce

computational time, the distributed sparse matrix solver was used. Each particular problem was decomposed into several domains and sent to 8 CPUs (*central processing unit or cores*). The convergence on heat is based on the norm of the N-R load (*Newton-Raphson criteria*) and program-controlled with established tolerance and minimum reference value. The automatic time stepping was activated, including transient effects for all degrees-of-freedom. The Newton-Raphson method was used to solve the resulting system of equations using the Mechanical APDL (*ANSYS parametric design language*) Solver in ANSYS.

Thus, the general work flow of the multi-scale thermal modeling can be summarized schematically as shown in Figure 44.

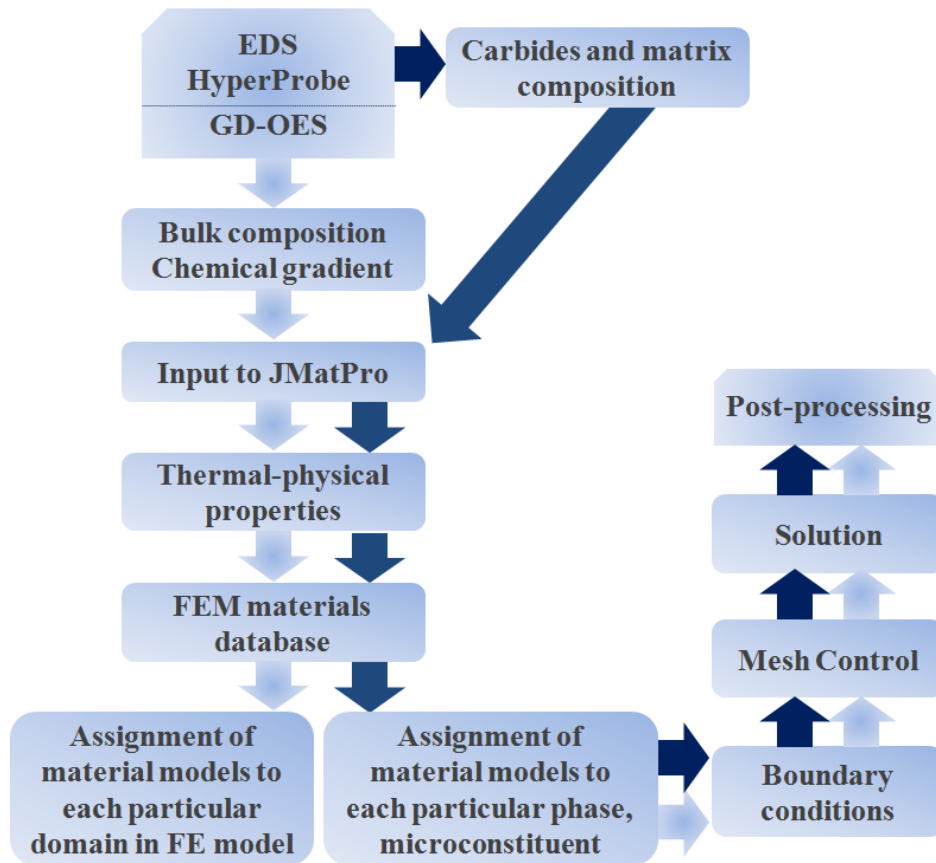


Figure 44. General work flow of multi-scale FE thermal approach

The light and dark arrows correspond to the bulk and micro-scale modeling respectively. The main difference is the scale considered and the way that the properties are generated and assigned for different domains; but traditional FE modeling steps are obeyed: 1) meshing and its quality control, 2) boundary condition descriptions, 3) convergence and stability controls, 4) solution, and 5) post-processing. The FE modeling was easily managed with the integrated WB environment, which linked the different types of analyses and provided control tools.

In summary, the main steps of the integrated FE approach, which enables one to track the history of the roll during the hardening HT, are summarized in the schematics of two procedures and two post-processing schemes below. Scheme I in Figure [45](#) shows the CAD model of the actual roll geometry with the advanced meshing techniques and quality controls. The multi-layered structure of the HSS shell is built based upon experimental optical emission spectrometry (*OES*) analysis of the as-cast material, where the number of layers is dictated by compositional variations, hence, desired accuracy. Nonlinear material properties were generated with thermodynamic software, using the same OES data, and assigned to each relevant domain in the FE model. Each individual layer was considered to be isotropic and homogenized, which is been analyzed in a detailed manner revealing the microstructural response to the HT by direct comparison with microstructural observations. Boundary conditions for most of the models were described as constant surface temperatures or/and tabulated data obtained from pyrometer readings (*or infrared camera*), i.e. actual surface temperatures as a function of time, depending on the type of analysis (*or HT*) and unknowns in the problem (*e.g., time of heat penetration*).

The next step was the coupled thermal-stress analysis, where the thermal input was supplied from the thermal transient modeling results. For the stress-evolution analysis, the temperature loads are stored at particular time intervals and applied to the same meshed model,

assigning specific calculated temperatures at relevant nodes. Calculated thermal stresses in the roll body were first compared to predicted mechanical properties as a function of temperature, using thermodynamic software. Secondly, shear testing was performed at RT on radial composite samples at three locations: the HSS shell, intermix and core. The provided shear strength measurements from WHEMCO were also used to validate the numerical predictions.

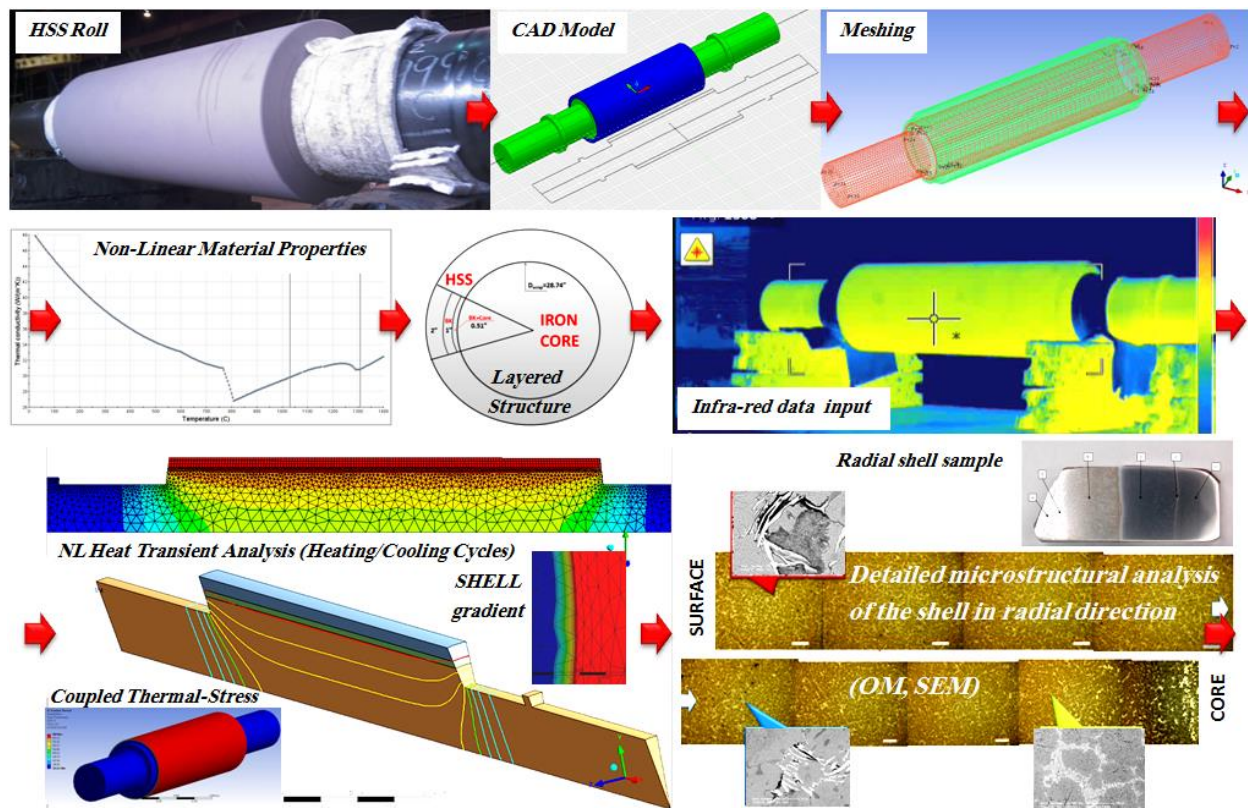


Figure 45. Scheme I. Multi-scale multi-physical FEM formulation: actual geometry→ CAD model→ Meshing→ Prediction of material properties as a function of temperature, using measured compositions→ Assignment of NL properties to each individual domain→ Apply pyrometer (or infra-red) readings as BCs→ perform transient heat analysis coupled with transient structural→ compare observed microstructure and calculated heating-cooling rates

Having defined numerically heating-cooling rates through the thickness of the HSS shell, continuous microstructure imaging (*OM and SEM*) of the hardened material was superimposed and compared. Additionally, the predicted CCT/TTT diagrams were also taken into account, relating cooling rates, soaking times to possible phase formations. Such comparison enables one to analyze the resulting continuous local transformations after the roll is processed. Furthermore, a point of interest in the HSS shell can be selected regarding, for instance, insufficient decomposition and dissolution of the interdendritic segregation next to intermediate layer. It can be studied in great detail, being sub-structured from the bulk FE model, using its calculated cooling-heating rates as boundary conditions for the “point-wise”, i.e. micro-scale, heat transfer simulation. For this step, the local microstructure was discretized with the aid of image-processing and CAD techniques. Scheme II in Figure [46](#) shows locally processed microstructure of the as-cast condition (*i.e. before the hardening HT*). A selected SEM micrograph for the thermal FE model was processed, using a logarithmic thresholding algorithm of Image J [\[94\]](#) to identify individual materials within the matrix. The image processing preserved all spatial data from original SEM images (*TIFF format*) through multiple levels of filtering. This process created continuous regions of material which would otherwise lead to mesh failure. Next the boundaries and regions of the matrix were identified in AutoCAD by transferring the image from raster to vector format. Then the CAD model of the micro-image could be transferred to ANSYS WB with subsequent standard FEM steps. Heat transfer of the considered micro-scale model was analysed based upon the nonlinear properties assigned to the individual sub-domains, considered carbides (*i.e. M_2C and MC*) and the matrix.

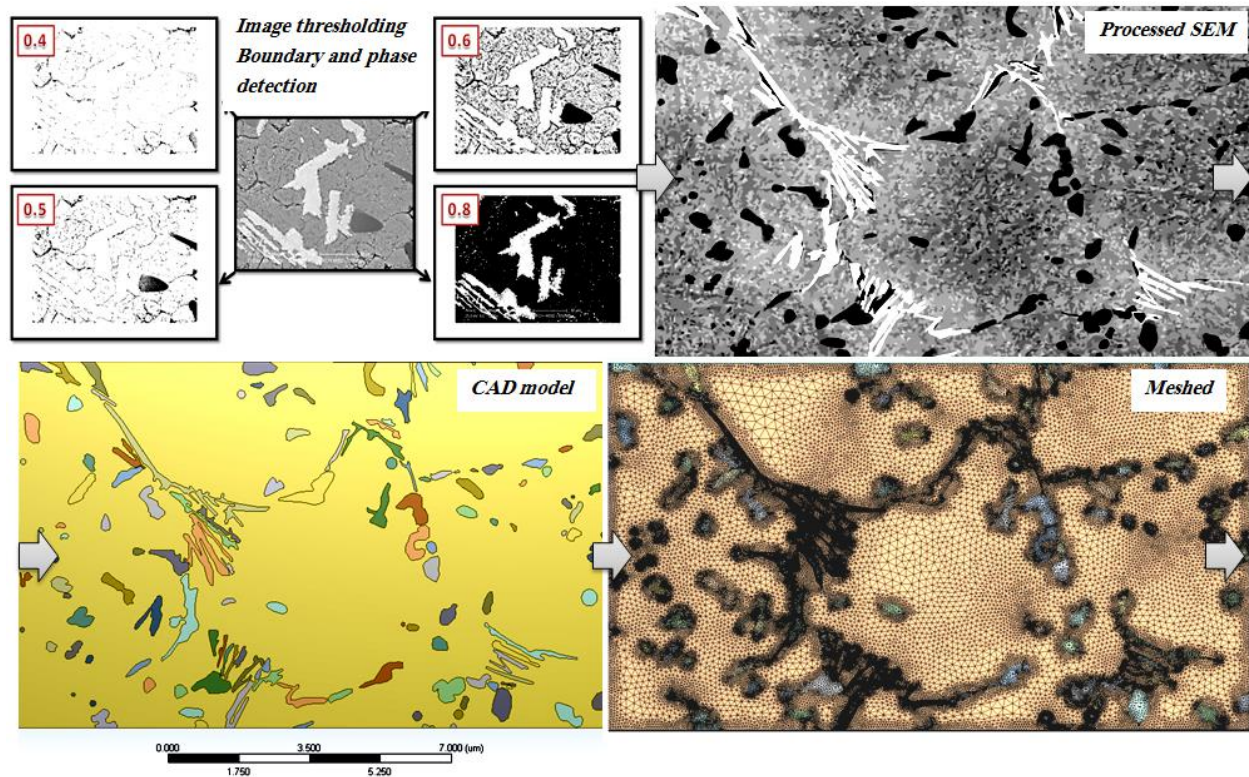


Figure 46. Scheme II. Image processing and FE discretization of a local point in the HSS shell: boundaries detection, vectorization of SEM micrograph→ transferring created CAD model to CAE→ meshing and BCs assignment

Thus, developed integrated multi-physical FE approach enables one to predict the thermal behavior of the composite HSS roll as a result of the hardening HT and associated thermal-stresses. The representation of the roll structure as multi-layered domains with individually generated material properties as a function of temperature were done first time on such application. The material database was not available in the open-source literature. The multi-scale phenomena associated with continuous local transformations, which take place through the thickness of HSS shell due to varying chemical composition and thermal gradients during HT, is simulated as a nonlinear heat transient problem. The observed partial carbides dissolution was explained based on FE results. The results discussion of the FE modeling can be found in the Section [4.4](#).

4.0 RESULTS AND DISCUSSION

This chapter covers thermodynamic-kinetic calculations (*see Section [4.1](#)*); microstructural analysis of as-cast, preliminary heat treated and hardened materials (*see Section [4.2](#)*); CFD simulations of horizontal spin casting (*see Section [4.3](#)*); and multi-scale multi-physical finite element modeling of the roll during heat treatment (*see Section [4.4](#)*). The experimental characterization, including ambient and high temperature X-ray diffraction analyses, hardness measurements and image processing, are covered in Section [4.5](#).

In this work, the properties of HSS rolls used in rolling mills were improved, extending their life by a factor of 1.5-1.7, according to customer's feedback from the first actual rolling campaigns using this new roll material. The design process combined microstructural characterization, experimental measurements, and simulations. The microstructures of the as-cast, conventionally heat treated (*before*), and the developed (*new*) heat treated steels were analysed and compared. Special care was given to the observation of the formation of carbides, which are especially critical to the material properties. Also investigated was the matrix material, in which the carbides were dispersed. The casting methods and heat treatment were ultimately optimized to provide finer distribution of the carbides, which greatly improved the roll performance. Another factor that was considered was chemistry. Thermodynamic-kinetics simulations showing the effects of weight percent of alloy content in the HSS were developed. They helped to guide the development of the heat treatments, final chemistry, and mechanical properties. Finite element analysis was used for multiple purposes. One was to evaluate the thermal stresses developed during the heat treatment process rolls, which are a composite of an outer HSS shell and ductile iron shaft in the middle. The result was important for predicting the delamination of the HSS shell

from the core. Transient heat transfer analysis of the heat treatment process was also studied at the meso scale. For the latter, detailed images of the carbide microstructures were modeled within the matrix. It was found that heat transferred much more readily along the interdendritic carbides that were formed.

The detailed microstructural investigation of HSS material produced by conventional and non-conventional approaches (*i.e. old and new spin casting and heat treatment*) is discussed in the following sections. Preliminary microstructural observations and hardness testing revealed microstructural variability and associated decrease in hardness along the HSS shell (*see Section [4.5.2](#)*), which was attributed to initial casting segregations (*see Section [4.2](#)*) and inadequate hardening, because of nonhomogeneous microstructural development from conventional HTs. It has been verified that the preliminary HT effectively homogenizes the matrix and solute-rich boundaries in refined casts, pre-conditioning the microstructure for the subsequent hardening HT (*see Section [4.2.2](#)*). The outline of microstructure evolution during HT routes is proposed in Section [4.2.4](#).

In order to understand the complex behavior of a multi-component HSS system during solidification and solid-state transformations, thermodynamic and kinetic modeling was performed using equilibrium and non-equilibrium approaches (*see Section [4.1](#)*). The HSS roll is relatively large, where uniform microstructure has to be developed and controlled throughout the HSS shell so that the roll body resists service loadings and environmental degradation. An integrated multi-physical and multi-scale approach is developed to simulate a local transformation, which can take place along the HSS shell. At the same time, the integrity of the composite roll structure must be maintained during the stress-strain evolution from the HT routes (*see Section [4.4.3](#)*). The FE thermal model of the HSS roll is developed, using actual data and thermodynamic-kinematic

predictions. This was done, considering HT thermal gradients, compositional variations, microstructural changes, and the decomposition behavior of the various carbides within the shell layer.

The experimental part validates the proposed concept of the non-conventional HT and model predictions, based on X-ray diffraction analysis, microhardness measurements, and microstructural analysis.

Integrated thermodynamic-kinetic predictions, CFD and multi-physical multi-scale FE modeling were performed in order to explain microstructural observations and to develop the new non-conventional HT. The purpose of the new HT is to alter the initial solidification microstructure, which consists of brittle eutectic solute-rich carbides located at the dendrite boundaries and to homogenize the chemical composition and microstructure of the matrix. This can be achieved by understanding the complete dissolution of the transient carbides, discussed in Section [4.2.3](#). Considerable carbides dissolution and decomposition behavior was achieved by a series of the heat treatments, where the main variable was the re-heating temperature. The structural integrity of the composite roll can be guaranteed by minimizing thermal and residual stresses and avoiding the core re-melting.

4.1 THERMODYNAMIC AND KINETICS PHASE TRANSFORMATIONS

The sequence of carbide precipitation during solidification for a fixed alloy composition is shown in Figure [47](#), using two different packages (*JMatPro* and *Pandat*). Notice that the presented temperature ranges are: 1300 to 900°C in Figure [47a](#), and from 1300 to 0°C in Figure [47b](#). The general behavior of the solidification path in the HSS material, which is mainly a function of

composition and cooling rate, is compared with experimental differential thermal analysis (DTA) reported in [54, 59, 106] and with observed as-cast microstructures, which will be discussed in Section 4.2.1.

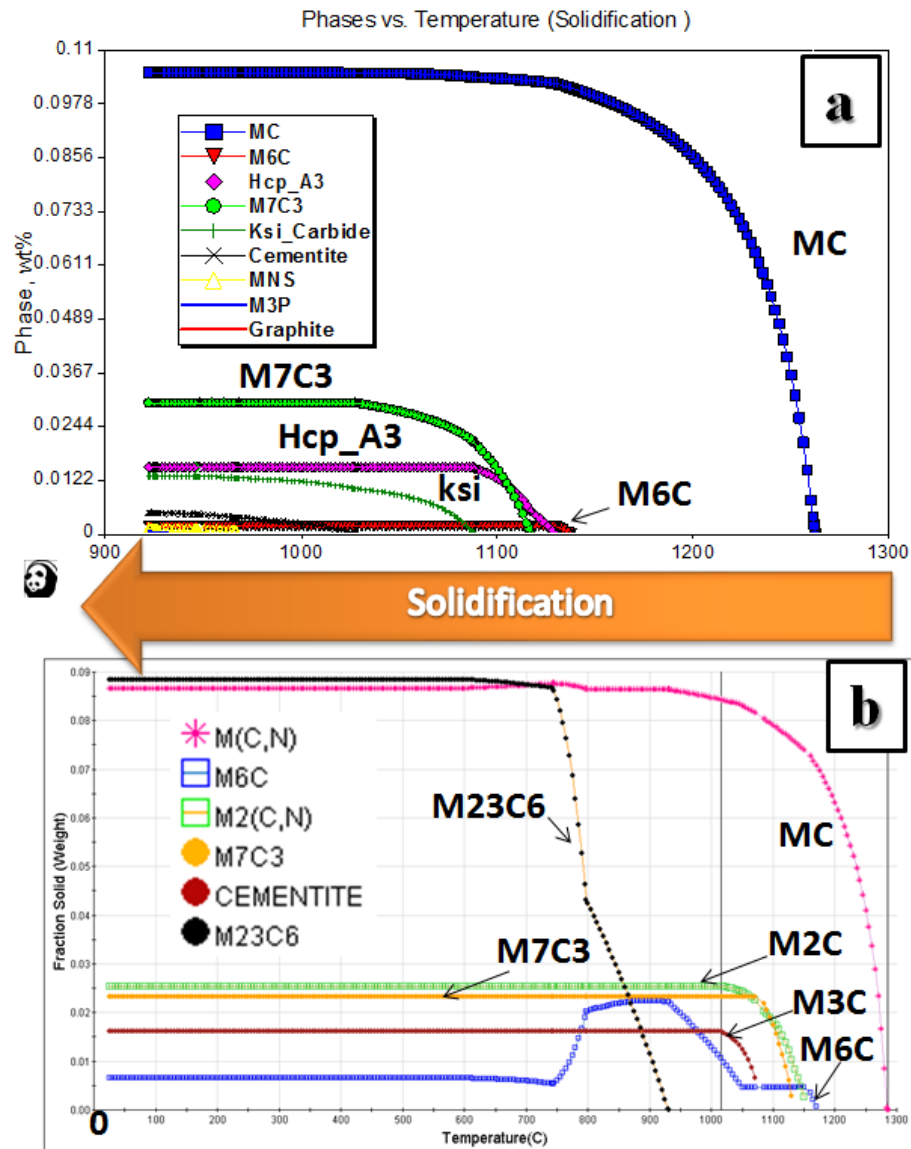


Figure 47. Predicted solidification patterns of fixed composition in: a) Pandat , b) JmatPro

As it can be seen from non-equilibrium predictions, the carbide precipitation sequences are almost identical using both software packages: $L \rightarrow \gamma \rightarrow MC \rightarrow M_6C \rightarrow M_2C \rightarrow M_7C_3 \rightarrow M_3C \rightarrow M_{23}C_6$. The exception is that some start temperatures of a phase formation could be slightly different, but in general the kinetics behavior resembles microstructural observations, as it will be shown later (see Section 4.2). For example, in Figure 47a the start temperature of MC is around 1265 °C, whereas in Figure 47b it is almost 1300 °C. The particular sequence of precipitation reactions can be explained based on the free energy of formation, which is an intrinsic property of each individual precipitate and defines a “barrier” for a crystal nucleation. For example, the prior alloy precipitation of MC, M_6C , M_2C etc. as in the above mentioned reaction is preferable, because these phases have the lowest free energy of formation. It is important to differentiate and understand the origin of the crystal nucleus and growth: in the liquid, or solid phase, or could be formed in both (*i.e. type of reaction and sequence of precipitation*). In other words, a precipitation could take place during solidification upon cooling from liquid or/and solid phase. This behavior will depend on the solubility product of the chemical compound. Hence, the diagrams (Figure 48) show the bulk chemical distribution as a function of temperature and related liquid-solid phase balance (*solidification direction on diagrams is right to left*). The depicted temperature range corresponds to existing liquid and solid phases simultaneously. The rate of slope changes, curvature and extremum points are clearly correlated to the proposed phase-carbides formation during solidification. For example, the maximum peaks of Mo and Cr correspond to Mo_2C and Cr_7C_3 formations respectively, where after that a decrease in bulk content is observed (Figure 48). The vanadium reduction starts from high temperature (1275°C) range as expected, because of the precipitation of eutectic MC carbides.

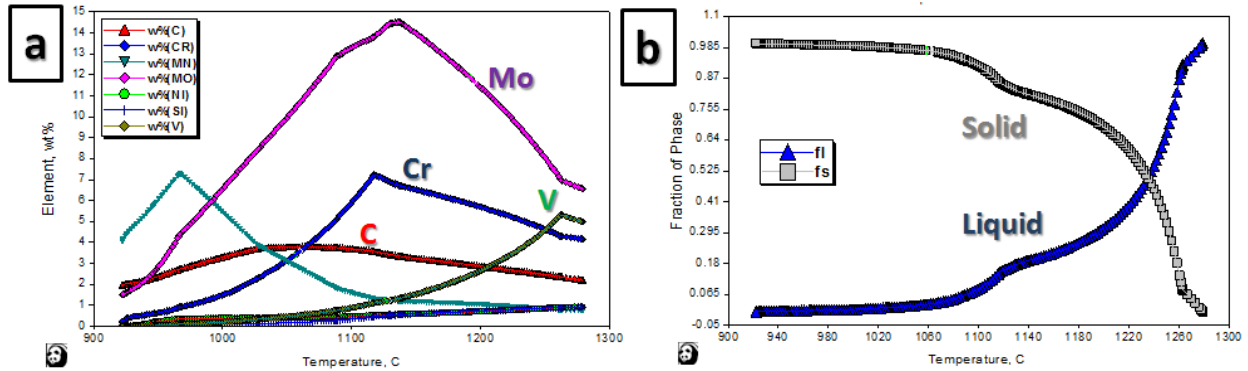


Figure 48. Solidification: (a) predicted bulk composition as function of temperature during solidification, (b) predicted solid and liquid phase balance

Another set of predicted data for the solidification stage is shown in Figure 49. Here, local carbon concentrations in individual phases (e.g., carbon concentration in eutectic MC (VC) and M_2C -type (Mo_2C) carbides, residual liquid and newly formed austenite) are shown as a function of temperature during solidification.

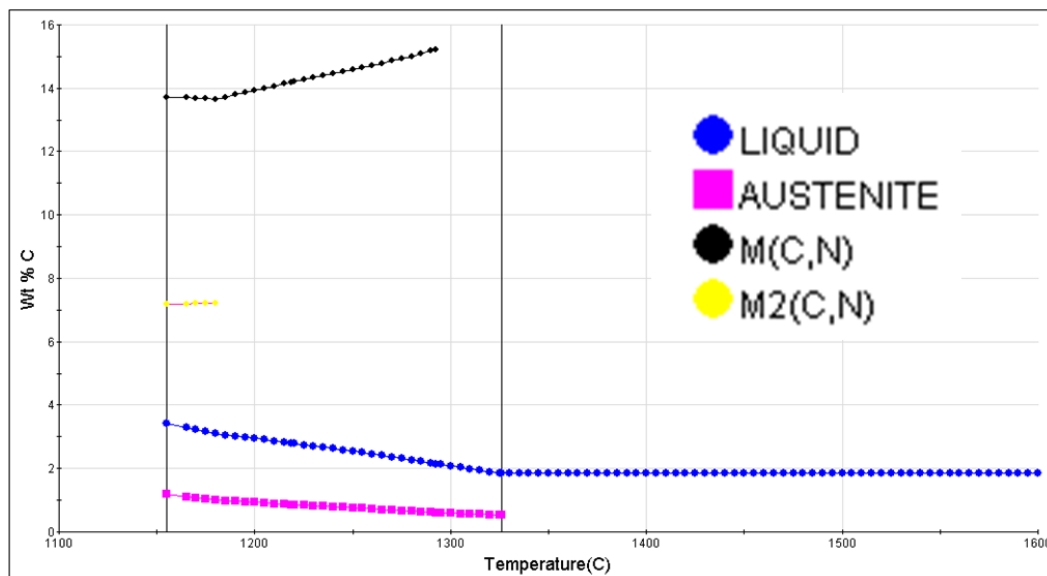


Figure 49. Predicted carbon concentration in individual phase during solidification

It is indicated by top (*black*) line in Figure 49, that MC (*as $M(C, N)$ on the image*) is supersaturated in carbon in comparison with other phases, therefore, it has the highest hardness as expected. The presence of these carbides in sufficient quantity and uniform distribution through the thickness of the working shell can drastically improve the wear resistance of the HSS roll. Also as it can be seen, the local carbon concentration in the residual liquid (*blue line*) and newly forming austenite (*purple line*) phases is increasing as temperature decreases. As it will be shown later by microstructural observations of as-cast structure in Section 4.2.1, the liquid phase is being pushed away by growing dendrites, becoming entrapped between interdendritic spaces. Therefore, the local concentration is enriched with alloying content, including carbon. An excess of it in the liquid phase and further solidification promotes new carbide nucleation and growth within interdendritic spaces, like, for example, M_6C (Figure 47b), M_2C (yellow line, Figure 49) and MC (*black line, Figure 49*). But again thermodynamic predictions without microstructural analysis could not clearly confirm the origin of the crystal nucleus, especially in heterogeneous alloys considered and without taking into account local interactions between centrifugal forces and solidification fronts. Moreover, as it will be discussed in Section 4.3, the fact that possible convective mixing in the molten metal responsible for the mass transport of newly nucleated solid particles in liquid is also not taken into account by thermodynamic-kinetic models. Simultaneously acting and co-existing two solidification fronts subjected to centrifugal field could promote chemical segregations and, consequently, local phase transformations as a function of spatial location. Hence, different precipitation order and solid-state transformations can be expected, but still driven by free energy of formation. Therefore, any predicted thermodynamic-kinetic results have to be interpreted by considering local composition, time, temperature, position in the shell, roll and type of the processing (*casting or heat treatment*).

As a practical interest to better understand solidification during the spin casting, some physical properties of individual phases were predicted as a function of temperature. For instance, in Figure 50, the density of liquid, austenite, MC and M₂C is shown. Knowing the precipitation sequence or/and free energy of formation of each phase and density, it becomes possible to predict the solidification segregation in a HSS shell due to the centrifugal force field.

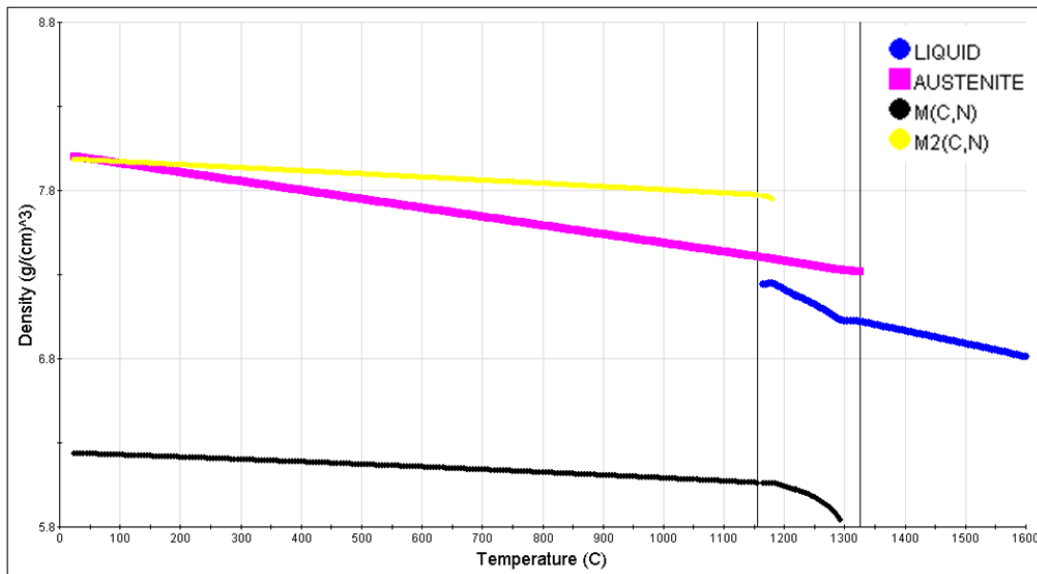


Figure 50. Predicted density of each phase during solidification

From Figure 50 it can be concluded that the M₂C carbide particles are the densest, and therefore, a higher amount of Mo₂C carbides at the surface of HSS shell is expected. This result can be confirmed with volume fraction measurements of eutectic carbides in the as-cast HSS, S-shell sample (Table 2), as a function of radial depth, Figure 51. Indeed, the M₂C carbide V_f is higher at the surface and more likely stable along the shell. The MC carbide has the lowest density, and hence it can be assumed that it might segregate closer to the internal surface of the shell tube. But it is not always a case: this prediction is not obvious in Figure 51, where the MC (VC) trend

line is declining closer to the core (*right side of Figure 51*). Presumably, this is related to that there is not enough time for these precipitates to diffuse back before certain amount of solid starts to form. It prevents the diffusion to the internal locations of the shell by the lower density particles. At the same time, more scattering of the MC amounts next to the bonding is found, which has the highest peak in location 9, approximately 50-55 mm down the surface. The turbulent mixing of the melt during solidification is a quite complex phenomenon with convection driven diffusion. According to the predicted non-equilibrium solidification diagrams in Figure 47, MC-type carbide, presumably, precipitates from the austenite for the particular alloy. Therefore, during the casting stage it can already be bounded in the solid- γ phase, which can produce a different character of the segregation (*Figure 51, MC line*).

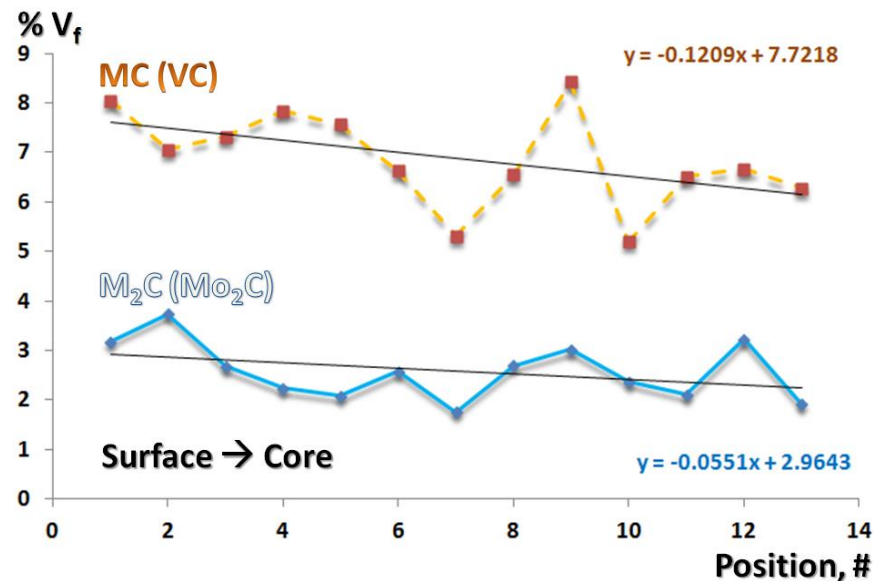


Figure 51. Radial measurements of volume fraction of eutectic carbides in as-cast shell (S-shell)

Additionally, the effect of carbon on liquid-solid phase field regarding temperatures was investigated by the equilibrium approach. For example, in Figure 52 the low and high carbon alloys are compared.

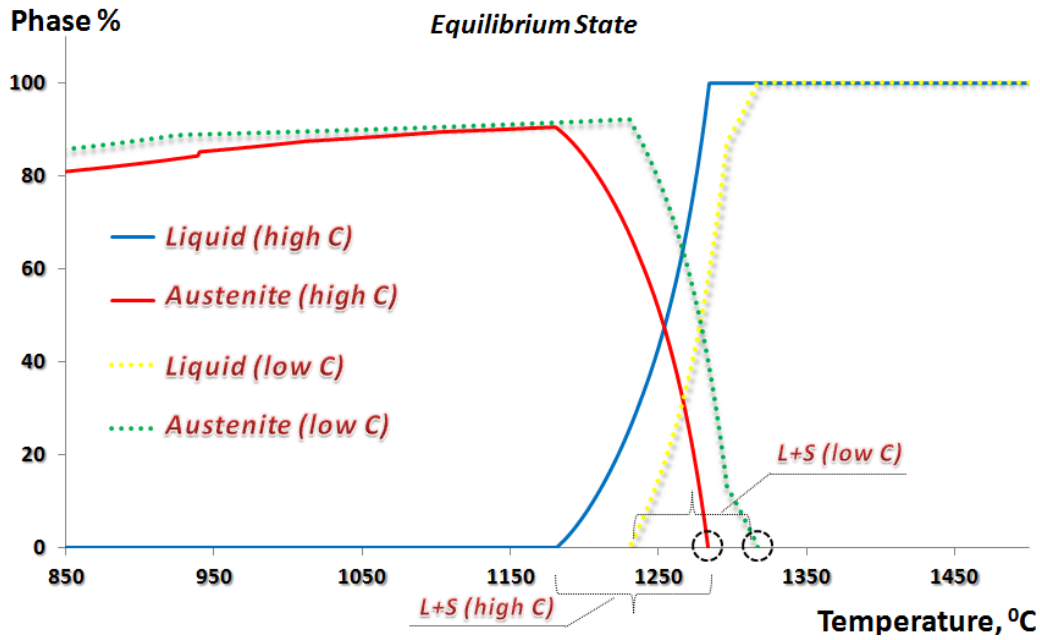


Figure 52. Comparison of low and high carbon groups and its effect on the predicted liquid-solid region

The solid lines are corresponding to the high carbon group, while the dashed ones are for the low carbon group. As it can be seen, the role of bulk carbon concentration is very significant: reduction in carbon shifts the solidification path to higher temperatures and narrows the two phase region, which means that earlier crystallization can be initiated and completed within shorter times, promoting finer as-cast microstructure without any additional cooling. This approach was used to modify the as-cast microstructure and validated with observed microstructural changes discussed in Section 4.2.1.

In order to reconstruct the complex behavior of local continuous solid-state transformations of the multi-phase heterogeneous alloy along the thickness of HSS shell as a function of several

inputs (*temperature, composition, location, microconstituents and phases*), the equilibrium 2-D carbon diagram was produced. The high temperature region is depicted from the general diagram and shown in Figure [53](#). Critical phase transformation temperatures and phases are verified with the previous dilatometry studies on the HSS material and microstructural data of alloys under consideration.

Figure 53. Predicted equilibrium carbon diagram at the high temperature region

Evidently, from this predicted diagram (*Figure 53*), it can be concluded that completely different phases can be originated even with small carbon concentration changes; hence, in the case of compositional variation in the shell location, several unexpected compounds can be formed after HT. For instance, assume that the shell has a linear carbon variation from the surface to the core from 1.6%-2.6%, similar to what is shown in the diagram. Then when isothermal HT is

applied in the temperature range, e.g., 900 °C and 1000 °C, two horizontal lines would be drawn, which intersect with phase boundaries in the diagram. At sufficiently long holding time during isothermal conditions at these temperatures will allow the roll to reach equilibrium, resulting in the intersected phases occurring at the particular location in the shell with that particular local carbon concentration. The results are summarized in Table 4, where multiple complex reactions occur with respect to position (*varying carbon concentration levels*), depending on the selected temperature. The same phenomenon takes place in the actual HSS shell, which also depends upon isothermal and continuous cooling conditions. These predictions have been confirmed with systematic microstructural observations discussed in Section 4.2.

Table 4. Predicted transformations as a function of temperature and %C variations

T, °C	WT. %(C)	REACTION EQUATION
900	1.85-1.89	$BCC_{A2} + FCC_{A1} \rightarrow M_6C$
900	1.90-2.14	$BCC_{A2} + FCC_{A1} \rightarrow M_6C + M_{23}C_6$
900	2.15-2.17	$BCC_{A2} + FCC_{A1} + HCP_{A3} \rightarrow M_6C + M_{23}C_6$
900	2.18-2.43	$BCC_{A2} + FCC_{A1} \rightarrow M_{23}C_6 + HCP_{A3}$
900	2.44-2.72	$BCC_{A2} + FCC_{A1} \rightarrow M_{23}C_6$
1000	1.83-1.98	$BCC_{A2} + FCC_{A1} \rightarrow M_6C$
1000	1.99-2.25	$BCC_{A2} + FCC_{A1} \rightarrow M_6C + M_7C_3$
1000	2.26-2.87	$BCC_{A2} \rightarrow FCC_{A1} + M_7C_3$
1000	2.88-2.91	$BCC_{A2} + M_7C_3 \rightarrow FCC_{A1} + M_{23}C_6$
Note: BCC- body centered cubic, FCC- face centered cubic, HCP- hexagonal closed pack phase		

A second series of compound formation takes place if we assume a fixed composition through the thickness of the HSS shell. In this situation, the local transformations behavior becomes more predictable and can be controlled by two parameters during HT, i.e. temperature and cooling rates. In this case, the shell is considered to be homogeneous, i.e. no compositional variations; and long-range diffusion is neglected. For this imaginary vertical line (*or cross-section in 3-D case*) is drawn on the predicted diagram (*Figure 53*), depending on the given carbon content (*the rest of composition is fixed*). As an example, the resulting equilibrium phase diagram for particular carbon content is shown in *Figure 54*. As it can be seen, the austenite start temperature is around 1325 °C. The corresponding predicted carbon concentrations in each phase as a function of temperature is given in *Figure 55*.

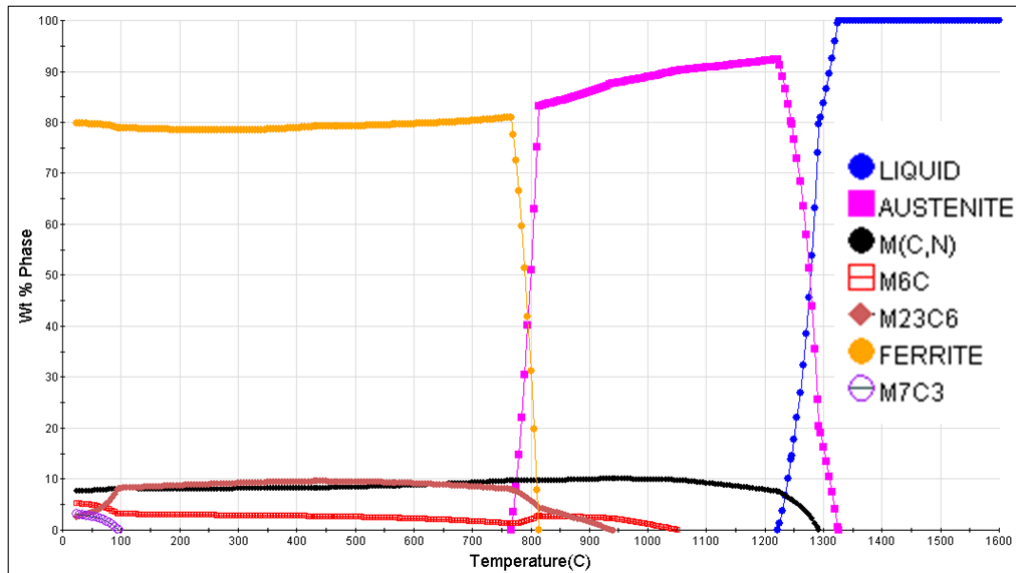


Figure 54. Predicted equilibrium phase fractions as a function of temperature (fixed composition)

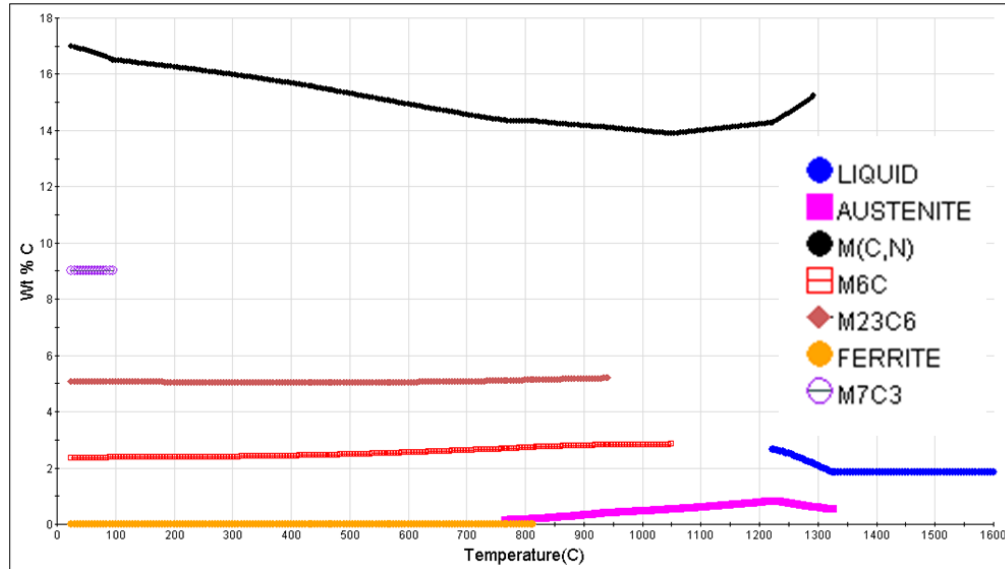


Figure 55. Predicted carbon concentration in each phase as a function of temperature (equilibrium)

Notably, equilibrium predictions do not reflect some products, for example, Mo_2C , presumably, due to its decomposition into M_6C and MC from reacting with austenite. The latter two are present in Figures [54](#) and [55](#). In contrast, Mo_2C is included and considered in the non-equilibrium simulations of solidification predictions like it was shown previously in Figures [47](#) and [50](#).

Thermodynamic behavior of the intermix region and ductile iron core (*Figure 56*) were also predicted and compared to microstructural observations. The thermo-physical properties were also used as an input to material database of FE models.

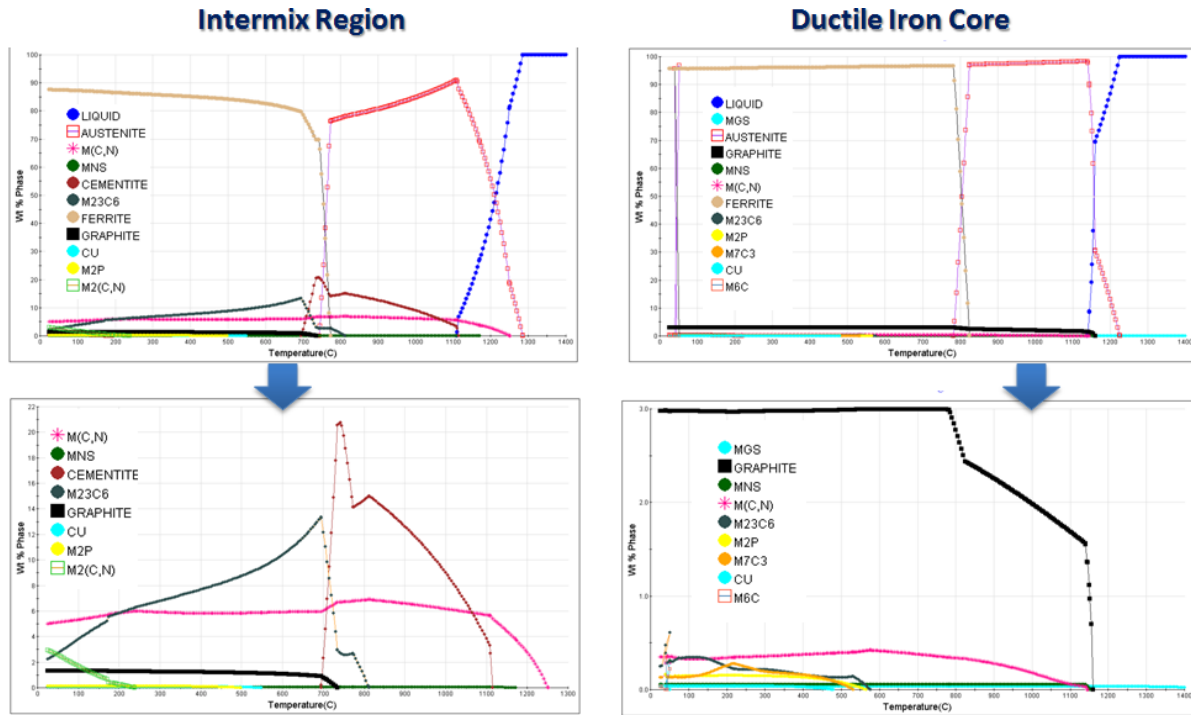


Figure 56. Equilibrium diagrams of intermix and core materials

The TTT/CCT (*time-temperature-transformation and continuous-cooling-transformation*) diagrams that were calculated using the information from the heat treatment used for the HT refinement studies are shown in Figures [57](#), [58](#). These diagrams were used during subsequent low temperature heat treatments to produce the fine scale alloyed carbide precipitation and final microstructure.

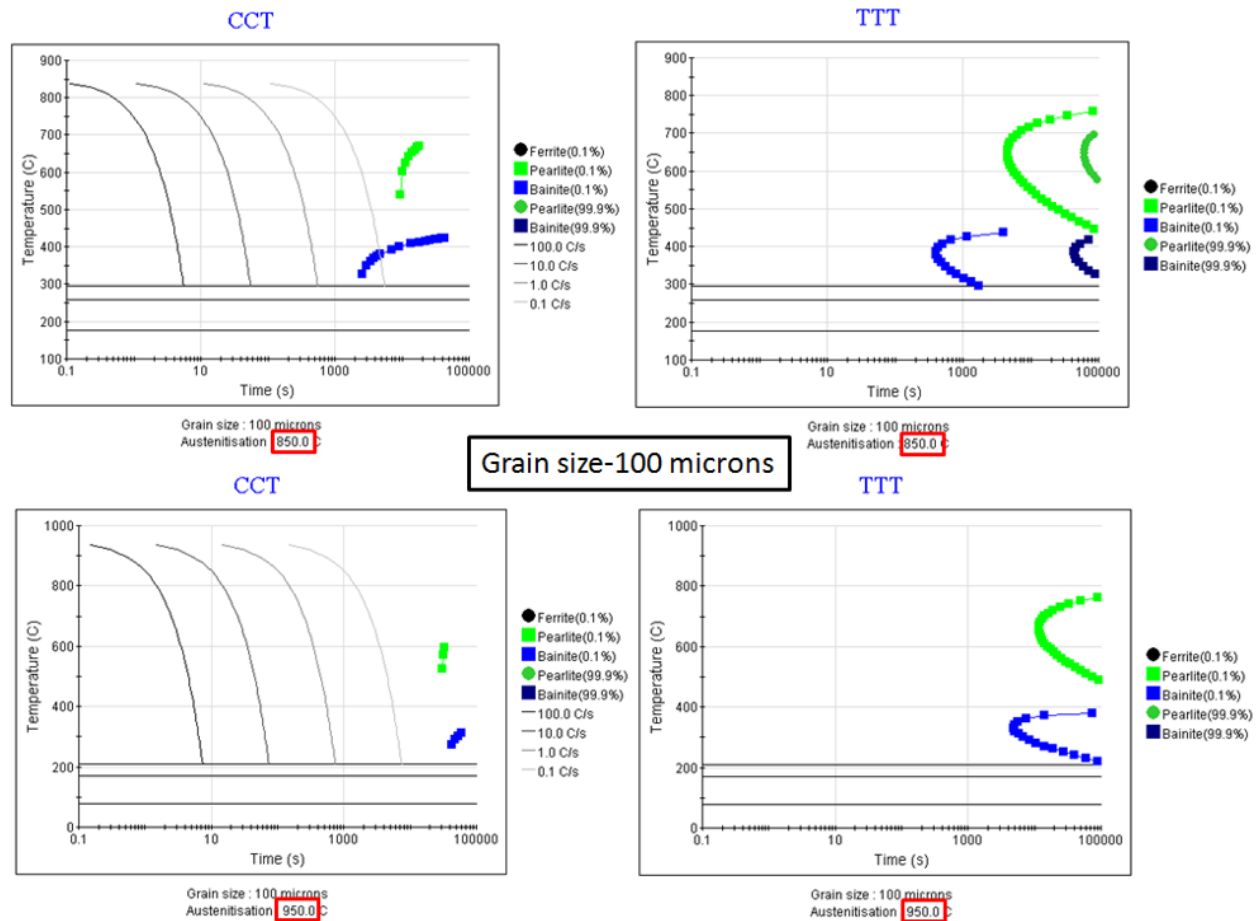


Figure 57. Predicted CCT-TTT diagrams (100 μ m grain size)

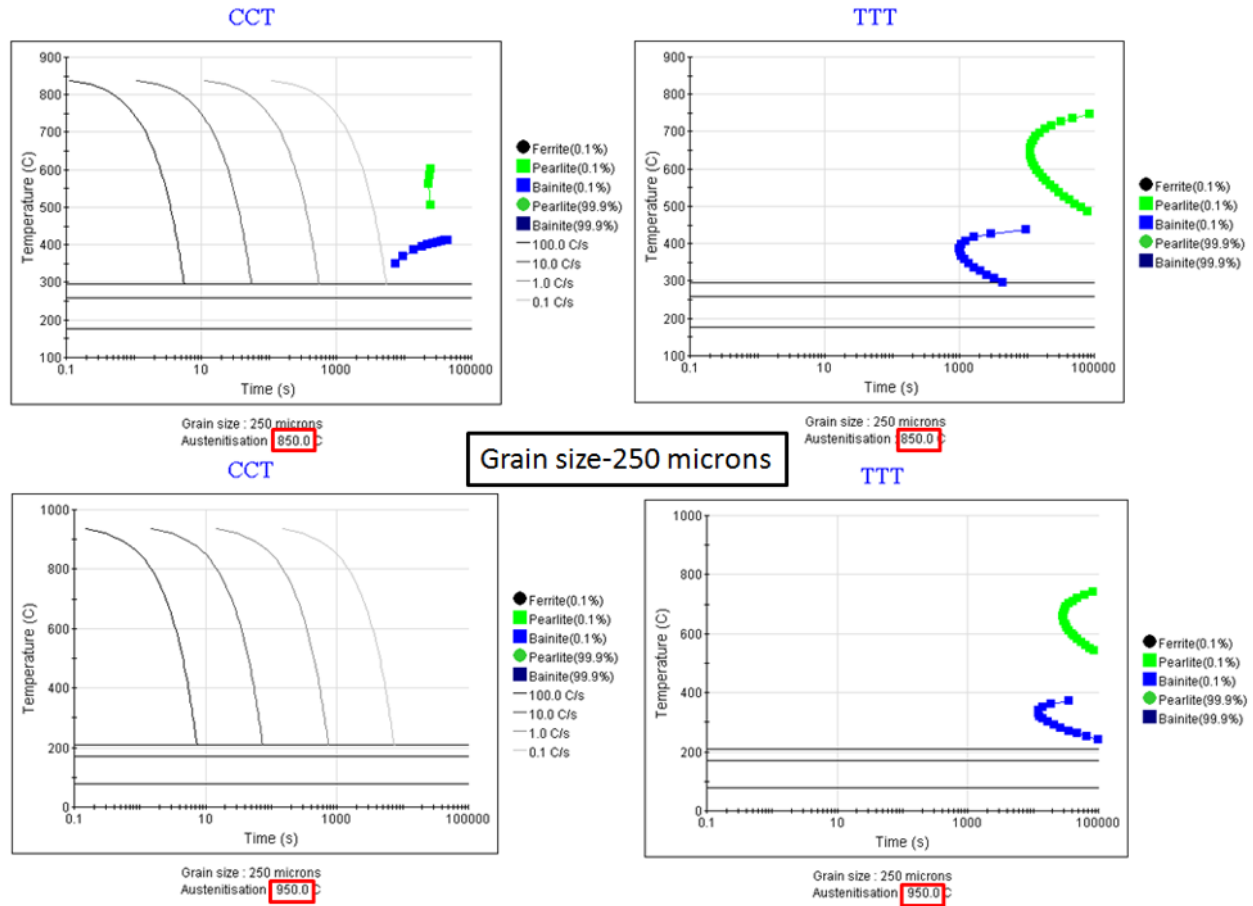


Figure 58. Predicted CCT-TTT diagrams (250 μm grain size)

The CCT diagrams (*Figures 57, 58*) also indicated that in case of the conventional HT, in particular, cooling rate conditions, a mixture of pearlite and bainite regions can be obtained at depth of 2" or more below the surface. This observation was confirmed by the presence of pearlite colonies at the intermix region. Presumably, this result is due to the following combined factors: the presence of a thermal gradient, local compositional changes, insufficient heat penetration and slow cooling rates. In general, the pearlitic-like features can be found even after combined HT conditions, especially closer to the intermix region in the conventional shell. It starts out at triple points and grain boundaries and then occupies the prior austenite grains. In most of the cases, the phase fields are not affected at cooling rates of more than 1 $^{\circ}\text{C/s}$, according to the simulated results.

Higher austenitization temperature (T_γ) causes an enrichment in solutes of the austenite (*i.e. higher hardenability*) and, hence, shifts the transformation start temperature of ferrite and pearlite to the right (*longer times*), therefore, brings to effect the suppression of these microstructural components during cooling (*Figures 57, 58*). Also the start transformation temperature for bainite (B_s) and martensite (M_s) are shifted to lower temperatures. This observation is in agreement with theoretical and empirical equations of the B_s and M_s , which are strongly dependent on the austenite chemical composition. For example, at relatively high austenitization temperature (T_γ), the carbon content of the austenite increases, and the austenite grain size also becomes coarser; both of these factors are well-known to depress the B_s and M_s temperatures. In some cases, the M_s is very low and it can be sub-zero. In these circumstances cryogenic quenching might be required; otherwise, at moderate cooling and isothermal holding the reduced bainite formation can be facilitated. Similarly the effect of the austenite grain size is well-understood, that coarse grains shift the phase fields on the diagrams to the right, hence, reducing the ability to form ferrite or pearlite for a certain cooling rates.

Overall, it can be summarized that when the liquid starts to solidify, the primary austenite dendrites begin to nucleate and grow at the liquid-solid interface until they impede each other. They then form an interdendritic eutectic segregation with subsequent precipitation inside it, containing the following carbides: M_2C , MC , M_6C , and M_7C_3 depending on local composition of the liquid. Inside prior austenite cells MC , $M_{23}C_6$ and other phases, for example, bainite, pearlite, are expected. Hence, two types of reactions can take place upon cooling: peritectic and eutectoid, which is confirmed with the observed microstructural evolution (*see Section 4.2.4*). Austenite is formed down to approximately 750°C . When the temperature corresponds to a two-phase region ($750\text{-}820^\circ\text{C}$), proeutectoid precipitates are formed from the austenite, until the eutectoid

temperature is reached. Below the eutectoid, depending on the local composition and cooling, the remaining austenite can transform to pearlite, bainite or remain untransformed.

Precipitation kinetics analysis during solid-state transformations showed that carbide volume fraction and particles size are strongly related to the quench and isothermal holding temperatures. For the case of a thermally instable material at service temperatures, it is expected that M_2C diminishes in approximately 11-14 hours, whereas the volume fraction of MC and M_6C start to slightly increase at the end of the M_2C transformation and can be raised 2-3 times with respect to its original amount. Therefore, friction can be increased during a rolling campaign, affecting the quality of the strip. Also $M_{23}C_6$ reaches its maximum amount in 28 hours of up to 7 times the original amount, with particle size increasing by about 2-3.5 times. In contrast, M_7C_3 is almost unaffected. The MC particle size can be slowly increased 1.1-1.4 times in 10-12 days; M_6C has a higher rate increasing in size up to 2-2.5 times. The described irreversible structural transformations have to be minimized to prevent the formation and the interconnectivity of eutectic interdendritic carbides. To be able to obtain a high secondary hardening, i.e. red hardness response, it is essential to eliminate the formation and interconnectivity of the eutectic carbides. This interdendritic segregation has a very slow response to heat treatments, because of the very slow kinetics of dissolution. Therefore, the matrix has to be enriched with carbide forming elements to form fine alloyed carbides and promoting secondary hardening.

In conclusion, the detailed description of phase transformation models (*TTT/CCT*) can be found in [83], simulation of mechanical properties as a function of cooling rates in [84] and solidifications in [85]. Both thermodynamic packages provided thermo-mechanical, physical properties of the alloys as a function of temperature and microstructure. This data was used as an input for material models (*see Sections 3.5*). Predicted phase products, second phase particles and

micro-constituents resemble actual behavior of the HSS material during solidification and solid-state transformations, which was confirmed with microstructural observations and analysis (*see Section 4.2*). Equilibrium and non-equilibrium predictions suggested that the lower carbon group material has a different solidification path: much higher solidification temperatures and narrower two phase region (*liquid-solid*). It can positively affect the microstructure refinement without the need of additional cooling systems. Secondly, the HSS material has a high hardenability, according to predicted CCT curves.

4.2 MICROSTRUCTURAL ANALYSIS

Systematic advanced microstructural studies were conducted in order to understand the effect of the individual HT processing steps (*i.e. as-cast* \rightarrow *preliminary HT* \rightarrow *hardening HT*), Figure 59. These studies were conducted on the radial samples machined from various commercial HSS work rolls, having different compositions as indicated in Table 2. The types of carbides, their precipitation sequence, morphology and phase balance were determined as a function of radial depth in the HSS shell. The results illustrated that there are many microstructural peculiarities related to individual samples and their respective HT, but three main general observations could be made for the conventional HSS material (*ID 1-4 in Table 2*):

- I) the solute-rich interdendritic eutectic boundaries, consisting of hard phases, are mostly not affected by any sort of conventional HT;
- II) compositional variations along the HSS shell facilitate nonhomogeneous microstructure, hence, the mechanical properties will not be consistent;

III) development of pearlitic colonies as a function of radial position were observed, starting at the intermix region, nucleating from triple points and the carbide-matrix interface; these colonies filled-up the prior austenite grain and sub-grain structures.

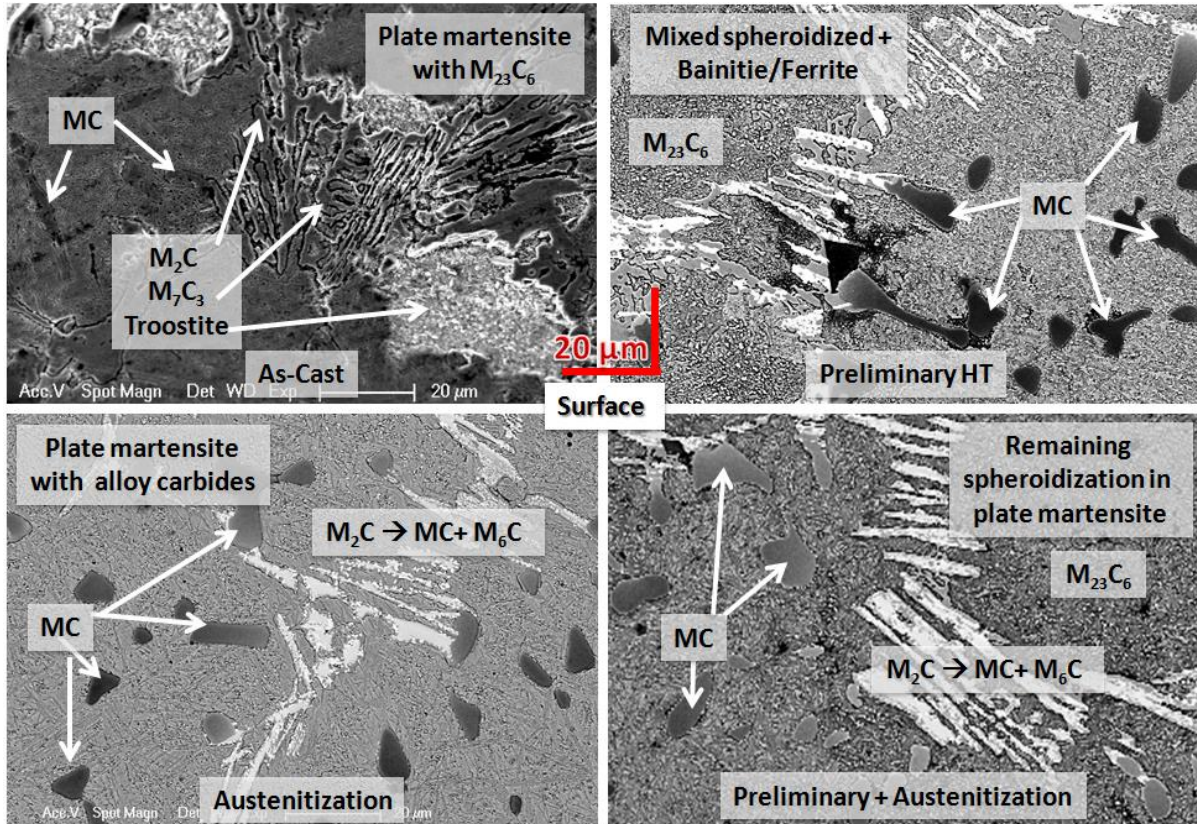


Figure 59. Effect of different HT on surface of HSS shell (top left: P0-cast; top right: P0-P; bottom left: P0-A; bottom right: P0-P+A, Table 2)

Figure 59 presents micrographs showing the effects of the heat treatments given in Table 2 for the P0 group (ID 1-4). As can be seen in the micrographs, the eutectic interdendritic carbides (M_2C , MC) either do not change at all, or only partially decompose after conventional casting and

HT routes. But the matrix is found to vary depending on the type of HT, the presence of undissolved secondary carbides, and whether the material stays nonhomogeneous.

From re-heating-re-melting experiments on low carbon S-shell material ([Table 2](#)) it is found that M_2C carbides after higher T_γ become less connected due to the transformation into M_6C and MC, which is a well-accepted reaction. These decomposition products are precipitated along the boundaries for the case of rapid cooling, whereas the matrix stayed homogeneous. A re-melting experiment (*hold at 1200°C for 2 hrs.*) reproduced a mushy-state of the material. It was found that the applied gradient cooling affected the morphologies of MC carbides within the same sample, as depicted in [Figures 60, 61 and 62](#). The figures correspond to rapid, moderate, and slow CR, respectively. The MC carbides precipitated along the boundaries as inside austenite grains in coral-like shapes. Since the experiment was conducted on small samples (*dia. 12 mm, thick. 2 mm*) machined from the same surface of HSS cast material, it is assumed that the compositional variation is negligible. Also the preliminary HT, i.e. pre-conditioning effect, is not taken into consideration.

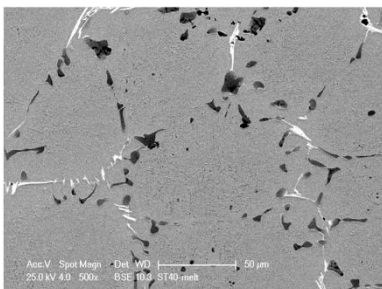


Figure 60. Clean γ -eutectic cells with decorating M_2C and MC

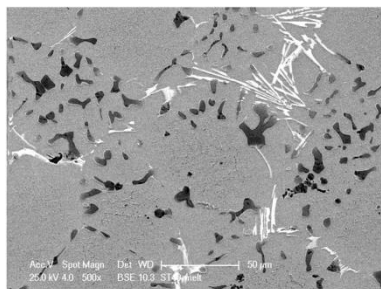


Figure 61. Formed petal-like MC inside γ -eutectic cells

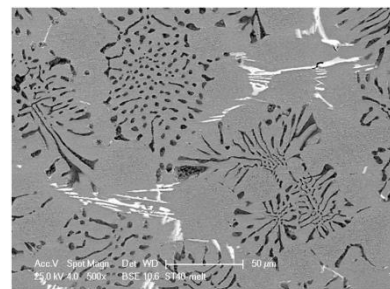


Figure 62. Coral-like MC developed inside γ -eutectic cells

Regarding the second general microstructural observation made above, earlier analysis of microstructural variability and the associated decrease in hardness through the thickness of conventional HSS shell led to an assumption of continuous local transformations as a function of thermal gradients, heating-cooling rates, compositional segregations, and spatial coordinate.

For example, the radial variation in microstructure of the sample is shown in Figure 63 with its Rockwell C (*HRC*) hardness taken from surface to the core, and corresponding optical micrographs (*OM*) are superimposed. The topmost arrow indicate the microstructural boundaries and its development towards the core with undesirable coarsening of the carbides, and brittle and non-uniform phase distributions.

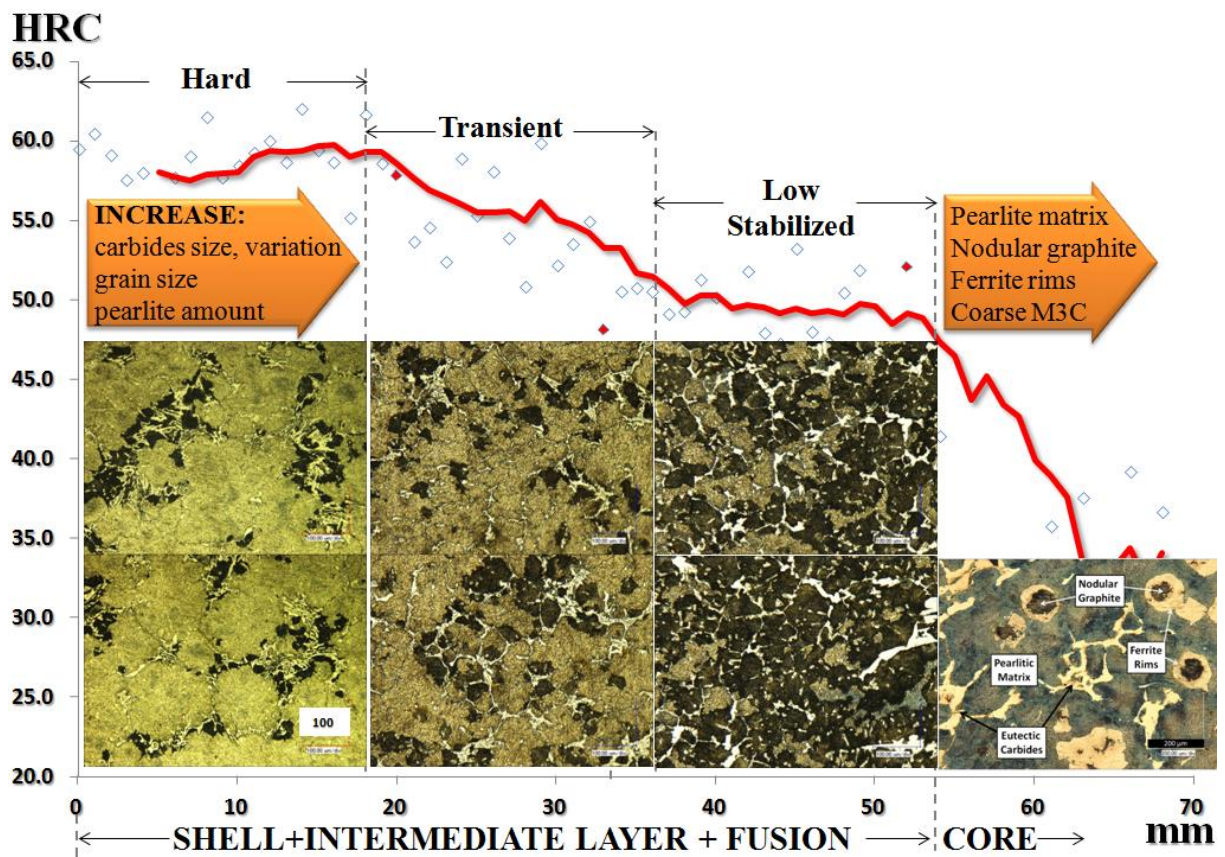


Figure 63. Radial HSS shell with conventional microstructure (P0-cast) and associated *HRC* hardness profile

The diamonds at the top of the Figure 63 give the actual HRC measurements, with the scale being along the ordinate. A moving average of the HRC data was computed using 5 points and is given by the solid red line. As can be seen, the hardness decreases by 15 HRC numbers through the depth of the HSS sample into the intermix region (*first 50 mm along the x axis*), rapidly declining in the core region. The decrease in hardness in the core is as expected. However the decrease through the depth of the HSS shell will be responsible for decreased life of the roll. To increase the life, it was desired to create changes to casting and HT methods in order to maintain the high hardness (*at least HRC 60*) throughout the entire depth of the HSS shell.

Figure 64 shows the chemical composition versus depth for the same sample given in Figure 63. It was found that the composition of the shell is also varies with depth, Figure 64, presumably producing the observed microstructural and hardness variation observed in Figure 63.

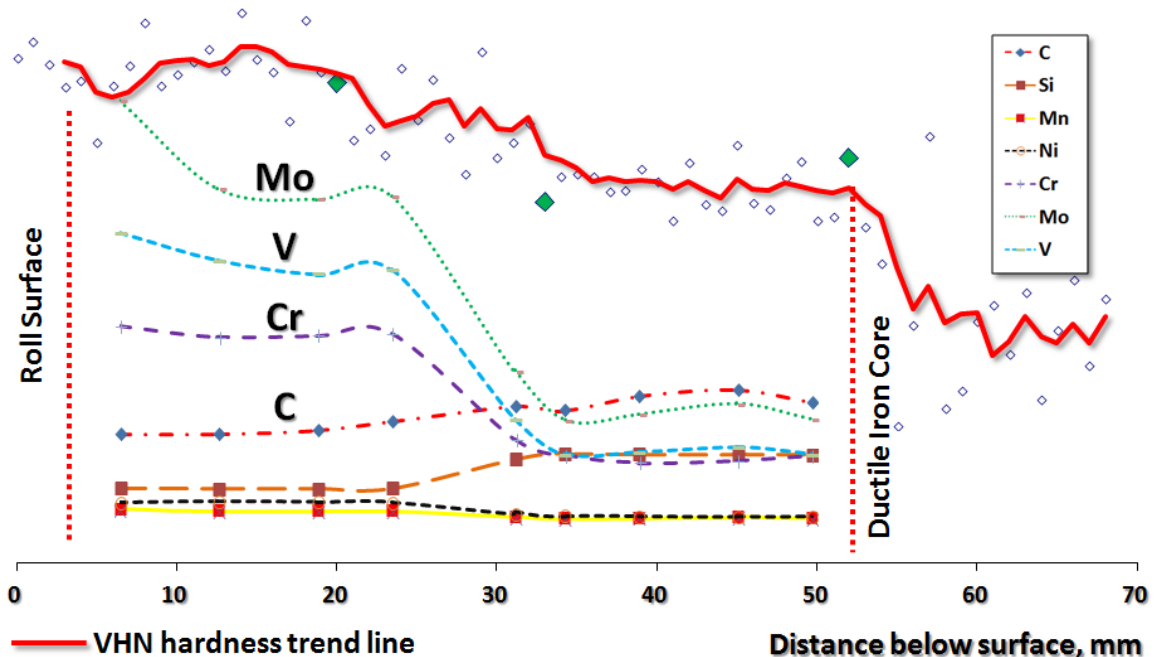


Figure 64. Hardness profile vs. bulk chemical variations (conventional case)

This issue of chemical dilution is mainly related to the casting (*mixing*) of the core material with the shell. The higher carbon content forces alloy elements into the mix, diffusing and forming brittle coarse carbides at the intermix region. It is well-known that carbon is an interstitial solid-solution strengthening element. Its concentration variation can lead to tremendous changes in microstructure properties, especially at the intermix region (*mixed HSS and nodular ductile iron*). In this region, the carbon gradient is relatively high, leading to formation of brittle carbide networks. Moreover, its variation within the HSS shell itself leads to local phase changes, non-uniform distribution of carbides, varying morphology and crystalline structures. Usually with increased carbon content higher attainable work hardness is expected. However, in the highly alloyed HSS shell (*Table 1*), coarse interdendritic carbide networks and secondary precipitates in the matrix can be formed and, therefore, the bulk hardness becomes considerably lower than expected (*Figure 63*).

The precipitated carbides in the matrix are found to be increased in conventional cast, and their growth is more likely related to, so called, “over-aging reaction.” That is, the heat from solidification and solid-state transformations from pouring the core material, affects the relatively cooled HSS shell, which remains in contact with the molds. Depending on the size of the roll body, the core solidification might take more than 36 hours, and the shell is being exposed from inside to energy released during this time. Keeping in mind the dilution of Mo and increase of Si at the intermix region shown in *Figure 64*, when combined with the slow cooling would produce the observed development of gradient of pearlitic colonies discussed next. The observations of unexpected pearlite within conventional as-cast HSS shell at the boundaries (*Figure 63, dark phase*) are corroborated by reference [106], which explains the occurrence of troostite by eutectoid transformation of destabilized austenite due to segregated molybdenum to the interdendritic

regions. Molybdenum affects the stability of austenite in pearlite region. Increase of Si content (Figure 64, see legend) can also facilitate pearlitic-sorbitic formation [44].

Figure 65 shows analogy between micrographs, taken at the intermix zone of conventionally casted and heat treated “P0-P+A” material (Table 2), and schematics of pearlite development by Arzamasov [44]. The schematic (top, Figure 65) corresponds to one local point; whereas the superimposed microstructure is related to several locations within intermix from surface to near the core.

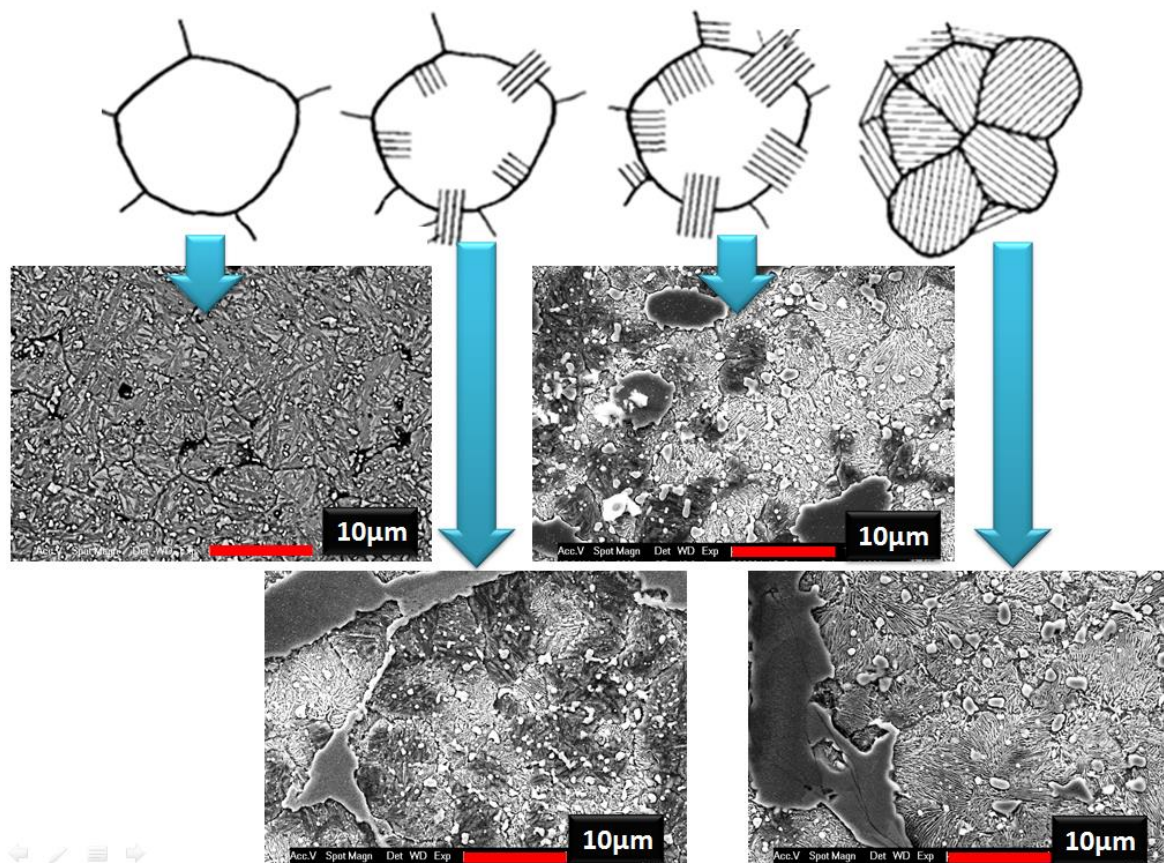


Figure 65. Continuous pearlite development in conventional HSS material within intermix region (surface to core; analogy with pearlite colonies development for rail steel by Arzamasov, [44])

As it can be seen, the degree of the pearlite development depends on a location: coarse pearlite colonies are observed closer to the core as a function of local chemical composition, thermal gradients and slow cooling rates. The character is similar to that of eutectoid steel (*e.g., rail steel*): the pearlite lamellar starts to develop from the grain boundaries; then it “fills” up the sub-grains inside eutectic cells gradually, producing coarse structure next to the fusion line. The sub-grains are also coarser next to the fusion line as a result of conventional heat treatment and slow cooling rates. Also in addition to pearlite colonies within intermix region, coarse, globular Cr-rich carbides ($M_{23}C_6$) are formed mainly at the sub-grain boundaries, increasing in size closer to the fusion line (*left-to-right, Figure 65*). This location also contains coarse cementite (M_3C) and blocky eutectic carbides. The coarse pearlitic structure with coagulated carbides can be explained by higher temperature at this location and slower cooling rates; hence, longer exposure to the residual heat, possibly coming from the core and from the transformational reactions. The local continuous phase transformations along the shell can be also proved by varying interlamellar spacing of the developing pearlite (*i.e. the averaged sum thickness between neighboring ferrite and cementite plates*), which is increasing to the right. These are not modified by any conventional HT.

In summary, as it was covered in the Section [1.1](#), the dendrite segregation is the fundamental issue of the large ingots and cast products. It is the interdendritic segregations, relatively coarse secondary precipitation and partially dissolved transient carbides observed in the matrix of conventionally HT roll that became the major factor to be investigated in this work. As it will be shown in Section [4.2.3](#), partially dissolved epitaxial, Mo-rich, carbides are incoherent and spread around the dendrite boundaries, consuming alloying vanadium from the matrix. Another case is related to the Cr/C ratio, which can produce a relatively coarse secondary

precipitation in the matrix after conventional HT. It is well-known, that Mo, Cr, V alloying elements can be substituted and are often rejected from the matrix in case of their excess, binding with carbon and forming secondary precipitates ($M_{23}C_6$) in the matrix. Usually the nucleation sites for such carbides are triple points, martensite laths, plates, high dislocation density points, and boundaries [107]. And it is likely normal to expect these carbides, but when the degree of coagulation (*spheroidizing growth and increase of distances between carbides*) is high and the carbides are incoherent with the matrix and not affected by any conventional HT, then the matrix remains without sufficient alloy content. It results in decreased wear properties, nonhomogeneous oxidation behavior, and a possible increase in friction.

Thus it was decided to focus on the causes of such variability in the HSS shell by detailed systematic microstructural investigation of original and improved materials. The main focus was made on refinement of as-cast structure and development of more effective heat treatment routes to produce relatively homogenized shell with uniform increased mechanical properties.

4.2.1 Analysis of as-cast microstructure

Two HSS shell samples in as-cast condition were compared, one from the high ($P0$ -) and low ($S0$ -) carbon groups from Table 2. The same samples were re-heated and partially re-melted, reaching “mushy” condition (*i.e. mixed solid and liquid phases*). In Figure 66a an example of dendritic coalescence is shown after re-melting followed by slow cooling (*described in Section 4.2.1*) and compared to actual dendrite cluster formation in case of centrifugal casting (*Figure 66b, highlighted areas with a dash line*). The microstructure shown in the Figure 66a was formed as a result of re-melting the as-cast HSS shell material without centrifugal forces under laboratory conditions (*inert atmosphere*). In Figure 66 possible directions of dendrite growth are shown with

white arrows, as it was visualized and explained in [108]. As can be seen, the dendrite area is more homogeneous; whereas the interdendritic zones are fully packed with eutectic complex carbides (Figure 66a, dark and white phases: V-rich and Mo-rich, respectively), lowering the toughness of the material. Figure 66b shows a mixed case of both: equiaxial grains and dendrite clusters. In the presence of the centrifugal force and controlled unidirectional solidification, the dendrite formation is preferably equiaxed instead of the columnar cluster formations. However, this is not always the case, since multiple interrelated factors (*spin casting parameters, the precipitation sequence of microconstituents, Gibbs free energy of formation, etc.*) can impact solidification.

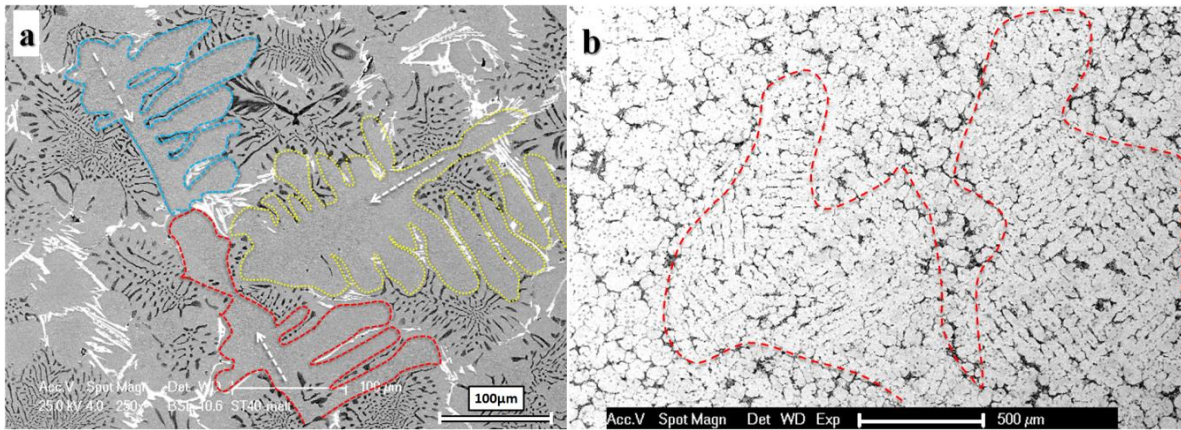


Figure 66. (a) Re-melted HSS as-cast material in the lab conditions (no centrifugal field): example of dendrite growth and formation of solute-rich boundaries with coral-like eutectic MC carbides, V-rich (dark grey) and M_2C , Mo-rich (white) at accelerated air cooling; (b) example of dendrite clusters formation in centrifugal field (Murakami etching; clusters highlighted with curved dash-lines)

In general, it can be concluded that there are two types of carbides that are forming during and after solidification: 1) eutectic, and 2) precipitated carbides [37, 53]. The eutectic carbides are

basically segregated at the interdendritic regions, nucleating from the melt, whereas the secondary precipitation takes place in the matrix as solid-state transformation. The matrix, depending on the cooling rate can be martensitic, tempered martensitic, or bainitic. Usually, with high carbon content, plate martensite is expected, but the lath-type matrix can be also observed [37], especially after HT and in the case of local segregations at the boundaries. Due to the complexity and variety of microconstituents at the boundaries, the interdendritic region can be characterized very differently, for example: a) “eutectic interdendritic solute-rich boundaries” (*author’s preference*); b) “dendrite segregations”; c) “interdendritic eutectic carbides”; d) “brittle eutectic carbide networks”. But the concept is the same. In Figure 67, the EDS line scan across the boundary of S0-shell sample is shown.

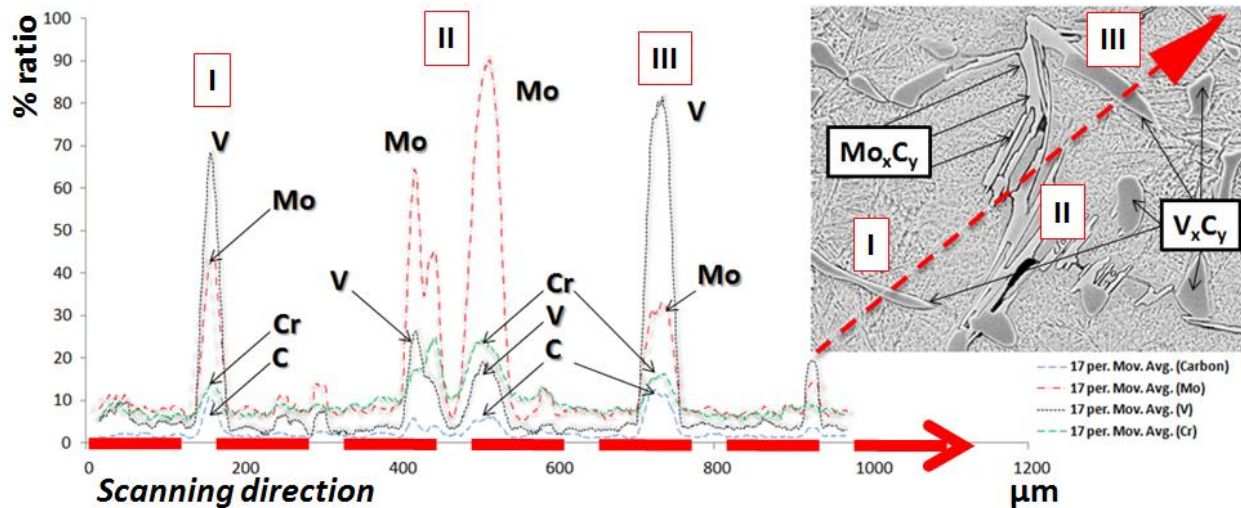
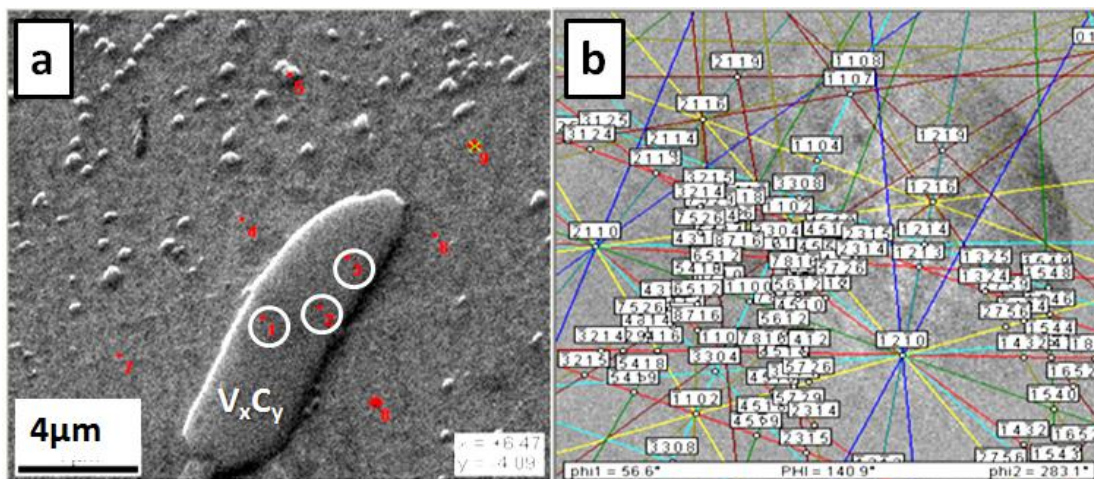


Figure 67. EDS line scanning of the solute-rich eutectic boundaries in the refined cast (S-shell)

Obviously, while crossing different microconstituents, the peaks in the EDS spectrum fluctuate, indicating local non-stoichiometry within and around the carbides. Therefore, different crystalline structures of the carbides are expected, which is confirmed with EBSD (*electron*

backscatter diffraction, Kikuchi pattern technique) analysis of V_xC_y eutectic carbide with the aid of JEOL and Philips systems (see Section 3.2.4). An example of point-wise EBSD scanning and related Kikuchi pattern for an arbitrary point is shown in Figure 68. The two methods, using their supplied databases (similar to XRD libraries, e.g. ICSD database), offer different V_xC_y formula for different points within carbide's scanned area. This result means that the local equilibrium is not reached, because of the non-stoichiometric solid solution. Therefore, the atomic-scale transformations can also occur at elevated temperatures, rearranging the crystal lattice sites and leading to more complex carbides than is typically expected. The common criterion to assess the roll quality is the carbide volume fraction, but the type of crystalline structure must be of particular interest too. Confirming detailed studies [64] also showed that, for example, eutectic vanadium carbide is composite, which can consist of VC, V_6C_5 , V_8C_7 with the face centered cubic (fcc), hexagonal and simple cube superlattice crystalline structures, respectively, and additionally having considerable amount of coherent (partially coherent) MC-type nano-particles.



An example of 2-D EDS mapping of the eutectic boundaries in a conventional P0-cast material (*high carbon and Cr/C ratio*) is shown in Figure 69, where the distribution of chemical elements is depicted. It is clearly seen that the main alloying elements, such as: C, Cr, Mo and V, are concentrated within the carbide area, therefore, the surrounding matrix is locally destabilized, comprising of martensite and troostite pearlite simultaneously.

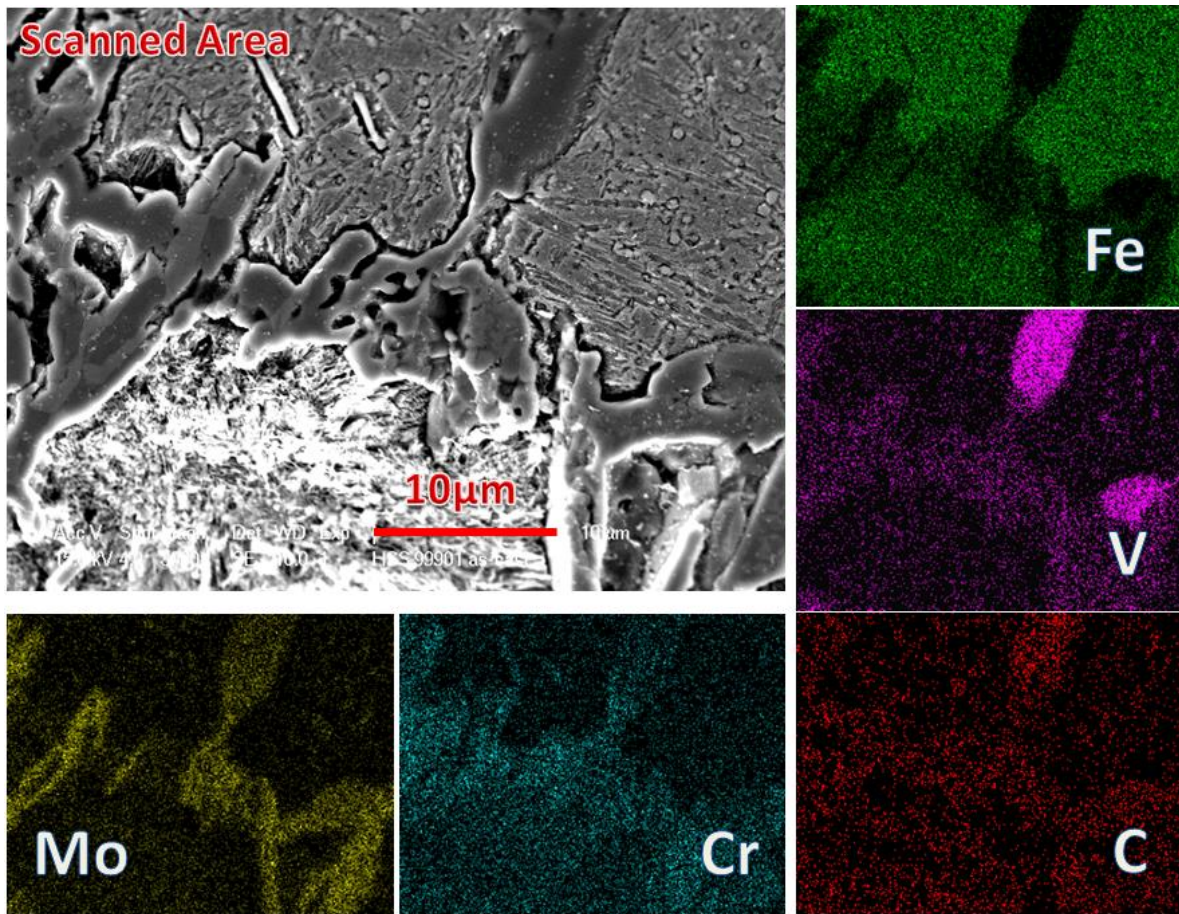


Figure 69. 2-D EDS mapping of eutectic boundary region in the conventional cast, including fibrous-like troostite pearlite (Cr-rich fibers and Mo-rich tips) and eutectic M₂C (Mo_xCr_yC), MC (V_xC_y) carbides

The analyzed eutectic carbides have relatively high melting points; hence, they remain almost unchanged after HT. At the same time mechanical properties depend on these carbides,

their type, morphology and distribution. The eutectic γ -cell size is almost the same after several HTs (*e.g., preliminary, austenitization and tempering*) in the final product, because the prior austenite boundaries are not sufficiently mobile due to high carbon concentration and other alloying elements at the interdendritic boundaries. Hence, the as-cast structure is likely “initial condition”, dictating the microstructural evolution during subsequent HTs. Therefore, the as-cast microstructure had to be refined, which could be achieved in two main ways: 1) by optimization of casting parameters (*pouring temperature, time intervals between operations and rotational speed*), and 2) adjustment of the alloy content (*carbon equivalent*), shifting the solidification path to higher temperatures and shrinking the temperature range of a dual phase region with the liquid phase. As a consequence, finer and more homogenized as-cast microstructure is formed, which facilitated faster kinetics during hardening HT. Figures [70](#), [71](#), [72](#), [73](#) depict the main features of the matrices and some boundary regions of conventional (*Figure 70, 71*) and refined (*Figure 72, 73*) cast. For conventional cast (*P0-group, Table 2*) in *Figure 70* fibrous-like troostite pearlite is demonstrated at the eutectic carbide boundaries, where the top of the fibers is a Mo-rich tip (*bright white*). Conventional matrix is shown in *Figure 71* reach with Cr-carbides, $M_{23}C_7$. Solute-rich boundary rims of the refined cast are shown in *Figure 72*, which contain fine eutectic carbides and secondary alloy carbides in the matrix (*Figure 73*).

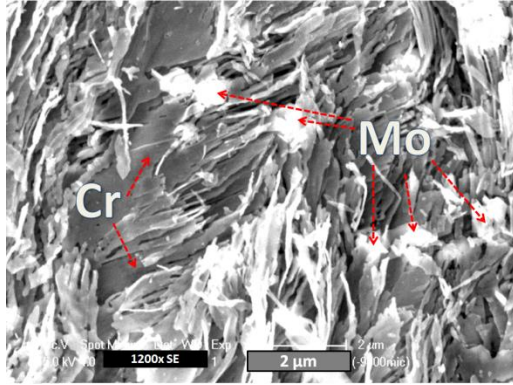


Figure 70. Conventional cast showing fibers of troostite with Mo-rich tips

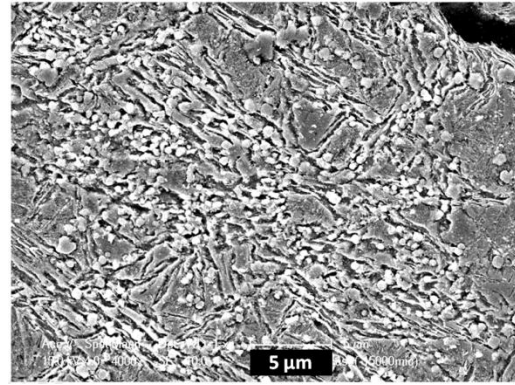


Figure 71. Conventional cast showing $M_{23}C_6$ (Cr-rich) in conventional matrix

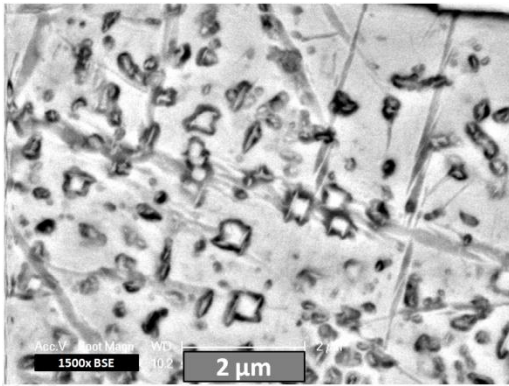


Figure 72. Refined as-cast solute-rich boundary' rims with fine $(Mo-V-Cr)_x C_y$ (white); $(Cr-Mo)_x C_y$ (dark)

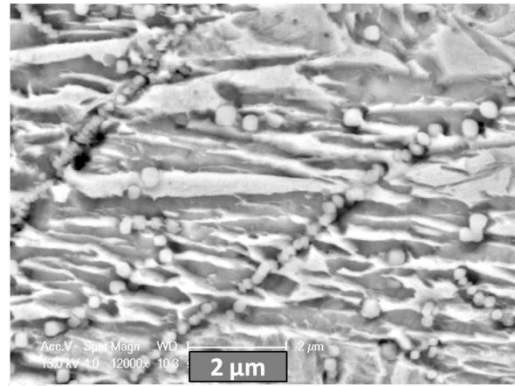


Figure 73. Refined as-cast mixed matrix with fine secondary precipitation along α' plates

The low carbon group shows refined dendrite equiaxed grains and uniform as-cast microstructure with fine secondary Mo-rich (*Figure 73*) carbides precipitated in the matrix, in contrast with the Cr-based (*Figure 71*) carbides observed for conventional case.

Figure 74 schematically presents a summary of the as-cast microstructure observations, corresponding to the surface location in the shell, for both the conventional and refined cases. For

the reader, it is recommended to keep in mind two main locations of the microstructure, classifying the carbides: interdendritic boundaries and the matrix, because each has a different local content and origin. As a reminder, the interdendritic boundaries are solute-rich due to the rejection of alloying content by propagating dendrites during crystallization. At the same time, the local matrix content is also different, especially of the two considered alloys, having high and low carbon concentrations, P0-cast versus S-shell (Table 2), respectively.

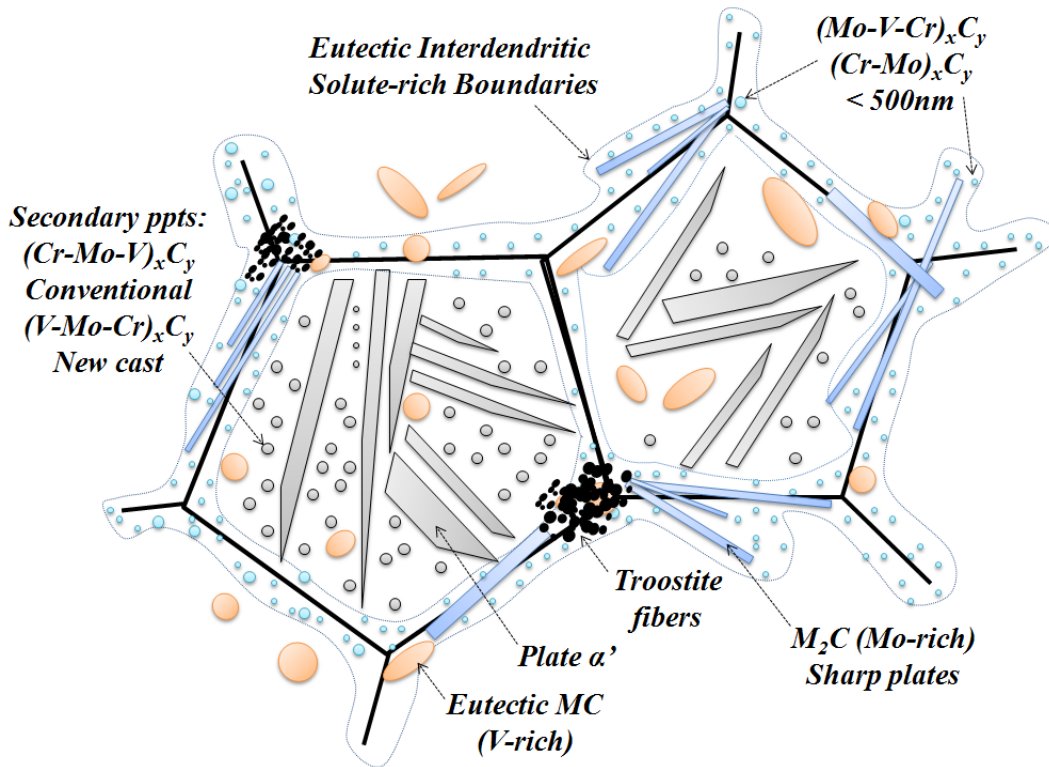


Figure 74. General schematic of as-cast microstructure

Describing the final crystallized state after solidification, it can be concluded that a very heterogeneous microstructure is being formed, containing two types of the carbides: eutectic and secondary. As an assumption, the first ones are formed at the high temperatures directly from the liquid, or could be bounded with a newly formed austenite, depending on local concentration. The

second ones are precipitating upon cooling as a result of the solid-state transformations. The eutectic austenite cells are usually filled up with MC-type carbides, which might have different morphologies, such as: idiomorphic, petal-like and chrysanthemum-type. The conventional cast had mixed MC carbides, mostly as separated, individual particles. But in the middle of the shell, the mixed columnar and equiaxed dendrites were observed with chrysanthemum-type MC carbides. Their configuration is controlled by local composition and cooling rate.

The matrix has high hardenability in both considered cases even without accelerated air cooling or quenching. But longer exposure to high temperature can promote coarsening of the carbides. It is also assumed that the prior austenite grain (*eutectic cells*) boundaries are immobile due to the excess of alloy content. These grains size is dependable on solidification, controlled by casting parameters. Speaking of martensitic transformations, the growing martensitic plates impinge each other, reaching the eutectic cell boundaries. The supersaturated solid-solution rejects some alloying content upon cooling, forming secondary precipitation within matrix. Usually the precipitates are observed along martensite plate boundaries, internal defects, and high dislocation density regions. It was found that the secondary precipitation in the matrix upon cooling during solidification has different local composition for each considered material in as cast condition, for example, Cr-based precipitates were found in conventional cast (*Figure 71*), while V-rich- in the new cast (*Figure 73*).

The interdendritic boundaries due to even higher amount of alloying content, facilitate different types of the carbides within boundary rims, making them very brittle. Moreover, the retained austenite was mainly found at these interdendritic segregations, which could harmlessly effect the performance due to possible transformations ($\gamma \rightarrow \alpha'$). In other words, potential martensitic transformations at the boundaries have even more deleterious effect, making the

boundaries embrittled. In general the microstructures of two considered alloys have similar microconstituents and phases, but the main difference is the local composition of the carbides and matrix. Also the eutectic austenite grain size is finer and more equiaxed in the new cast. It was achieved by lowering the carbon content, therefore, promoting earlier high temperature solidification.

The above mentioned observations, literature review and on-site investigation of the spin casting manufacturing stage suggest that it is necessary to establish a better quality control and more consistency to produce a solid, thick HSS shell. It can be achieved through controlled unidirectional solidification from the outer shell tube surface.

As it was shown previously as introduction in Figure [59](#) and will be discussed next, that deleterious eutectic interdendritic carbide networks are not considerably affected by any sort of conventional HT due to their stable behavior at relatively high temperatures. Hence it was suggested that the main eutectic carbides have to be initially refined and uniformly distributed in the matrix at the casting stage in order to avoid a possible formation of the brittle carbide networks, which lead to intergranular cracking [[12](#), [37](#), [39](#)].

For the casting control it was suggested to implement more advanced live-monitoring methods, using non-destructive testing and evaluation (*NDT/NDE*) methods; for example, the electro-magnetic acoustic resonance (*EMAR*) non-contact technique enables one to observe and thus control the solidification front in large ingots [[109](#)].

4.2.2 The role of preliminary heat treatment

As it was found, the preliminary HT had more effect on interdendritic carbides for the initially refined cast. It was found that the preliminary high temperature treatment has several beneficial

pre-conditioning effects: 1) matrix homogenization, or elimination of local segregation; 2) as-cast stress relief (*reduced bulk hardness, see Section 4.5.2*); 3) modification of eutectic interdendritic brittle networks by localized diffusion; 4) spheroidization of the matrix producing spherical alloy carbides ($M_{23}C_6$), which are uniformly distributed and conditioned for the subsequent high temperature austenitization; and 5) the “roughening” of the coarse sharp eutectic M_2C .

For most of the cases (*P0-P, S0-P, SPH-P in Table 2*), a partial decomposition of M_2C and the interdendritic region was observed up to a certain degree, depending mainly on the initial cast conditions, local compositional segregation, and radial position. For example, in Figure 75 two cases, corresponding to the surface location, are compared after identical preliminary HT.

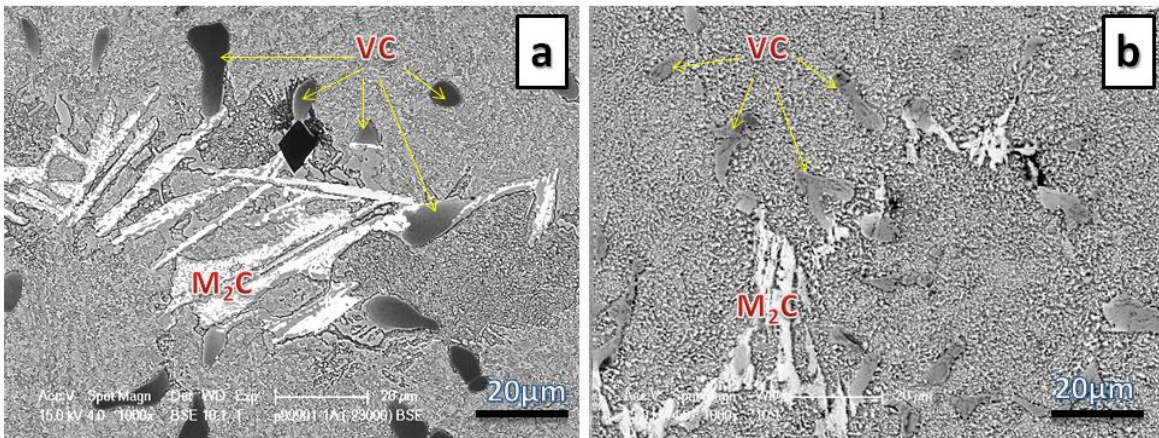


Figure 75. Effect of initial as-cast condition and different bulk composition on response to preliminary HT:

(a) P0-P (conventional), (b) SPH-P (refined cast)

For the P0-cast, having higher bulk carbon content, coarser eutectic γ -cell, and more severe local segregations, there are no significant modifications observed at interdendritic boundaries, Figure 75a. For example, Figure 76 shows considerable local segregation in the vicinity of solute-

rich boundaries and a nonhomogeneous matrix in the P0-P sample after preliminary HT, which was revealed by the EDS line scanning technique.

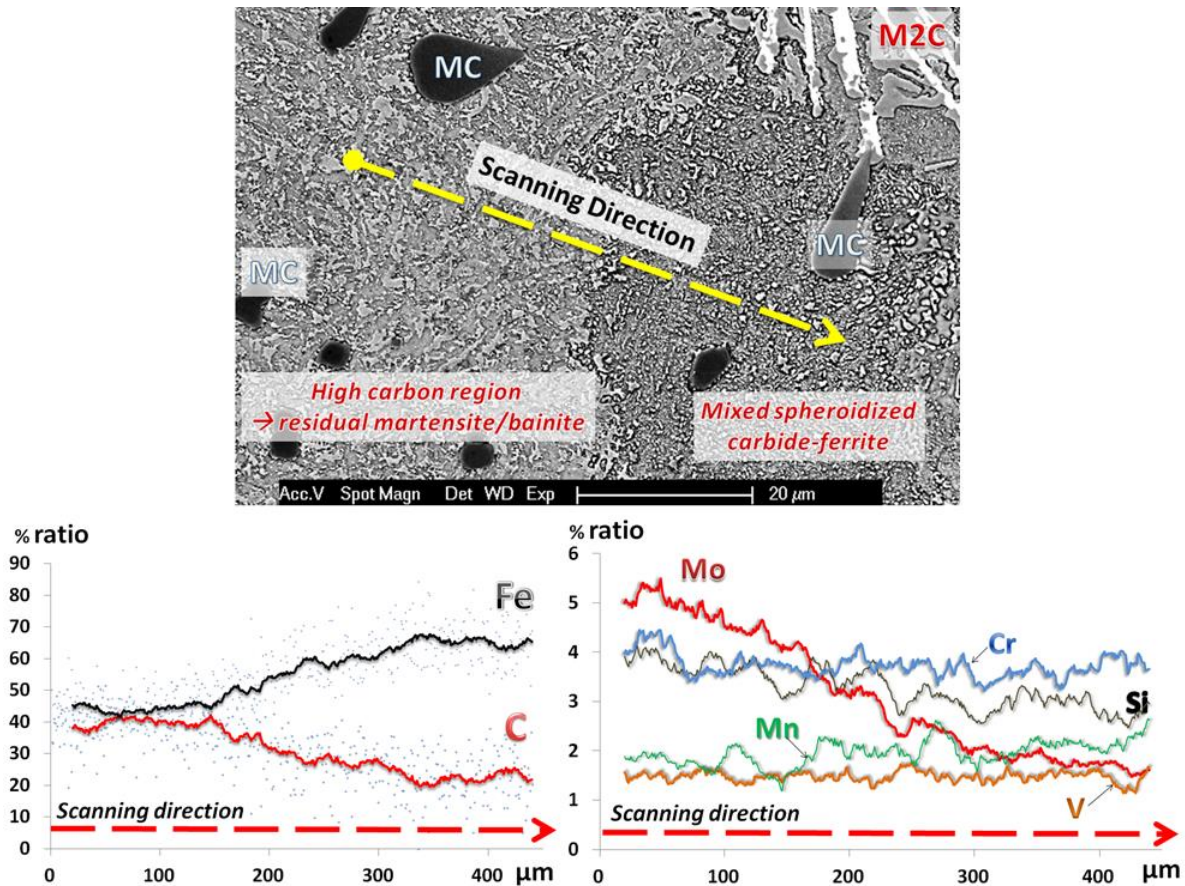


Figure 76. EDS line scanning, showing local segregation and nonhomogeneous matrix of conventionally cast HSS material (P0-P) after preliminary HT nearby solute-rich eutectic boundaries

Notably, observed fine, local spheroidization within and around eutectic carbides corresponds to previously existing troostite in the same positions. Analyzing the eutectic interdendritic regions along the shell, it can be concluded that the degree of spheroidization is increasing from surface to the intermix zone with its origin at prior eutectic boundaries. The size of coagulated carbides becomes coarser from the surface down to the core, which slows down its

dissolution at the austenitization stage, especially during conventional HT. The plate martensitic matrix of the as-cast material, also responded differently, producing internal mixed “island-like” coagulated features due to bulk and local alloy segregation. The non-homogeneity remains for the conventional cast after preliminary HT (Figure 75a, 76), where the bottom plots of the EDS line scans show that the partially coagulated matrix has more alloying content (*C, Mo, Cr, Si*). In contrast the right side of the micrograph is more spheroidized, hence, the alloy content is reduced in this region, but Fe and Mn are increased. Local vanadium distribution is more likely uniform for the both considered regions in the matrix.

Another example of micro-segregation for the conventional cast case, corresponding to middle position in the HSS shell, is demonstrated in Figure 77. Here, unaffected, V-rich, complex blocky carbides are surrounded with coarse coagulated alloy carbides, formed from the plate martensitic matrix. And, visible fine pearlitic lamellar, which increases towards the intermix region, is observed.

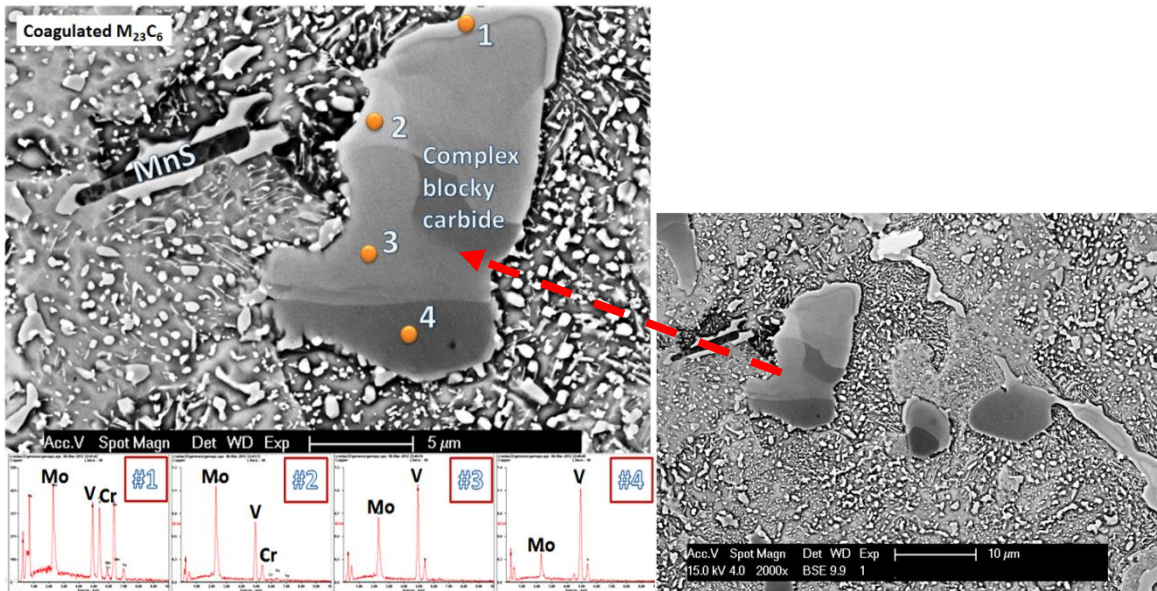


Figure 77. EDS spot scans on V-rich complex blocky carbide unaffected by preliminary HT

Samples S0-P and SPH-P are from the improved casts with lower carbon content, Figure 75b, and they demonstrate more homogeneous spheroidization in both the matrix (Figure 78) and the solute-rich boundaries (Figure 79). Furthermore, the eutectic carbides are more disperse, having rough edges, Figure 79.

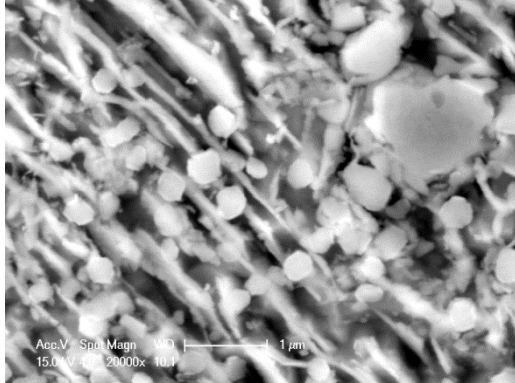


Figure 78. Preliminary HT (SPH-P). Mixed spheroidized and lamellar matrix structure with eutectic MC, precipitated (V-Mo-Cr)_xC_y alloy carbides and new spheroidized ppts

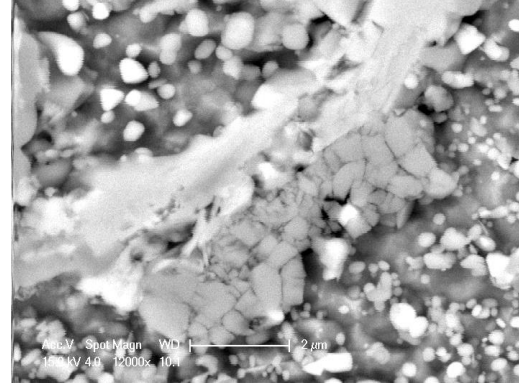


Figure 79. Preliminary HT (SPH-P). Interdendritic boundary with friable M₂C (white) and MC (dark)

Fine epitaxial “peanut-like”, Mo-V, carbides, described in [56, 57, 58] are mostly found surrounding the M₂C, Mo-rich, eutectic carbides. It is found that after non-conventional high austenitization, the amount of such carbides is considerably reduced due to their dissolution. But for the conventional cast with hardening HT, similar carbides are present in large quantities and their origin is mostly related to the solute-rich rims of the boundaries rather than the M₂C decomposition, because the holding times were not long enough to reach high T_γ. As it will be shown later for the austenitization stage (see Section 4.2.3), similar epitaxial carbides are mainly coming from the partial decomposition-dissolution of M₂C and eutectic γ-cell reaction as it was

discussed above. The effect of preliminary HT on the refined cast is summarized schematically in Figure 80.

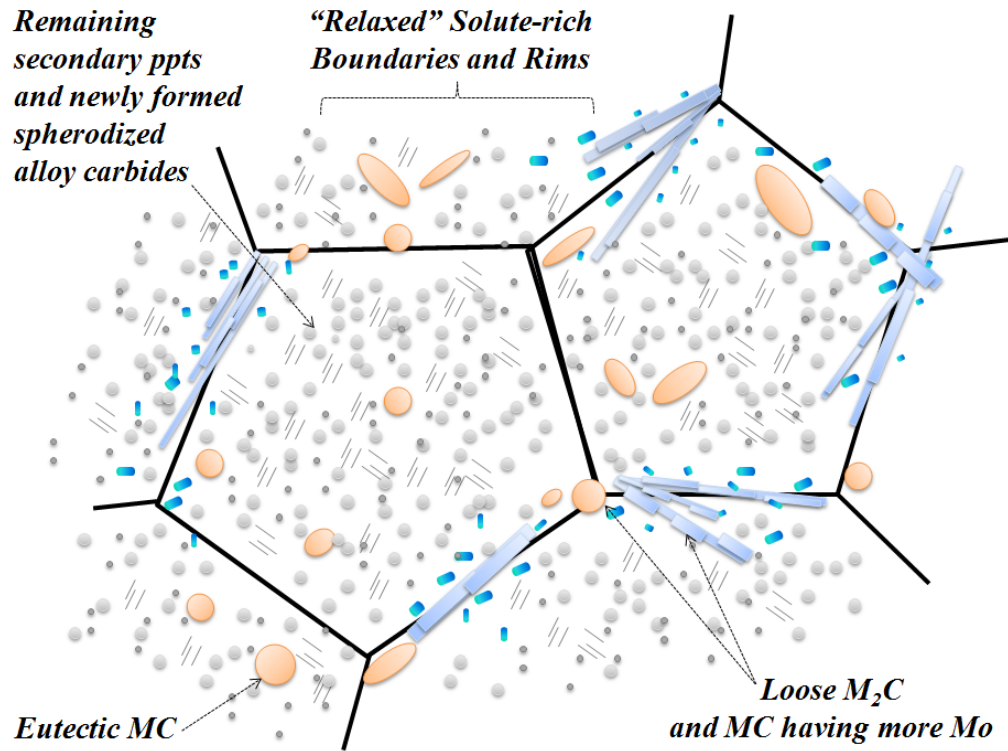


Figure 80. Schematic of preliminary heat treated microstructure for the refined cast material

It can be concluded that preliminary HT produced low hardness matrix and promoted non-coherent alloyed carbides spheroidization. In the new refined cast the carbides were relatively finer and more uniformly distributed in comparison with conventional cast, increasing surface energy; hence, improving dissolution behavior during subsequent high temperature hardening. Perhaps more significantly, the preliminary HT more effectively homogenizes matrix and boundary transitions of the refined cast. This spheroidized precipitation can be easily re-dissolved equally in the matrix during new hardening HT. Local segregations were eliminated by diluting the alloying content from the solute-rich boundary rims. As a result, the properly employed austenitization

temperature and exposure time can eventually promote sufficient dissolution and uniform chemical distribution in the matrix throughout the shell.

4.2.3 Hardening response using conventional and non-conventional heat treatments

The wear behavior is a function of the material's red hardness. It is very important to maintain relatively high hardness of the matrix throughout the shell thickness, which can be achieved by proper dissolution of solute-rich interdendritic eutectic boundaries and secondary carbides having a size of less than 500 nm. The nature of secondary precipitates in the as-cast condition was found to be strongly dependent upon alloy composition. When using conventional HT routes on HSS rolls, such secondary carbides remain and coarsen. Hence, a classical, high-temperature tool steel hardening approach was adopted for the HSS cast rolls. A non-conventional HT was developed to focus on the dissolution of precipitated secondary Cr-rich carbides (*shown previously, see Section 4.2.2*) and transient “peanut-like” Mo-V epitaxial carbides in the matrix, such as those seen in Figures [81](#) and [82](#). As a result, oxidation and wear resistance will be improved. At the same time, interdendritic eutectic solute-rich boundary networks were modified, improving the fracture toughness of the HSS shell material.

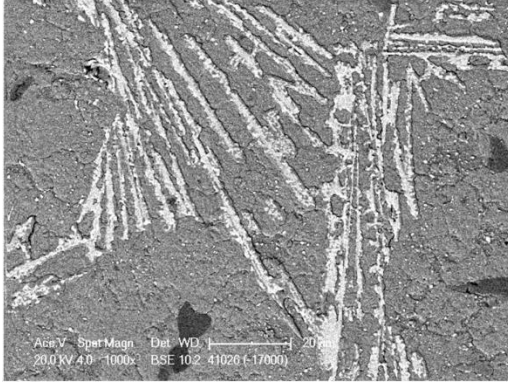


Figure 81. Partially transformed M_2C with fine Mo-V epitaxial carbides (conventional HT, CA41)

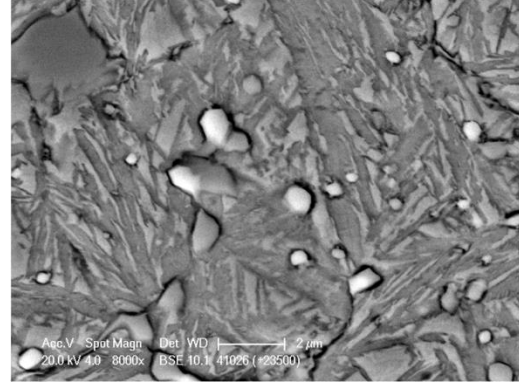
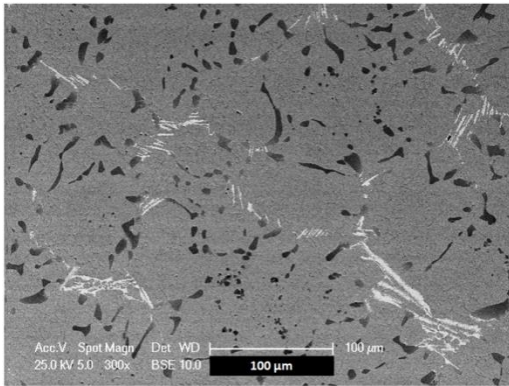


Figure 82. Zoomed transient Mo-V epitaxial peanut-like carbides (conventional HT, CA41)

A compromise must be met in the hardening HT between austenitization and tempering. Proper dissolution of transformational carbides, enriching the solid solution, enhances the secondary hardening during tempering, which improves red hardness of the material. The carbide-forming elements (*C, Mo, V, and Cr*) are substitutional, causing a local distortion of the crystalline lattice. However, with proper tempering HT, a secondary fine ($<200nm$) precipitation of V-rich carbides was observed to be uniformly distributed inside eutectic γ -cells, Figure [84](#), which improves wear resistance of the matrix. The dissolved Mo and Cr improve friction and oxidation behavior of the matrix, respectively. Hence, it is important to dissolve fine carbides found in the as-cast material in the vicinity of Mo_2C carbides (Figure [81](#)) as well as the peanut-like epitaxial undissolved carbides (Figure [82](#)).

The matrix is the most responsive to HT, when compared to the various types of carbides. Fine sub-grain structures can be developed inside prior austenite grain boundaries, which are not mobile due to the presence of stable carbides at high temperatures. The size of the sub-grain is a function of quenching from the austenite region. With the proper control of austenitization and high tempering procedures, the alloying content in the matrix can be increased, facilitating

secondary precipitation of fine alloy carbides, improving the thermal stability of the microstructure. The hardenability of the shell material was sufficiently high and was not affected by austenite enrichment and lowered martensite start temperature. A uniform, tempered martensitic structure was observed throughout the shell, whereas the conventional material could have pearlitic colonies closer to the intermix region discussed in Section [4.2.1](#).



**Figure 83. Broken interdendritic carbide networks
(non-conventional approach, P9DT)**

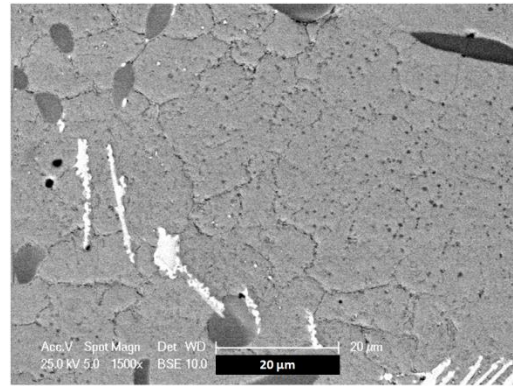


**Figure 84. Improved matrix with (V-Cr-Mo)_xC_y
precipitates, <200 nm (non-conventional, P9DT)**

In order to control the retained austenite levels after higher austenitization and to maintain a stable matrix, double and triple high tempering HTs are performed. The resulting microstructures are compared (*materials P9DT and P9TT in Table 2*). Thermal stability is achieved by double and triple tempering. The improved strength of the matrix was validated with micro-VHN hardness testing (*see Section [4.5.2](#)*). The observed alloyed carbide precipitation is shown in Figure [85](#). Carbide's coarsening is not observed. The total carbide volume fraction is slightly increased after triple tempering (*see Section [4.5.3](#)*). This can be explained by the decomposition of the retained austenite. The fact that the matrix was not affected after the long high temperature triple tempering

implies that the matrix is quite stable and resistant to tempering due to the alloying elements in solid solution, which promotes additional fine precipitation of alloyed carbides. It can be concluded that the major effect of higher HT is related to an enrichment of the matrix by increased carbide dissolution, leading to solid-solution strengthening.

The precipitated special carbides from martensite remain fine ($<500nm$) and uniformly dispersed in the matrix (*Figure 85*). No coagulations are observed, meaning that there is a sufficient amount of alloying content in the matrix, which is well conditioned after dissolution of the secondary and transient carbides. In *Figure 85*, the microstructures are shown corresponding to the double and triple tempering HT. The finely dispersed, precipitated carbides are of the type $(V-Mo-Cr)_x C_y$, according to EDS analysis (*Wt%: C (31.36-45.75); V (19.43-22.48); Mo (8.38-10.84); Cr (2.5-4.15)*). Additionally, the fine sub-grain structure can also be distinguished inside the matrix, improving fracture toughness.

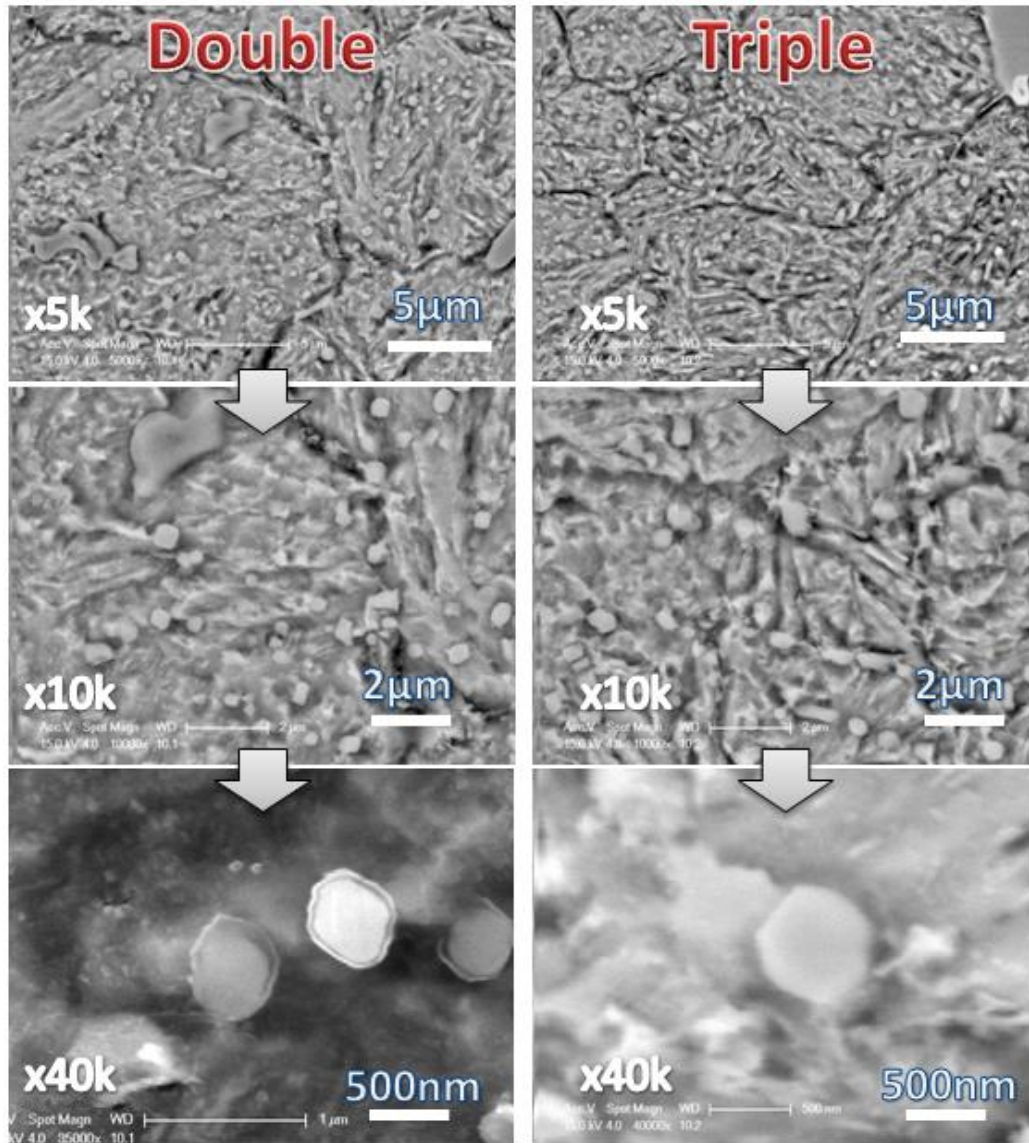


Figure 85. Comparison of microstructures after high temperature double (P9DT-left) and triple (P9TT- right) tempering HT

Therefore, the thermal stability of the matrix was achieved, which was verified with multi-step tempering techniques, promoting secondary precipitation of special alloy carbides. These special nano-size alloying carbides, of the $(V-Mo-Cr)_x C_y$ -type, were found to be uniformly precipitated throughout the matrix, meaning that the matrix is enriched with alloy content after proper dissolution of the transient and solute-rich eutectic boundaries after higher austenitization

HT. No coarsening of the grain size or carbides was observed. The XRD results confirm that the retained austenite is reduced down to 2-5% after proper hardening HT (see Section [4.5.1](#)).

The Figure [86](#) schematically represents the generalization of the influence of the developed high temperature HT.

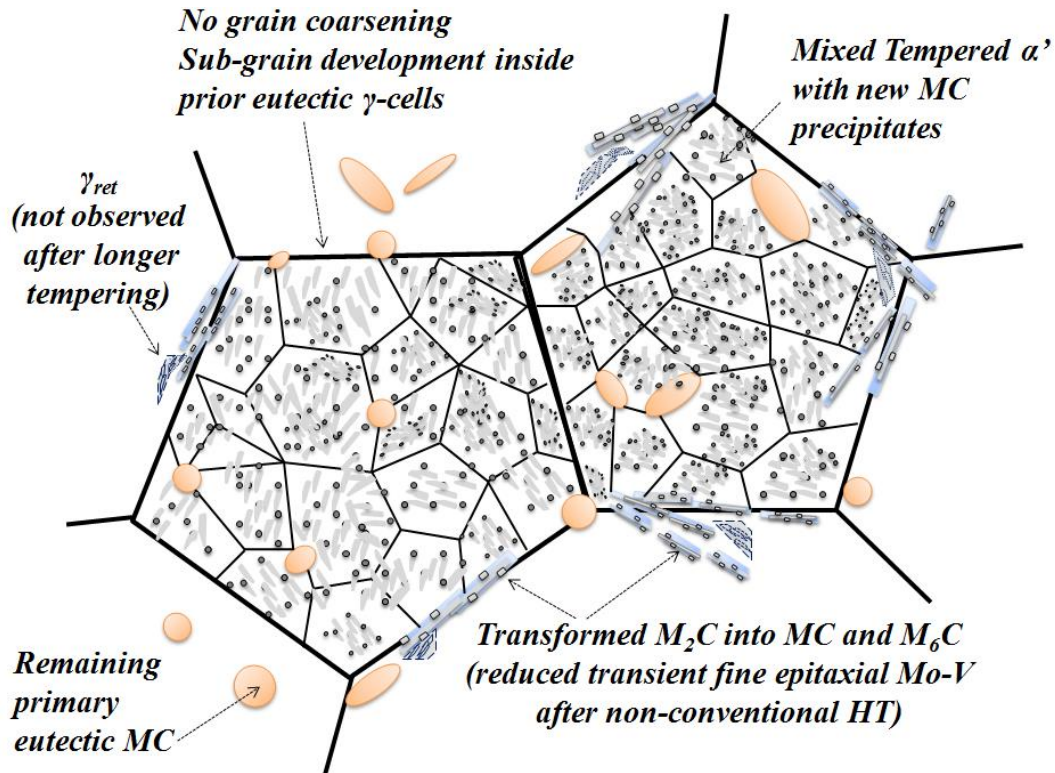


Figure 86. Generalization of the high temperature HT influence on the preliminary refined as-cast material

Thus, this observed solid-state transformational behavior causes several significant effects:

- 1) an increase of the matrix hardness during cooling from the HT, due to additional solid-solution from carbide dissolution;
- 2) the matrix becomes more tempering resistant due to the effect of the solid-solution;
- 3) secondary hardening from the formation of fine special alloy precipitates (*V-rich*), which compensate the loss of matrix hardness due to the tempering process;

- 4) higher tempering temperatures more efficiently transforms retained austenite;
- 5) The developed non-conventional HT modifies the interconnectivity of eutectic interdendritic carbide networks, increasing fracture toughness.

4.2.4 Proposed model of microstructural evolution in HSS material

In summary, the microstructural evolution after different processing steps (*as-cast* \rightarrow *preliminary HT* \rightarrow *hardening HT*) is schematically shown in Figure [83](#). In general, it can be seen that the austenite grains maintain their original size throughout, because the grain boundaries are not mobile enough as a result of the solute-rich concentration. The long martensitic plates are developed inside these grains, impinging each other, and are stopped by the boundaries. Hence, the as-cast structure initially has to be refined to promote rapid kinetic response during HT in order to develop fine microstructure required for improved mechanical properties. The preliminary HT, performed on the refined as-cast material, more efficiently homogenizes the matrix, pre-conditioning the interdendritic boundaries and slightly affecting the surface of eutectic carbides, making it rougher. Notice that the sub-grains within eutectic γ -cells can be developed after high temperature austenitization as a function of cooling rate from austenite region and uniformly dispersed eutectic and precipitated carbides, having a pinning effect on the grain boundary growth. These internal sub-grains enhance mechanical properties, for example, fracture toughness. This is another important reason, why eutectic carbides, which are controlled by solidification, and newly precipitated alloy carbides, coming from solid-state transformations, in particular, dissolution reactions, have to be present in sufficient amount and being uniformly distributed in the matrix. Eutectic interdendritic segregations are also modified after non-conventional HT, where more complete dissolution of M_2C and solute-rich boundary rims are observed, enriching the matrix

with the alloying content. Moreover, the boundaries became less interconnected, also improving fracture toughness.

The systematic detailed analysis of the precipitated carbides in the matrix for different HT conditions for the low and high carbon alloys can be summarized as follows, based on detailed and systematic microstructural characterizations along the HSS shells:

- 1) Secondary alloy carbides can be found in the as-cast condition as a result of solid-state transformations at moderate temperatures due to the slow cooling rates and excess carbon. For the high carbon alloy, these carbides are found to be of the type $(\text{Cr-Mo-V})_x\text{C}_y$, $(\text{Mo-Cr-V})_x\text{C}_y$, $(\text{Mo-V-Cr})_x\text{C}_y$; whereas for the low carbon alloy, the carbides are detected to be primarily $(\text{V-Mo-Cr})_x\text{C}_y$. For the high carbon case, the carbides are relatively coarse with irregular shapes, where the degree of coagulation is increased closer to the intermix region (*from the effects of bulk segregation and slow cooling*); for the low carbon case, the carbides are 1.5-2 times finer, have a higher surface energy and a more uniform distribution in the matrix.
- 2) Spheroidized alloy carbides can be found after the preliminary HT. For the case of high carbon content, the spheroidization is not uniform due to the local segregations. At the surface, a mixed, partially spheroidized structure is observed. Coarser spheroidized alloy carbides are found around the eutectic boundaries, at the same locations where the troostite pearlite was present. The degree of spheroidization and coagulation is higher closer to the intermix region, where the pearlite was mostly developed. For the low carbon case, homogenization was achieved. The rims of the solute-rich boundaries were dissolved; the fine and regular shape spheroidized alloy carbides were found in the matrix from surface to the bond line.

- 3) For the low carbon case, transient epitaxial carbides can be observed near eutectic boundaries after conventional austenitization HT, as a result of incomplete M_2C decomposition. At higher austenitization temperatures, these peanut-like carbides are completely dissolved. The dissolution behavior of interdendritic segregation for the high carbon case is more complex due to the presence of stable carbides formed after casting and preliminary HT steps highlighted above in 1) and 2). The mixture of irregular secondary alloy carbides, non-uniform spheroidized carbides, and partially dissolved products from M_2C , M_7C_3 were less likely affected by any sort of the HT.
- 4) For the low carbon material, the fine precipitation of the special alloy $(V-Cr-Mo)_x C_y$ carbides, having a size less than 200nm, can be observed after double and triple tempering HT (*Figure 85*). No coarsening of the structure is observed. The thermal stability is achieved, because of the enriched alloy content in the matrix after efficient dissolution and hardening HT.
- 5) At least, three types of V-rich carbides can be distinguished: eutectic (*from solidification*), decomposed from M_2C , and precipitated after tempering.

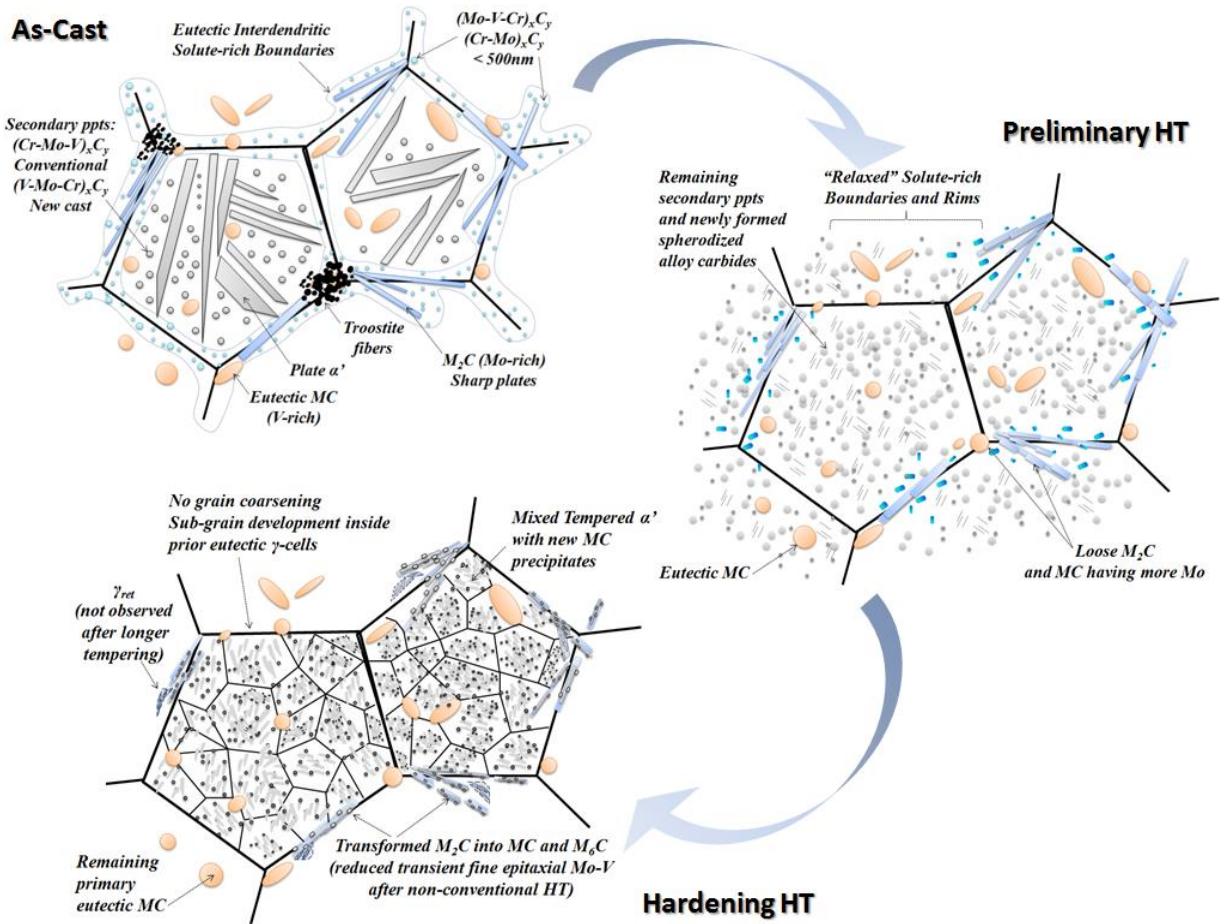


Figure 87. Microstructure evolution after different processing routes

The microstructural observations for each considered sample are summarized in Table 5, where samples ID, condition and descriptions are given.

Table 5. Summary of microstructural observations

#	ID	Condition	Observations
1	P0	Cast	Nonhomogeneous, coarse grains; troostite around M2C; eutectic MC, M2C (Mo), M7C3 (Cr); secondary M23C6 (Cr); M6C, M3C at intermix
2	P0	P	Nonhomogeneous spheroidized; high degree of secondary carbides coagulation and pearlite development closer to the intermix; coarse M3C; complex blocky V-rich carbides
3	P0	A	Plate martensite with fine epitaxial carbides; highly alloyed brittle boundary rims (retained austenite); partially decomposed M2C; mixed pearlite lamellas and coagulated secondary carbides remain closer to the intermix;

<i>Table 5 (continued)</i>			
			coarse M3C present and fish-bone like morphology remaining; connected networks of carbides; clusters of coral-like MC inside grains observed in the middle
4	P0	P+A	Less connected boundaries and relaxed rims; coarse spheroidized Cr-rich carbides remain after austenitization; tempered martensite plates and sub-grains developed; M7C3 decorate boundaries; coarse M6C; coarse blocky M3C along the boundaries
5	S0	P	Homogenized spheroidized matrix with epitaxial fine Mo-V carbides and decorated with sharp M2C plates along the boundaries; partially relaxed boundaries; rod-like and coral-like VC are found inside gamma cells and along the boundaries;
6	S0	A	Nonhomogeneous MC distribution with irregular morphologies, predominantly coral-like filling up the grains; plate martensite with internal segregations, containing secondary alloy ppts and partially dissolved epitaxial Mo-V carbides; pearlite and coarse M3C at the intermix
7	S02	P+A	More complete dissolution of M2C, but epitaxial carbides remain; more homogeneous matrix with mostly MC, some at the boundaries
8	S-shell	Cast, no core	Uniform cast with disconnected M2C, increased idiomorphic MC content with some radial fluctuations; rod-like MC can be found; some troostite at M2C; plate martensite with secondary ppts
9	BTK	Worn shell	Tempered plate martensite matrix with secondary ppts; retained austenite at the boundaries between MC and M6C from M2C transformed; rod-like and coral-like MC inside cells; some cracks along the brittle connected carbides; pearlite development from the boundaries, filling up the cells decorated with brittle M3C closer to intermix
10	HTC	Worn shell	High density of MC complex-regular, coral-like inside cells; coarse wide M2C; mixed pearlitic structure and spheroidization along the boundaries closer to the intermix; epitaxial fine carbides
11	CPC	Worn shell	Mixed petal-like (coarse) and coral-like VC (finer) in the matrix; M2C considerably dissolved and spheroidized along the boundaries; no transition between shell and core; clean matrix with fine ppts
12	SPH	P	Homogenized matrix and boundaries; fine uniform spheroidization ; loose M2C; fine structure, less interconnection
13	CA41	P+A+DT	High density of idiomorphic MC in the matrix and some at the boundaries; decomposed M2C with epitaxial around; tempered martensitic matrix with fine secondary ppts
14	P9DT	P+A+DT	Clean and homogenized matrix with fine MC-precipitation; refined prior grains and developed sub-grains; more complete dissolution of epitaxial products; idiomorphic and rod-like MC; retained gamma at the boundaries; fine secondary alloy ppts in the matrix
15	P9TT	P+A+TT	Reduced amount of Mo-carbides at the boundaries; retained gamma is almost not observed; more complete transformation to MC and M6C at the boundaries; stable boundary regions closer to the intermix- no pearlite development
<i>Note: Cast- centrifugal horizontal casting; P-preliminary HT; A-austenitization; DT-double tempering; TT-triple tempering; ppts-precipitation</i>			

In Table 6, the proposed microstructural evolution is summarized in terms of the eutectic γ -cell units. The atlas-like table contains generalized schematics with accompanying actual SEM micrographs, corresponding to the matrix and the boundaries for each particular case (*as-cast*, *preliminary HT and hardening HT*).

Table 6. General schematics of microstructure evolution in HSS shell during HT

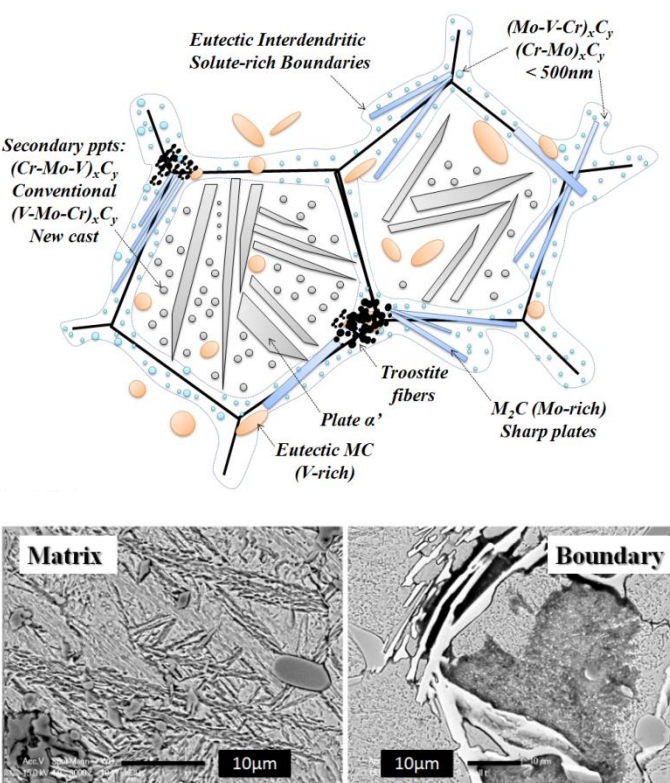
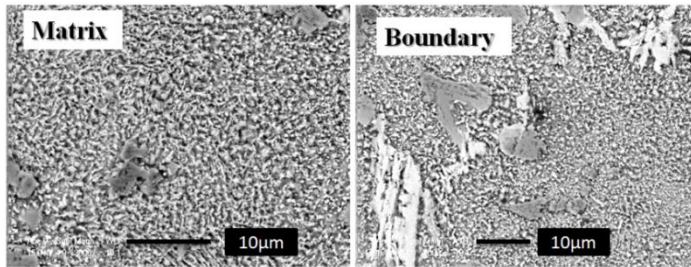
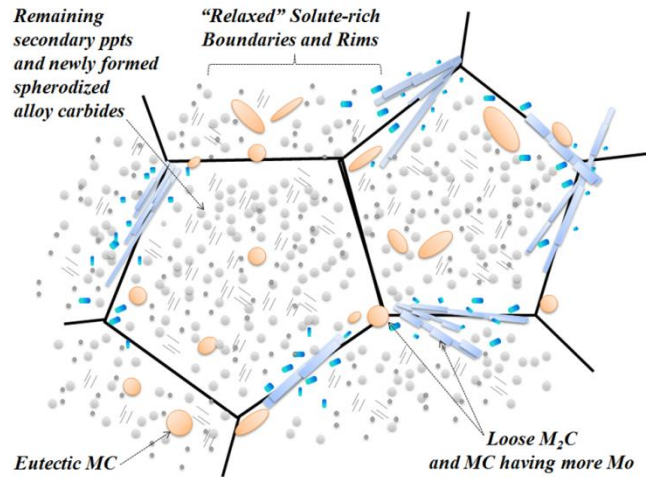
As-Cast	SCHEME 1
	<p>Matrix: tangled martensite (plate, lath)/bainite structure or coarse bainite as a function of solidification and cooling rates during solid phase transformation; plate martensite is stopped by prior dendrite boundaries; fine alloy secondary carbides $(Cr-Mo-V)_x C_y$ (conventional) and $(V-Mo-Cr)_x C_y$ (new cast) precipitated inside the dendrites. Idiomorphic and petal-like MC</p> <p>Prior boundaries: interdendritic Mo-V-Cr-C solute-rich; $<250nm (Cr-Mo)_x C_y$, and $<500nm, (Mo-V-Cr)_x C_y$, dispersed carbides; troostite pearlite (Cr-Mo rich) at eutectic M_2C; Mo-rich and eutectic idiomorphic MC-carbides.</p>

Table 6 (continued)

Preliminary HT

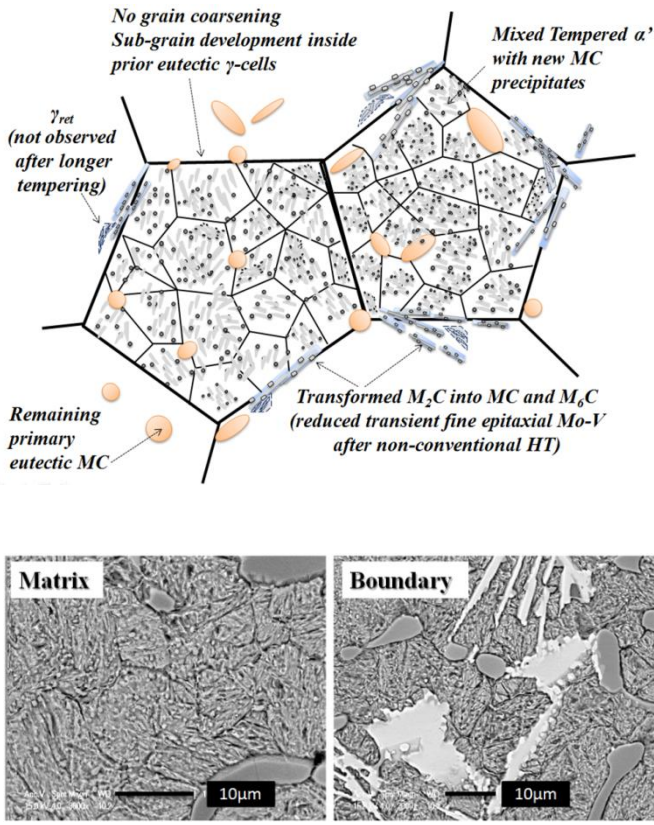


SCHEME 2

Matrix: uniform, homogenized spheroidite-fibrous-like soft structure (high surface energy) with uniformly dispersed remaining secondary precipitates $(V-Mo-Cr)_x C_y$ and newly formed spheroidized alloy carbides from martensitic matrix .

Prior boundaries: loose interdendritic alloyed zones with friable eutectic M_2C , Mo-rich and MC carbides containing more Mo.

Table 6 (continued)

After High Temperature Hardening HT	SCHEME 3
 <p>No grain coarsening Sub-grain development inside prior eutectic γ-cells</p> <p>Mixed Tempered α' with new MC precipitates</p> <p>γ_{ret} (not observed after longer tempering)</p> <p>Transformed M_2C into MC and M_6C (reduced transient fine epitaxial Mo-V after non-conventional HT)</p> <p>Remaining primary eutectic MC</p> <p>Matrix</p> <p>Boundary</p> <p>10μm</p> <p>10μm</p>	<p>Matrix: tempered lath martensitic with eutectic and <500nm precipitated carbides $(V-Mo-Cr)_x C_y$ due to high solute supersaturation; reduced retained austenite; sub-grain development as a function of cooling rate (martensite + possible fine bainite at moderate cooling) and alloy content effecting M_s. No prior grain coarsening</p> <p>Prior boundaries: transformed M_2C into M_6C and MC with transient epitaxial Mo-V peanut-like fine carbides in the vicinity of primary M_2C as a decomposition product (conventional) and dissolved after non-conventional Mo-rich zone and carbides are dissolved. Reduced residual austenite after longer tempering.</p>

Thus, the refined as-cast microstructure properly responded to the refined HT (*preliminary pre-conditioning of the matrix, high temperature austenitization and double tempering*) with adjusted soaking times, accelerated cooling paths and optimal dissolution temperature, facilitating the formation of relatively fine sub-grains and secondary alloy precipitation hardening. Figures [88a](#), [88b](#), [88e](#) compare the developed spin cast microstructure with advanced CPC (*continuously*

poured for cladding, Table 2) material, Figures [88c](#), [88d](#), [88f](#) respectively. It can be seen that the developed, as-cast product has a more refined structure with uniformly distributed fine eutectic carbides and interdendritic networks that are discontinuous, meaning that the solidification path is highly refined and the non-conventional HT alters the brittle boundaries, respectively. With regard to HT, the proper as-cast structure is a necessary precursor to facilitate proper microstructural evolution and optimization during subsequent final hardening. The eutectic cell size is almost the same in the final hardened product as in the cast state. With the new alternative HT, the eutectic interdendritic solute-rich networks are modified.

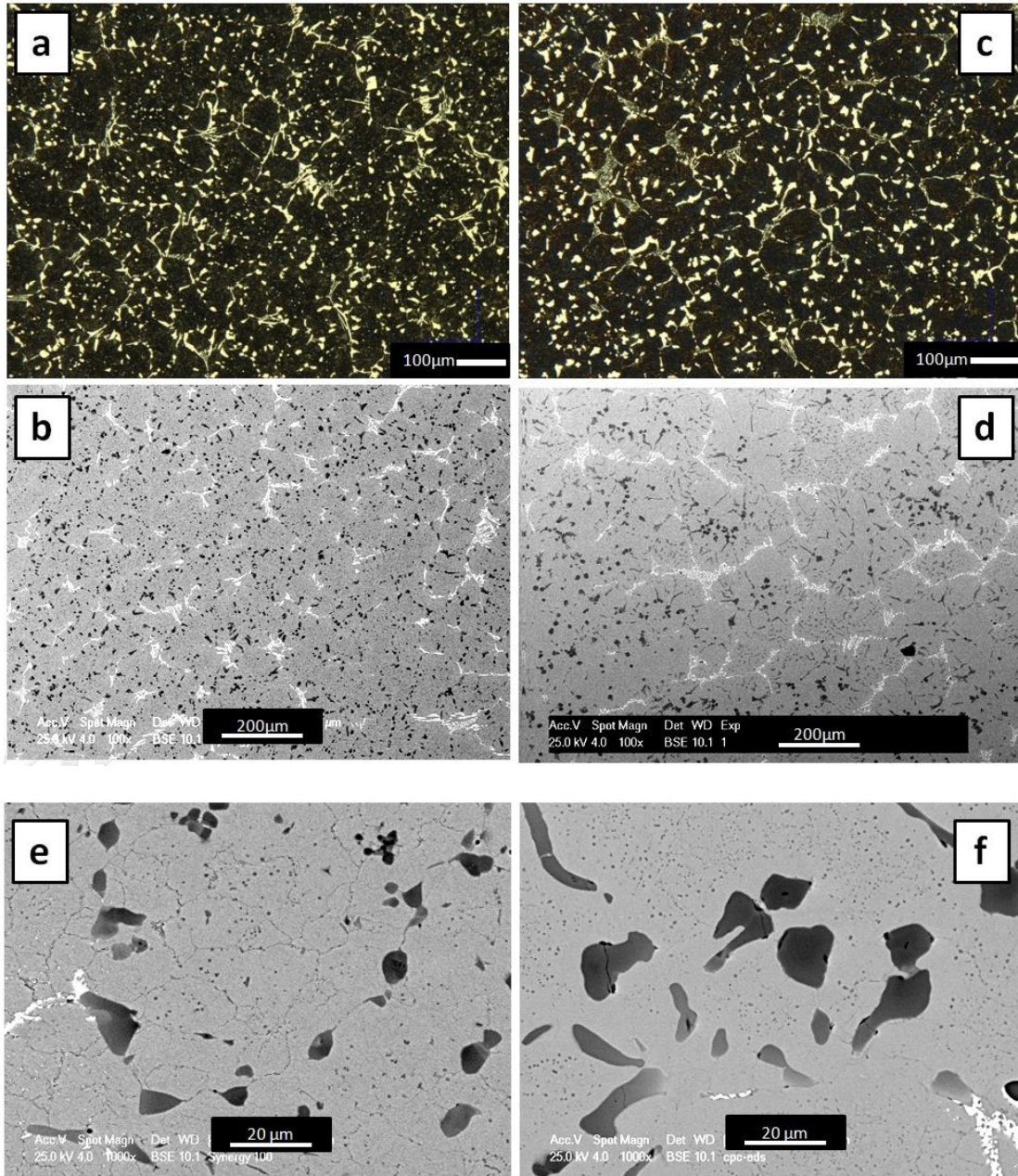


Figure 88. Non-Conventionally heat treated spun-cast HSS roll (a, b, e) versus CPC roll (c, d, f)

4.3 CFD APPROACH TO EXPLAIN CAST SEGREGATIONS

The results of the spin casting CFD simulation are shown in Figure [89](#), where the velocity vector field during the distribution of the melt inside the spinning mold is depicted for arbitrary $t_i \div t_n$ ($n > i$) time steps during the casting process. The orientation of the spinning liquid is shown by the dark arrows. The maximum volume of the cast occurs at a time t_n , hence, the shell tube is completely formed at that time (*two parallel red regions*). As can be seen, the turbulence of the spinning melt changes with time and location depending on the amount of the poured material and the “feeding-arm” (*inlet*) position and geometry. The concentric-like arrows on top (*Figure 89*) of each depicted time steps are showing more condensed local volumes in the forming shell tube along the longitudinal direction. It was also found that experimental alloys with different carbon concentration (*i.e. different heats, see properties in Section [3.5.1](#)*) propagate with different velocities inside the spinning mold, hence, the pouring and solidification processes take different time. For instance, the distribution of liquid for the conventional HSS material is relatively sluggish, which is attributed to higher viscosity associated with the original composition and casting process.

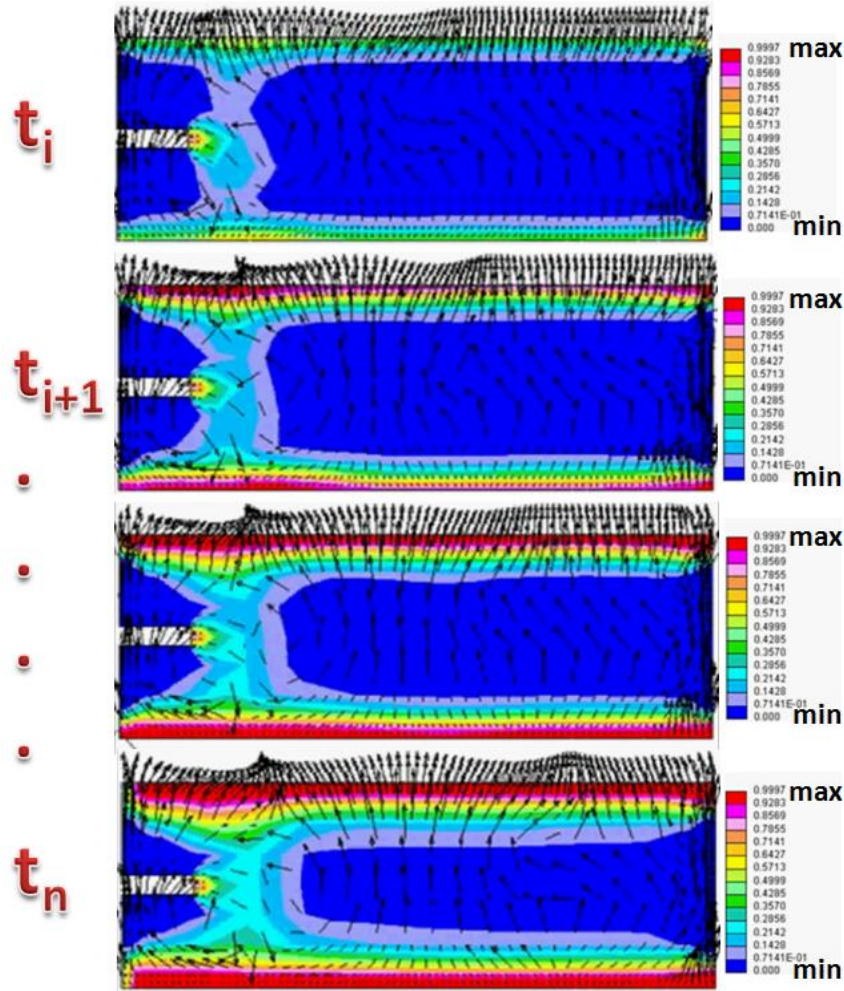


Figure 89. Velocity vector field distribution from 3-D CFD simulation of horizontal spin casting of the melt subjected to the centrifugal forces, [110]

Thus, preliminary 3-D CFD of the horizontal centrifugal casting process showed that local turbulences along the roll can take place depending on a position of the “feeding” arm, pouring rates and temperatures (Figure 89). The distribution of the melt inside the mold is directly related to the melt properties (*viscosity and diffusivity*), which are a function of temperature and alloy composition. It was concluded based on observed air circulation inside the molds that the air entrapped inside the chamber can facilitate a second solidification, which has a direction that goes from the inner to the outer diameter of the shell. In contrast, the main solidification front propagates

from the inner surface of the mold to the centre by the thermal conduction. These two opposing boundary conditions in the presence of the centrifugal field promote convective mixing of the melt and solid phase. The newly formed solidification fronts mix with each other: the higher density phases migrate to the outer shell, the lighter-to the inner. Hence, for the case of improper unidirectional casting control (*i.e., improper blend of pouring temperature, angular velocity, kinetics of precipitation, cooling rate and change in viscosity*), a mixed columnar and equiaxed structure is usually formed. Such a result leads to nonhomogeneous mechanical properties along the shell thickness. The eutectic segregation (*e.g. coarse columnar dendrites, coarse brittle interdendritic carbides*) can be observed in the middle of the HSS shell of the conventionally cast material. These are attributed to the complex local convective mixing and rejection of the residual solute-rich liquid during the imposed slow cooling. These results helped to understand the pouring process of the HSS melt and its influencing parameters.

Foremost, an improved alloy was designed. The carbon was adjusted to improve the liquid-phase viscous behavior and to shift the solidification to a higher temperature range. As a result, the dual-phase region (*liquid-solid*) was shrunk. The faster crystallization also creates a finer as-cast microstructure, which promotes rapid kinetic response during HT.

4.4 FINITE-ELEMENT MODELING

The transient thermal analysis was performed on several models (*see Section [3.5.2](#)*) to investigate various devised HT paths (*rapid heating and step-wise quenching-cooling*) taking into account time-varying boundary conditions and temperature-dependent material properties. The problem was highly nonlinear and required an iterative solution. The thermal load steps were specified,

reflecting the HT path, while the time step size was controlled with automatic refinement, depending on convergence criteria and ongoing calculated results.

This section covers results of thermal simulations on 1-D radial (*see Section [4.4.1](#)*), axisymmetric (*see Section [4.4.2](#)*) and coupled thermal-stress analysis of 3-D full-scale (*see Section [4.4.3](#)*) roll models. The results of nonlinear heat transfer through the microstructural point are discussed in Section [4.4.4](#).

4.4.1 Sub-structured 1-D radial thermal models

Figure [90](#) illustrates dynamics of the heat front propagation in radial 1-D 11-layers model from the surface of the roll through the core at different time steps, showing heating (*top 3 figures*) and cooling (*bottom 2 figures*) cycles in continuous HT.

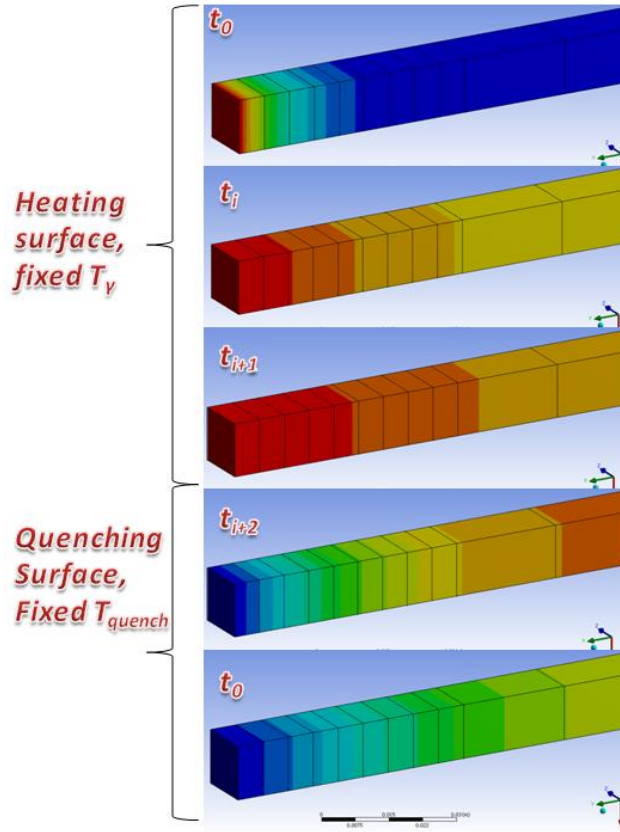


Figure 90. Example of transient FE analysis of heating and quenching cycles (each section in the shell 6mm)

The resulting temperature profiles, for both 3- and 11-layer 1-D radial models as a function of time, are shown in Figure 91 simultaneously. These plots (Figure 91) are corresponding to two theoretical BCs and one pyrometer surface reading (see Section 3.5.2). The CAD model (11-layers) is superimposed, relating surface, intermix and bonding locations to particular thermal plots. The thermal response at the bonding is shown with two lines (black-3-layer; blue-11 layer), so as at the intermix location (purple for 3-layer, brown-11-layer). Other two single lines (cyan-intermix; red-bonding of 3-layer model), coming from T_{i2} , correspond to Case III loading. The two lines, corresponding to applying the theoretical austenitization temperatures ($T_{\gamma 1}$ and $T_{\gamma 2}$) to the surface, are horizontal. Numerically speaking, the surface “gains this temperature

instantaneously”, because the temperature is assigned as BC, while the actual pyrometer line is increasing at the beginning of the heating.

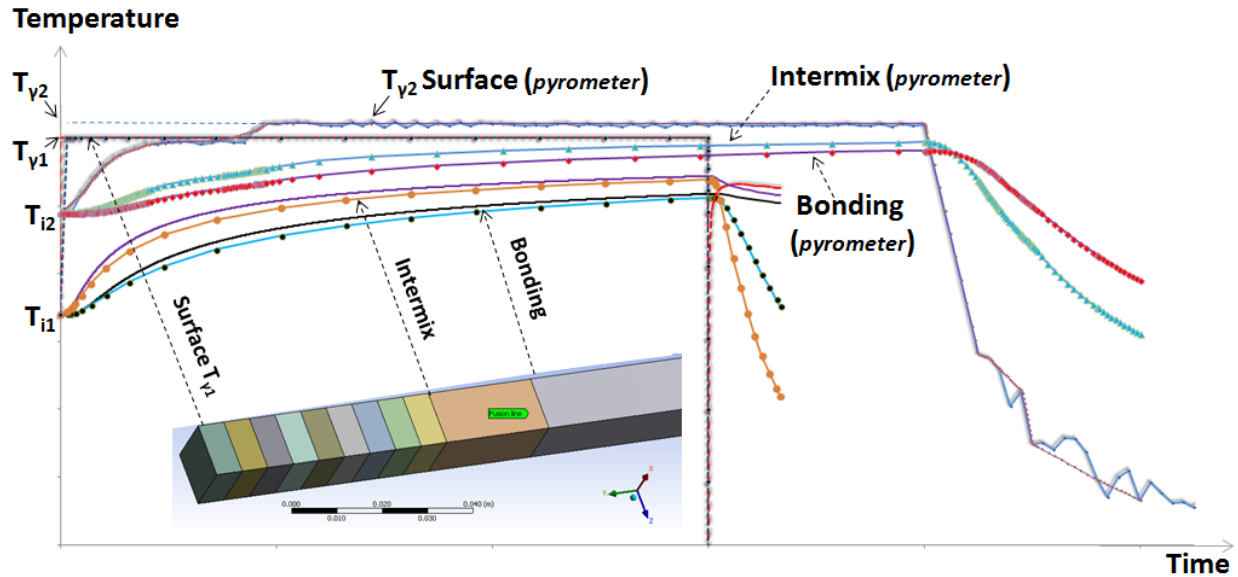


Figure 91. Predicted thermal profiles of 1-D models (3 vs. 11 layers): Case I ($T_{\gamma 1}$ - T_{i1}), Case II ($T_{\gamma 2}$ - T_{i2}) and Case 3 (pyrometer, $T_{\gamma 2}$ - T_{i2})

A direct implication of theoretical constant surface temperature enables one to predict the time necessary for the heat front to propagate to a particular depth, which is vital to know during the actual HT in order to avoid re-melting of the core. As can be seen, starting from two corresponding initial conditions, the temperature at the intermix and bonding increases during the heating. For both theoretical cases, the thermal profiles, corresponding to the 3-layer model are always slightly higher than for the 11-layer (*intermix and bonding locations*). It means that the heat transfer was different through the layers. A more homogenized model (*new as-cast material*), truly consisting of only of 3 layers, shows better response to HT. It requires less time to heat through the HSS shell, hence, consumes less energy. Therefore, going back to the spin casting

discussion, it is very important to have uniformly developed, as-cast microstructure, to provide stable thermo-physical properties. Another important observation concerning the HT itself suggests that if the pre-heating temperature is not sufficiently high, then it might lead to considerable temperature differences in the shell, like in the Case I, where the initial temperature is much lower than the design temperature. Consequently, high thermal gradients are created at the beginning of the HT, hence, increasing risk of thermal shock.

A closer look at the same results of Case I, pyrometer line and a critical temperature differences is given in Figure 92.

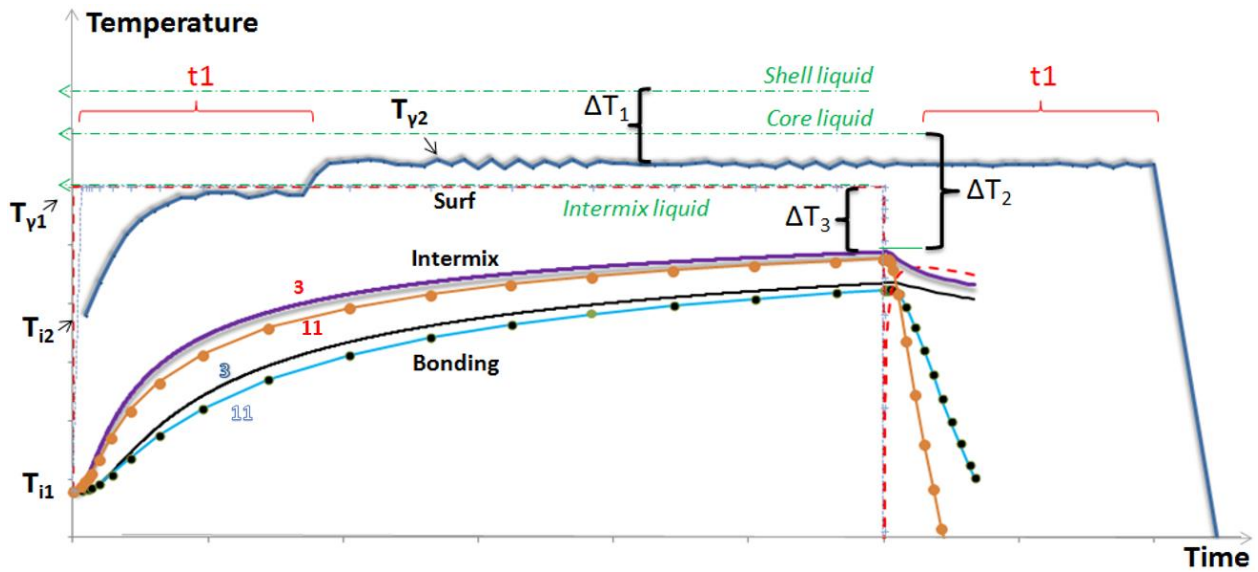


Figure 92. Comparison of 3 and 11-layers models ($T_{\gamma 1}$) with actual pyrometer readings ($T_{\gamma 2}$) vs. critical melting temperatures of individual layers

Each region (*surface, intermix, and core*) must remain below their respective melting temperatures. As it can be seen in the Figure 92, the surface temperature is limited by ΔT_1 , the intermix by ΔT_3 , and the bonding by ΔT_2 . These critical temperatures were also predicted using actual relevant chemical compositions for each location and thermodynamic analysis. A very

important insight learned from this result is that the temperature limitations of the HT would not only be from the core material, but more probably from the intermix and bonding regions, formed between the HSS shell and core.

The highlighted time interval “t1” in the pyrometer curve, shows the amount of time required to reach the desired soaking temperature. The total HT time should be adjusted accordingly.

Since the new as-cast material was much more uniform, it was eventually decided to consider only a 3-layer model. The resulting temperature curves from Case III with superimposed CAD model are shown in Figure 93, where actual pyrometer temperature data is applied to the surface of the model.

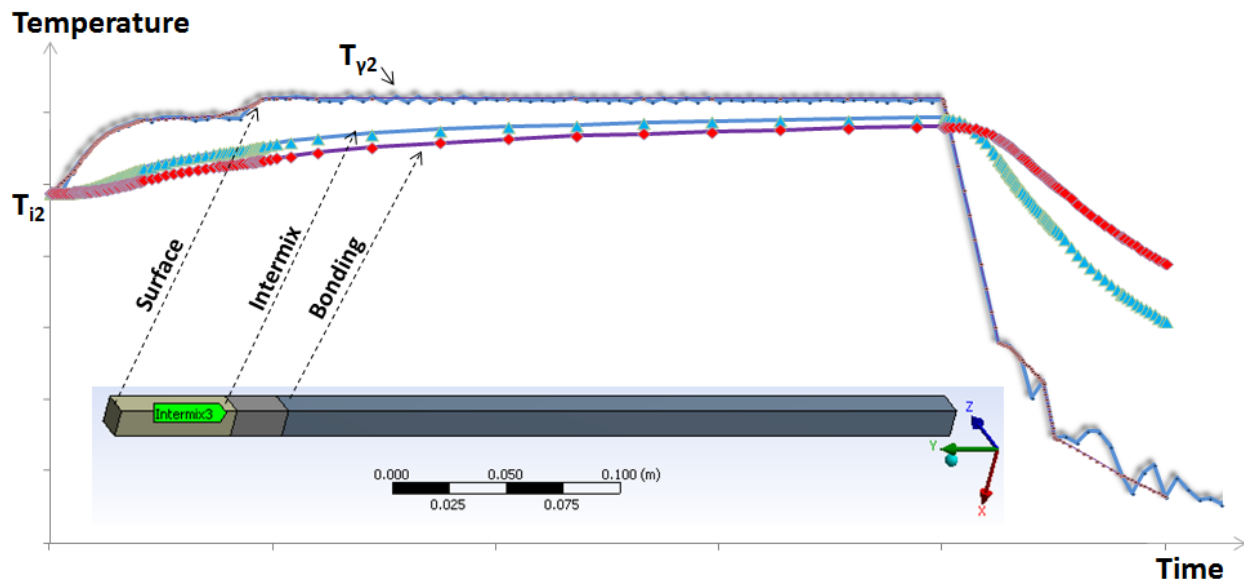


Figure 93. Pyrometer thermal loading (T_{y2}) at the surface and related response at the intermix and bonding

As can be seen in Figure 93, the temperature at the intermix and bonding almost reaches the surface temperature by the end of the HT. This is necessary to achieve the desired non-

conventional HT with the new as-cast material. The related temperature difference within layers is plotted in Figure 94 as a function time. The top red line corresponds to the complete shell thickness, i.e. between surface and bonding. The calculated thermal gradients in the layers are shown in Figure 95.

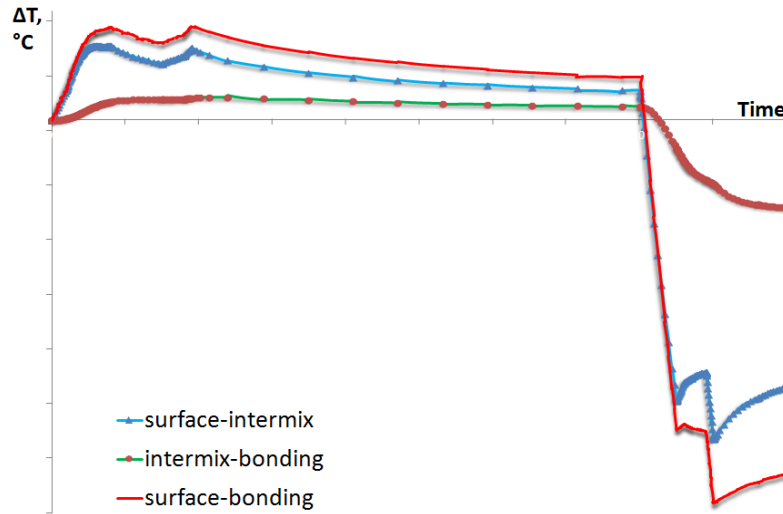


Figure 94. Temperature difference within layers

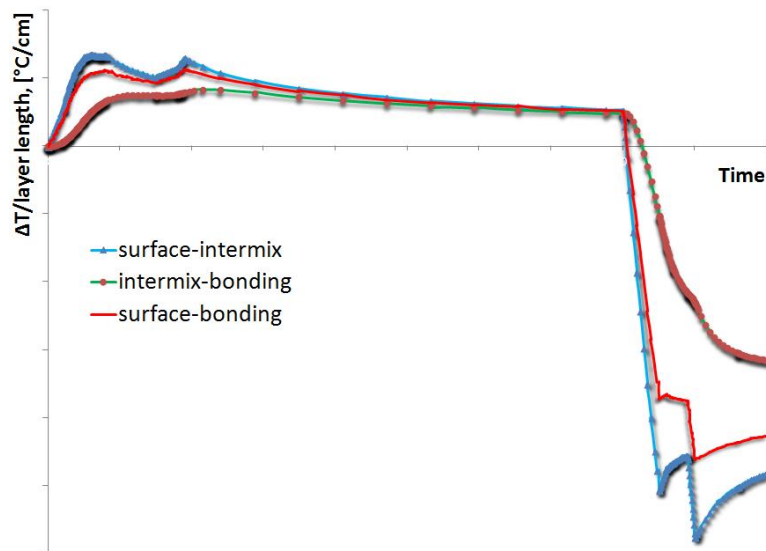


Figure 95. Predicted thermal gradients in the HSS layers

As expected the most severe thermal gradients are at the beginning of the heating and during quenching. Notably, the thermal gradient behavior is quite different in each individual layer. That is why based on the developed composite model, the thermal-stresses can be more accurately calculated for particular domains and compared with relevant high temperature mechanical properties, assessing the strength and structural integrity of the roll during HT.

4.4.2 Axisymmetric thermal model

Using the three developed homogenized domains (*shell*, *intermix*, and *core*) for the 1-D model and special BCs described in Section [3.5.2](#), the heat transfer analysis was also conducted for the axisymmetric and full-scale roll models. The resulting thermal profiles for an arbitrary time steps (t_i and t_{i+1}) are shown in Figure [96](#).

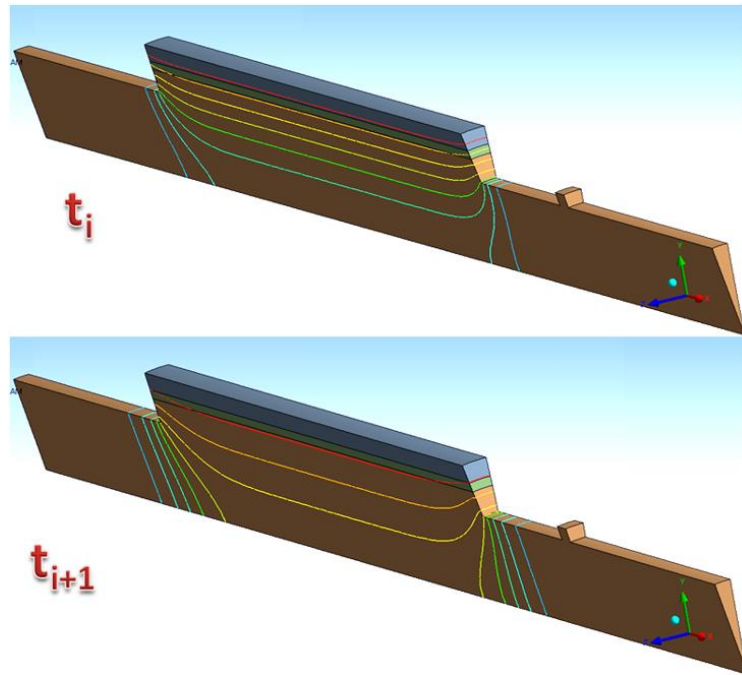


Figure 96. Isotherms at arbitrary times, showing heat front propagation

Applying additional convection BCs (*see Section 3.5.2*) at the journals and comparing to 1-D models (*Figure 97*) there was no considerable difference observed at the center of the roll. But the transition from the roll body to the journals (*or “roll necks”*), which can be considered as a “stress-concentrator”, experiences higher thermal gradient (*Figure 97, top*). It which can endanger the roll integrity at the edge, especially, at the interface between shell and core due to thermal stresses.

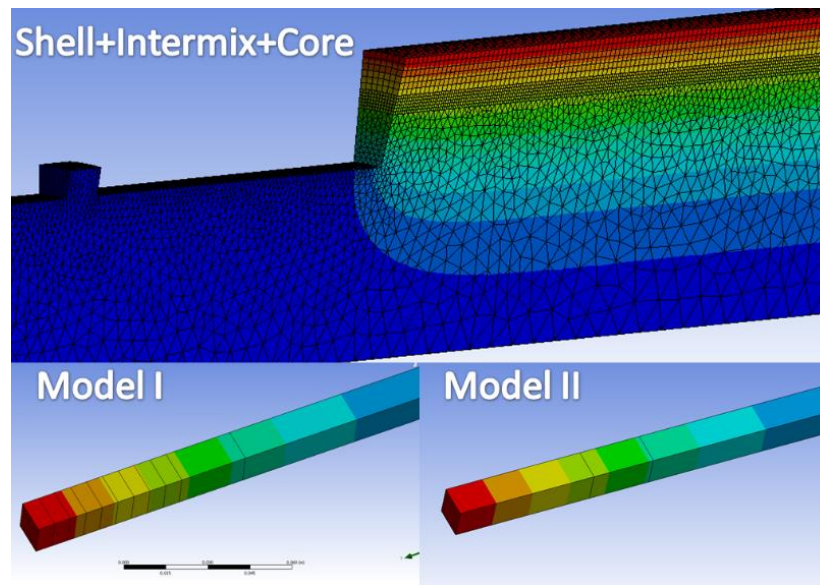


Figure 97. Comparison of axisymmetric and 3-, 11-layer 1-D radial models

4.4.3 Coupled thermal-structural analysis of the full-scale HSS roll

The developed FE thermal modelling with homogenized domains enabled one to compare theoretical and measured temperatures and relate them at critical times and penetration depths. It was concluded that during heating-cooling cycles with residual heat from prior HT steps (*initial conditions, pre-heating*), a considerable amount of thermal gradient is generated. That is why the

thermal-stress analysis is required for the whole roll body. Figure 98 shows predicted thermal fields in the full roll body, which were eventually used for the coupled thermal-stress analysis.

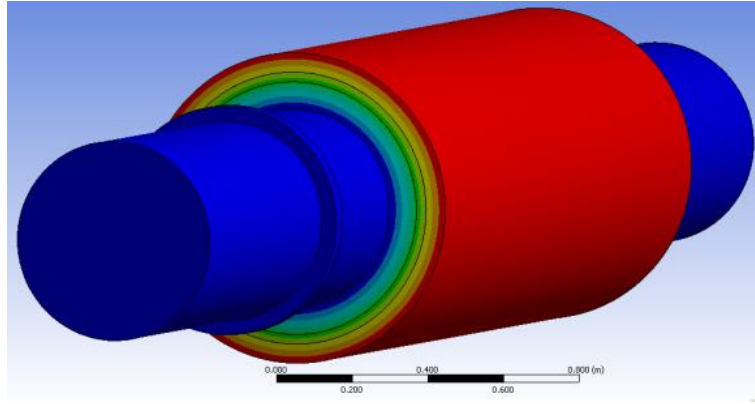


Figure 98. Thermal profiles in (a) axisymmetric model compared with 1-D cases, (b) full-scale roll model

The calculated temperature distribution as a function of time during heating and cooling was used to predict the thermal stress-strains. The resulting thermally induced von-Mises stresses in the roll body and composite shell are shown in Figure 99 (*top and bottom*). It was found that some thermal gradient states (*e.g., transition from heating to quenching*) can cause the HSS shell to be more stressed at the external and internal sides simultaneously, while the thermal stress in the middle is minimal (*Figure 99, cyan line, right bottom*). The highest stresses were found at the necks of the roll as expected.

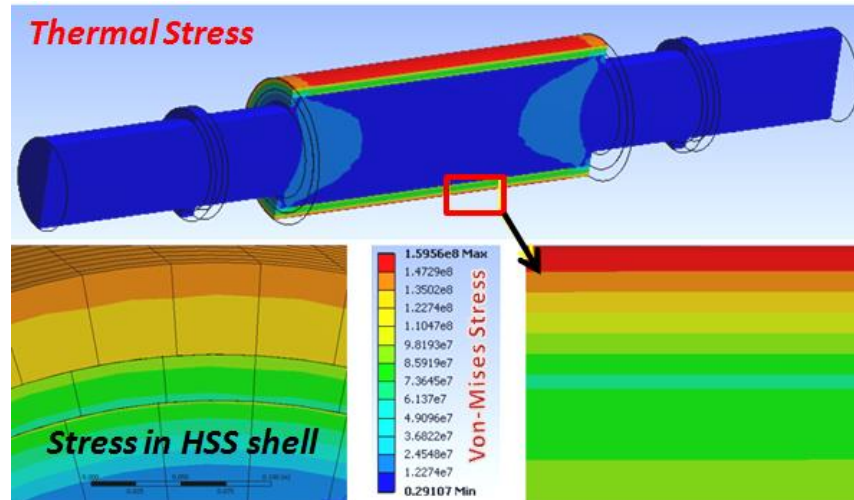


Figure 99. Predicted thermal-stresses due to thermal gradients

The calculated thermal strains and stresses profiles in the full-scale roll model are given in Figures [100](#) and [101](#), respectively, and compared with superimposed HT temperature profile (*red-dot line*).

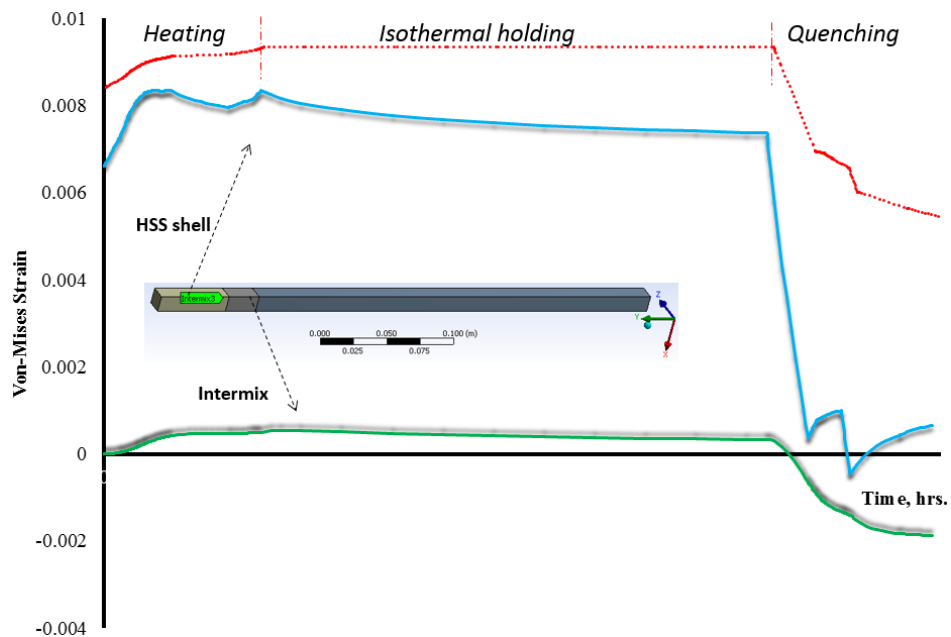


Figure 100. Resulting thermal strains in the HSS shell and intermediate layer

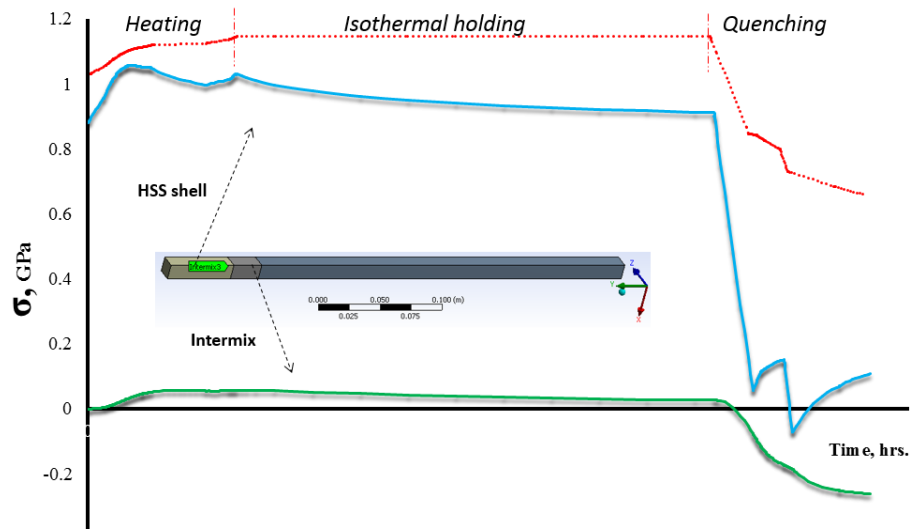


Figure 101. Resulting thermal stresses in the HSS shell and intermediate layer

As expected the highest thermal stress-strain conditions were found to be during heating and quenching (*Figures 100, 101*). The evolution of thermal stresses during the HT simulation was compared to the predicted mechanical properties at relevant temperatures given in *Figure 102*, and actual shear tests performed on radial samples (*surface, bonding, and core*) at RT.

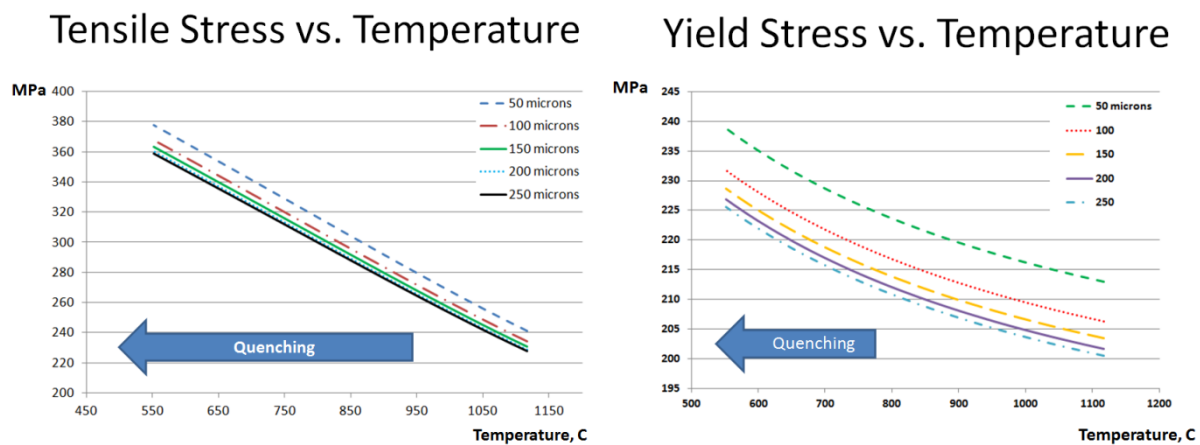


Figure 102. Predicted mechanical properties of HSS shell during quenching as a function of the grain size

In general, the stress-strain development at the roll center can be compared to the predicted thermal gradients in the HSS shell for 1-D model. The shell experiences considerably higher stresses than the intermediate layer. But bearing in mind lower strength of the intermix and bonding, the predicted stresses can be critical to these regions. It was recommended to do the pre-heating at higher temperatures before austenitization in order to avoid a thermal shock or/and exceeding stresses and strains. The quenching is also recommended to be less “aggressive” due to the same safety reasons, keeping in mind that the hard phase microstructure can still be formed, because developed material has a high hardenability. Secondly, the grain coarsening will not be expected due to remaining solute-rich prior austenite grain boundaries even after high temperature HT.

In conclusion, based on these results, a series of special recommendations were made regarding the initial conditions (*pre-heating*) and quenching regimes of the roll, where maximum thermal gradients are being developed, which potentially could lead to relatively high thermal stress-strain conditions. The holding time was also adjusted with respect to applied HT, preventing de-bonding and re-melting. Hence, the new non-conventional HT was developed in order to achieve the proper microstructural properties and maintain structural integrity of the HSS roll. The actual details of the HT and associated improvements are considered proprietary and cannot be discussed.

4.4.4 Micro-scale heat transport

Figure [103](#) displays an example of meso-scale heat transport analysis, where a part of the as-cast microstructure (*Figure 103a*) is divided into finite elements (*Figure 103b*) and time-varying boundary conditions are applied, simulating heating (*Figure 103c*) and cooling cycles (*Figure*

[103d](#)). In the model, there are three main isotropic, homogenized constituents considered: 1) martensitic matrix (*bright grey*), 2) eutectic MC carbides, V-rich, in petal-like and idiomorphic morphologies (*dark grey*), and 3) M_2C , Mo-rich, eutectic interdendritic carbide networks (*white*). It is found that the heat flux advances faster through the Mo-rich zones than the main propagating heat front. In contrast, during quenching the heat dissipation is being retarded in the same Mo-rich regions. Such response is attributed to the higher thermal conductivity and lower heat capacity of Mo-regions, respectively, in comparison with V-rich carbides and the surrounding matrix. Advancing or retreating heat fluxes are highlighted with the curved dash lines, and the temperature gradient fronts are shown with vertical dashed lines. For the heating cycle, the total heat flux is higher at the Mo-carbide-matrix interface and moreover, it propagates within Mo-rich zones faster than the heating front itself. During the quenching cycle, it is noted that there is a residual heat flux concentrated at separated Mo-rich areas behind the cooling front. This transient analysis resembles the observed partial M_2C decomposition, which starts at the carbide-matrix interface (*Figure [103e](#), before HT and Figure [103f](#), after HT*) and reflects the possible sequence of transformations. The temperature distribution can be calculated in millisecond intervals, enabling one to register minor changes in the system related to nonlinear material behavior.

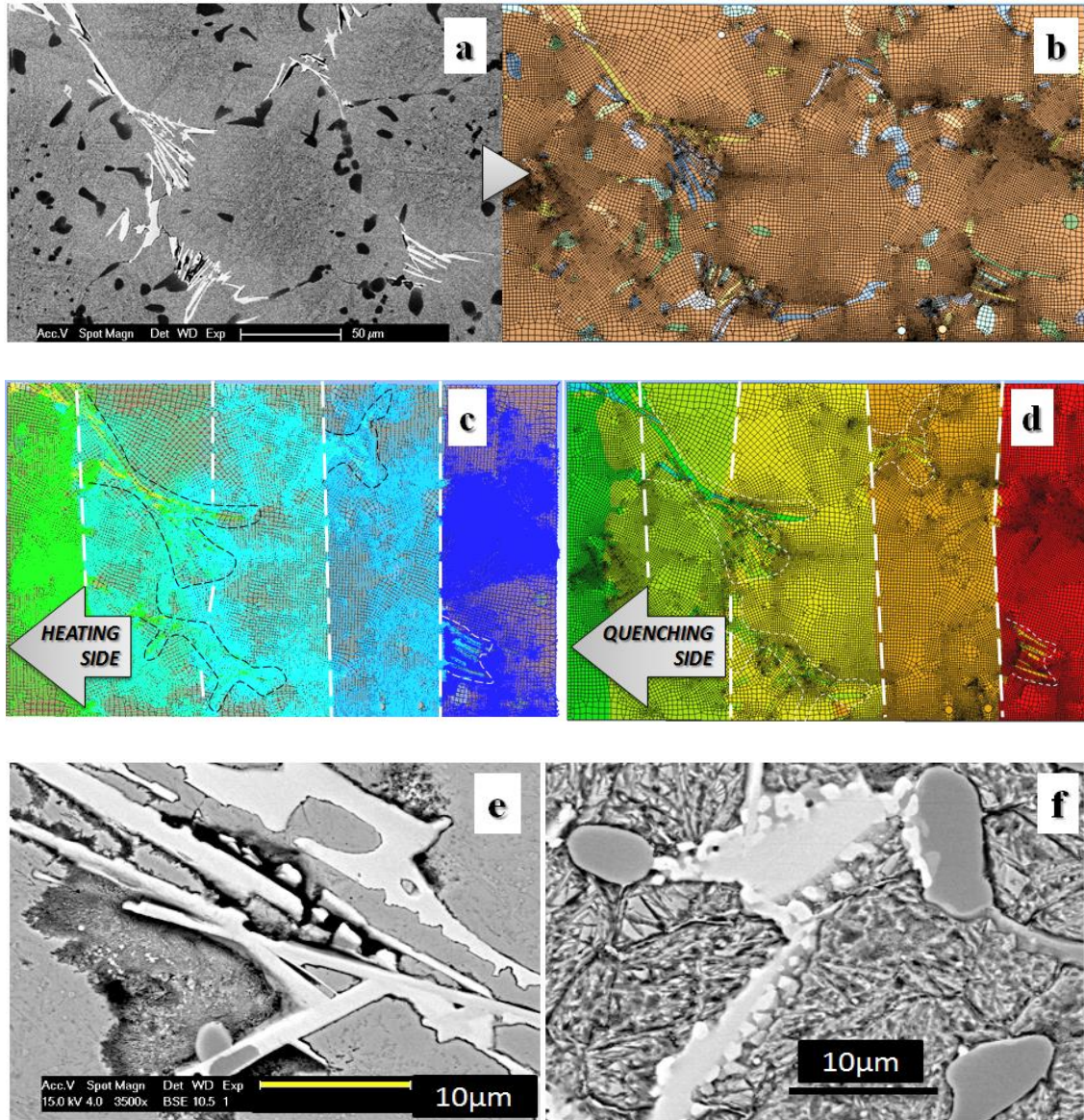


Figure 103. Example of nonlinear FE micro-scale heat transport simulation and its comparison with resulting microstructure: (a) SEM image of the as-cast microstructure; (b) meshed FE model of actual SEM image given in (a) ; (c) predicted total heat flux developed during heating cycle (heat flow- from left to right, vertical dash lines are the propagating heat front, the curved dash lines are the advancing flux at the Mo-rich boundaries); (d) directional heat flux (horizontal axes, negative direction, from right to left) due to quenching the left edge (vertical dash lines are the propagating heat flux (negative direction); curved lines are the residual retarded flux in the Mo-rich zones, leaving the cool front behind); (e) zoomed as-cast Mo-rich eutectic interdendritic carbides with troostite pearlite (dark area) as in (a); (f) resulting decomposed M_2C into M_6C and MC after high temperature hardening (after (c), (d) HT).

The next two post-processing Schemes III and IV are given in Figures [104](#) and [105](#), respectively, regarding actual microscopic observations. As it was shown, the maximum heat flux is found to be at the carbide (M_2C) -matrix interface, facilitating local microstructural transformations. The same type of solid-state reaction is observed in real life, where M_2C is the first eutectic to decompose into MC and M_6C (bottom part of Figure [104](#)). Figure [104](#) shows a direct comparison between total heat flux behavior from the thermal micro-scale model and resulted microstructure after the same HT (conventional case). The top of the image relates the remaining, i.e. partially decomposed, interdendritic segregation enriched with Mo, to the total heat flux propagating through such areas, predicted with FEM. The bottom portion of this image shows the same zoomed local situation, proving the assumption of increased localized heat transfer at the carbide-matrix interface. The simulated heat flux is compared to undissolved complex M_2C carbide, possibly due to insufficient heat penetration and/or soaking times.

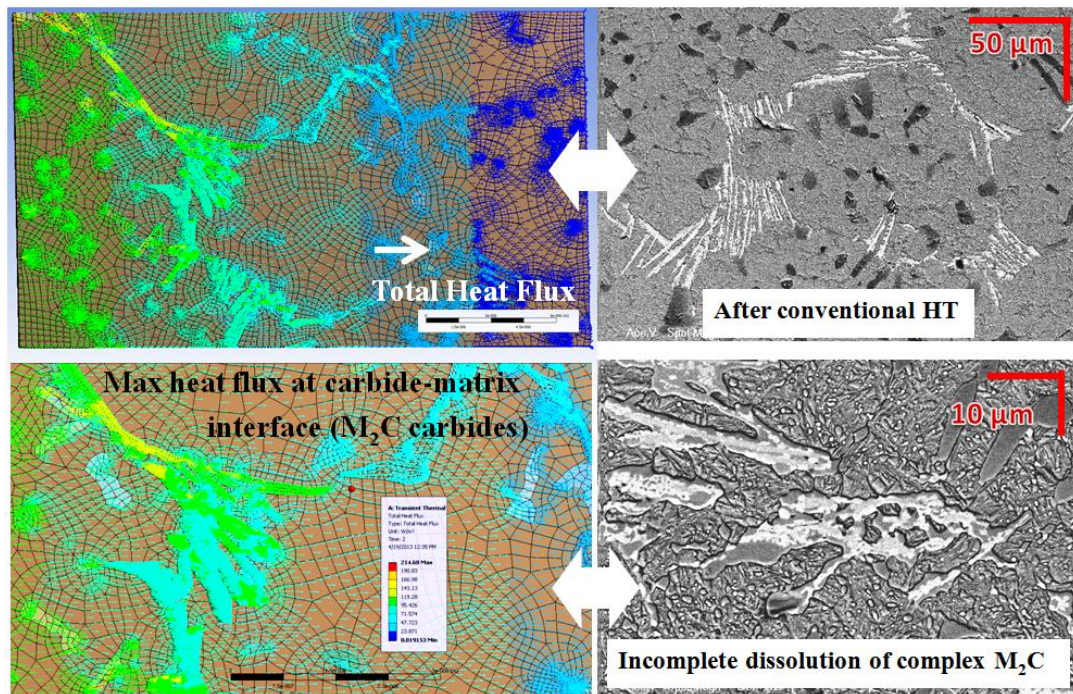


Figure 104. Scheme III: comparison of simulated heat fluxes and conventional hardened microstructure

The supplemental Scheme IV in Figure 105 is basically SEM/EDS analysis provided to the micro-scale FEM post-analysis, which helped to explain and relate the predicted and observed incomplete carbide decomposition during conventional HT. It shows detailed microscopic observations of the transient epitaxial products that originated near the same segregations, which are more likely to form from incomplete decomposition of M_2C and due to delayed heat extraction from the system and from the solid-state transformations, predicted with developed micro-scale FE model. This observation is very important from the point of carbide dissolution behavior and precipitation sequence, which is explained and visualized for the first time in this way for particular HSS alloy based on comparison with meso-scale heat transfer. In real life, developing such thermal fields during milliseconds between microconstituents with changing individual material properties as a function of temperature will not be physically possible to capture or measure. Moreover, the new non-conventional HT approach is designed in such a way that takes into consideration the above mentioned observations, which enables time to sufficiently dissolve the transient epitaxial products, enriching the matrix with alloy content, therefore, improving mechanical characteristics of the HSS shell.

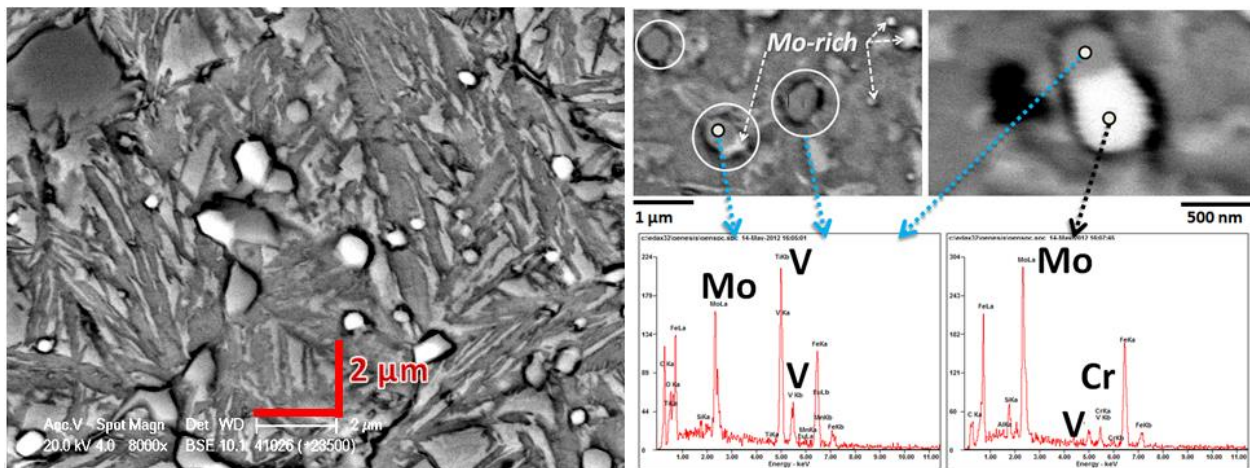


Figure 105. Scheme IV: detailed microscopic observations, validating the micro-scale FE simulation

In conclusion, the proposed microstructural model offers an alternative applied way to analyze micro-scale thermal behavior of micro-constituents and the surrounding matrix, using a basic set of thermal characteristics, in contrast with the traditional view, where phase transformations are characterized by surface energy, morphology of the particles, Gibbs free energy of formation, diffusion, dissolution kinetics, and others. The predicted micro-scale heat transfer behavior reveals and explains observed microstructural transformations: incomplete carbides dissolution and precipitation sequence. The developed micro-scale heat transfer model is based on thermo-processing data and microstructural observations. It was used in the development of the new non-conventional HT.

4.5 EXPERIMENTAL CHARACTERIZATION

The current chapter covers X-ray diffraction analysis performed at room and elevated temperatures (*see Section [4.5.1](#)*); bulk and microhardness analysis of the considered material (*Table [2](#)*), including individual matrix measurements (*see Section [4.5.2](#)*); and image processing combined with phase balance analysis (*see Section [4.5.3](#)*).

4.5.1 Ambient and in-situ high temperature X-Ray diffraction analysis

With the aid of XRD, the crystal structure of the HSS shell materials was studied through the analysis of the following factors: 1) influence of the casting segregations in the composite shell; 2) the role of different conditions (*as-cast; preliminary HT; austenitization; combination of preliminary HT and austenitization. Note: after austenitization the tempering was done*); 3) the

compositional effect (*low vs. high carbon*); 4) type of casting method (*horizontal spin casting and continuous pouring for cladding*); 5) in-situ phase transformations in laboratory conditions and related oxide formations up to 1200°C. The volume fractions of individual phases and carbides are calculated based on the area under the scanned XRD profiles. Peak intensities, curve shifts and broadening are considered to be less affected by experimental error as compared to the actual phase transformation phenomena.

Figure 106 shows an example of the XRD results for the three locations for the BTK material. The additional intensity peaks indicated in Figure 106, corresponding to the intermix region (Loc3) plot, are related to the formation of M_3C carbides due to the back diffusion from the core (*higher carbon content*).

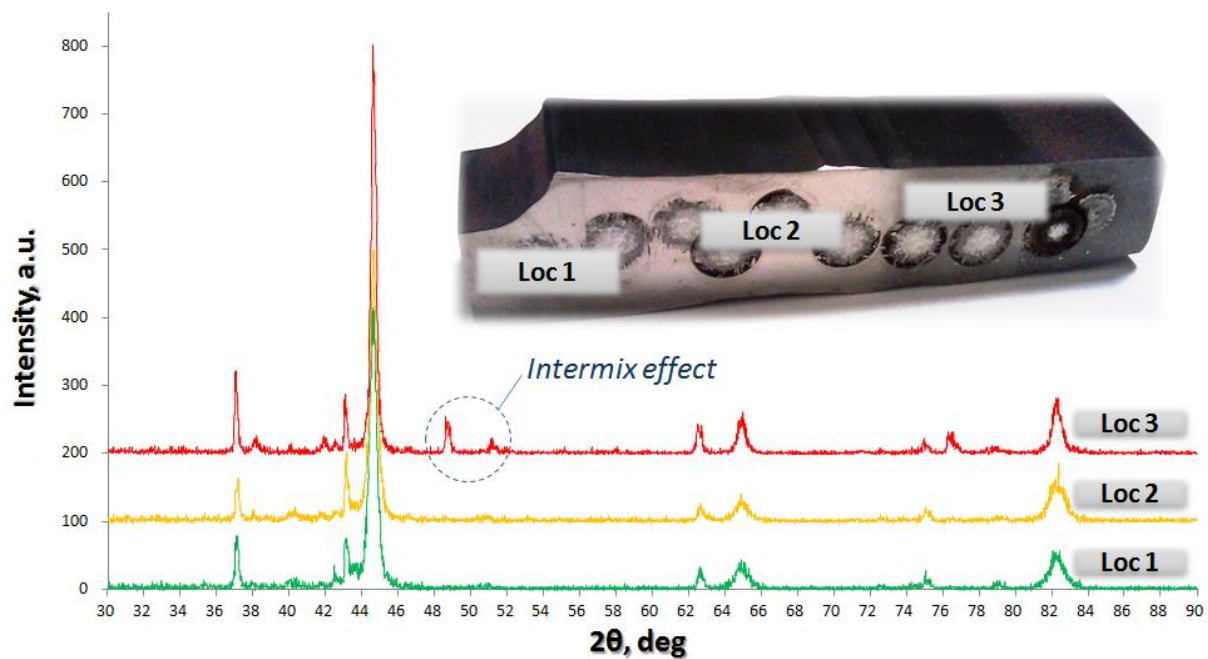


Figure 106. Example of conventional XRD profiles for different locations in HSS shell (BTK): surface (Loc1), middle (Loc2) and bonding (Loc3)

The effects of different HTs on the crystal structure of HSS materials were investigated and summarized in Figure 107, which corresponds to the surface location.

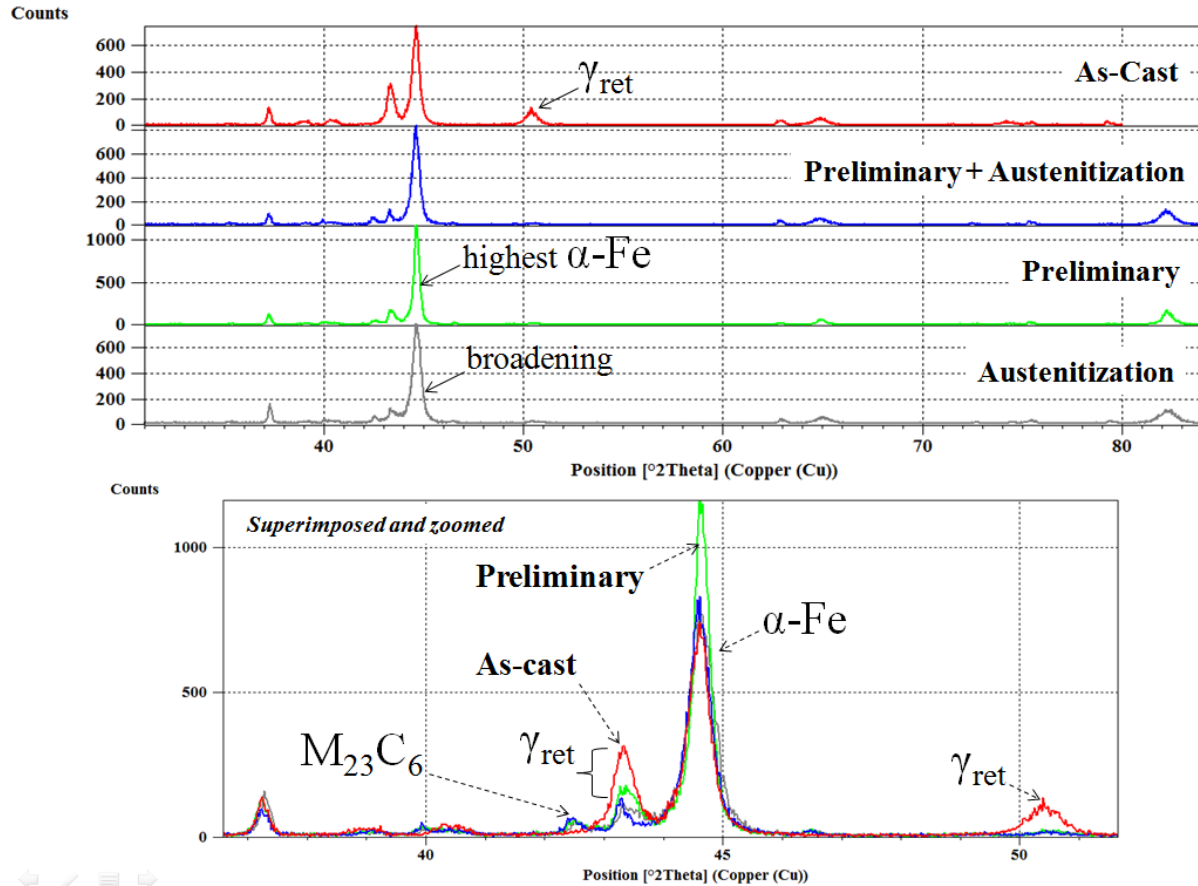


Figure 107. HT effect on crystal structure of high carbon P0 HSS shell: as-cast, combined preliminary and austenitization, individual preliminary and austenitization conditions

From Figure 107 it can be seen on the zoomed image at the bottom that the as-cast P0 structure contains significant amount of retained austenite (γ_{ret} : 20-25%), which is reduced by approximately 50-60% after preliminary HT (*green profile*); whereas the alpha-iron peak is increased in this case. The effects of preliminary HT can be explained by observed total spheroidization in a homogenized ferrite matrix. The retained austenite amount reduces further to

4-10%, depending on a location in the shell, after adding the austenitization HT on as-cast or combined with preliminary HT. No significant difference is seen in intensity amplitudes between the austenitization and combined HT scenario. The only distinction is that the peaks are slightly broader in the case of direct austenitization on as-cast condition, which is related to residual crystalline distortion and high density dislocation structures. For instance, the peak of α -iron after the austenitization HT is slightly broader and shifted (*grey profile in Figure [107](#)*), meaning that the phase has higher dislocation density, i.e. more strain is induced. It explains the difference between HTs with and without preliminary HT (*or soft annealing*). In other words, direct application of an austenitization HT for as-cast structure produces a more brittle material, which is not favorable for fracture toughness requirements. Especially, keeping in mind that in this case, the strength was not affected significantly, this is shown by hardness measurements in Section [4.5.2](#).

Similar crystalline behavior was observed for the middle point in the HSS shell and next to the bond line, except the intensity of the α -iron peak is increased closer to intermix by 1.5-2 times. At the same time, the amount of retained austenite and eutectic carbides is decreased gradually toward the bonding region, i.e. closer to the fusion line.

Also in Figure [107](#) (*bottom portion*) a new peaks corresponding to secondary alloy carbides, $M_{23}C_6$ ($Cr_{21}Mo_2C_6$), appear as a result of transforming retained austenite after HTs. The peak's intensity of $M_{23}C_6$ is at the same level after both: austenitizing and combined HT cases; whereas it is slightly higher and broader after only preliminary HT. This XRD data corresponds to observed related microstructures, where, for example, the preliminary heat treated material contained considerable amount of spherical carbides precipitated from the matrix.

Speaking of the compositional influence on crystal structure, the main observed effect of combined lower carbon content and higher austenitization on XRD patterns is that the peaks, corresponding to secondary Cr-rich carbides (M_7C_3), observed in the conventional material after standard heat treating practice, are minimized or not evident, confirming the assumption of the critical carbide's dissolution behavior. The more uniform the chromium is distributed, the more uniform oxidation layer builds up especially at the carbide-matrix interface, therefore, improving thermal barrier and wear behavior. Additionally, the MC-type carbide's peak is 1.7 times higher for the improved as-cast case (*refined as-cast microstructure*).

The resulting in-situ high temperature XRD scanning plots with respect to particular temperatures were compared and shown in Figure [108](#) for low (*S-shell*) and high carbon (*P0-as-cast*) materials.

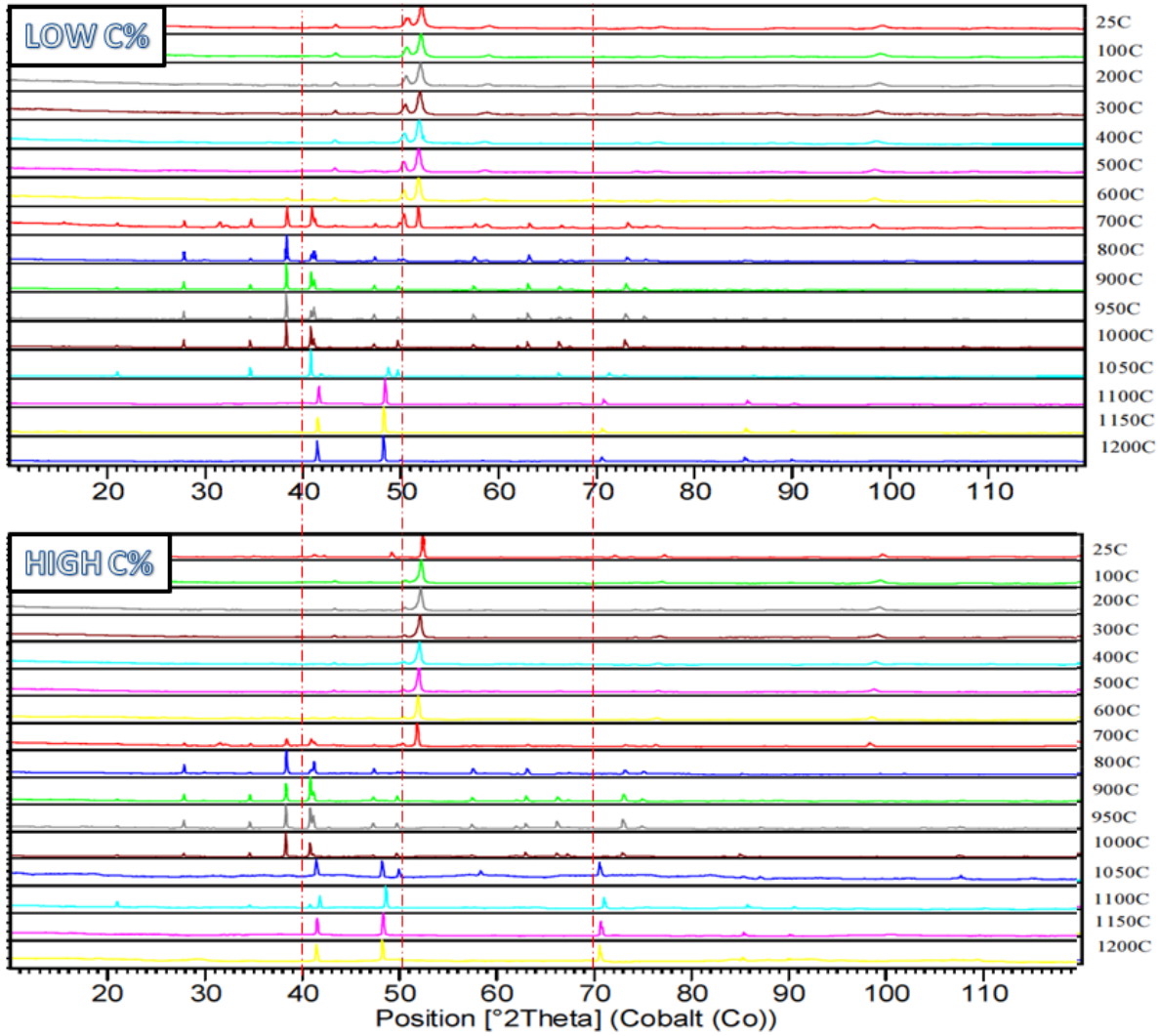


Figure 108. In-situ HT-XRD diffractograms for as-cast P0 and S-shell materials (high vs. low %C)

There are three main distinguishable temperature intervals, corresponding to structural transformations and related oxide's formations: 1) 25-700°C (*lattice expansion, Figure 109; first oxides formation at 500°C*); 2) 700-1000°C ($\alpha \rightarrow \gamma$, *austenite rearrangements, intensive oxide growth*); 3) 1000-1200°C (*austenite and MC region, oxide composite formed*). In spite of the noise and peaks coming from the oxidation, in general, it can be concluded that two considered alloys behave similarly regarding the main phase transformations, which correspond to predicted phase equilibrium diagrams (*see Section 4.1*).

Example of lattice expansion behavior in S-shell samples up to 500°C (*before significant oxidation*) is shown in Figure 109. It is seen, that the intensity peaks are growing and shifting to the left as temperature is increased, as a result of the increasing non-uniform thermal strains. The micro-strains of individual phases could be calculated, using d-spacing measurements, but it was not part of this work.

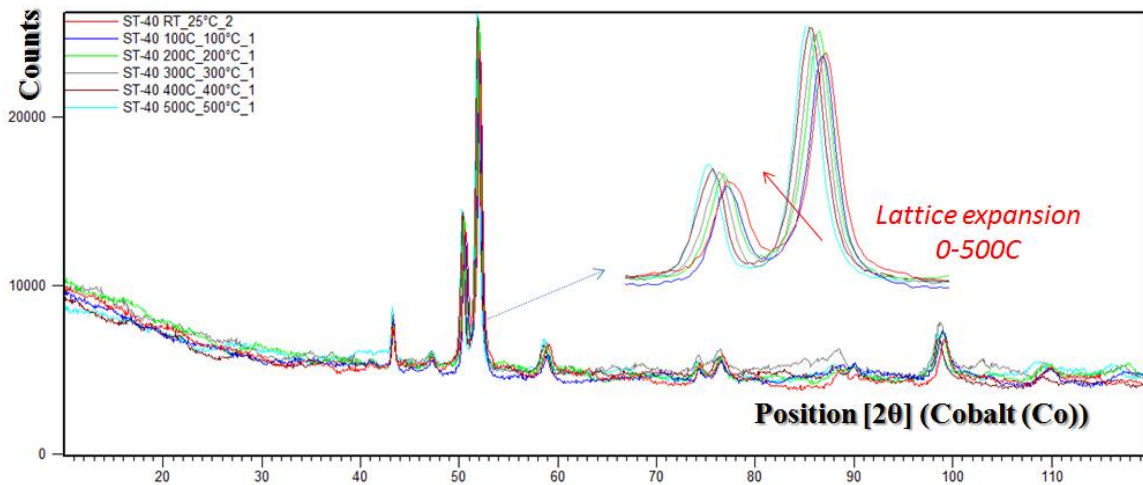


Figure 109. Example of lattice expansion behavior

The summary of detected oxides in laboratory conditions as a function of temperature is given in Table 7. This was not reported before for the particular alloy composition and temperature range. The registered oxide peaks confirm the complex composite oxides formation as a function of temperature and related microstructure at a given time. The rate-dependent oxidation is affected by the local equilibrium between the oxide layers and the material, which experiences phase changes that have to be taken into account for the actual in-service performance. If the HSS material is thermally stable, then only oxides indicated are formed in the same service environment, and the rolls' oxidation behavior is predicted and controlled. Thus, the quality of the rolled material would depend on current microstructure, co-existing with developed oxides.

Table 7. Detected oxides vs. temperature

Temperature, °C	Compound Name	Chemical Formula
500	Chromium Oxide (1/1.01)	Cr ₁ O _{1.01}
600	Magnetite	Fe ₃ O ₄
700	Magnetite Hematite Carbon Dioxide - Iv	Fe ₃ O ₄ Fe ₂ O ₃ C ₁ O ₂
800	Diiron Molybdenum (IV) Oxide Iron Oxide	Fe ₂ Mo ₁ O ₄ Fe ₂ O ₃
900	Diiron Molybdenum (IV) Oxide Hematite Magnetite low	Fe ₂ Mo ₁ O ₄ Fe ₂ O ₃ Fe ₃ O ₄
1000	Diiron Molybdenum (IV) Oxide Magnetite low	Fe ₂ Mo ₁ O ₄ Fe ₃ O ₄
1100	Wuestite	Fe _{0.92} O ₁
1200	Wuestite	Fe _{0.916} O ₁

Thus, phase transformations and oxide formation in particular spin cast HSS material have been studied for the first time, using in-situ HT-XRD. It was shown that the oxidation (*dry laboratory environment*) relates to the phase transformations. The observed solid-state transformation behavior of alloys was confirmed with the predicted equilibrium diagrams (*see Section 4.1*). The main oxide formation starts to occur between 600-700°C, which is consistent with sources in the literature [31, 32, 33].

In conclusion, all 15 provided radial samples (*see Table 2, Section 3.1*) were investigated with conventional X-ray diffraction analysis (*Cu-radiation*) in order to assess their crystallographic properties as a function of composition, radial location, and HT (*see Section 3.2.7*). The results show that crystal structure can vary depending on the location in the conventional HSS shell, whereas the improved cast material shows consistency even after being heat treated, meaning that no long-range diffusion occurs between the shell and core. More

advanced in-situ XRD (*Co-radiation*) was conducted on two coupons from the shell surface in the as-cast condition (*P0-cast* and *S-shell*, Table 2) at elevated temperatures in dry air atmosphere in order to reveal crystallographic changes during solid-state transformation and formation of relevant oxides at high temperatures, which is a key to understanding the diffusion reactions in-situ. In-situ high temperature XRD correlates to the thermodynamic predictions given in Section 4.1 (*equilibrium and non-equilibrium phase diagrams of Figures 53 and 47, respectively*). The testing revealed the lattice expansion behavior and the formation of new oxides as a function of temperature and phase transformations.

4.5.2 Bulk and microhardness analysis

In Figure 110 an example of a VHN hardness profile is shown, which is superimposed onto an optical image (*OM*) image of a conventional radial sample (*P0-cast*). The three main zone can be distinguished based on the hardness profile and macro-etching effect (*dark and white areas on the surface*): 1) hard zone; 2) hardness reduction; 3) low stabilized.

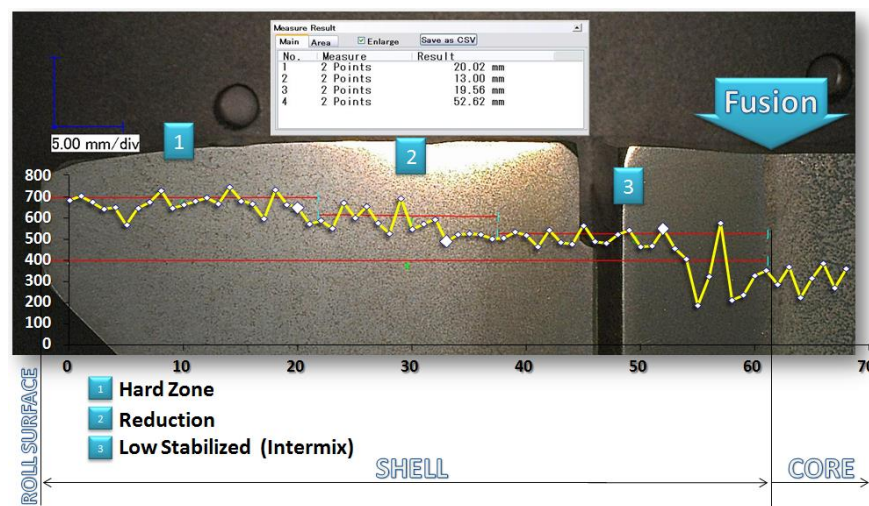


Figure 110. Example of VHN hardness measurements along the conventional radial sample (P0-cast)

In Figure 111, VHN profiles along the conventional HSS shells (*P0-samples, high carbon group, Table 2*) after different HTs are shown. The lines represent an averaged data: 5 actual values as one point on a curve. As it can be seen, bulk hardness measurements and microstructural observations (*discussed in Section 4.2*) of the conventional material indicate almost no effect of any sort of conventional HTs (*yellow, purple and green lines*). The only exception is the hardness measured after preliminary HT, showing considerable reduction, or softening (*red line, Figure 111*). These were the original measurements made, stimulating the current work in developing a more efficient HT, which would homogenize the hardness through the shell.

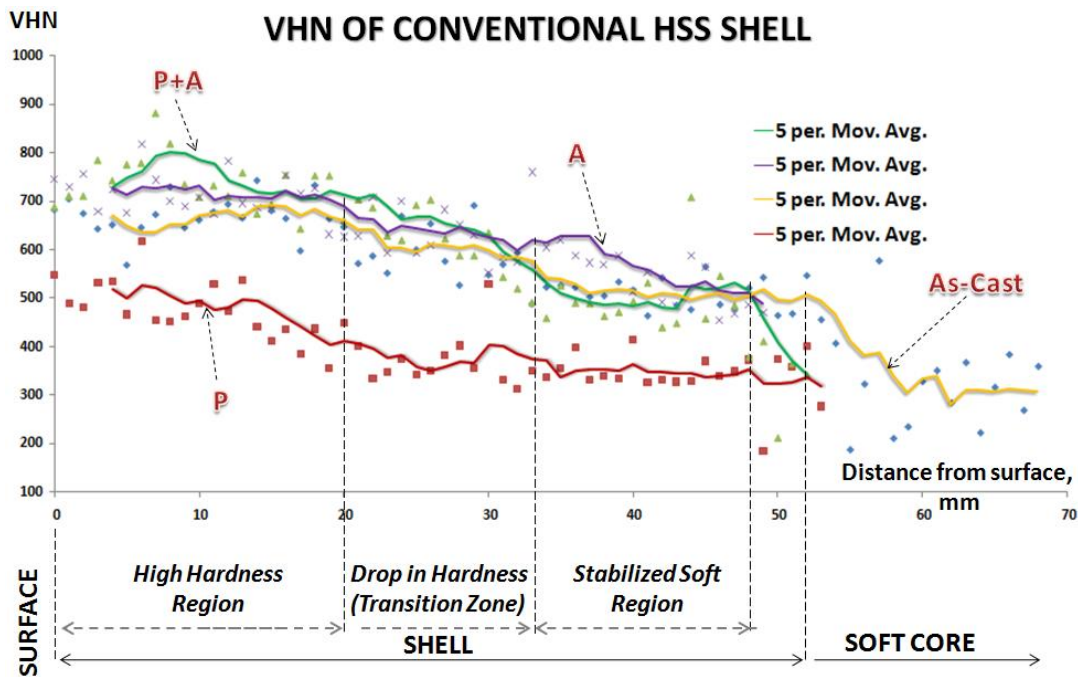


Figure 111. Averaged VHN profiles of conventional material (P0 samples, Table 2) vs. HT

More complete hardness data of samples from the Table 2, corresponding to overall bulk HRC profiles, are shown in Figure 112. In general, the hardness drop at the fusion line between the shell and core is expected for the studied cases. But the rate of the hardness decrease at this

bonding region depends on the centrifugal casting (*mixing*) and the width of the intermix zone, which is controlled by the casting rate and time intervals between solidification and pouring. An exceptional example is the CPC sample, which shows an immediate drop, because it has no transient region due to its different casting method (*continuous pouring for cladding*). Most significantly, the red line (*P9DT*) located above most of the profiles shows uniform, stable hardness from the surface to the bonding. It was formed by the non-conventional HT applied to the refined cast (*dash blue line below*).

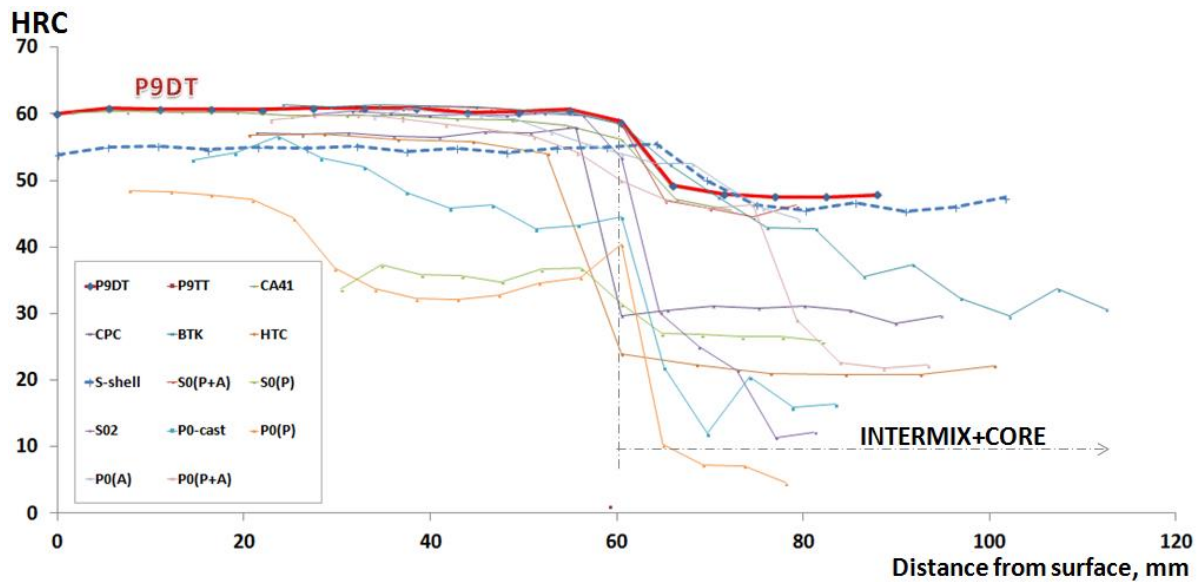


Figure 112. Overall bulk HRC profiles of HSS radial samples

Just the data comparing the conventional (*original*) and non-conventional (*improved*) approaches is given in Figure [113](#). The hardness of the new cast and new HT (*Type I*) in the figure stays uniform at 60 HRC right up until the core is encountered. The material starts as the as-cast (*Type II* in Figure [113](#)), which is also uniform until the core is encountered, but at a lower hardness (HRC 55). If the original HT is applied to the new cast (*Type III* in the Figure [113](#)), surface

hardness is improved (*HRC 60*), but it decreases to $< \text{HRC } 50$ toward the core. It is still an improvement over the conventional cast and HT (*Type IV in Figure 113*), which has an HRC hardness that is also non-uniform, not exceeding *HRC 55* and decreasing drastically from about 20mm depth to the core at 60 mm. Thus, the new material produced by the new cast and HT (*Type I*) has superior hardness characteristics when compared to the original material (*Type IV*), and thus is expected to have superior service life.

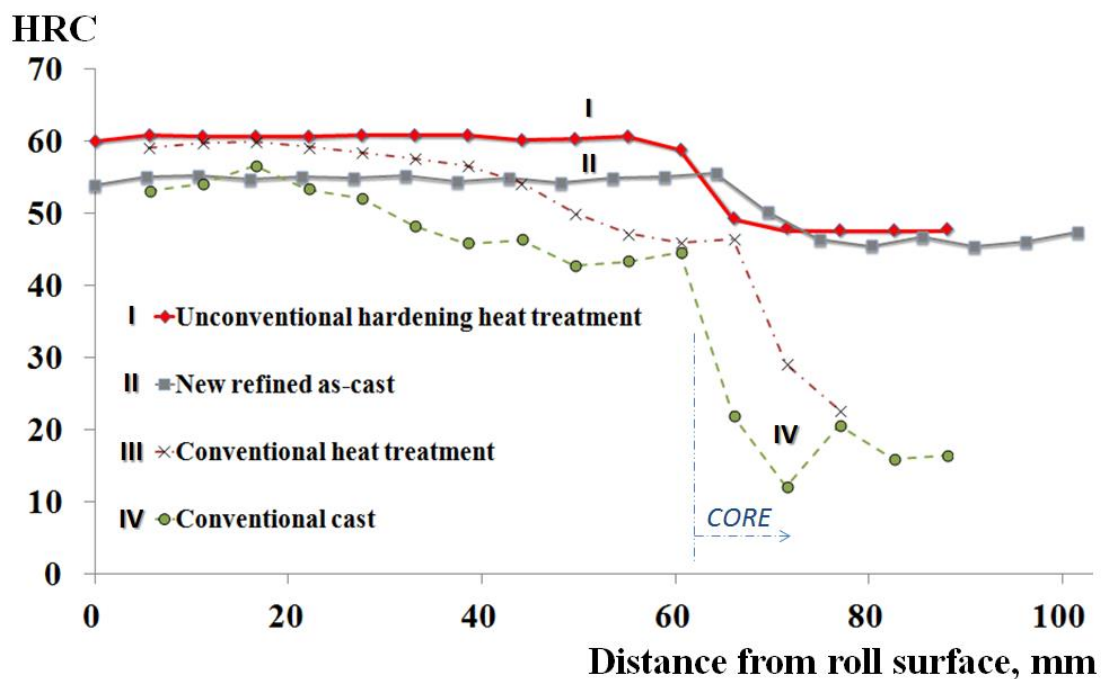


Figure 113. Selected bulk HRC profiles of conventional and improved materials

In order to validate the initial assumption concerning the matrix enrichment with alloying elements after a higher austenitization HT, micro-VHN hardness measurements were performed. Figure 114 shows an example of micro-indents in the matrix and boundaries.

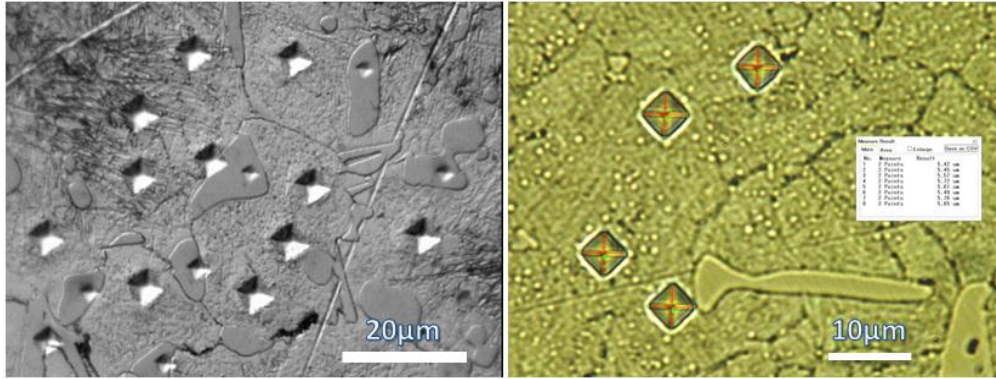


Figure 114. Micro-VHN of the matrix and carbides (Olympus and Keyence OM)

A series of indentations were made at the surface, middle and next to the bond locations, considering material condition and HT type, Figure 115.

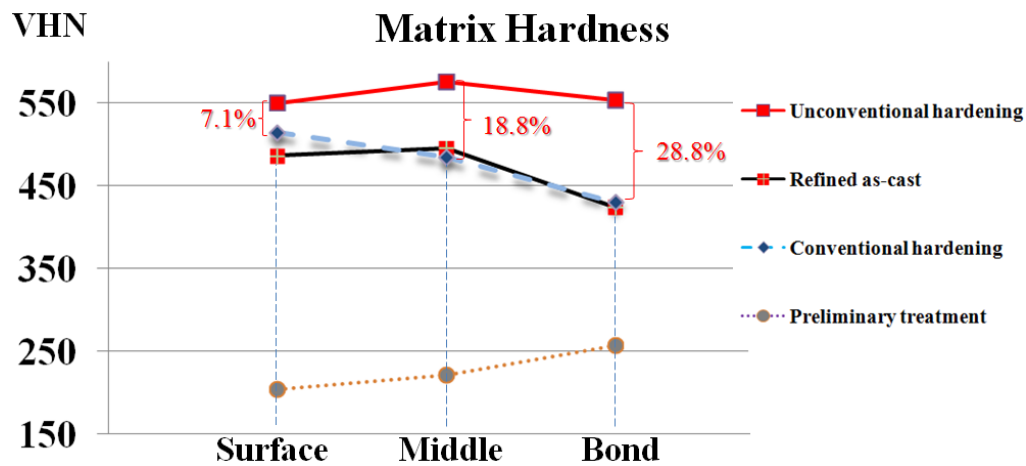


Figure 115. Micro-VHN of the matrix

From Figure 115 it is seen that the matrix strength is increased by as much as 7%, 18%, and 28% at the surface, middle and bonding region, respectively, and becomes more uniform after the new HT (*red curve*). Clearly, the shell is now heated with sufficient time and uniformity; therefore, the matrix is well homogenized, which can be concluded by comparing the as-cast condition (*decrease in hardness closer to the intermix zone*) and after the non-conventional HT

(no reduction). Additionally, looking at the conventionally hardened matrix profile and refined as-cast, it is evident that there is almost no difference. This result was also shown with the bulk hardness measurements mentioned in Figure [111](#), where initial as-cast values almost remained at the same levels to those of the conventionally heat treated material. When examining Figures [111](#) and [115](#), it can be suggested that the effect of preliminary HT is to soften the matrix of the bulk material. It was shown that this was achieved through matrix spheroidization, i.e. formation of incoherent spherical alloy carbides (see Section [4.2.2](#)). The matrix softening of the as-cast can cause a reduction in hardness that is 2.5-2.7 times lower. The subsequent hardening then increases it up to 3 times. Thus, the bulk hardness can be increased by 1.2-2 times after the hardening HT.

After triple tempering the hardness remained uniform along the shell (*P9TT*, Figure [112](#)), and a reduction of only 2 HRC points was measured, bringing the total value down to 58 HRC. Thus, with non-conventional HT, higher and more uniform attainable hardness is achieved along the HSS shell in the radial direction. The matrix shows enhanced response to the high temperature hardening as a result of the secondary precipitation of fine alloy carbides and increased matrix hardness.

Additionally, some relevant observations of the area of indentation itself were made, using SEM. Local micro-deformations in the vicinity of HRC indenter (*RT*) were located and given in Figure [116](#). The tangential stresses are schematically shown with the arrows on the sample surface. The improved matrix of P9DT was deformed plastically without any sign of cracks; although eutectic Mo-, V-carbides contain multiple parallel cracks that were oriented perpendicular to the tangential force direction (Figure [116](#)). By default, the carbides are 3-4 times harder than the matrix and, evidently, cannot be plastically deformed. But due to their separate and uniform

dispersion, the cracks do not connect and propagate through the matrix; they are basically entrapped within these fine carbides.

It is worthwhile to mention the role of carbide morphology and shape- that more round, idiomorphic carbides, e.g. MC (*dark phase*) might not have any crack-like features at all, presumably, due to their “by-passing” the stress field. In contrast, any boundary changes or sharpness plays a significant role as a stress concentrator within the area of the carbide; hence, brittle cracks can easily propagate from these spots.

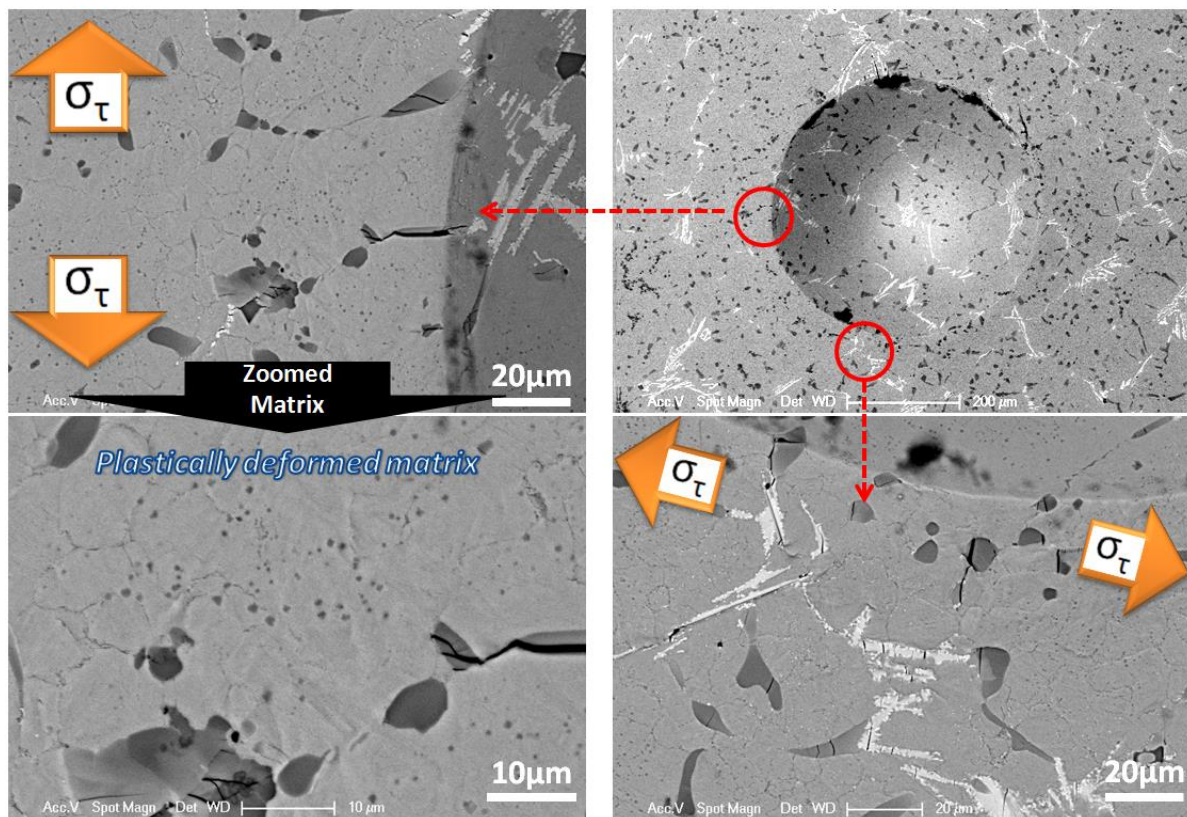


Figure 116. HRC indenter and local deformation of the matrix (P9DT)

Moreover, the refined as-cast structure, with finer prior austenite grain boundaries and fine sub-grain structure promotes higher toughness when compared to the conventional cast. These

types of simple findings help one to visualize and surmise the carbide-matrix response to in-service loading and how to select the proper carbide configuration, which can be controlled by the solidification rate and HT.

In conclusion, the hardness measurements of the bulk material and the matrix were performed, validating the development of the improved high temperature hardening HT. The bulk HRC measurements of all considered alloys were compared and analyzed, to find where the improved HSS material demonstrates the highest and uniform attainable hardness in the shell. The micro-hardness measurements (*VHN*) of the enriched matrix showed increased values along the shell in contrast with the conventional samples. Additionally, some assumptions and observations of local deformations after HRC hardness testing in the vicinity of indentation areas were made, confirming proper fracture toughness behavior of the matrix.

4.5.3 Image processing and phase balance analysis

The observed microstructural and hardness behaviors enabled one to identify the boundaries of the shell material, intermediate layer, fusion line, and the ductile iron core. The microstructures were found to consist of eutectic segregates, prior austenite grain boundaries, sub-boundaries, eutectic carbides inside of prior austenite cells, and precipitates with different degrees of coagulation and distribution as a function of the radial depth in the HSS shell.

Figure [117](#) demonstrates OM image processing of conventional P0-cast material, where all of the various carbides are highlighted simultaneously in different color with automatic boundary detection. The similar used color means that the selected particles are in the same size range. The particles' boundaries can be automatically traced using good quality images with adjusted balance

and contrast. But geometrical criterions have to be established in order to differentiate the different types of carbides in this case, filtering out the stored data spread-sheets.

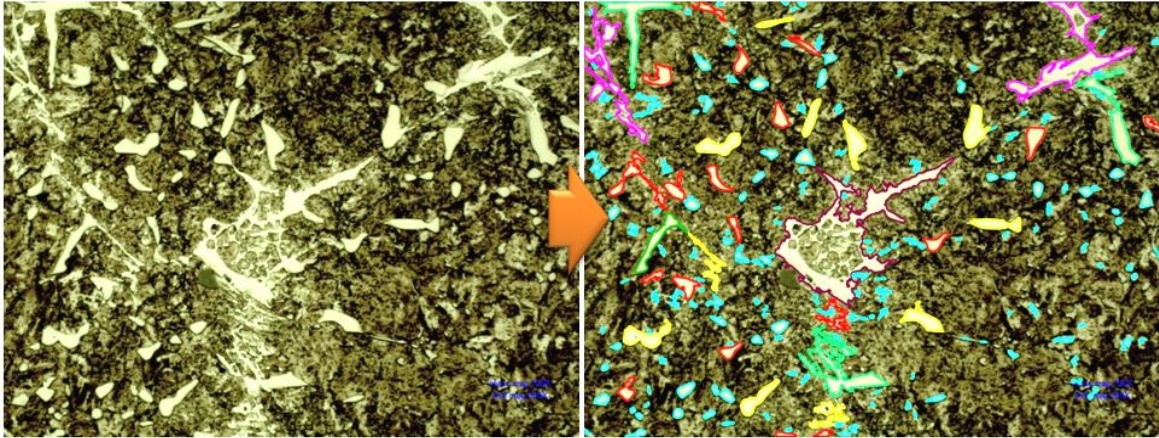


Figure 117. Example of OM processing for individual carbides identification in P0-cast (Pax It)

In Figure [118](#), an example of SEM processing is demonstrated, where MC (VC) and M_2C (Mo_2C) carbides can be easily recognized by dark gray and white colors, respectively.

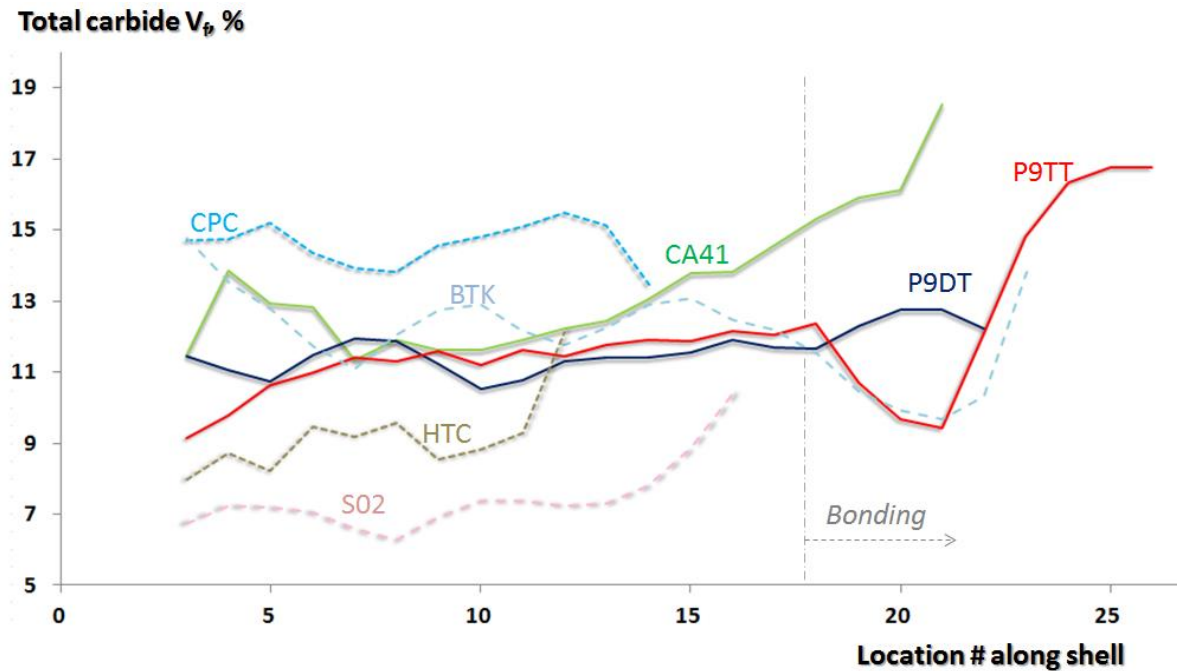


Figure 119. Total carbide volume fraction along the HSS shells

An example of measured individual carbides in the final hardened state (*P9DT*) is shown in Figure [120](#); where from surface to the core a volume fraction of eutectic MC (*VC*) and M_2C (Mo_2C) is plotted with imposed trend lines. Some possible scattering and non-uniformities are attributed to the “natural” segregation issues as a result of the centrifugal casting process and different densities of precipitates, which is discussed in Sections [4.2.1](#) and [4.3](#). This example clearly shows that “heavier” Mo-precipitates migrated to the outer surface, but “lighter” V-based particles- to the inner core. Nonetheless, the scattering is minimized by improving the cast and the shell, which has a more uniform hardness profile. In addition to these main eutectic carbides, the precipitation is observed through the matrix, comprising of nano-size, uniformly distributed alloy carbides (*V-rich*), improving mechanical properties.

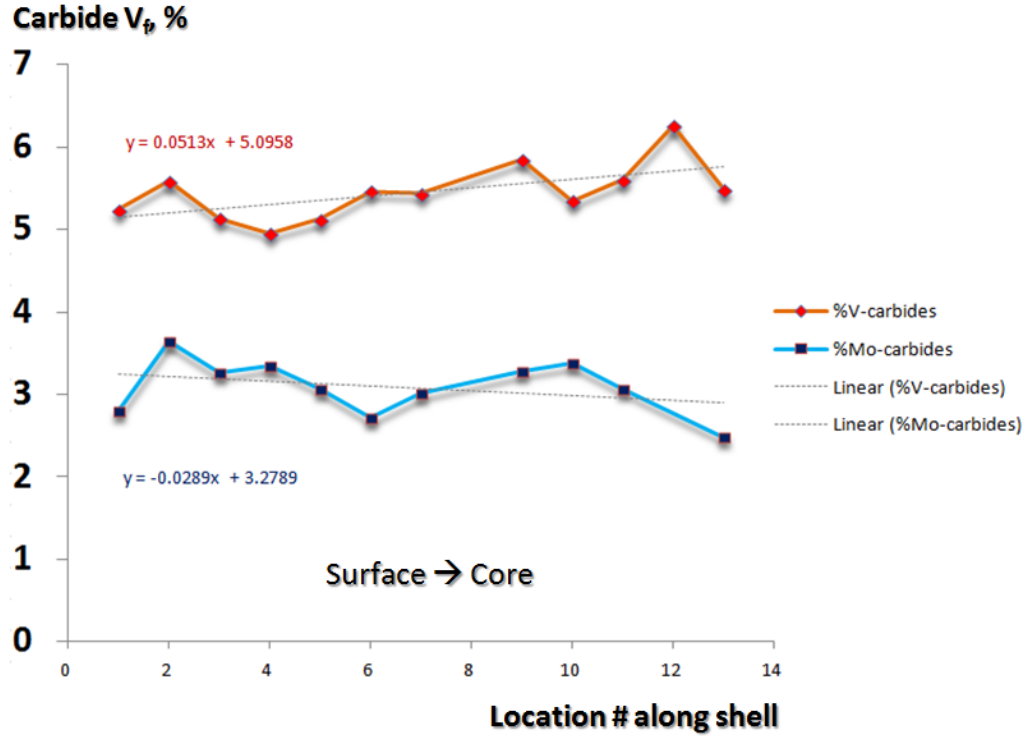


Figure 120. Volume fraction (%) of VC and Mo₂C along the P9DT HSS shell

The morphology of the carbides can be characterized by geometrical concepts such as: feret (*distance between pixel pairs*), skewness (*% area with respect to its own centric axis*), circularity, median, feret angle (*angle between max and min feret*), and solidity. Figure [113](#) shows an example of the MC carbide configurations in the same material (*P9DT*) as a function of distance from the roll surface. The circularity of MC carbides increases closer to the fusion line, while the feret trend lines decreases. The upward convex and downward convex shapes of the circularity plot and feret plots represent the dependence of circularity on feret. They reach their respective maximum or minimum in the middle of the shell. Such detailed graphical analysis helps to understand morphological variations of eutectic carbides through the thickness of the HSS shell and relate it to the controlling factors: 1) crystallization phenomenon in the centrifugal force field, 2) segregation behavior due to spin casting (*density effect and convective mixing*), 3) possible

compositional variations due to pouring the core material, affects the shape of carbides and nucleation at the intermix zone.

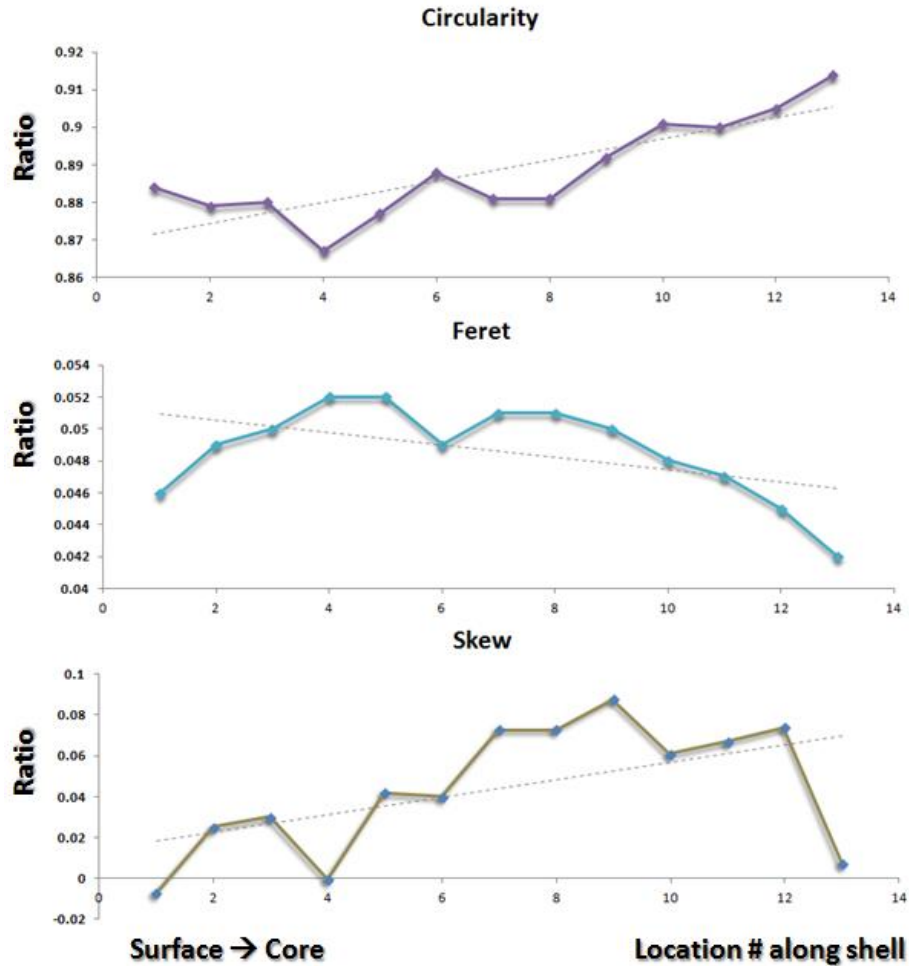


Figure 121. Example of geometrical changes of VC along the P9DT shell

In conclusion, the phase balance analysis was performed on all compositions using the image processing techniques. The types and total volume fraction of the respective carbides were determined. In general, it was found that the HSS material can contain about 6-15% of carbides in total. The refined HSS material has a uniform carbide distribution in the matrix with depth, with a total amount (10-12%). An increase in total amount of carbides by 1.1-1.2 times in the improved

HSS (*P9TT*), as a result of additional tempering, confirms the observed complete decomposition of M_2C and secondary precipitation of fine V-rich alloy carbides. Carbide morphology was characterized as a function of position in the HSS shell by introducing geometrical concepts such as: feret, skew, circularity, median [94]. Some measurements were shown for eutectic MC carbide distribution and morphology variations along as-cast shell related to centrifugal casting segregations, which depend on density and precipitation sequence of the phases and particles.

The conducted phase balance analysis based on OM and SEM image processing enabled the quantity of individual microconstituents to be assessed, including the shapes and morphological features of the particles and distribution as a function of radial distance. The results indicate that better quality control has been established during the spin casting operations. The uniform distribution of eutectic carbides with the rounded shapes in the matrix and along the HSS shell improves mechanical characteristics of the roll; specifically its wear resistance and fracture toughness are increased.

5.0 CONCLUSIONS

In order to improve the quality and performance of HSS horizontally spin cast rolls, a complex integrated approach, a “road map,” for the roll manufacturer was developed. The microstructure was refined and homogenized through the thickness of the working roll shell; therefore, the thermo-mechanical properties of the HSS shell material were improved. Practical guidance has been developed, focusing on proper chemistry selection and improvement of HT processing parameters, taking into account the structural integrity of the composite roll structure and modified heat treating practice. To attain the main goals, the program was divided into several phases: I) baseline characterization, II) simulations-predictions and III) post-characterizations. It included several approaches: 1) microstructural characterization of the conventional and modified HSS materials (*see Section [4.2](#)*); 2) numerical methods, including: CFD (*see Section [4.3](#)*), FEA (*see Section [4.4](#)*) and thermodynamic-kinetic simulations of the heterogeneous alloys (*see Section [4.1](#)*); 3) experimental characterization (*see Section [4.5](#)*).

A series of radial samples machined from the barrel of industrially produced centrifugally horizontally cast HSS work rolls were investigated. The samples were in either the as-cast, annealed, or fully hardened conditions, including worn HSS material that has been in an actual service environment (*see Section [3.1](#)*). Initial microstructural observations of conventional material after different HT conditions showed the same pattern for all the samples, where brittle eutectic interdendritic carbide networks remained unchanged. The gradual coarsening from surface to the bonding and matrix non-homogeneities lead to low fracture toughness and poor attainable hardness, which decreases through the thickness of the HSS shell (*see Section [4.2](#)*). It was decided that the cast structure had to be refined, which could be achieved by improving the alloy design

(see Section [4.1](#)) and adjusting the spin casting process based on CFD (see Section [4.3](#)). The effective hardening of the material was developed by proper non-conventional HT application, influencing dissolution of unstable carbides and interdendritic segregation (see Section [4.2.3](#)). For this step, multiple inspections and advanced analyses were performed, using modern experimental equipment and computational approximation software.

The dissolution of carbides, phase transformations, matrix hardening and oxide formation have been studied, using in-situ HT-XRD (see Section [4.5.1](#)), re-heating-re-melting experiments with accelerated air cooling, thermodynamic-kinetic and FE predictions. An integrated FE model of the HSS roll has been developed (see Sections [3.5](#) and [4.4](#)) based on actual and predicted thermodynamic-kinematic data, which considers HT thermal gradients, compositional variations, microstructural changes, and carbide decomposition behavior within the work HSS shell. These results were in turn used to develop a non-conventional HT, which alters the eutectic interdendritic solute-rich boundaries, homogenizes the matrix, and completes the dissolution of transient carbides, promoting an enhanced matrix response with uniformly distributed alloying nano-size carbides (*V-rich*). The microstructural evolution was studied in great details, comparing all provided alloys and HTs (see Section [4.2.4](#)). The thermal-stress-strain history of the roll during HT was simulated using ANSYS (see Section [4.4.3](#)), the results of which were used to establish safe technological parameters for the hardening HT with accelerated quenching methods.

The matrix is enriched with alloying content and homogenized after higher austenitization, which is demonstrated by nano-size alloy secondary precipitation and uniform increased microhardness (*VHN*) of the matrix (see Section [4.5.2](#)), where the increase in hardness numbers is approximately 18% on average with a standard deviation of 10%, depending on the location in the shell in contrast with conventionally heat treated HSS shell matrix. Moreover, the bulk Rockwell-

C (*HRC*) hardness measurements at room temperature through the HSS shell thickness also show uniform, stable hardness values from surface down to the core (*Line I, Figure [113](#)*), validating the efficiency of the new alternative HT process.

The structural integrity of the rolls, while being high temperature hardened, was taken into account and simulated with the aid of a multi-scale, multi-physical finite-element model. From that, the optimal HT parameters were selected, regarding available equipment and its capacity. Experimental in-situ HT-XRD, thermodynamic-kinetic predictions, and re-melting-re-heating data were used as inputs to the model. Therefore, the carbide-matrix dissolution-transformation behaviors were analyzed and predicted in order to achieve thermal stability of the matrix. The austenitization temperature and time were adjusted, leading to better dissolution and decomposition of the carbides, enriching the matrix with alloying elements, and breaking the interdendritic carbide networks, which improved strength and toughness. A supersaturated matrix facilitated improved local oxidation behavior at the carbide-matrix interface.

The developed multi-scale computational approach was based on sub-structuring and microstructural image-based FE modeling (*see Sections [3.5.2.4](#) and [4.4.4](#)*). The fundamental interpretation of the multi-layered structure helped to understand kinetics phenomena associated with carbide-matrix decomposition, i.e. continuous local transformations in the HSS shell. The developed model provided more insight into a complex non-linear heat transfer phenomena and related microstructural features in the material. Micro-scale heat transport simulations (*see Section [4.4.4](#)*) revealed the maximum heat fluxes at the carbide-matrix interface in eutectic interdendritic Mo-enriched zones, which is attributed to the higher thermal conductivity of Mo-constituents. The results were validated with observed partial decomposition of particular carbides.

The preliminary feedback from the customers (*hot rolling finishing mills*) confirmed that the performance of the new developed roll grades (*Synergy 100*) was increased by 1.5-1.7 times, based on the intervals between maintaining grinding operations and amount of rolled material before that.

6.0 SUMMARY

The research work resulted in multiple novel contributions, including:

1. Integrated computational-experimental approach has been developed to study microstructural evolution in the working shell of HSS rolls for finishing hot rolling mills. These research results were used to develop a non-conventional hardening HT, enabling one to modify the brittle eutectic interdendritic structure and to dissolve transient, unstable carbides. As a result, the matrix is homogenized and enriched with alloying content, facilitating secondary hardening, and hence, thermal stability.
2. Developed a coupled thermal-structural FE model to simulate the stress evolution in the composite roll body, ensuring structural integrity during hardening processing and accelerated cooling.
3. Developed a sub-structuring and image-based FE modeling method that enables one to simulate nonlinear heat transfer in the bulk material at the micro-scale. The fundamental interpretation of the multilayered structure helps to understand kinetics phenomena associated with carbides and matrix decomposition, i.e. continuous local transformations. The micro-scale heat transport reveals the microstructural response of a local point in the HSS shell, during heating and quenching cycles. This approach offers an applied alternative way to analyze complex micro-scale behavior of micro-constituents and the surrounding matrix.
4. Advanced in-situ HT-XRD was conducted on spun cast HSS materials for the first time in the open literature, enabling analysis of solid-state transformation and related high temperature (*up to 1200°C*) oxide formations in dry air.

5. Optimized HSS alloy facilitated as-cast refinement by changing the solidification path to higher temperatures without any equipment modifications or additional cooling systems. The effect of the standard preliminary HT on the refined structure became more significant: the homogenized matrix with reduced compositional variations and incoherent fine alloy carbides in the matrix facilitated increased dissolution during the hardening steps. Refined as-cast structure also promoted faster kinetics during the final hardening steps.
6. The research data is used for the new roll grade development- “Synergy 100”, the service life of which is 1.5-1.7 times higher, according to customer’s feedback.

7.0 FUTURE RESEARCH

Based on the results presented in this work, the following research directions are recommended in order to optimize the manufacturing (*casting and heat treatment*) and extend the service life of the HSS work rolls:

- Continuation of multi-physical simulation and modeling, including coupled mechanical, thermal and CFD analyses. For the 3-D CFD part, the vertical and horizontal casting procedures have to be analyzed and compared, including solidification models under centrifugal forces and two phase turbulent flows. Moreover, the static and spinning pouring of the core material, corresponding to the horizontal and vertical casting respectively, have to be included into consideration. The effect of the core solidification on the HSS shell has to be also studied.
- Development of an FE model of the complete mill assembly is also proposed, in order to simulate in-service conditions, defining vibration characteristics of the system and actual stress-strain conditions in bearings, joints and contact zones as a function of the geometrical and materials characteristics. The fracture mechanics and deterioration simulations are suggested as a part of a rheological study of the material behavior, based on friction contact mechanics and tribology.
- Microstructural image-based numerical simulations to understand a micro-scale diffusion, heat transfer and mechanical behavior of the HSS roll material, taking into account carbides morphology, distribution and thermo-physical properties. For example, by knowing the individual mechanical properties and assigning them to

each considered phase in the meso-scale FE model (*see Section 4.4.4*), it becomes possible to conduct virtual tests, simulating the mechanical response of the system. With this in mind, the effect of carbide morphology and distribution in the matrix can be investigated. The same discretized model can be used to study local deformation behavior and cracking issues.

- In-situ analysis of the carbides decomposition-dissolution behavior using high temperature X-Ray diffraction (*HT-XRD*), high temperature transmission electron microscopy (*HT-TEM*), and Hyper-Probe analysis. Crystalline properties, micro-strain and thermal expansion of the carbides and matrix as a function of temperature can be studied.
- The interdependence of each condition (*i.e. as-cast, preliminary, austenitization, and tempering*) as a function of composition, temperature and times have to be further refined and optimized. An experimental study will include dilatometry measurements and interrupted quench re-heating experiments.
- To validate improved mechanical properties, it is recommended to develop a hot wear setup resembling in-service conditions to study oxidation behavior with the aid of imaging systems. The strength and preferential growth of the oxides have to be studied.
- A new alloy development will be studied with the lab centrifugal heats. The intermediate layer and bonding will be optimized and validated with shear testing.
- NDT/NDE approach is proposed at different stages of the roll manufacturing, related to solidification and microstructural evolution, enabling a better quality control and automation.

- Further refinement of the casting is proposed, considering feeding arm re-design, electro-magnetic stirring and vibration mixing.
- For the as-tempered product, the surface hardening techniques will be examined to try to increase the surface properties of the roll body and journals. The core and journal design is considered, taking into account potential load capacity increase in the hot rolling stands.

BIBLIOGRAPHY

- [1] A.C. Reardon, Metallurgy for the Non-Metallurgist, Second edition, 2011, ASM International
- [2] M. Boccalini, H. Goldenstein, Solidification of high speed steels, International Materials Review, Vol.46, No.2, 2001
- [3] H.Sorano, N.Oda, J.Zuccarelli, History of High Speed Steel in Japan, Hitachi Metals, LTD Roll Company, MS&T Conference Proceedings, 2004
- [4] M.Hashimoto, T.Tanaka, T.Inoue, M.Yamashita, R.Kurahashi, R.Terakado, Development of Cold Rolling Mill Rolls of High Speed Steel Type by Using Continuous Pouring Process for Cladding, <http://vanitec.org/wp-content/uploads/2012/09/2002-Mitsuo-HASHIMOTO-V-2002.pdf>
- [5] J.Sato, K.Iwanaga, A.Tomioka, K.Nishiguchi, H. Nnakashima, H. Ishida, High-quality Work Roll Manufacturing Technology Using New Electro Slag Re-melting (ESR), http://www.kobelco.co.jp/english/ktr/pdf/ktr_30/001-006.pdf
- [6] <http://www.lhforge.com/rollingMillEquipment.htm>
- [7] J. Badger, Grindability of Conventionally Produced and Powder-Metallurgy High-Speed Steel, Annals of the CIRP Vol. 56/1/2007
- [8] P.Matteazzi, F.Wolf, Mechanomaking of high speed steel AISI M2: powder consolidation, Materials Science and Engineering, A248 (1998) 19–34
- [9] J. Richter, J. Cwajna, J. Szala, Quantitative assessment of new high-speed steel substrate and PVD wear-resistant coatings, Materials Characterization 46 (2001) 137 – 142
- [10] J.Richter, Application of Vickers indentation for assessment of PVD TiN coated new nonledeburitic high-speed steels, Surface and Coatings Technology 162 (2003) 119–130
- [11] R.A.Mesquita, C.A. Barbosa, Spray forming high speed steel—properties and processing, Materials Science and Engineering, A 383 (2004) 87–95
- [12] T. Kobayasahi, 1939- Strength and toughness of materials / Toshiro Kobayashi, 2004
- [13] K.C.Hwang, S.Lee, H.C.Lee, Effects of alloying elements on microstructure and fracture properties of cast high speed steel rolls Part II: Fracture Behavior, Materials Science and Engineering, A254 (1998) 296–304
- [14] K.C. Hwang, S. Lee, H.C. Lee, Effects of alloying elements on microstructure and fracture properties of cast high speed steel rolls Part I: Microstructural analysis, Materials Science and Engineering A254 (1998) 282–295

- [15] Video lecture “Hot Rolling Mill”, Hogskolan Dalarna University, Filmed at SSAB in Borlänge, source: <http://youtu.be/AuuP8L-WppI>
- [16] K. H. Schroder, Work rolls for plate mills and for roughing stands of hot strip mills/Steckel Mills, ESW-“The specialist of work rolls for hot rolling of flat products”, Tennek, Austria
- [17] Hanguang Fu, Qiang Xiao, Xing Jian-Dong, A study on the crack control of a high-speed steel roll fabricated by a centrifugal casting technique, Materials Science and Engineering, A 474 (2008) 82–87
- [18] K. Marsden, Y.Adonyi, Physical simulation of solid/liquid centrifugally cast bimetallic interfaces, Proceedings at the 43rd Annual Conference of the Iron and Steel Institute, Charlotte, NC, Oct. 28-30, 2001
- [19] I. Kiss, V. Alexa, V.G. Cioata, Experimental Research of the Thermal Stress in the Rolling Mill Rolls, The Scientific Collection of the University of Ruse, Vol.47, Serial 1.1, 2008 (*in English/Bulgarian*)
- [20] C.B. Pinca, G.O. Tirian, The study of thermal regime of the hot rolling mill cylinders, 10 International Research/Expert Conference, Trends in the Development of Machinery and Associated Technology, TMT 2006, Barcelona- Lloret de Mar, Spain, 11-15 September, 2006
- [21] WHEMCO/United Rolls technical reports and presentations
- [22] M. P. F. Sutcliffe, Rolling of Thin Strip and Foil: Application of a Tribological Model for “Mixed” Lubrication, Journal of Tribology, Jan 2002, Vol. 124, pp. 129-136
- [23] T.Udomphol, Rolling of metals lecture, Suranaree University of Technology, 2007, source: <http://www.scribd.com/doc/175013508/Rolling-of-Metals>
- [24] G.I. Dieter, Mechanical metallurgy, SI metric edition, McGraw-Hill, 1988
- [25] Remn-Min Guo, A semi-analytical solution of von Karman rolling equation with infinitely rigid rolls, Iron and Steel Technology, AISTech, Vol.10, No.11, pp.65-80, 2013
- [26] K.Gotoh et al., Effects of roll surface Deteriorations on scale defect in hot rolling, ISIJ, Vol.84, No.12, 1998 (*in Japanese*)
- [27] V.I.Kaplanov, A.G.Prisyazhnyi, Simulation of contact friction in the hot rolling of steel sheet, Steel in Translation, 2008, Vol.38, No.9, pp.714-718
- [28] K. Marsden et al., Fracture mechanics-based acceptance criteria of CVC rolls of a hot strip mill, Iron and Steel Technology, AISTech, Vol.10, No.11, pp.108-121, 2013
- [29] https://upload.wikimedia.org/wikipedia/commons/1/18/Kontakt_Spannungsoptik.JPG
Image by Reibungsphysik (Own work) [Public domain], via Wikimedia Commons

- [30] Video material “Rolling in Abaqus”, work by SANuragAbaqus, source: <http://youtu.be/E1d4WKkbtY>
- [31] A. Molinari, G. Straffelini, A. Tomasi, A. Biggi, G. Corbo, Oxidation behavior of ledeburitic steels for hot rolls, *Materials Science and Engineering A280* (2000) 255–262
- [32] Q. Zhu, H.T. Zhu, A.K. Tieu, M. Reid, L.C. Zhang, In-situ investigation of oxidation behavior in high-speed steel roll material under dry and humid atmospheres, *Corrosion Science* 52 (2010) 2707–2715
- [33] Q. Zhu, H.T. Zhu, A.K. Tieu, C. Kong, Three dimensional microstructure study of oxide scale formed on a high-speed steel by means of SEM, FIB and TEM, *Corrosion Science* 53 (2011) 3603–3611
- [34] A.Molinary, M.Pellizzari, Tribological behavior of spin cast high speed steels for hot finished rolls: effect of carbides on friction, wear and toughness, *Rolls 2003*, International Convention Center, Birmingham, UK
- [35] Gwidon W. Stachowiak, *Wear: materials, mechanisms and practice*, 2005, Tribology in practice series, John Wiley&Sons, Ltd., England
- [36] C.Vergne et al., Analysis of the friction and wear behavior of hot work tool scale: application to the hot rolling process, *Wear*, 250 (2001), 322-333.
- [37] C.K. Kim, J.I.Park, S.Lee et al., Effects of Alloying Elements on Microstructure, Hardness, and Fracture Toughness of Centrifugally Cast High-Speed Steel Rolls, *Metallurgical and Materials Transactions*, V.36A, Jan, 2005-87
- [38] A.Molinari, A.Tremea, M.Pellizzari et al., High Speed Steels for Hot Rolls with Improved Impact and Thermal Fatigue Resistance, *MS&T*, Vol.18, 2002
- [39] R. D. Mercado-Solis and J. H. Beynon, Simulation of thermal fatigue in hot strip mill work rolls, *Scandinavian Journal of Metallurgy* 2005; 34: 175–191
- [40] S.M. Hwang, C.G. Sun, S.R. Ryoo, W.J. Kwak, An integrated FE process model for precision analysis of thermo-mechanical behaviors of rolls and strip in hot strip rolling, *Computer Methods in Applied Mechanics and Engineering*, Section 191 (2002) 4015–4033
- [41] A.Gulyaev, *Physical Metallurgy*, Vol.2, pp.90-101, Moscow, 1978
- [42] L.S.Konstantinov, Centrifugal casting of cast iron, Moscow, 1959 (*In Russian, Константинов Л. С., Центробежное литье чугуновых отливок, М., 1959*)
- [43] S.B. Udin, S.E. Rosenfeld, M.M. Levin, Centrifugal casting, Moscow, 1962 (*In Russian, Юдин С. Б., Розенфельд С. Е., Левин М. М., Центробежное литье, М., 1962*)
- [44] B.N. Arzamasov, *Materials Science, Mashinostroenie*, Moscow, 1986 (*In Russian*)

- [45] A. Bedolla-Jucuinde et al., SEM study on the M7C3 carbide nucleation during eutectic solidification of high-chromium white irons, Carl Hanser Verlag, Munich, Germany, Z.Metallkd. 96, (2005), 12, pp. 1380-1385
- [46] H.Di et al., Microstructure and eutectic carbide morphology of the high speed steel strips produced by twin roll spin casting process, Journal of Materials Science Technology, 2003, Vol.19, No.5, pp.472-474
- [47] M.Rappaz, Probabilistic modeling of microstructure formation in solidification process, Acta metal.mater, Vol.41, No.2, pp.345-360, 1993
- [48] L.Nastac, Modeling and simulation of microstructure evolution in solidifying alloys, Kluwer Academic Publishers
- [49] L.Nastac et al., A computer model for simulation of multi-scale phenomena in the centrifugal casting of metal-matrix-composites, Materials proceeding in the computer age, EDS. V.R. Voller and H.Henein, Proceedings of TMS meeting, Nashville, TN, 2000
- [50] L.Nastac, K.Marsden, CFD modeling of macro-segregation and shrinkage in large diameter steel roll casting: chill study, Proceedings of 1st International Conference on Ingot Casting, Rolling and Forging, Germany, June 2012
- [51] Hanguang Fu, Qiang Xiao, Jiandong Xing, A study of segregation mechanism in centrifugal cast high speed steel rolls, Materials Science and Engineering A 479 (2008) 253–260
- [52] S.V.Cibrov, Research and Development of the spin casting technology of iron-based rolls, Moscow, 2006, Dissertation (*in Russian*)
- [53] Y.Luan et al., Effect of solidification rate on the morphology and distribution of eutectic carbides in centrifugal casting high-speed steel rolls, Journal of Materials Processing Technology, 210 (2010) 536-541
- [54] M.Boccalini et al., “Effects of Vanadium Content and Cooling Rate on the Solidification of Multi-Component White Cast Iron”, International Conference on the Science of Casting and Solidification, 2001
- [55] Yichuan Pan, Hua Yang, Xiangfa Liu, Xiufang Bian, Effect of K/Na on microstructure of high-speed steel used for rolls, Materials Letters 58 (2004) 1912– 1916
- [56] Fu-sheng PAN, Wei-qing WANG, Ai-tao TANG, Li-zhi WU, Ting-ting LIU, Ren-ju CHENG, Phase transformation refinement of coarse primary carbides in M2 high speed steel, Progress in natural Science: Materials International 21(2011), 180-186
- [57] Fu-sheng Pan et al., “Phase Transformation Refinement of Coarse Primary Carbides in M2 High Speed Steel”, Progress in Natural Science: Materials International, 21 (2011) 180-186

- [58] Dennis W. Hetzner, Refining carbide size distributions in M1 high speed steel by processing and alloying, *Materials Characterization* 46 (2001) 175 – 182
- [59] M.Hashimoto, O.Kubo, Y.Matsubara, Analysis of carbides in multi-component white cast iron for hot rolling mill rolls, *ISIJ International*, Vol.44 (2004), No.2, pp.372-380
- [60] Xu Liujie, Wei Shizhong et al., Phase structure and fine microstructure of in-situ vanadium carbides in cast high-vanadium high-speed steel, *Metals and Materials International*, Vol.12, No.5(2006), pp.371-375
- [61] Z.Tianming, W.Qinjuan, S.Xuding, F.Hanguang, Effect of Casting Technology on Microstructure and Phases of High Carbon High Speed Steel, *China Foundry*, V.8, N2, 2011
- [62] ASM Handbook, Vol.1, Properties and Selection Irons, Steels, and High-Performance Alloys, 10th Edition, ASM International, 1990
- [63] A.G.Khachaturyan, Theory of Structural Transformations in Solids, Mineola, NY: Dover Publication, Inc., 2008
- [64] Y.Luan et al., “A Study of the Carbides in High-Speed Steel Rolls”, *Materials Science Forum* Vols. 638-642 (2010) pp 3356-3361
- [65] G.V. Samsonov, G.Sh.Upadhaya, V.S.Neshpor, Physical Materials Science of Carbides, Kiev, 1974, Publisher “Naykova Dumka” (*In Russian*)
- [66] V N Lipatnikov et al., “Phase Transformations in Non-Stoichiometric Vanadium Carbide”, 1999 *J. Phys.: Condens. Matter* 11 163
- [67] Tool Steel, 4th Edition, ASM, 1980, pp.110, 127, 682-694
- [68] W.E. Bryson, Heat Treatment, Selection, and Application of Tool Steels, second edition, Hanser Publications, 2005
- [69] H.Fu, Y.Qu et al., “Investigations on Heat Treatment of a High-Speed Steel Roll”, *JMEPEG* (2008), ASM International, 17:535-542, DOI: 10.1007/s11665-007-9174-4
- [70] F.Hanguang, Effect of quenching temperature on structure and properties of centrifugal casting high speed steel roll, *China Foundry*, 2009, Vol.6, No.1, pp.15-19
- [71] G.Hoyle, “Recent Developments in High-Speed Steels”, *Metallurgical Reviews*, Volume 9, 1964 pp. 49-91(43), ISSN 0076-6690
- [72] A.K. Sinha, Ferrous physical metallurgy, Butterworth Publishers, 1989, pp.544-564
- [73] S.M.Musa, Computational nanotechnology modeling and applications with MATLAB, CRC Press, 2012, p.31

- [74] W.D.Lian, G.Legrain, P.Cartraud, Image-based computational homogenization and localization: comparison between X-FEM/levelset and voxel-based approaches, Computational Mechanics, Vol.51, Issue 3 (2013), pp.279-293, <http://link.springer.com/article/10.1007%2Fs00466-012-0723-9>
- [75] C.L. Richardson et al., An XFEM method for modeling geometrically elaborate crack propagation in brittle materials, International Journal for Numerical Methods in Engineering, 2009, www.math.ucla.edu/~jteran/papers/RHSHT10.pdf
- [76] U. Hanoglu, Siraj-ul-Islamand, B. Sarler, Thermo-Mechanical Analysis of Hot Shape Rolling of Steel by a Meshless Method, Procedia Engineering 10 (2011) 3173–3178
- [77] T.Rabczuk, J.-H. Song, T.Belytschko, Simulations of instability in dynamic fracture by cracking particles method, Engineering Mechanics, Vol.76, (2009), pp.730-741
- [78] R.Sharma, P.Mahajan, R.K. Mittal, Image based finite element analysis of 3-D-orthogonal carbon-carbon (C/C) composite, Proceedings of the World Congress on Engineering, 2010, Vol.II, WCE, London, U.K., http://www.iaeng.org/publication/WCE2010/WCE2010_pp1597-1601.pdf
- [79] OOF: <http://www.ctcms.nist.gov/oof/>
- [80] G.T.Charras, R.E. Guldborg, Improving the local solution accuracy of large-scale digital image-based finite-element analyses, Journal of Biomechanics, Vol.33, Issue 2, pp.255-259, (2000), <http://www.jbiomeSection.com/article/S0021-9290%2899%2900141-4/abstract>
- [81] K.V. Redkin et al., Multi-scale finite-element modeling and microstructural evaluation of centrifugally cast high-speed steel finishing rolls, Iron and Steel Technology, AISTech, Vol.10, No.10, pp.69-84, 2013
- [82] H.L.Lukas et al., Computational thermodynamics. The Calphad method, University Press, Cambridge, 2007
- [83] N. Saunders et al., The calculation of TTT and CCT diagrams for general steels, www.sentessoftware.co.uk/media/2540/ttt_cct_steels.pdf
- [84] Z. Guo et al., Modeling phase transformations and material properties critical to the prediction of distortion during heat treatment of steels, International Journal of Microstructures and Materials Properties, Vol.4, No.2, 2009, pp.187-195, www.sentessoftware.co.uk/media/14611/ijmmp.pdf
- [85] Z.Guo et al., Modeling of material properties and behavior critical to casting simulation, Materials Science and Engineering, A 413-414, (2005), pp.465-469 <http://www.sentessoftware.co.uk/media/2528/casting-05.pdf>
- [86] <http://ansys.com/Products/Simulation+Technology/Fluid+Dynamics>

- [87] <http://www.cd-adapco.com/products/star-cd>
- [88] <http://www.esi-group.com/software-services/virtual-manufacturing/casting>
- [89] <http://www.finitesolutions.com/Products/SOLIDCast.html>
- [90] <http://www.comsol.com/cfd-module>
- [91] <http://openfoam.com/features/>
- [92] <https://sites.google.com/a/bioquant.com/main/>
- [93] <http://www.paxcam.com/products/imaging-software/pax-it-imaging-software/>
- [94] <http://rsb.info.nih.gov/ij/>
- [95] B. V. Balakin, Experimental and theoretical study of the flow, agglomeration and deposition of gas hydrate particles, University of Bergen, Norway, PhD Thesis, 2010
- [96] G. I. Pisarev, V. Gjerde, W. Peng, H. A. Dijkstra, B. V. Balakin, A. C. Hoffmann. Experimental and computational study of the 'end of the vortex' phenomenon in reverse-flow centrifugal separators. *AIChE Journal*, 58, 1371-1380, 2012.
- [97] B.V. Balakin, A.C. Hoffmann and P. Kosinski. The collision efficiency in a shear flow. *Chemical Engineering Science*, 68, 305-312, 2012.
- [98] J.W. Telford, "A Theroretical value for von Karman's constant", *PAGEOPH*, Vol.120 (1982) <http://link.springer.com/article/10.1007%2F00876650#page-1>
- [99] Theory reference for the mechanical APDL and mechanical applications, Release 12.0, 2009, ANSYS
- [100] <http://www.autodesk.com/products/autodesk-autocad-raster-design/overview>
- [101] F.G. Rammerstorfer, A.F. Plankensteiner, F.D. Fischer, T. Antretter, Hierarchical models for simulating the mechanical behavior of heterogeneous materials: an approach to high speed tool steel, *Materials Science and Engineering A259* (1999) 73–84
- [102] A. Okabayashi, H.Morikawa, Y.Tsujimoto, Development and Characteristicis of High Speed Steel Roll by Centrifugal Casting, Kubota Corporation, Amagasaki-city, SEAIISI Quarterly, Japan, 1997
- [103] J. Lecomte-Beckers, J.T.Tchuindjang, E.Pirard, J.Breyer, Physical Metallurgy of a HSS material for Hot Rolling Mill Rolls, 14th IAS Rolling Conference, San Nicolas, Argentina, 2002
- [104] M. Wießner, M. Leisch, H. Emminger, A. Kulmburg, Phase transformation study of a high speed steel powder by high temperature X-ray diffraction, *Materials Characterization*, N59 (2008) 937-943

- [105] ASM Handbook, Vol.3, Alloy Phase Diagrams, 10th Edition, ASM International, 1998
- [106] J.Tchoufang Tchuindjang, J.Lecomte-Beckers, Study of the origin of the unexpected pearlite during the cooling stage of two cast high-speed steels, Solid State Phenomena Vols. 172-174, pp.803-808, 2011
- [107] K.Kaneko et al., Characterization of carbides at different boundaries of 9Cr-steel, Materials Science and Engineering, A 374 (2004), 82-89
- [108] J.Domitner et al., “3-D Microprobe Analysis of Dendritic Structures in Steel”, Materials Science and Technology, 2010, pp 908-916
- [109] M.Hirao, H. Ogi, EMATS for science and industry: non-contacting ultrasonic measurements, Springer, 2003
- [110] K.V.Redkin et al., 3-D CFD simulation of horizontal spin casting of high speed steel roll, abstract 1B.00085, 66th Annual Meeting of the American Physical Society, Division of Fluid Mechanics, Vol.58, No.18, November 2013, Pittsburgh, <http://meetings.aps.org/Meeting/DFD13/Event/204682>
- [111] M.Onink et al., “The Lattice Parameters of Austenite and Ferrite in Fe-C Alloys as a Functions of Carbon Concentration and Temperature”, Scripta Metallurgica, Vol.29, (1993), pp 1011-1016
- [112] M. Wiebner et al., “Phase Transformation Study of a High Speed Steel Powder by High Temperature X-Ray Diffraction”, Materials Characterization, 59 (2008), pp 937-943
- [113] S.S. Babu et al., “In-situ Observations of Lattice Parameters Fluctuations in Austenite and Transformation to Bainite”, Metallurgical and Materials Transactions, A 36A (2005), pp 3281-3289
- [114] P.G. Shewmon, Diffusion in solids, 1963, McGraw-Hill Book Company, Inc.
- [115] M. Boccalini, A. Sinatora, Microstructure and Wear Resistance of High Speed Steels for Rolling Mill Rolls, 6th International Tooling Steel Conference
- [116] A. Tremea, M. Grespi, Work rolls behavior in the roughing stands at South American hot strip mills, 48th Rolling Seminar- Processes, Rolled and Coated Products, 2011, Santos, SP, Brazil
- [117] S. Wei, J. Zhu, L. Xu, Effects of vanadium and carbon on microstructures and abrasive wear resistance of high speed steel, Tribology International, 39 (2006) 641–648
- [118] J. Richter, Tribological evaluation of high-speed steels with a regulated carbide phase, Materials Characterization, 50 (2003) 339 – 347

- [119] C. Rodenburg, W.M. Rainforth, A quantitative analysis of the influence of carbides size distributions on wear behavior of high-speed steel in dry rolling/sliding contact, *Acta Materialia* 55 (2007) 2443–2454
- [120] A. Okabayashi, H. Morikawa, Y. Tsujimoto, Development and characteristics of high speed steel roll by centrifugal casting, Kubota Corporation, Amagasaki-city, SEISI Quarterly, Japan, 1997
- [121] J. Lecomte-Beckers, J.T. Tchuindjang, E. Pirard, J. Breyer, Physical Metallurgy of a HSS material for Hot Rolling Mill Rolls, 14th IAS Rolling Conference, San Nicolas, Argentina, 2002
- [122] A.O. Chernyavsky, Finite element method: basis of practical implementation, 2003, South Ural State University, SUSU Press. (*In Russian*)
- [123] P. Smolinski, Finite element method, course lectures, 2009-2012, University of Pittsburgh
- [124] P.Tong, J.N. Rossetto, Finite element method: basic technique and implementation, 1977, MIT Press.
- [125] <http://www.ansys.com/Products/Workflow+Technology/ANSYS+Workbench+Platform>
- [126] <http://union.es.com/technical-service-and-support>
- [127] A. Molinari et al., Influence of microstructure and chromium content on oxidation behavior of spin cast high speed steels, *Materials Science and Technology*, 2001, Vol.17, pp.425-430
- [128] G.F. Vander Voort, E.P. Manilova et al., Study of selective etching of carbides in steel, Proceedings of DGM, 2004 www.dgm.de/past/2004/metallographie/download/686_60.pdf
- [129] H.L. Lukas, S.G. Fries, Bo Sundman, Computational Thermodynamics. The CALPHAD Method, Cambridge University Press, 2007
- [130] <http://www.compu therm.com/>
- [131] <http://www.sentessoftware.co.uk/jmatpro.aspx>
- [132] S.H. Davis, Theory of Solidification, Cambridge Monographs on Mechanics, New York, Cambridge University Press, 2001